Technische Universität München
Department Chemie
Lehrstuhl für Physikalische Chemie I

# MOBILE LASER-INDUCED FLUORESCENCE SET-UP FOR MOTOR OIL CONSUMPTION MEASUREMENTS AND LASER DESORPTION SOURCE FOR STUDIES OF SOOT FORMATION

Eduardo Alonso-Gil

Vollständiger Abdruck der von der Fakultät für Chemie der Technischen Universität München zur Erlangung des akademischen Grades eines
Doktors der Naturwissenschaften
genehmigten Dissertation.

| | |
|---|---|
| Vorsitzender: | Univ.-Prof. Dr. S. Günther |
| Prüfer der Dissertation: | 1. Univ.-Prof. Dr. U. K. Heiz |
| | 2. Univ.-Prof. Dr. R. Niessner |

Die Dissertation wurde am 08.01.2015 bei der Technischen Universität München eingereicht und durch die Fakultät für Chemie am 30.01.2015 angenommen.

To María Luisa Henar Velasco Gallego


**“Theory guides, experiment decides”**

**(Izaak Maurits Kolthof, 1894-1993)**

# Acknowledgments

My highest gratitude is to Prof. Dr. U. Boesl. He gave me four years ago the chance to carry out my PhD thesis in Germany. Thus one of my dreams has become reality, to be doctor. This is just another step on the way to become Professor and maybe, in the best case, a scientist so well worldwide recognized as U. Boesl is. He is by far the best scientist that I have ever met and what is more important to me, he is a wonderful person. With him, I have discussed science, thought and performed experiments, but also I have learnt to be patience with results that seem to never come. Rigor, persistency, passion and curiosity are abilities and feeling that any investigator must hold. Scientist must also have in my opinion three skills; capacity of analysis, ability of questioning all what its eyes have seen (or have believed to regard) and a huge patience reservoir. Ulli has all what I mentioned and something else that one can only gain with the pass of the time; wisdom. I would like to express my gratitude to Prof. Dr. U. Heiz to let me be part of his group, where I have been so comfortable working and nearly living this last period of my life. His dedication, his kindness and his welcome were an example for me, and will serve as guidance in my life. I want to mention here also to Prof. Dr. F. Esch with who I have talked so much about so many things; science, politics, people, languages, but the best; about life. His enthusiasm will accompany the rest of my life. I thank to Dr. Kelnberger and Menhard (Innolas Laser-GmbH) their will to cooperate with us as well as the effort and patience employed in fixing and solving OPO problems. Besides I thank Bacher and Dr. Hatmann (BMW-AG) for their time and ideas. I am very grateful to my group colleagues; Stephan, Christoph, Kathy, Dragan and Jörn. With them I have had a lot of fun and enjoyed doing science. Kathy has been my major support in the long, hard, lonely and sometimes exhausting but funny and fascinating life in laboratories. I will be always grateful to some very especial colleagues of my department; Brad, Kathrine, Aras, Phillip, Martin and Daniel. Thanks for your time, comprehension, respect, advices, affection and smiles. You all supported me more than you imagine. I must admit that nothing would have been accomplished without the help of the glass, electronic and mechanical workshops, as well as without help of Danni, Tauchmann and Eckinger. I want to give thanks to my family: Gustavo, Raquel, Haydée, Soledad y Gonzalo that despite the distance has made this trip much easier. I am eternally grateful to May. Without the love of her, all this had not been possible or made any sense. This work is dedicated to her, as I wish and want to dedicate my entire life, time and future successes. I am pretty sure that you will be each day the best in my life. Finally I thank very much to Bayerische Forschung Stiftung (BFS) for granting me with a three year scholarship.

# Abstract

Oil consumption measurements have still the most interest and utility for car engineers. It is considered to be of crucial importance for testing new engine designs. Besides, engine efficiency is probed by means of oil consumption as well as it serves to decipher cylinder behavior at any speed and load (3D map). In this work a mobile apparatus which measures in-situ and on-line oil consumption in an accurate, precise and quantitative way is presented. An oil consumption instrument based on sulfur trace analysis was developed and optimized for marketing purposes. It is based on sulfur traces existing in oil. Firstly, molecules containing sulfur in oil are oxidized. Conversion of sulfur content to $SO_2$ with a yield close to 100% is achieved in a very robust, straightforward and homemade glow discharge cell. The nonthermal plasma generated is capable to break easily simple and double carbon-sulfur bounds. The resulting sulfur is then oxidized within a minimum percent of oxygen (3%). Secondly, fluorescence of $SO_2$ induced by laser is easily recorded and employed to monitor consumption of oil and in consequence to perform definitive engine tests. A high tech, but simple as well as compact laser was designed in cooperation with InnoLas Laser-GmbH. Interferences at the operation conditions (3 mbar and 230 °C) and UV wavelengths (220.6 nm) are only due to NO. The long lived fluorescence of it makes possible its subtraction via mathematical corrections. Linearity of integrated fluorescence versus concentration was demonstrated over two orders of magnitude (0.034 ppm to 3.4 ppm). Concentration as low as 28 ppb were easily detected even in presence of much higher NO concentration. The time resolution can be as fast as 1.6 second per measurement. Final prototype is ready to be commercialized without big changes or further developments.

Moreover, this work contains a theoretical description and an experimental explanation of the setting up of a laser induced time of flight mass spectrometer based on multiphoton ionization. A pulsed laser desorption source working at high vacuum was fixed to a two-step short linear time of flight mass spectrometer. The resulting system incorporates all the necessary devices to carry out studies of thermolabile molecules desorbed from the bulk or a pre-selected matrix. The system was used to analyze formation of soot by desorbing polyaromatic hydrocarbon. These sorts of molecules are formed in combustion engines and it could occur that upon certain condition of dehydrogenation, or more complex reactions, transformation in soot may occur. In this work decacyclene ($C_{36}H_{18}$) was desorbed under different photon fluences to investigate its cluster formation as well as the fragmentation pattern.

# List of abbreviations and units

| | |
|---|---|
| A | Ampere |
| amu | Atomic mass unit |
| Ar | Argon |
| BBO | β-borium borate |
| BMW-AG | Bayerische Motoren Werk Aktiengesellschaft |
| BNC | Bayonet Neill-Concelman |
| CCD | Charge-coupled device |
| CL | Confidence limit |
| COM | Communication port |
| CQ | Collisional quenching |
| CSALB | Cross sectional area laser beam |
| Da | Dalton |
| DFG | Difference frequency generation |
| DWSM | Double wavelength switching mode |
| e | Extraordinary |
| EII | Electron impact ionization |
| FC | Fluorescence cell |
| FRET | Fluorescence resonance energy transfer |
| FT-IR | Fourier transform infrared |
| FWHM | Full width half maximum |
| GDC | Glow discharge cell |
| $H_2S$ | Sulphhydric acid |
| HC | Hydrocarbons |
| He | Helium |
| HR | High reflection |
| HT | High transmission |
| Hz | Hertz |
| IC | Internal conversion |
| IR | Infrared |
| IRIDS | Infrared ion depletion spectroscopy |
| ISC | Intersystem crossing |

| | |
|---|---|
| ISHG | Intracavity second harmonic generation |
| J | Joule |
| K | Kelvin |
| LA | Laser ablation |
| LAN | Local area network |
| LD | Laser desorption |
| LIDAR | Light detection and ranging |
| LIF | Laser induced fluorescence |
| LxWxH | Length, width, height |
| m | Mili |
| MCP | Microchannel plate or multichannel plate |
| MPI | Multiphoton ionization |
| N·m | Newton·metre |
| NA | Numerical apperture |
| Nd:YAG | Neodymiun-doped yttrium |
| Ne | Neon |
| NO | Nitric oxide |
| NTP | Nonthermal plasma |
| o | Ordinary |
| OC | Oil consumption |
| OPA | Optical parametric amplifier |
| OPO | Optical parametric oscillator |
| PAH | Polyaromatic hydrocarbon |
| PC | Personal computer |
| PCs | Pockels cells |
| PL | Prediction limit |
| PMT | Photomultiplier tube |
| ppb | Parts per billion |
| ppm | Parts per million |
| ppt | Part per thousand |
| QMS | Quadrupole mass spectrometer |
| r.p.m | Revolutions per minute |

| | |
|---|---|
| REMPI | Resonance enhance multiphoton ionization |
| Re-TOF | Reflectron time of flight |
| S | Singlet state |
| s | Second |
| SA | Scattering amplitude |
| sccm | Standard cubic centimeter per minute |
| SHG | Second harmonic generation |
| SHV-BNC | Security high voltage-BNC |
| SNR | Singnal to noise ratio |
| SO2 | Sulfur dioxide |
| sr | Steradians |
| STD | Standard deviation |
| T | Triplet state |
| TCP/IP | Transmission control protocol/internet |
| TCR | Thermal coefficient of resistance |
| TTGIM | Two temporal gate integration method |
| THG | Triple harmonic generation |
| UV | Ultraviolet |
| V | Volt |
| VIS | Visible |
| VOC | Volatile organic compound |
| W | Wolfram |
| WL | Wavelength |
| η | Yield |
| µ | Micro |
| ω | Harmonic |

# Part A: Mobile Laser-Induced Fluorescence Set-Up for Motor Oil Consumption Measurements

# 1. Introduction

Combustion engines are still the most frequently used engines in; motorcycles, large boats, many light aircrafts and especially in cars. The so called 4-stroke engines are able to develop high power which is necessary to transport enormous amounts of frights, raw materials or people. The mechanics of such engines is currently quite complicated. They have been largely investigated, developed and improved in the last hundred years. The most important parts of an engine are the pistons and the cylinders. These are plotted in figure 1.1. and described with more detail in the following.

- **Cylinder:** Cylindrical vessel in which a piston makes a motion up and down.
- **Piston:** Cylindrical component which makes movements up and down within the cylinder.
- **Combustion chamber:** The space above piston in which the combustion of the fuel-air mixture takes place and which is inside and at the top of the cylinder.
- **Intake and exhaust ports/valves:** Ports that carry fresh fuel-air mixture into the combustion chamber and the products of combustion out of it.
- **Crankshaft:** A shaft that converts reciprocating motion of the piston into rotary motion.
- **Connecting rod:** A rod that connects the piston to the crankshaft.
- **Spark plug:** An ignition-source in the cylinder head that initiates the combustion process.
- **Reed valve:** Fuel/air check valve.

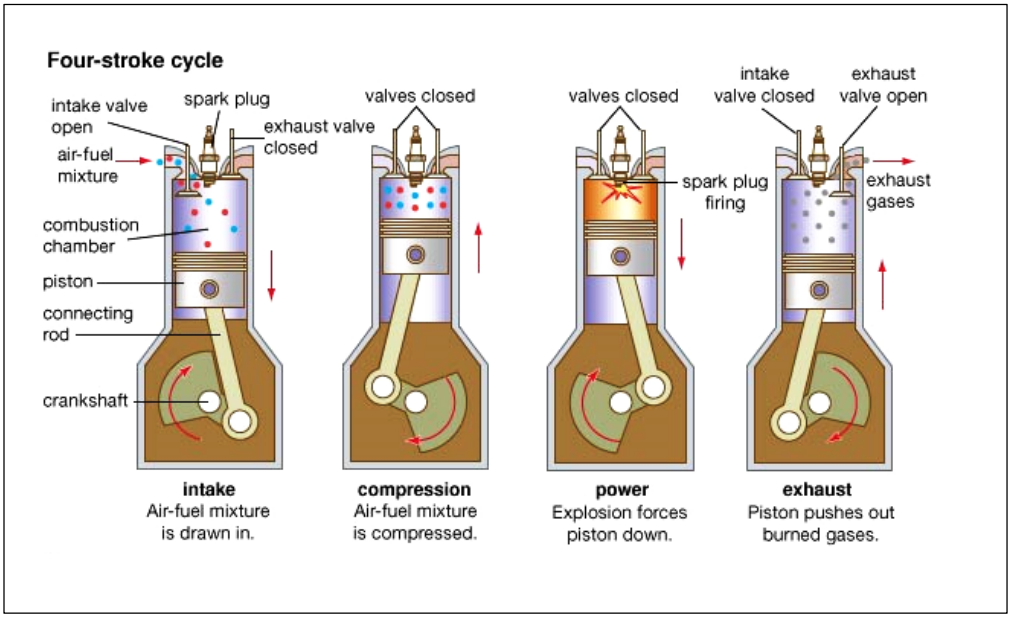


Figure 1.1. Working on and mechanical parts of a four stroke combustion engine.

The entire process taking place in a four-stroke combustion engine consists of four steps; intake stroke (induction), compression stroke (compression), power stroke (power-combustion) and exhaust stroke (exhaust). Those can be represented thermodynamically by an idealized Otto-cycle (fig. 1.2). However, in reality the Otto-cycle is not accomplished but a pseudo Otto-cycle is followed instead. Figures 1.2 shows the four different steps which are part of an Otto-cycle and what occurs in every of them. Besides, a theoretical perfect thermodynamic Otto-cycle is described in a diagram of pressure $(p)$ versus volume $(V)$. These four steps are: 1) adiabatic (isentropic) compression, 2) constant volume heat transfer, 3) adiabatic expansion, and 4) constant volume process. In an engine these four steps are preceded by another in which a mass of air is drawn into the cylinder at constant pressure. In practice the cycle is different and the real $p - V$ diagram consists of the same five steps, but with much softer transitions between each. This results in a much "rounded" Otto-cycle as one can observe from figure 1.2.

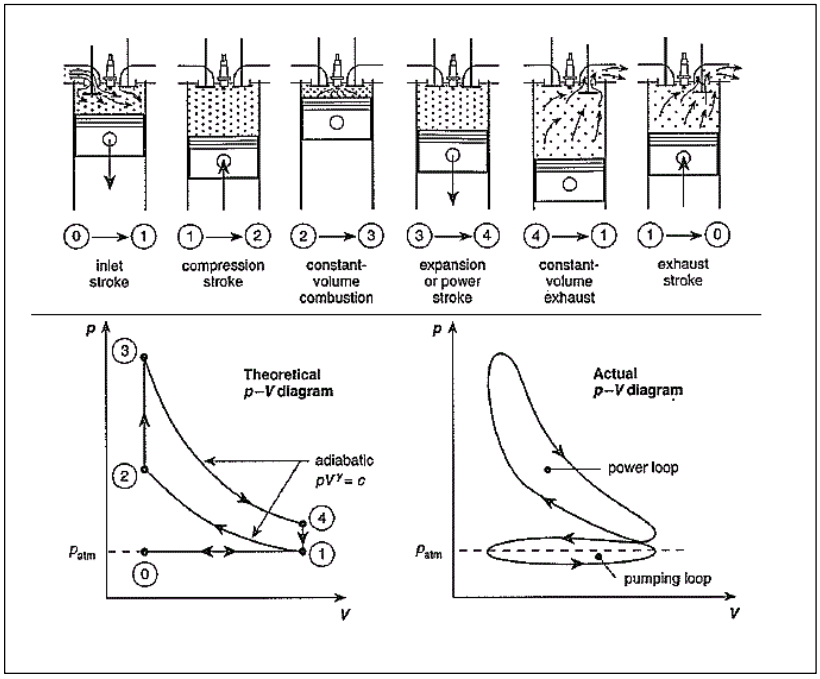


Figure 1.2. Combustion engine consisting of five different steps or four strokes.

The most critical part in an engine, in terms of design, is the piston. This has to stand the toughest conditions produced by chemical reactions as well as it must face up high pressures and temperatures. The piston is made out of a material capable to not react with the fuel and the sub-products of the combustion. This material is frequently stainless steel.

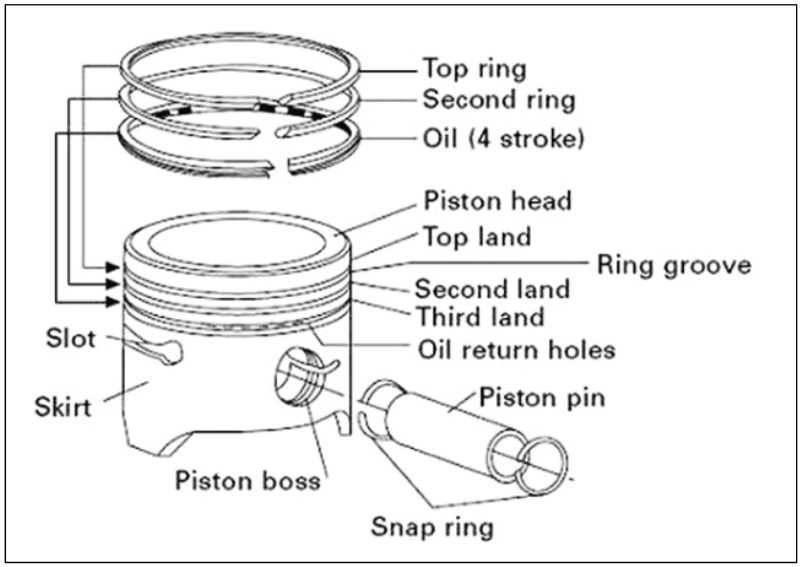


Figure 1.3. Sketch of a piston employed in a four stroke combustion engine.

Figure 1.3 shows a sketch of a piston. It contains several pieces, but the most interesting one in terms of efficiency and oil consumption are rings and specially the oil ring. Rings are the only pieces which are in contact with the internal wall of the cylinder. This ring slides up and down constantly together with the piston. Between them and inner wall of cylinder, frictions are produced. Therefore lubrication by means of oil is strictly necessary at this space. Oil protects the piston and the internal wall from degradation as well as corrosion. The more speed and load the more oil is consumed. The efficiency, speaking in fuel consumption, power development and durability of the engine depend on this critical issue. Hence, it is very important to understand processes affecting to it. With this regard, measurement of oil consumption serves as an invaluable help. Nowadays, there exists still the necessity to develop a method with which this is possible in a precise, accurate and in-situ way. For instance, methods based on trace compounds added to or contained in the motor oil have demonstrated to be the best approach. The amount of these traces in the exhaust gas delivers information about the motor oil consumption for every revolution per minute (r.p.m) and load (crankshaft torque). Organic molecules employed as tracers up to now, such as pyrene, are temperature sensitive and its utilization gives rise to wrong data and erroneous interpretations.

This work is based on a temperature insensitive tracer. Atomic sulfur present in exhaust was encountered to be a perfect choice as a tracer. Sulfur can be completely oxidized to $SO_2$. In this work, a nonthermal plasma (NTP) produced in a glow discharge cell (GDC) is found to be optimal for this task. Then this $SO_2$ can be detected and quantified by means of laser induced fluorescence (LIF). For this purpose an apparatus containing a fluorescence cell (FC) and an innovative optical parametric oscillator (OPO) laser was designed and constructed.

# 2. Oil consumption methods

## 2.1. Conventional methods

Conventional methods are based on volume or weight measurements. They are the so called gravimetric and volumetric methods, and they are a not on-line method to measure oil consumption. They are time consuming and in consequence very expensive. Theirs fundament and procedure are simple. The engine is filled with a well-known amount of oil. Then, the engine runs under determined speed and load conditions. Some hours later (8-10), the remaining oil is extracted and measured. Nowadays it is possible to measure a very small change in volume and/or weight. Despite this fact and the consequently feasible precision, the duration of tests is still being an inconvenient. Due to this and to difficulties of the so called drain step, accuracy of such methods is still very low. Cook et al. introduced in the 90s an on-time gravimetric method [1]. With this technique it was possible to measure oil consumption at real time for the first time. However, the big statistical deviations in the measurements, made that the techniques was discarded. After this study, others were established where the oil level was measured via ultrasounds [2] or in a capacitive way [3]. The volumetric way is less affected by the movements or the relatively tough conditions in the engine test desk, but now it is the varying temperature which is affecting the measurement most. Mathematical corrections can be performed for avoiding inaccuracies but then, it is necessary to know the dependence of the oil density on the engine temperature.

## 2.2. Trace methods

The methods based on analysis of trace compounds are different from conventional methods in several aspects. In these techniques substances which are only present in the oil, and sometimes in fuel, are detected by a complex analytical technique. With variation of its amount over the time one can learn how large the oil consumption is. The use of tracers added to the oil has also disadvantages, for instance reactions might occur between them and substances contained in oil. This could change the physical and chemical properties of the oil. There are currently two different sorts of added tracers depending on whether they are radioactive or non-radioactive.

### 2.2.1. **Radioactive tracer**

The radioactive method measures the radioactivity of one isotopic atom added to the oil. The most utilized so far has been the isotope 82 of bromine ($^{82}$Br) [4]. This atom substitutes itself with hydrogens contained in hydrocarbons. The lifetime is of 35.5 hours and the final product is the 82 isotope of Krypton ($^{82}$Kr), which is stable and non-toxic. This is a very sensitive method giving rise to a time resolution of 20 min. The saving in time is considerable in comparison with conventional methods. This is the reason why it is still in use. The main inconvenience of the method is the hazard when manipulating radioactive elements as well as the long time necessary for obtaining bureaucratic approval to handle them. A second radioactive method is based on tritium (T). The substitution of H by T does not change the chemical and physical properties of the oil considerably. However, the lifetime is ca. 12 years which makes it very inconvenient regarding waste treatment.

### 2.2.2. **Non-radioactive tracer methods**

The so called trace methods are currently the most employed between those concerning in-situ and on-time oil consumption analysis. Many tracers have been used. Pyrene was a very convenient and promising one [5, 6]. An apparatus was developed already by the Chemical-physics department of TUM. (Püffel et al. [7]). It was able to measure the oil consumption based on detection of pyrene in the exhaust gas. Despite the advantages of being a reliable and a fast method, it had a big disadvantage, decomposition of pyrene at high temperatures (high speed and load) gave rise to malfunctions. This caused that use of pyrene as tracer was ruled it out.

In the last few years sulfur has unveiled itself as the better tracer candidate. Some of the disadvantages of using that molecule which reduces the sensitivity considerably are still present in commercial apparatus. Thus companies such as Horiba Ltd. [8] and Da Vinci Emission Services Ltd. [9, 11, 12] use fluorescence methods to detect low concentrations of $SO_2$. Despite the fact that both use light detection at atmospheric pressure, none of them accomplished in a doubtless way the efficient conversion of sulfur into $SO_2$ or, what is even more problematic, could not eliminate totally interferences from NO. In the apparatus described in this work this problem have been resolved satisfactorily. The measurement of the sulfur amount via Selective Laser Induced Fluorescence (SLIF) at rough vacuum is without any doubt the best approach ever developed. The big drawback which is the fully conversion of sulfur into $SO_2$ has been overcome by the use of a Nonthermal Plasma (NTP).

## 2.3. Comparison

Table 2.1 contains most known oil consumption methods with their advantages and inconvenient.

| Method | Advantage | Inconvenient |
|---|---|---|
| **Gravimetric & Volumetric** | + Low apparatus effort<br>+ Continuous measurements feasible | - Only lubricants balance measurable<br>- Relatively low accuracy<br>- Highly time consuming |
| **$^{82}$Br-Method** | + Accurate measurement of radioactivity<br>+ Short half-life | - Radioactive tracer<br>- High equipment costs |
| **Tritium-Method** | + Does not influence the oil properties<br>+ Accurate measurement | - Radioactive<br>- Long half-life<br>- High cost |
| **Halogen-Method** | + High temporal resolution<br>+ Simple to calibrate | - Corrosion problems<br>- Converter necessary |
| **Pyrene-Method** | + High temporal resolution<br>+ No toxicological problems<br>+ Accurate measurement<br>+ Converter not necessary | - Under certain conditions very inaccurate<br>- Time consuming calibration |
| **EI-Quadrupole MS-Method** | + Simple approach<br>+ No additional tracer necessary<br>+ High temporal resolution | -Very inaccurate |
| **Zn-Method** | + No artificial tracer addition<br>+ Good accuracy<br>+ High temporal resolution | - Variable concentration of Zn in oil<br>- Strong adsorptions problems<br>- Memory effects |
| **$SO_2$-Methode** | + High sensitivity depending on detector<br>+ Good temporal resolution depending on the detector<br>+ No additional tracer | - Exhaust gas treatment necessary<br>- Sulfur in fuel can be problematic |

Table 2.1 Comparison between most used methods to measure oil consumption (Taken from [10]).

## 2.4. Literature


1. Cooke, V. B., *SAE Tech. Paper Ser.*, 1990, 900814.
2. Graf, F.; Köck, K., *MTZ*, 1995, 56, p. 424.
3. *Tribologie Messtechnik* , Technical Information. 1993.
4. Zellbeck, H.; Bergmann, M.; Rothig, J.; Seibold, J.; Zeuner, A., *TriboTest*, 2000, 6(3), pp. 251-265.
5. P.K. Püffel, W. Thiel, U. Boesl, *SAE Tech. Paper Ser.*, 1991-01-3460.
6. P. Püffel, W. Thiel, R. Frey, U. Boesl, *SAE Tech. Paper Ser.*, 1998, 982438, pp. 1-7.
7. Püffel, P., ReonanteLasermassenspektrometrie zum Spurennachweis von Ölbestandteilen in Abgasen von Verbrennungsmotoren. Herbert Utz Verlag, München, 1998.
8. Da Vinci. Emissions Services, Ltd. http://www.davinci-limited.com/
9. MEXA-1170SX. Horiba, 2011.
10. Laserspektroskopische Spurenanalytik von Ölbestandteilen in Abgasen von erbrennungsmotore, Stefan Sellmeier, (PhD Thesis), 19.07.2011.
11. Froelund, K. *SAE Tech. Pap. Ser.* 2000, No. 2000-01-2876.
12. Froelund, K.; Steven, F.; Smith, B. *SAE Tech. Pap. Ser.* 2005, No. 2005-01-3715.

# 3. Conversion of sulfur containing molecules into $SO_2$

## 3.1. Sulfur containing molecules in oil

There are several substances contained in the oil. Those which contain at least one atom of sulfur are the important ones. Unluckily, number, size and quantity of every molecule containing sulfur are not known and besides, it is nearly impossible to determine. In fact, it is not even known in most cases for engine developers or car engineers, since their composition is under patent. Nevertheless, some molecules containing sulfur can be selected to perform tests with set-up described in the following. Those molecules would be of course representative for those contained in oil. If their sulfur atom is converted to $SO_2$, oil-consumption measurements can be carried out. In our approach a new innovative and efficient way of conversion has been employed, namely a nonthermal plasma.

## 3.2. Conversion to $SO_2$

The conversion of sulfur into $SO_2$ ought to be total. This means that 100 % of the sulfur bounds must be dissociated and the resulting sulfur oxidized to $SO_2$. There are two main techniques to achieve such difficult challenge. The most common, but not so efficient one is the pyrolysis method which is carried on in an oven. Another innovative way, in which our approach is based on, utilizes nonthermal plasma produced in a glow discharge cell (GDC). It has been proved in the previous work of S. Sellmeier et al. [1] that only by using plasma conversion sulfur is 100% transformed into $SO_2$.

### 3.2.1. **Conventional methods, pyrolysis**

Pyrolysis produced in an electrical ceramic oven is the common method used by most of the commercialized systems ([2], [3], [4]). Those work normally at atmospheric pressure and are fed by an engine exhaust rich in molecules containing sulfur. The oven can reach temperatures up to 1000 K. However, not all compounds of interest are completely oxidized to $SO_2$. This is reported in table 3.1. [5].

| Compound | Representative for | Minimal temperature for complete thermal conversion (K) | Minimal discharge current for complete plasma conversion (mA) |
|---|---|---|---|
| **Sulfuric hydrogen** | | 620 | 2 |
| **Carbonyl sulfide** | Sulfur-containing carbonyls | 1070 | 6 |
| **Dimethyl sulfoxide** | Sulfoxide | 870 | 3 |
| **Thiophene** | Sulfur-containing aromatics | Not possible | 1.5 |
| **Dibenzothiophene** | Sulfur-containing condensed aromatics | Not possible | 1.5 |
| **Diethyl sulfide** | Sulfides | 970 | 4 |
| **Diethyl disulfide** | Disulfides | 800 | 1.5 |

Table 3.1. Comparison of the two methods employed for the conversion of molecules containing sulfur into $SO_2$.

It is necessary to emphasize that compounds such as thiophene and dibenzothiophene were only partially converted by thermal methods. This seems to indicate that all the compounds which contain an atom of sulfur in a condensed ring, are not fully converted into $SO_2$ with the use of an oven. On the other hand it was demonstrated [1, 5] that the conversion by nonthermal plasma is 100 % efficient. Furthermore, it is faster, cheaper and consumes less energy.

### 3.2.2. Generation of nonthermal plasma (NTP) with a glow discharge cell (GDC)

A glow discharge cell (GDC) is a device where nonthermal plasma (NTP) is created by establishing a differential potential between two electrodes. A very straightforward, easy to handle and robust GDC was designed for this specific purpose (fig. 3.2). It was produced handmade at the glass workshop of the TUM chemistry faculty. The present model has of course two electrodes. The first one consists of a wire of elementary wolfram (W) and the second one is a Swagelok® stainless steel nut. This nut serves as connection between the glow discharge cell (glass) and a stainless steel pipe which conducts the engine exhaust into the fluorescence cell (FC). The wolfram wire can behave both as an anode or a cathode. Both configurations were tested with very similar results regarding plasma stability and sulfur oxidation.

Different electro-physical behaviors can be observed within a cell where a difference of potentials is applied to its electrodes. Three main regimes are observed (fig 3.1). In the case of our setup the

used regime is the one called normal glow (glow discharge) which produces continuous and steady plasma (no flickering).

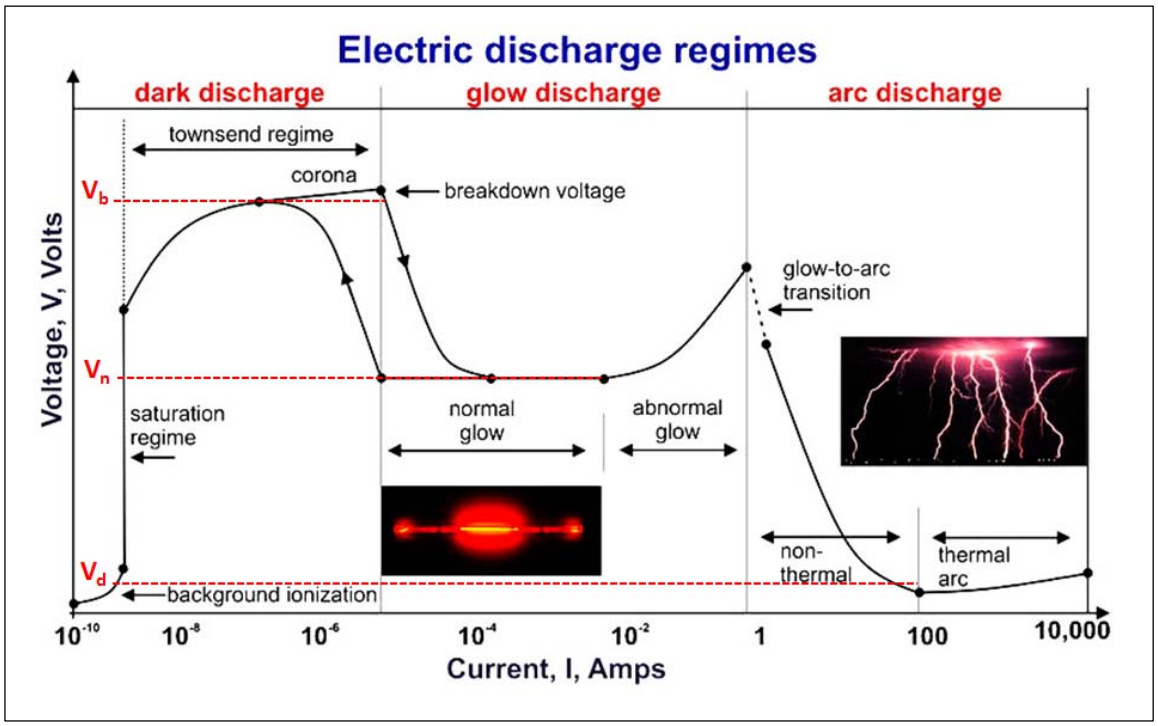


Figure 3.1. Different electric discharge regimes and characteristics voltages of a self-sustaining gas discharge (adapted from [7]).

The voltages involved in the different regimes are:

- $V_b$ = breakdown voltage (dark discharge) occurring in Townsend regime.
- $V_n$ = normal cathode fall of potential (normal glow discharge).
- $V_d$ = arc voltage (arc discharge) split in nonthermal and thermal arc.

The NTP is produced applying a current of $7.5 - 8\ mA$ and a voltage in the range of $670 - 690\ V$. This means a consume of energy over time equal to: $E \cdot t = V \cdot I \cdot \frac{t}{60} = 0.092\ J\ min$ . According to nomenclature in figure 3.1 the value of the normal cathode fall of potential is $Vn = 670 - 690\ V$. In this region, and as it was experimentally proved, the potential $V$ is constant over an current range which goes from $\sim 10^{-3}$ to $10^{-2}$ A. At too low voltage and current values plasma is not produced and at medium ones plasma shows a flickering behavior with a certain and constant

frequency. When the current is increased till $10^{-2}\ mA$ it gets stabilized. Once this limit is reached, the current can be slightly decreased till $8 \cdot 10^{-3}\ mA$ without losing the continuity of the plasma. In figure 3.2 the employed model of glow discharge cell is shown. The upper design incorporates a SHV-BNC connector whereas the lower one is the initial design. The BNC is connected to the wolfram wire through a gold pin. Figures 3.3 and 3.4 show a glowing GDC.

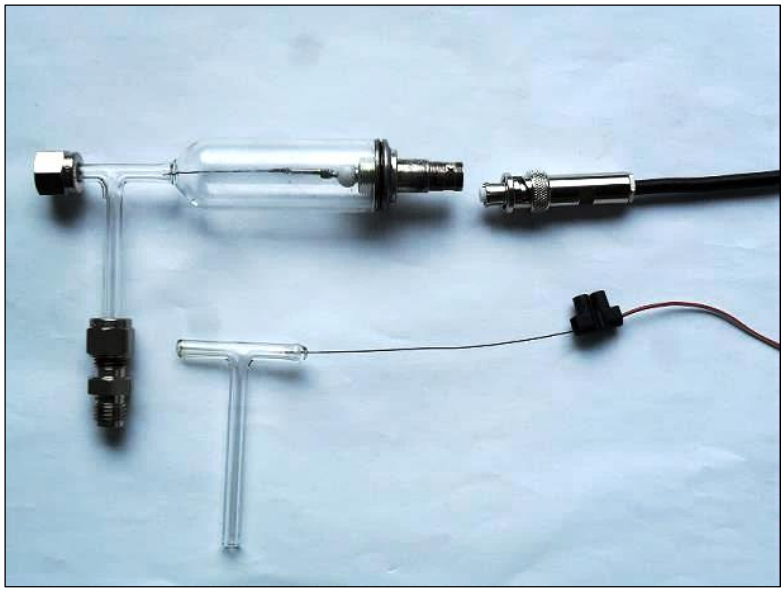

Figure 3.2. Comparison of final and first GDC prototype. Upper one incorporates a SHV-BNC connector attached to the glass. This makes totally safe the device.

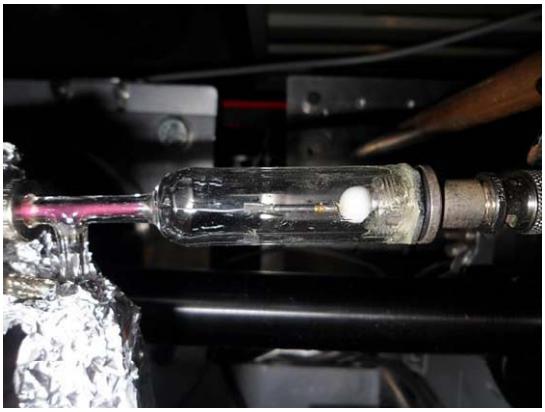

Figure 3.3. Glow discharge cell under operation (NTP on the left).

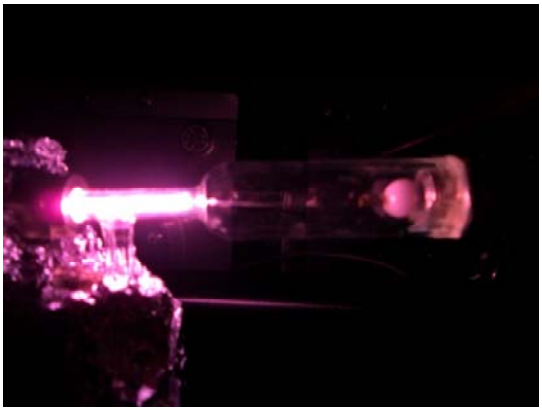

Figure 3.4.Glow discharge cell. Emission of pink light is perfectly appreciated.

3.2.2.1. ***Reactions: Fundamental species***

Reactions ongoing within nonthermal plasmas are many. They have been described in detail in many publications ([8-9]). $N_2$ and $O_2$ (Air: 78% of $N_2$, 21% of $O_2$) are species that will be always present in our gas stream because either they come from exhaust or are externally added. The apparatus incorporates a nozzle which is necessary to introduce extra air. This is orthogonal to the one acting as probe [1] and it is necessary to increase oxygen per cent till 3% [1]. This is the lowest amount needed to perform quantitatively sulfur oxidation. When the GDC is turned on $N_2$ and $O_2$ transform themselves according to following reactions [10]

$$e + O_2 \rightarrow e + O(P^3) + O(P^3) \quad (3.1)$$

$$e + O_2 \rightarrow e + O(P^3) + O(D^1) \quad (3.2)$$

Equations 3.1 and 3.2 show that molecular oxygen is dissociated producing ground state and excited atomic oxygen. In addition molecular nitrogen is dissociated producing ground state and excited state atomic nitrogen,

$$\mathrm{e} + \mathrm{N_2} \rightarrow \mathrm{e} + \mathrm{N}(\mathrm{S}^4) + \mathrm{N}(\mathrm{S}^4) \quad (3.3)$$

$$\mathrm{e} + \mathrm{N_2} \rightarrow \mathrm{e} + \mathrm{N}(\mathrm{S}^4) + \mathrm{N}(\mathrm{D}^2) \quad (3.4)$$

Furthermore, electron-ion pairs are produced through various electron impact ionization processes,

$$\mathrm{e} + \mathrm{N_2} \rightarrow 2\mathrm{e} + \mathrm{N_2^+} \quad (3.5)$$

$$\mathrm{e} + \mathrm{O_2} \rightarrow 2\mathrm{e} + \mathrm{O_2^+} \quad (3.6)$$

In the conditions given within a glow discharge cell (electrical discharge processing), the rate coefficients for electron-impact dissociation and ionization reactions strongly depend on the electron mean energy (kinetic energy) of the discharge plasma.

One very abundant species generated in the plasma is ozone ($\mathrm{O_3}$). This comes out from reaction between $\mathrm{O_2}$ and $\mathrm{O}$.

$$\mathrm{O}(\mathrm{P}^3) + \mathrm{O_2} \rightarrow \mathrm{O_3} \quad (3.7)$$

$$\mathrm{O}(\mathrm{D}^1) + \mathrm{O_2} \rightarrow \mathrm{O_3} \quad (3.8)$$

The generation of ozone from air in the glow discharge cell was proven under normal GDC working conditions ($8\,mA$ & $690\,V$). Figure 3.5 shows a quadrupole mass spectrometer (QMS) signal of ozone (47.73 amu) ionized by electron impact obtained for different $N_2$ and $O_2$ concentrations. From time marks 0 to 60 the only molecule in the gas stream was $N_2$ (GDC-OFF). At 60 (time / a.u.) glow discharge cell was turned ON. After that, oxygen concentration was decreased over time till the GDC was turned OFF (300 time / a.u.). Besides, at 300 (time / a.u.) only nitrogen was present in stream and at 325 (time / a.u.) air (78% $N_2$, 21% $O_2$) was switched ON, again.

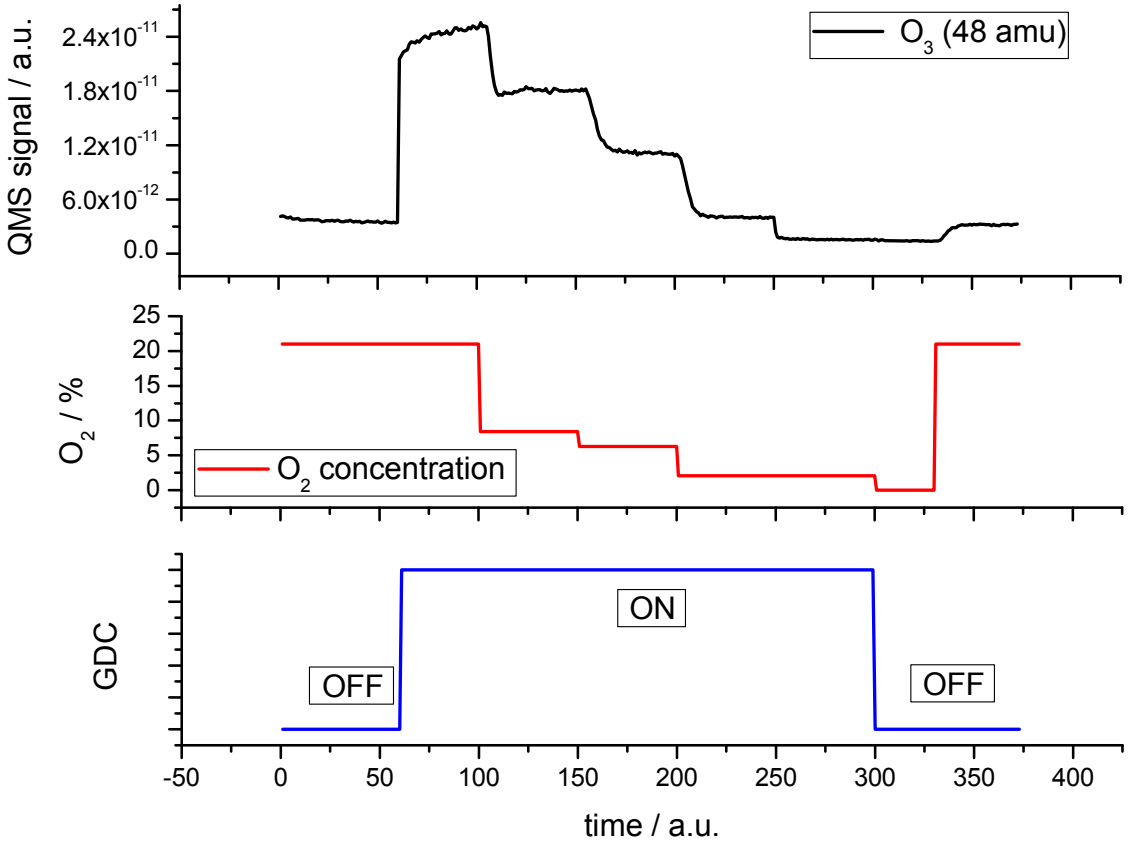


Figure 3.5. Signal of ozone recorded at a quadrupole mass spectrometer. Different amounts of oxygen and nitrogen were set, and GDC was turned ON and OFF.

In humid air mixtures (water presence) OH radicals are generated according to the following processes,

*Electron-impact ionization*

$$e + O_2 \rightarrow 2e + O_2^+ \tag{3.9}$$

and similar ionizations to produce species such us $N_2^+$, $H_2O^+$ and $CO_2{}^+$.

*Electron-impact dissociative ionization*

$$e + O_2 \rightarrow 2e + O + O^+ \quad (3.10)$$

*Charge transfer reaction*

$$N_2^+ + O_2 \rightarrow N_2 + O_2^+ \quad (3.11)$$

*Formation of water cluster ions*

$$O_2^+ + H_2O + M \rightarrow O_2^+(H_2O) + M \quad (3.12)$$

*Dissociation of water clusters*

$$O_2^+(H_2O) + H_2O \rightarrow H_3O^+ + O_2 + OH \quad (3.13)$$

$$O_2^+(H_2O) + H_2O \rightarrow H_3O^+(OH) + O_2 \quad (3.14)$$

$$H_3O^+(OH) + H_2 \rightarrow H_3O^+ + H_2O + OH \quad (3.15)$$

Figure 3.6 shows signals from different mass channels of a quadrupole mass spectrometer (QMS) when a mixture of hydrocarbons (HC, benzene, toluene and propane) were added to the gas mixture. GDC was turned ON to observe generation of amounts of products ($N_2$, $O_2$, OH and $H_2O$) for different total hydrocarbon concentrations. $N_2$ and $O_2$ concentrations decreased when more ppm of HC were added whereas OH and $H_2O$ species increased. Finally concentration of added oxygen was increased and GDC was turned ON. This resulted in a high $O_2$ QMS signal while $N_2$, OH and $H_2O$ species were inexistent. In chapter 7 is discussed how the extra amount of water within a gas stream could contribute to increase the amount of OH, $H_2O_2$ and $H_2O$. This effect results in a depletion of $SO_2$ fluorescence signal.

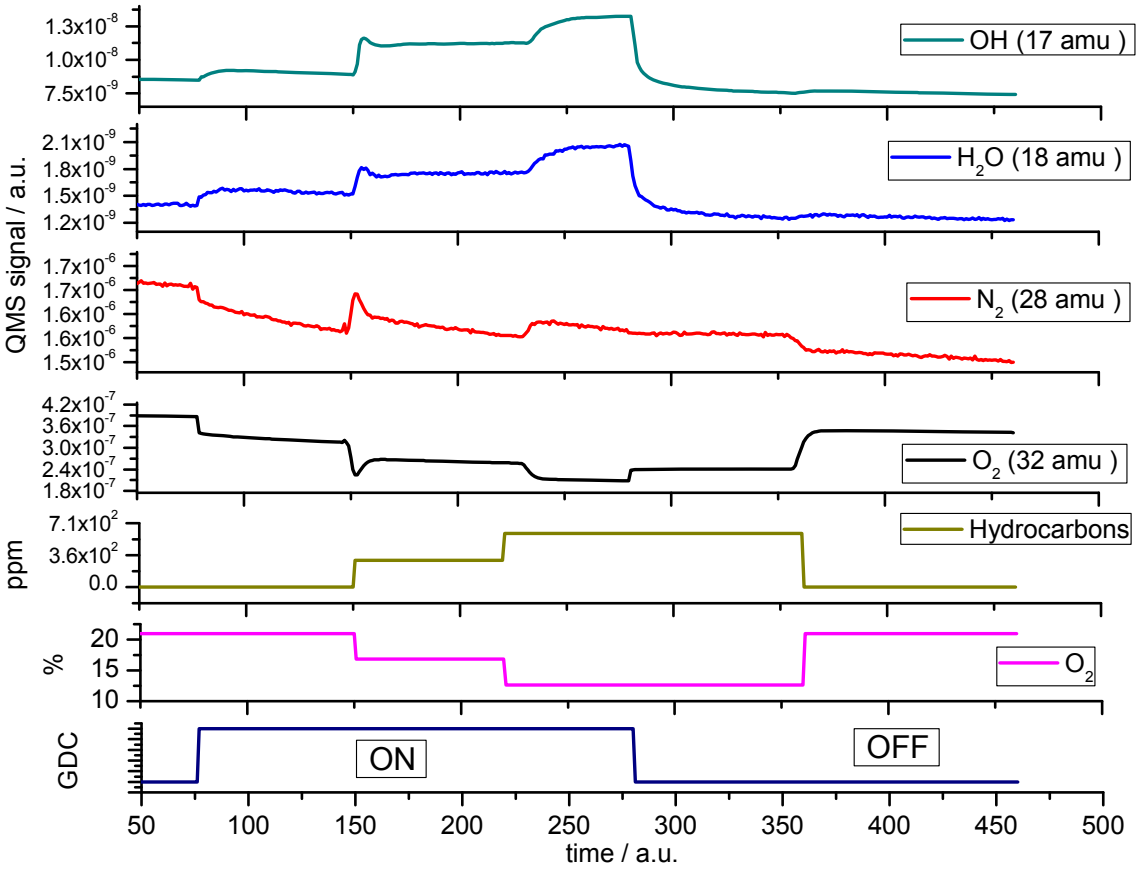


Figure 3.6. Fundamental species ($N_2$, $O_2$, OH and $H_2O$) encountered in nonthermal plasma when hydrocarbons are added to the stream. Concentration of hydrocarbon is referred to total amount of benzene, butane and toluene.

### 3.2.2.2. *Nitrogen species*

Several nitrogen containing species have been found in the nonthermal plasma when this is produced in presence of air. Complex mixtures of $N_xO_y$ gases exist within the plasma depending on the N/O ratios [10]. Species of oxidation states of nitrogen; I, II and IV were found. Figure 3.7 shows the variation of $N_2O$, NO, $NO_2$, and $O_2$ and $N_2$ concentration are changed (same cycle as in figure 3.5). All species decrease when the amount of $O_2$ was diminished even with the increment of $N_2$. This result can be explained in base to all reaction occurring within the GDC. This measurement was made to achieve knowledge about possible fluorescent molecules. Complexity of plasma and reactions taking place in there are beyond the purpose of this work.

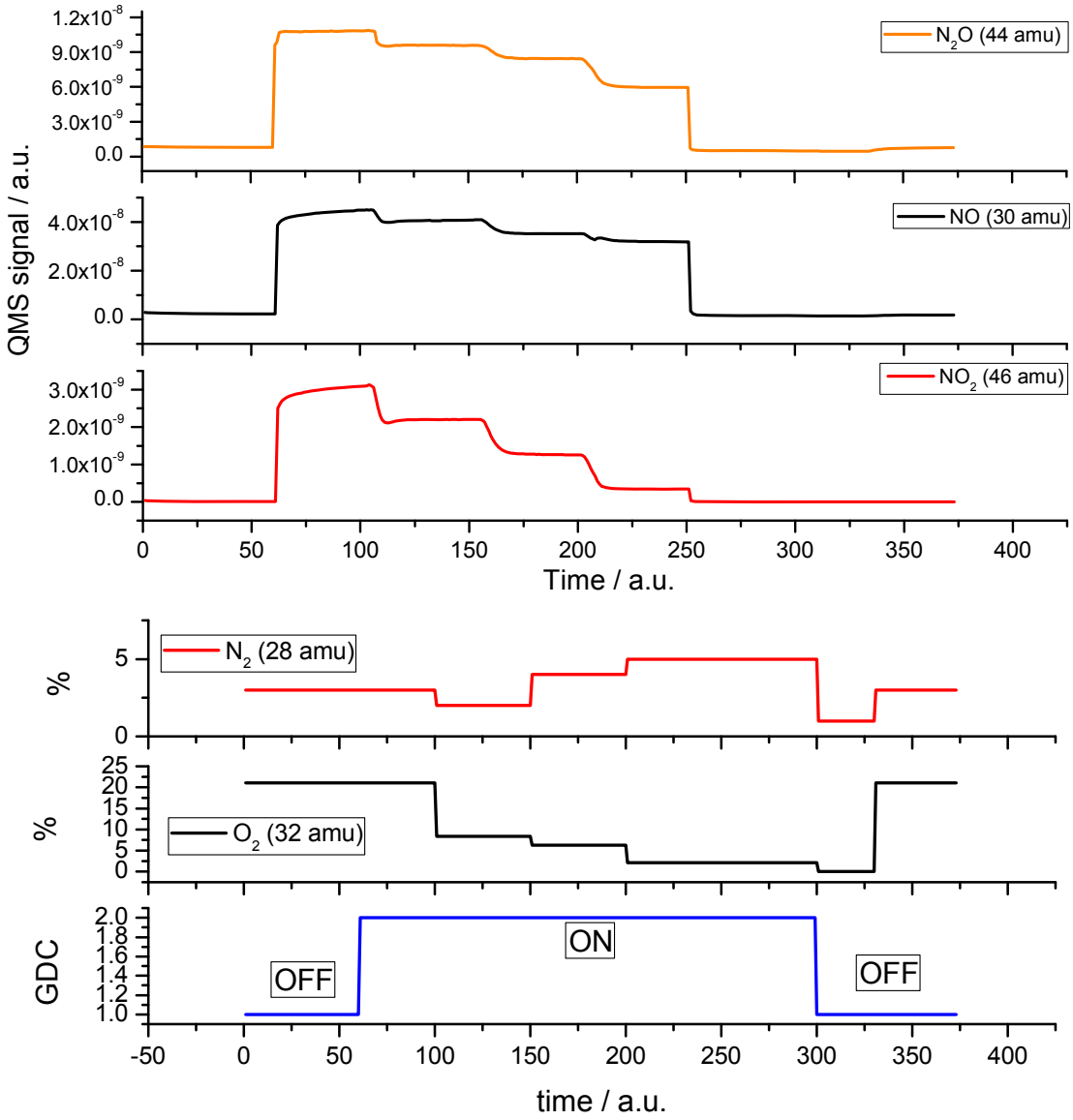


Figure 3.7. Quadrupole mass spectra of the nitrogen species with $O_2$ and $N_2$ concentrations

### 3.2.2.3. ***Pollutants***

It has been demonstrated that nonthermal plasmas (NTPs) are a tool to efficiently remove pollutants. The oxidation and decomposition of several organic compounds have been studied by the use of a GDC. Volatile organic compounds (VOCs) [14], volatile aliphatic and aromatic hydrocarbons [15], or halogenated molecules [9-10] can be reduced or oxidized (depending on oxygen content) giving rise to simple gases such as $SO_2$, $NO_2$, $H_2S$, $NH_3$, $CO_2$, CO, etc.

Some relevant reactions occurring within the plasma are,

$$OH + OH \rightarrow H_2O_2 \quad (3.16)$$

$$O_3 + H_2O_2 \rightarrow OH + OH + O_2 \quad (3.17)$$

$$OH + Pollutans\ (or\ R) \rightarrow Products \quad (3.18)$$

In figure 3.8 is shown how good the NTP is as a tool to remove organic compounds present in the exhaust. This is of a great importance since products of reaction may be capable to produce interferences due to their own fluorescence. During this measurement an increasing concentration of butane, benzene and toluene (same cycle than in fig. 3.6) has been monitored by a QMS over the variation of $N_2/O_2$ ratio. Table 3.2 shows HC, air and $N_2$ flows (sccm), and concentration of $N_2$ (% v) and HC (ppm). It is clearly visible that the amount of $CO_2$ increases over the time as it is expected from the increment of hydrocarbon concentrations. GDC was turned off at time 320. Between time 320 and 375 an increment of $CO_2$ signal is visible. This may result in a misleading if one does not consider fragmentation due to butane and toluene within an electron impact (EI) source (QMS). As it can be seen in NIST electron impact mass spectra a fragment with mass equal to 44 amu is produced [11, 12]. Presence of $N_2O$ at this channel was ruled out since 44 mass should not increase when GDC is turned on.

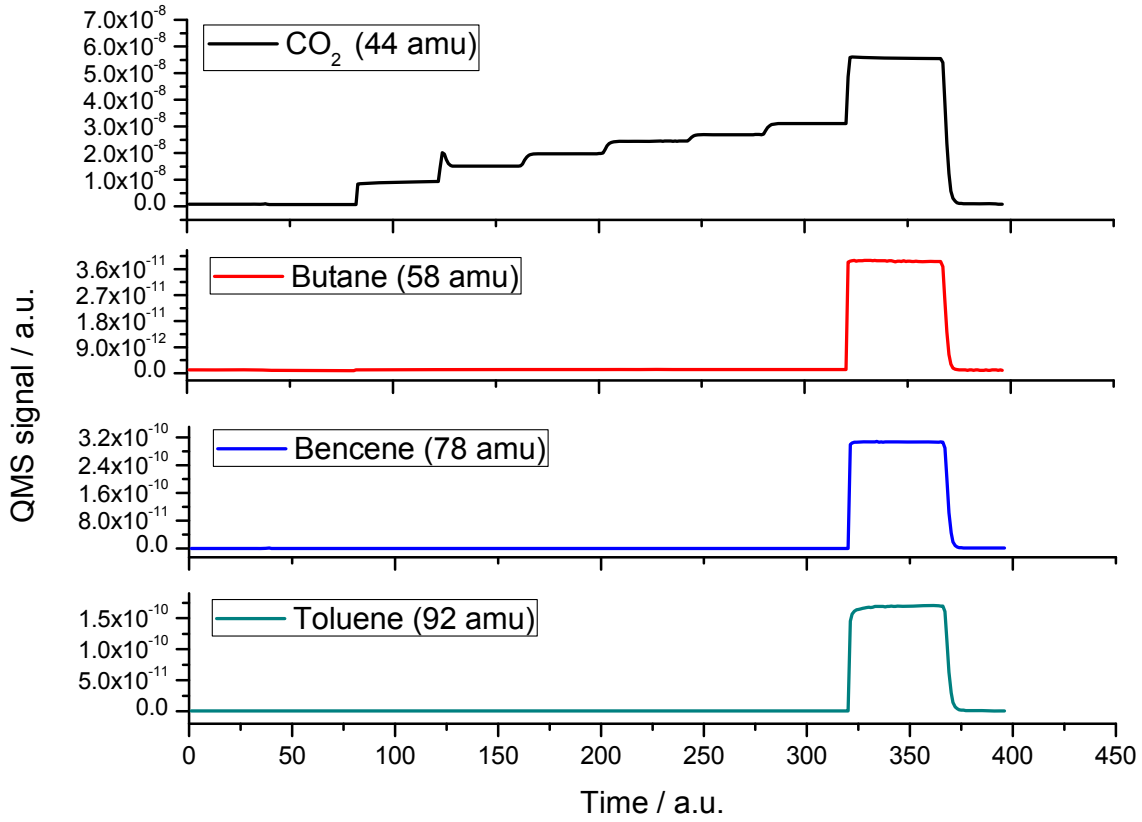


Figure 3.8. Quadrupole mass spectrometric signal versus time for butane, benzene and toluene with increasing concentrations of them.

| Flow HC / sccm | Flow air /sccm | Flow $N_2$ /sccm | $N_2$ / % vv | $O_2$ / % vv | Concentration HC / ppm | Time / a.u. | GDC |
|---|---|---|---|---|---|---|---|
| 0 | 500 | 0 | 78.0 | 21 | 0 | 0-40 | OFF |
| 0 | 250 | 250 | 89.0 | 10.5 | 0 | 40-80 | OFF |
| 0 | 250 | 250 | 89.0 | 10.5 | 0 | 80-120 | **ON** |
| **50** | 250 | 200 | 79.0 | 10.5 | 150 | 120-160 | **ON** |
| **100** | 250 | 150 | 69.0 | 10.5 | 300 | 160-200 | **ON** |
| **150** | 250 | 50 | 49.0 | 10.5 | 450 | 200-240 | **ON** |
| **200** | 250 | 50 | 49.0 | 10.5 | 600 | 240-280 | **ON** |
| **250** | 250 | 0 | 39.0 | 10.5 | 750 | 280-320 | **ON** |
| **250** | 250 | 0 | 39.0 | 10.5 | 750 | 320-360 | OFF |
| 0 | 500 | 0 | 78.0 | 21 | 0 | 360-400 | OFF |

Table 3.2. Stream concentration of measurement corresponding to figure 3.9 (and 3.6). Benzene (500 ppm), toluene (500 ppm) and butane (500 ppm) are hydrocarbons (HC) contained in the gas mixture.

#### 3.2.2.4. ***Organic molecules containing sulfur***

Oxidation and fragmentation (dibenzothiophene) of several molecules such as $H_2S$ and those containing sulfur were studied already in the work of S. Sellmeier [1]. Herein only the main reactions involving conversion of molecularly bound sulfur into $SO_2$ are written.

*Oxidation of $H_2S$ or molecules containing sulfur (SH-R or RS-R) [9, 13]*

$$HS - R\ (RS - R) + O \rightarrow RSO + H(R) \quad (3.19)$$

$$H_2S + O \rightarrow HS + OH \quad (3.20)$$

$$H_2S + OH \rightarrow HS + H_2O \quad (3.21)$$

$$HS + O_2 \rightarrow SO + OH \quad (3.22)$$

$$HS + O \rightarrow SO + H \quad (3.23)$$

$$HS + HS \rightarrow H_2S + S \quad (3.24)$$

$$SO + O \rightarrow SO_2 \quad (3.25)$$

$$SO + OH \rightarrow SO_2 + H \quad (3.26)$$

$$SO + O \rightarrow SO_2 \quad (3.27)$$

$$SO + O_2 \rightarrow SO_2 + O \quad (3.28)$$

$$OH + SO_2 \rightarrow HOSO_2 \quad (3.29)$$

$$O_2 + HOSO_2 \rightarrow SO_3 + HO_2 \quad (3.30)$$

$$SO_3 + H_2O \rightarrow H_2SO_4 \quad (3.31)$$

Radicals tagged as R follow other reactions giving rise to simple gases such as NO, CO or $CO_2$. The functioning of these reactions was demonstrated during the realization of this work in several calibrations made with $H_2S$ and the measurement of fluorescence emitted by $SO_2$. $H_2SO_4$ was never formed during our experiments even in the presence of a lot of amounts of water (16 %). This result obtained in the homemade and self-designed GDC differs from that observed in a corona discharge reactor (wire-to-cylinder, [13]). J. Jarrige el al. [13] found how $SO_2$ already decreased with an amount of 2.3 % (volume) of water. In his work contrary as expected the increment of OH concentration, radical more reactive than $O(P^3)$, did not improve the oxidation ratio of $H_2S$ but it reacted with $SO_2$ to form $H_2SO_4$. Moreover, it must be pointed out that $H_2SO_4$ generation is highly dependent on the pressure. The depletion of $SO_2$ fluorescence in humid gases has been observed at atmospheric pressure [14], but luckily the apparatus herein explained works at 3 mbar.

## 3.3. Literature


1. Laserspektroskopische Spurenanalytik von Ölbestandteilen in Abgasen von Verbrennungsmotore, Stefan Sellmeier, (PhD Thesis), 19.07.2011.
2. Horiba, MEXA-1170SX.
3. Da Vinci. Emissions Services, Ltd. http://www.davinci-limited.com/.
4. Lubrisense, http://www.lubrisense.com/.
5. S. Sellmeier, E. Alonso, and U. Boesl, *Anal. Chem.*, 2014, 86 (1), pp 380–389.
6. X. Hu, J. J. Zhang, S. Mukhnahallipatna, J. Hamann, M.J. Biggs, P. Agarwal, *Fuel* 82(2003), 1675-1584.
7. http://www.plasma-universe.com/Electric_glow_discharge.
8. J. A. Broekaert, *Journal of analytical atomic spectrometry*, Vol. 2, September 1987, 537-542.
9. Y. H. Bai, J. R. Chen , X. Y Li, C. H. Zhang, *Reviews of Environmental Contamination and Toxicology Volume* 201(117-136).
10. B. M. Penetrante, M. C. Hsiaoy, J. N. Bardsley, B. T. Merritty, G. E. Vogtliny, A Kuthiz, C P Burkhartzand J R Baylessz, *Plasma Sources Sci. Technol.* 6 (1997) 251–259.
11. http://webbook.nist.gov/cgi/cbook.cgi?ID=C106978&Units=SI&Mask=200#Mass-Spec.
12. http://webbook.nist.gov/cgi/cbook.cgi?ID=C108883&Units=SI&Mask=200#Mass-Spec.
13. J. Jarrige, P. Vervisch, *Plasma Chem Plasma Process* (2007) 27:241–255.
14. S. Futamura, A.H. Zhang, T. Yamamoto, *Journal of Electrostatics*, 42 (1997) 51-62.
15. A. Koutsospyros, S.-M. Yin, C. Christodoulatos, K. Becker, *International Jornal of Mass Spectrosmetry* 233 (2004) 305-315.

# 4. Laser induced fluorescence

## 4.1. Fluorescence

Electronic excited states of a molecule are involved both in absorption or emission processes. In case of emitted energy some characteristic physico-chemical parameters (wavelength, lifetime, etc.) are related to mechanisms that a molecule follows in its deactivation. During the absorption of a photon by a molecule, an electron is pumped up to a higher energy level. Electronic transitions, usually involve rotational and vibrational excitation. The absorbed energy can be afterwards emitted according to different phenomenon such as spontaneous emission, which is the so called fluorescence, or phosphorescence. Before these processes occur, non-radiative deactivation may be involved. This means that before the photon is finally emitted, there exists energy dissipation by collisions or other mechanisms. In fluorescence measurements performed at rough vacuum, collisional deactivation does not play a dominant role. This is basically due to low pressure kept in the fluorescence cell (3 mbar).

The final photon emission is vertical according to the Franck-Condon principle. The resulting fluorescence spectrum shows the vibrational structure of the fundamental electronic level. Let us now assume that the rovibronic level, with vibrational and rotational quantum number $\upsilon_k^{'}$ and $J_k^{'}$ respectively, in the excited state, is populated by optical pumping transition, $E_i \rightarrow E_k$. This molecule can then emit spontaneously a photon of the same or other energy to the lower level $(\upsilon_i^{''}, J_i^{''})$. This process occurs after a time named as, the mean lifetime. The spontaneous transition probability $\mathcal{P}_{ik}$ is proportional to the square of the matrix element,

$$\mathcal{P}_{ik} \propto |\int \psi_k^* r\, \psi_i d\tau_n d\tau_{el}|^2 \tag{4.1}$$

where $r$ is the vector of the excited electron and integration extended over all nuclear and electronic coordinates. Following the Born-Oppenheimer approximation the total wave function can be separated according to,

$$\psi = \psi_{el}\psi_{vib}\psi_{rot} \tag{4.2}$$

with electronic, vibrational, and rotational wave functions. If the electronic transition does not depend on the nuclei separation, then we can write,

$$\mathcal{P}_{ik} \propto |M_{el}|^2 |M_{vib}|^2 |M_{rot}|^2 \tag{4.3}$$

Where $M_{el}$ represents the electronic matrix element that depends on the coupling of the two electronic states, and it is known as integral of the transition momentum. This momentum can be related to an electronic, vibrational or rotational transition. The second term $M_{vib}$ is the Franck-Condon factordepending on the coupling of the vibrational wave functions between both states. The last factor,

$$M_{rot} = \int \psi_{rot}^{'} \psi_{rot}^{''} g_i d\tau_{rot} \tag{4.4}$$

is the called the Hönl-London factor. This depends on the orientation of the molecular axis relative to the electric vector of the observed fluorescence wave. Only the transitions for which the three factors are nonzero give rise to a line in an excitation fluorescence spectrum. The Hönl-London factor is zero unless $\Delta J = J_k^{'} - J_i^{'} = 0, \pm 1$. If an upper level is excited, each vibrational band consists of three sub bands, P ( $\Delta J = -1$) , Q ( $\Delta J = 0$) and R ( $\Delta J = +1$). They are commonly name as branches.

Since absorption mostly starts at the vibrational ground level of the electronic ground state, but fluorescence ends at vibrational excited levels of the electronic ground state, the envelope of fluorescence always exhibits a red shift with respect to the overall envelope of absorption. The extreme shift occurs when the fluorescence starts at the vibrational ground level of the electronic excited state. In this case, the characteristic dispersed fluorescence spectrum has equal but mirror inverted structure as the absorption one and shows a characteristic shift to higher wavelengths. This is represented in figure 4.1.

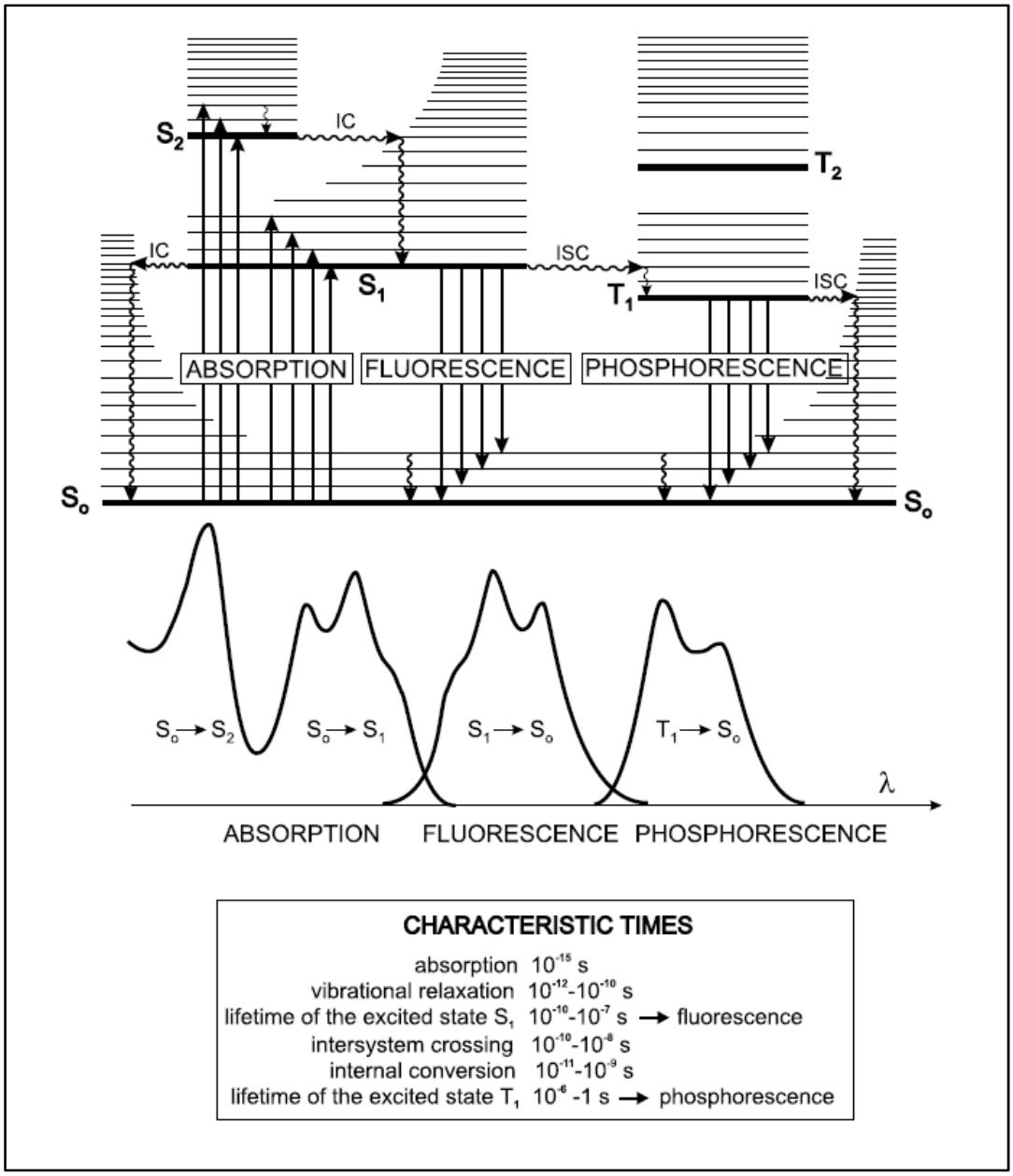


Figure 4.1. Typical Perrin-Jablonsky diagram (electronic transition diagram). (Taken from [1])

There have been so far several techniques and devices which exploit the fluorescence phenomenon. One of them is the generation of laser radiation when, for instance, the fluorescence takes places between a Fabry-Perot resonator (dye lasers). Another one is the utility of fluorescence in microscopy which allowed a noticeable improvement in resolution. In 2014 E. Betzig, W. Moerner and S. Hell were awarded with the Nobel Prize in Chemistry for the development of super resolved fluorescence microscopy.

## 4.2. Theory

### 4.2.1. Life time and fluorescence quantum yield

There are two different concepts that are of a special utility in fluorescence spectroscopy namely, the life time and the quantum yield. The probability $\mathcal{P}_{ik}$ that an excited molecules emits spontaneously a quantum ($h\nu_{ik} = E_i - E_k$) within a second, when a transition from a state $E_i$ to another state $E_k$ takes place, is defined as [12],

$$d\mathcal{P}_{ik}/dt = k_{ik} \tag{4.5}$$

with $k_{ik}$ is the so-called rate constant (events per second) for such a transition. If several transition paths from the $E_i$ to different lower levels $E_k$ are feasible, the total rate constant can be calculated as

$$k_i = \sum_k k_{ik} \tag{4.6}$$

Thus the variation of the population density $dN_i$ during a time interval of $dt$ because of a radiative decay, can be described as

$$dN_i = -k_i N_i dt \tag{4.7}$$

(equivalent to eq. 4.1) which after integration gives rise to

$$N_i(t) = N_{io} e^{-k_i t} \tag{4.8}$$

with $N_{io}$ being the population density at $t = 0$. After a time $\tau_i = 1/k_i$, the population density has been reduced to $1/e$ of its initial value. The mean spontaneous lifetime of the level $E_i$ is written as $\tau_i$ as one can see from the mean time definition.

$$\bar{t}_i = \int_0^\infty t \cdot \mathcal{P}_i(t) dt = \int_0^\infty t \cdot k_i \cdot e^{-k_i t}\, dt = \frac{1}{k_i} = \tau_i \tag{4.9}$$

where $\mathcal{P}_i(t)\, dt$ is the probability that a molecule in state $E_i$ emits a photon spontaneously within the time interval of t and $t + dt$.

The radiant power emitted from $N_i$ molecules on the $E_i \rightarrow E_k$ is

$$P_{ik} = N_i h\nu_{ik}\, k_{ik} \tag{4.10}$$

When several of those transitions from $E_i$ level occur to different lower levels $E_k$, then the radiant powers of the corresponding spectral lines are proportional to the product of the Einstein coefficient $k_{ik}$ and the photon energy $h\nu_{ik}$ .

The $E_i$ level of the $A$ molecule can be depopulated by collision-induced radiationless transitions (internal conversion IC in fig 4.1). This probability $d\mathcal{P}_{ik}^{coll}/dt$ depends on the density $N_B$ of the collision partner $B$, on the mean relative velocity $\bar{v}$ between $A$ and $B$, and on the collision cross section $\sigma_{ik}^{coll}$ for a collision that induces the transition $E_i \rightarrow E_k$ in the molecule $A$.

$$\frac{d\mathcal{P}_{ik}^{coll}}{dt} = \bar{v}\, N_B\, \sigma_{ik}^{coll} \tag{4.11}$$

This effect, induced emission, may become noticeable when the molecule is exposed to an intense radiation field. It contributes to depopulation of the $E_i$ level in the $|i\rangle \rightarrow |k\rangle$ transition according the following probability.

$$\frac{d\mathcal{P}_{ik}^{ind}}{dt} = \rho(\nu_{ik})B_{ik} \tag{4.12}$$

What determines the effective lifetime of a level $E_i$ is the sum of spontaneous, induced and collisional contributions. Therefore the lifetime becomes,

$$\frac{1}{\tau_i^{eff}} = \sum_k [k_{ik} + \rho(\nu_{ik})B_{ik} + \bar{v}\, N_B\, \sigma_{ik}] \tag{4.13}$$

The quantum yield also called fluorescence quantum yield, is related to the efficiency of the fluorescence process. It is defined as the number of emitted photons divided by the number of absorbed photons,

$$\eta_k = \frac{Photons\ emitted}{Photons\ absorbed} \tag{4.14}$$

The maximum value of it is 1.0 which means that every single photon absorbed results in a photon emitted. The quantum yield could also be defined in terms of the excited stated decay ratio.

$$\eta_k = \frac{k_f}{\sum_i k_i} \tag{4.15}$$

where $k_f$ is the rate of spontaneous emission of radiation and $\sum_i k_i$ is the sum of all rates of excited state decay (see fig. 4.1). Non-radiative rates are included. They could be: dynamic collisional quenching, near-field dipole interaction (fluorescence resonance energy transfer, FRET), internal conversion (IC), and intersystem crossing (ISC). The relaxation processes can be visualized with the use of Perrin-Jablonski diagrams (fig 4.1).

According to figure 4.1 several processes can be described and their rate constant named [1]:

1. Absorption of a photon which excites the molecule to a higher electronic level, $S_0 \rightarrow S_1$ or $S_0 \rightarrow S_2$.
2. Emission of a photon (fluorescence) with a rate constant $k_r$.
3. Energy dissipation by collisions. This is a non-radiative process which occurs with the rate constant $k_i$.
4. Internal conversion (IC).
5. Excited molecules can release some of their energy to molecules located nearby. The transfer of energy occurs in this case with the rate constant $k_q$ (collisional quenching, CQ) or with $k_t$ (FRET).
6. Transient passages can occur to a excited triplet state $T_1$. This takes place with a rate constant of $k_{isc}$ (ISC). Every $S$ state (with exception of the ground state $S_0$) is correlated to a triplet state of less energy. Triplet states are energetically not stable as all excited states.

Finally, the de-excitation of the molecule from a triplet state takes place following processes such of those described for the $S_1$ de-excitation.

1. Emission of photons with rate constant $k_p$ (phosphorescence).
2. Non-radiative energy dissipation with rate constant $k_i^{'}$.
3. Energy transfer to another molecule at distance (FRET) with rate constant $k_t^{'}$ or by collision with rate constant $k_q^{'}$.

It is important to mention that the quantum yield is measured in comparison with standards. For instance, the quinine sulfate in sulfuric acid solution is a common fluorescence standard.

### 4.2.2. Quenching

The so called quenching phenomenon is defined as the ensemble of processes which can decrease both the amplitude of fluorescence and the lifetime. Those could be excited state reactions, energy transfer, complex formation, collisional quenching [2, 3, 4] or even magnetic processes [5-9]. Moreover, quenching is highly dependent on temperature and pressure. Several studies have been carried out in liquid phase where molecular quenching, due to excited state reactions, was observed. However in gas phase the most common quenching is due to collisional processes. This depends in a great manner on the pressure. In the particular case of the $SO_2$ molecule, quenching has been observed at atmospheric pressures [3, 2, 4].

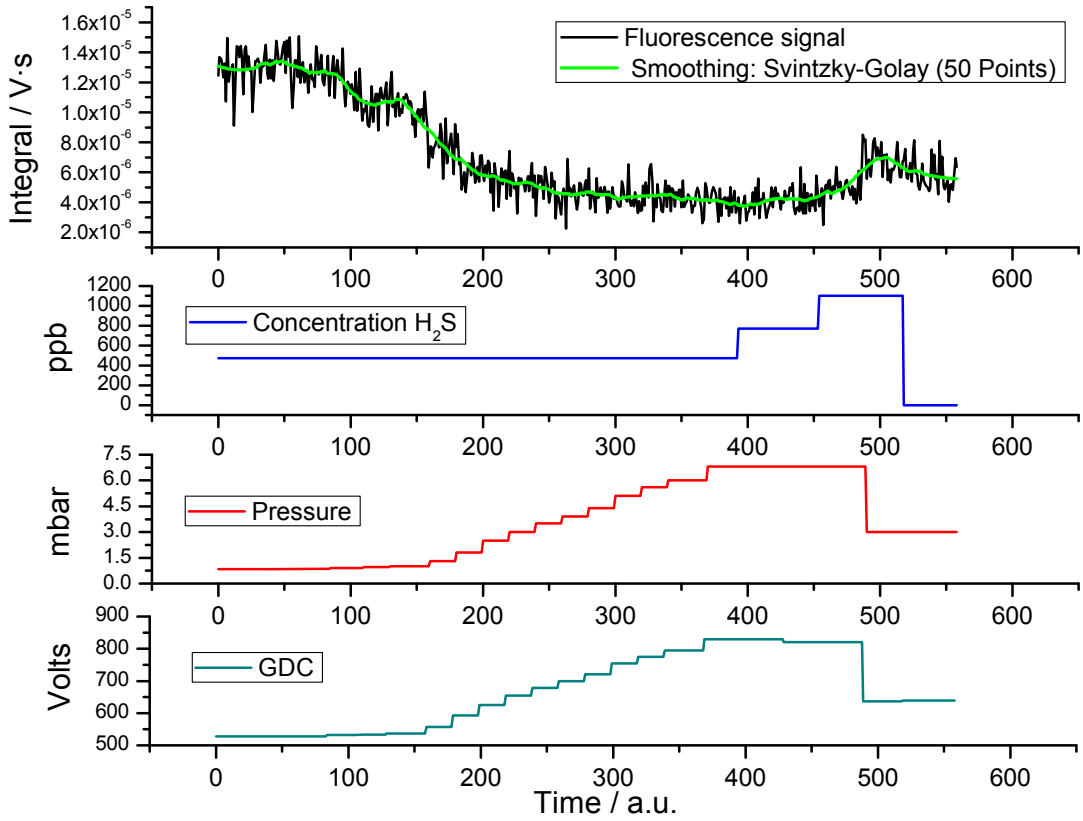


Figure 4.2. Variation of $SO_2$ fluorescence signal versus pressure and concentration variation.

GDC and FC are connected by a stainless steel pipe and in consequence they are at the same pressure. To proof how the pressure affects to the quenching of our $SO_2$ signal, a measurement of integrated fluorescence signal variation for several pressures was carried out. Voltage of GDC varies with pressure [6] however, not flickering behavior was observed during the whole measurement (steady NTP). A gas stream of dried air and $SO_2$ in concentration of 450 ppb was conducted into the fluorescence cell. The pressure was varied from 0.84 to 6.8 mbar. Figure 4.2 shows the value of integrated fluorescence signal versus the pressure in fluorescence cell (and in GDC). It can be seen in time interval from 0 to 400 that the bigger the pressure the lower the integral. In principle bigger pressure and higher voltage must result in an increment of $SO_2$ molecules and a better $H_2S$ oxidation efficiency respectively (correct voltage of GDC). Besides, taking into account that more $SO_2$ molecules enter in fluorescence cell, the integral should rise up. However, the integral of $SO_2$ fluorescence decreases which means that increase in pressure produces a quenching of $SO_2$ integral (shorter lifetime and fewer amplitude). However, the integral of $SO_2$ fluorescence decreases which means that increase in pressure produces a quenching of $SO_2$ integral (shorter lifetime and fewer amplitude). An explanation for this behavior cannot be given. However, from this observation it follows that the pressure in the fluorescence cell has to be kept as constant as possible and that the range around 3 mbar is optimal since there the dependence of the fluorescence signal on the pressure is small (fig. 4.3). From 400 to 540 the pressure is kept constant whereas the concentration increases which results in increment of the integral.

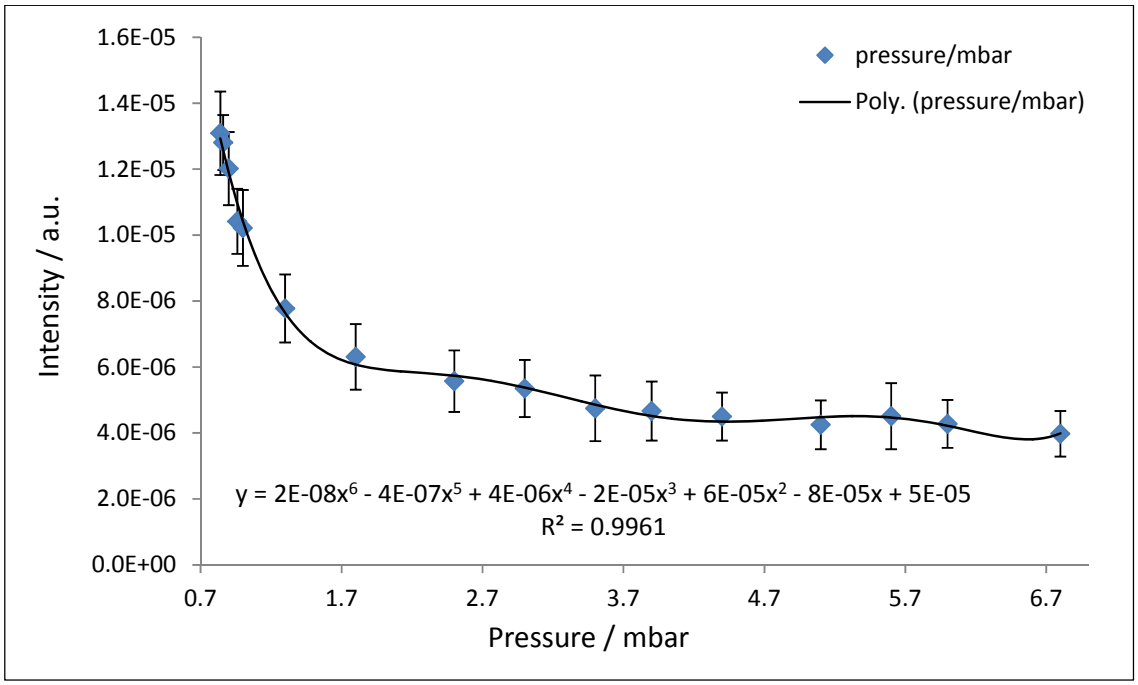


Figure 4.3. Average signal from fig. 4.2 vs. pressure (in agreement with ref. [4]).

## 4.3. Fluorescence induced by laser

Selective or laser induced fluorescence (SLIF) is a widely developed and studied technique in which a laser is used as an excitation source. LIF has been largely used to measure all kind of simple molecules such bi or tri-atomic as well as larger ones, such a hydrocarbons (HC) [11, 13]. The technique and most common apparatus have been described in detail elsewhere [12, 15, 16, 26 ]. The most important reason to use a laser is the feasibility to have an intense light source at a particular wavelength. Moreover, the wavelength range can be easily tuned in such devices making easier the probe of different molecules. There exist already lasers which can cover a broad range of the UV, visible and IR region (optical parametric oscillators, OPOs). The second most important feature of the laser is the narrow-medium bandwidth. This is measured as a spectral bandwidth (Gaussian) and is equivalent to the full width at half maximum (FWHM) of it. It depends on the kind of laser and on the pulse duration. Some dye laser have achieved 0.13 $cm^{-1}$ (less with an intracavity etalon) whereas, OPOs have attained bandwidths between 2.5 and 5 $cm^{-1}$. The pulse duration of lasers limits the FWHM. The relationship between the pulse duration and spectral bandwidth of the laser pulse can be written as $\Delta\nu\Delta t > \mathrm{K}$, where $\Delta\nu$ is the frequency bandwidth

with $\omega = 2\nu\pi$, $\Delta t$ is the FWHM of the time pulse and $K$ is a number which depends only on the pulse shape (see Table 4.1).

| Function | E(t) | K |
|---|---|---|
| Gauss | $e^{-(\frac{t}{t_0})^2/2}$ | 0.441 |
| Hyperbolic secant | $1/\cosh(\frac{t}{t_0})$ | 0.315 |
| Lorentz | $1/[1+\left(\frac{t}{t_0}\right)]^2$ | 0.142 |

Table 4.1.Values of constant K for different laser pulse shapes and its corresponding electrical field equation.

If the equality is reached in $\Delta\nu\Delta t > \mathrm{K}$, one speaks about a Fourier-transform-limited pulse or simply a transform-limited pulse. One can also calculate the minimum time duration of a pulse giving a spectrum with $\Delta\lambda$ (nm) at FWHM and central wavelength $\lambda_0$(nm),

$$\Delta t \geq K\frac{\lambda_0^2}{\Delta\lambda \cdot c} \tag{4.16}$$

According to eq. 4.16, the shorter pulse, the bigger the FWHM and the lower the spectroscopic resolution that can be attained. If the values from the OPO laser (InnoLas Laser-GmbH) $\Delta\nu = 5\ cm^{-1}$ and $\Delta t = 6\ ns$ are taken into account, the values of K is equal to 900. This a value much bigger than the one corresponding to a Fourier-transform-limit (0.441) of a Gaussian peak.

### 4.3.1. Selection of the $SO_2$ excitation wavelengths

In order to detect $SO_2$ concentrations one should select an absorption wavelength which has the maximum possible quantum yield. For $SO_2$ the most intense one corresponding to a quantum yield nearly 1 occurs at 220.6 nm. This corresponds to an excitation of the band $(132) \leftarrow (000)$, $[\mathrm{SO_2}(\tilde{\mathrm{X}}^1\mathrm{A_1}) + \mathrm{h}\nu \rightarrow \mathrm{SO_2}\ (\tilde{\mathrm{C}}^1\mathrm{B_2})]$ (fig 4.4). The numbers 1, 3 and 2 refer to excited quanta of the symmetric stretching, the antisymmetric stretching, and the bending vibrations of $SO_2$. The fluorescence dispersion spectrum covers a wavelength range between 240 and 420 nm, and it presents a maximum at 320 nm [15].

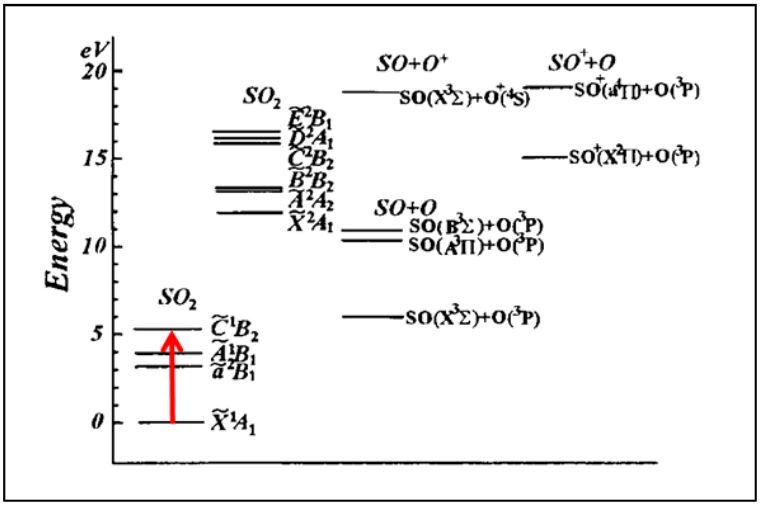


Figure 4.4. $SO_2$ excitation $(132) \leftarrow (000)$, $[SO_2(\tilde{X}^1A_1) + h\nu \rightarrow SO_2(\tilde{C}^1B_2)]$ [16].

This band is nearly at the limit of $SO_2$ predissociation, which takes places at wavelengths lower than 219 nm (fig. 4.5.),

$$SO_2 + h\nu\,(\lambda < 219.4\,nm) + SO(\Sigma^3_-) + O\,(P^3) \tag{4.17}$$

Figure 4.5 shows the absorption cross sections (a) and fluorescence intensity (b) spectra of $SO_2$ in a range from 215 to 225 nm [15]. It can be clearly seen that fluorescence decreases abruptly at lower wavelengths than 219 nm. Two wavelengths, peak and bottom one are indicated. Those were employed by Y. Matsumi et al. [15] to measure $SO_2$ concentrations without interferences. The subtraction of bottom fluorescence signal to the peak one turned out in a $SO_2$ fluorescence signal free of other fluorescent species or particles present in air (e.g. NO) as well as a better selectivity. This method of double wavelengths was used for S. Sellmeir [13] to measure oil consumption by using a dye laser (bandwidth of 0.13 $cm^{-1}$). This will be called in the following as; double wavelength switching mode (DWSM). In this work it has been demonstrated that such a procedure is not necessary when an OPO laser (5 $cm^{-1}$ of bandwidth) is employed. This is because the NO fluorescence (lifetime of 2000 ns) is avoided with another method called two temporal gate integration method (TTGIM).

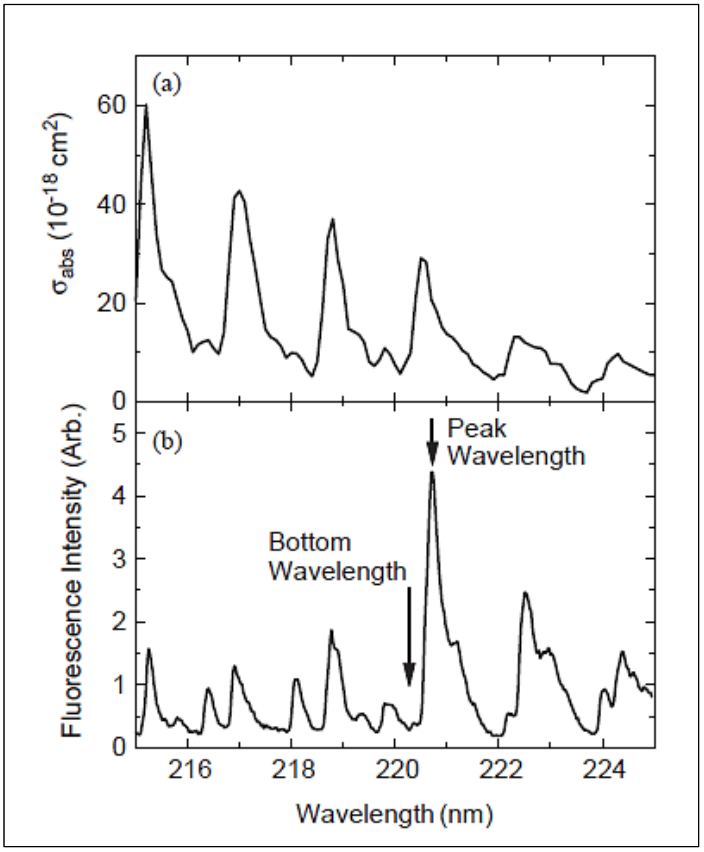


Figure 4.5. Absorption and fluorescence spectra of the $SO_2$.

There are other studies where the selected wavelength was a higher, 223 nm [17], 222 nm [18] or 226 nm [19]. However, in these particular cases apparatus and work conditions (atmospheric conditions) were much different than ours.

## 4.4. Detection of fluoresce (Photomultiplier tube: PMT)

For detecting fluorescence, a photomultiplier tube (PMT) was utilized. The employment of a PMT enables the collection of the light flux coming from the fluorescent molecule. The amplification of the light is produced by the photoelectron effect (fig. 4.6).

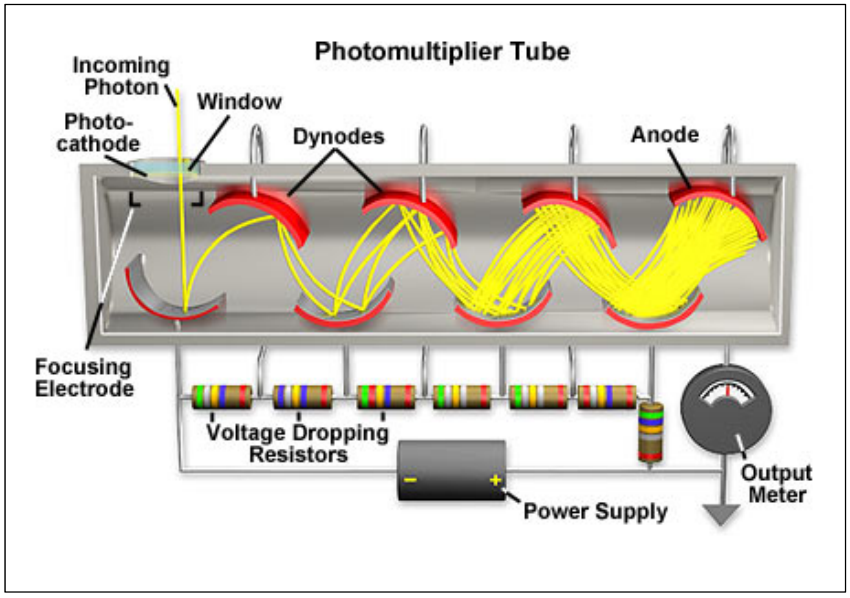


Figure 4.6. Schematic view of a photomultiplier tube [20].

PMTs are an excellent election for the detection of small amounts of light. This is because they overcome noise limitations by amplification of the photocurrent. Inside of these devices secondary-electron emission from internal dynodes is produced. This multiplies the number of photoelectrons. The photons enter into a vacuum tube through a glass or quartz window and hit the so called photocathode. After passing a focusing electrode the photoelectrons are led into a first cathode (e.g. Cu-Be) called dynode. From it an average $q$ of secondary electrons are emitted and lead into another dynode. The factor $q$ depends on the accelerating voltage and on the incidence angle as well as on the dynode material. A chain of N dynodes produces an amplification of $G = q^N$ (gain). Typical gains are in the range of $10^5$-$10^7$. Finally all the electrons hit an anode and the resulting signal is monitored in an oscilloscope [21]. The voltage detected in there is $V = i_a R$ . The anode current $i_a$ integrated over the time gives the total charge $Q_a = n_{Ph}\, e\, G$, with $n_{Ph}$ being the photon number, $e$ the electron charge and $G$ the gain. The voltage $V = i_a R$ follows the temporal behavior of the fluorescence with the prerequisite that time resolution of the detection system (PMT & oscilloscope) are fast enough.

In the case of fluorescence measurements a high time resolution is demanded, thereby the rise time of the anode pulse must be as short as possible. For a single released photoelectron the pulse rise time is caused by the spread of transit time for different secondary electrons. Their initial

velocities vary depending on the depth (penetration depth of the primary electrons) where they come from. The transit time between two electrodes located at a distance of $d$ and with a potential difference of $V$ is

$$t = d\sqrt{\frac{2m}{eV}} \tag{4.18}$$

with electrons having a mass of $m$ and starting at zero initial energy ($E_{kin}$). If they do have $E_{kin}$ the time difference is then,

$$\Delta t_1 = \frac{d}{eV}\sqrt{2mE_{kin}} \tag{4.19}$$

and for slightly different path lengths the time spread turns out to be

$$\Delta t_2 = \Delta d\sqrt{\frac{2m}{eV}} \tag{4.20}$$

which is similar to eq. 4.18. This time is commonly reduced by the mentioned focusing electrode located between the cathode and the first dynode. The resulting rise times are normally in the range of 0.5 to 20 ns (4 ns in case of used PMT).

The PMT must be located in orthogonal position (90°) with regard to the laser beam path. The spectral response, the quantum efficiency, sensitivity, and dark current are normally determined by the composition of the photocathode. Surface composition and geometry of the dynodes determines their ability of being electron multipliers. The gain of a photomultiplier is proportional to the number of dynodes (10-14) and to the voltage across them.

In the visible and UV region high sensitivity can be attained [5]. When a laser is tuned to a $\lambda_L$ of an absorption transition $E_i \rightarrow E_k$, the number of photons absorbed in time in the path length $\Delta_x$is

$$n_a = N_i n_L \sigma_{ik} \Delta_x \tag{4.21}$$

with $\mathrm{n}_L$ the number of incident laser photons per second, $\sigma_{ik}$ the absorption cross section per molecule, an $N_i$ the density of molecules in the absorbing state $|\mathrm{i}\rangle$. The amount of fluorescent

photons emitted per second from the level $E_k$ is

$$n_{Fl} = N_k k_k = n_a \eta_k \tag{4.22}$$

with $k_k = \sum_m k_{km}$ is the total spontaneous transition probability to all levels with $E_m < E_k$ and $N_k$ the density of molecules in the absorbing state $|\mathrm{k}\rangle$. The quantum efficiency of the excited (quantum yield, eq. 4.14) state $\eta_k = k_k/(k_k + R_k + \sum_i k_{iq}[M])$ gives the relation between spontaneous transition rate and the total deactivation rate. This includes radiation less transition rates, e.g. collision-induced transitions $R_k$, the quenching rate with regard to every molecule and its concentration. If the quantum yield (see Eq. 4.15) is equal 1 the number of photons emitted per second is equal to the photons absorbed ($n_{Fl} = n_a$). However, only a fraction $\delta$ of the fluorescence photons emitted in all the directions can be collected. $\delta$ depends on the solid angle (accepted by the fluorescence detector) according

$$\delta = d\Omega/4\pi \tag{4.23}$$

In addition, not every photon which hits the photocathode releases a photoelectron. The best photocathodes are 30% photo-efficient. $\eta_{ph}$ is called maximum quantum efficiency of the photocathode and the number of photons counted per second is [22]

$$n_{pe} = n_a \eta_k \eta_{ph} \delta = (N_i n_L \sigma_{ik} \Delta_x)\, \eta_k \eta_{ph} \delta \tag{4.24}$$

This formula is equivalent to equation 10.4, although the latter has been mathematically further developed. Since the final signal displayed onto the scope is proportional to the fluorescence collection efficiency $\delta$, it is truly important to design the collection optics in an optimum way. This is discussed in the next section.

## 4.5. Optical collection system

The optical collection system is one of the most critical parts of a fluorescence apparatus. The sensitivity and the limit of detection are quite dependent on them. In a typical apparatus for fluorescence measurements the optical collection system is located orthogonal to the light path, or in our case to the laser beam path. This minimizes light which comes from the light source,

such as reflections from the internal walls or scattering. It is worth to say that in our case, scattering from soot is negligible since the exhaust of the engine passes through a nonthermal plasma which burns all of them (chapter 3).

In prototype-II and III (see chapter 5), as well as in the first prototype (dye laser, see [13, 23]) two biconvex lenses were utilized to collimate the fluorescence coming from the excitation volume. The lenses are biconvex because of the low geometric aberration they exhibit. They were mounted in parallel to each other and at a distance of 10 cm with respect to their physical centers. Their focal length, $f$ is 100 mm and the diameter, $D$ is 100 mm. This gives a value of the f-number $f/\#$, equal to 1 according to $f/\# = f/D$. One can calculate the numerical aperture, $NA$ as follows,

$$NA = n \sin\theta = n \sin\left[arctan\left(\frac{D}{2f}\right)\right] \approx n \frac{D}{2f} \tag{4.25}$$

with $n = 1$ being the index of refraction of the medium between fluorescing source and lens (here vacuum) and $\theta$ is the half-angle of the maximum cone of light that can enter or exit the lenses. The result of eq. 4.25 is $NA = 0.5$. This is an important definition in order to know how good could be the $\delta$ value (eq. 4.23) which will inform about how much of the fluorescence can reach the photomultiplier. Thus we need to know the value of the solid angle $d\Omega$ which can be calculated according to

$$d\Omega = \sin\theta \, d\theta \, d\varphi \text{ or } \Omega = \iint \sin\theta \, d\theta \, d\varphi \tag{4. 26}$$

If we use now 4.26 and we assume the case of a cone with apex equal to $2\theta$ we obtain

$$\Omega = 2\pi \, (1 - \cos\theta) \, sr \tag{4.27}$$

with $sr$ is the so called steradian (dimensionless). If $\theta$ is now the half-angle of the maximum cone we can calculate $\Omega$. From eq. 4.25 we obtain $\theta = \pi/6$ which substituted in eq. 4.27 delivers a value for the solid angle of $\Omega = 0.842 \, sr$. By substitution in eq. 4.23 one obtains $\delta = 0.067$. This means that approximately 6.7% of the emitted light is collected by the PMT. The values herein calculated are used in chapter 10 for calculating signal strength.

The lenses which collect the emitted light from $SO_2$ in the range of 230-420 nm should have an antireflection coating ($R$ < 1.5%). This will avoid losses and therefore increase sensitivity. The values of the coating and other data can be found in appendix. The holder system of the lenses was designed to be able to adjust the focal length and with this the optimization of the signal intensity. This arrangement is located in the lower part of the fluorescence cell as it is explained in the chapter 6.

## 4.6. Filter

Filters have been widely utilized and developed ([14], [24]) for applications in spectroscopy methods. The way they work has been described elsewhere [25]. Depending on the effect that they have for transmission of wavelengths, filters can be of three kinds; band (wavelength) pass filter, long-pass filters or band (wavelength) and block filters. Together with the laser, the long-pass filter contributes to the selectivity of the technique. Besides, it is very important to avoid that the excitation light (220.6 nm) which is the most intense in the fluorescence cell, saturates the PMT and makes it blind for successive fluorescence light. In prototypes II & III the use of a long-pass filter was indispensable for detecting $SO_2$ fluorescence. It was selected to block wavelengths larger than 235 nm. However, the blocking of the light with $\lambda$ < 225 nm is not total (< 99% of absorption). This is the reason why there was still stray light even if no fluorescent molecules existed in fluorescence cell. This will be mentioned as scattering in chapter 7.

## 4.8. Literature


1. B. Valeur, M. N. Berberan-Santos, Molecular Fluorescence: Principles and applications, 2nd Edition, Wiley-Vch, 2013.
2. H.D. Metee, *The Journal of Chemial Physics*, Vol. 49, No.4, 15 August 1968, 1784-1793.
3. Luke, W. T., *Journal of Geophysical Research*, 1997, 102, pp. 16255-16265.
4. S, Butler, D. H. Levy, *J. Chem. Phys.* 66, 3538 (1977).
5. W. Stelson, X. Bao, *J. Air Pollut*. ControlAssoc., 38, 420, 198.
6. W. Steubing, *Annalen der Physik*, No. 8, 1921, 673-693.
7. H. Hayashi, Y. Sakaguchi, H. Abe, *Physica B: Condensed Matter,* Volume 164, Issues 1–2, June 1990, Pages 217–221.
8. H. Abe, H. Hayashi, *Chemical Physics Letters*, Vol. 187, No. 3, 6 December 1991, 227-232.
9. V.I. Makarov, I.V. Khmelinskii, *Chemical Physics* 146, (1990), 1-11.

10. W. Demtröder, Laser Spectroscopy: Experimental techniques, Vol. 1, pag. 27-29, Fourth edition, Springer (2008).
11. K. F. Greenough, A.B.F. Duncan, *J. Am. Chem. Soc.*, 1961, 83 (3), pp 555–560.
12. W. Demtröder, Laser Spectroscopy: Experimental techniques, Vol. 2, pag.; 27-28, 4th Edition, Springer 2008.
13. Laserspektroskopische Spurenanalytik von Ölbestandteilen in Abgasen von Verbrennungsmotore, Stefan Sellmeier, (PhD Thesis), 19.07.2011.
14. H. E. Bennett, W. R. McBride, *Applied optics*, Vol. 3, No. 8.
15. Y. Matsumi, H. Shigemori, K. Takahashi , *Atmospheric Environment* 39 (2005) 3177–3185.
16. S. Becker, C. Braatz, J. Lindner, E. Tiemann, *Chemical Physics* 196 (1995) 275-291.
17. J.C.D. Brand, P.H. Chiu and A.R. Hoy, *J. Mol. Spectrosc.* 60 (1976) 43.
18. J. B. Simeonsson, A.Matta, and R.Boddeti, *Analytical Letters*, 45: 894–906, 2012.
19. J. D. Bradshaw, M. 0. Rodgers, and D. D. Davis, *Applied Optics*, 15 July 1982 , Vol. 21, No 14.
20. Courtesy of http://micro.magnet.fsu.edu/index.html.
21. W. Demtröder, Laser Spectroscopy: Experimental techniques Volume 1, pag. 216, Fourth edition, Springer (2008).
22. W. Demtröder, Laser Spectroscopy: Experimental techniques, Vol. 2, pag. 27-28, Fourth edition, Springer (2008).
23. R. Naaman, V. Yakhot, and G. Fischer, *J. Chem. Phys*. 67, 5472 (1977).
24. C. B. Childs, *Journal of the optical society of America*, Vol. 51, No. 8, (08/1961), 895-897.
25. W. Demtröder, Laser Spectroscopy: Experimental techniques, Vol. 1, pag. 162, Fourth edition, Springer (2008).
26. S. Sellmeier, E. Alonso, U. Boesl, *Anal. Chem.*, 2014, 86 (1), pp 380–389.

# 5. Development of a new OPO-laser

The excitation source, a laser in our case, is one of the fundamental if not the most critical part of an apparatus which is based on laser induced fluorescence. It was pointed out in chapter 4 (section 4.3) which are the main advantages of a laser to excite molecules. In case of the oil-consumption measurement system described in this work, it has become the most important device. The measurements of oil-consumption in a test engine facility very usually demand a very steady, compact and easy to handle apparatus. However, none of the lasers available on the market did accomplish all the necessary requirements for such a purpose. Those are:

- Not based on or containing hazardous substances such as dyes.
- Energy stability over long periods of time and medium range (1 mJ) energy per pulse.
- Compact design, huge stability and small size.
- Cooling system incorporated.
- Relatively low divergence and small beam spot.
- Easy to handle and very familiar software.
- Relatively reduced cost.

Those were the demanding features for a laser that had to be incorporated in the improved version of the Prototype-I. In the Prototype-I which was setup by S. Sellmeier [1] a dye laser (Lambda Physics, Scan Mate 2C) was used. Measurements were carried out with this system in a highly satisfactory way. However, the laser was the main drawback for its commercialization as an oil-consumption measuring system based on LIF and working in a pressure range of 3 mbar. For that reason, a very close and intense collaboration was established between our institute, Lehrestuhl für Physikalische Chemie (Technische Universität München) [27] and the company InnoLas Laser-GmbH Holding (Krailling, Germany) [26] in the frame of a project and a PhD-scholarship financed by the BSF (Bayersiche Forschungs Stiftung) [28]. The last three years of very tight cooperation and intense research carried by R. Kelnberger, C. Menhard and our group, E. Alonso, S. Sellmeier and U. Boesl, gave rise to the first commercial OPO laser system worldwide integrated in a single solid housing as a whole. In following sections it is discussed the main physical processes of an OPO laser, and in particular the characteristics of a new InnoLas Laser-GmbH OPO are discussed.

## 5.1. New design of a mobile and compact optical parametric oscillator.

Optical parametric oscillators are based on a nonlinear optical process which occurs in crystals exhibiting birefringence. Those have the property of having a refractive index that depends on propagation of light path and polarization. This can be visualized in a better way if one considers two different axes; one ordinary $(o)$ and another extraordinary $(e)$ with different value of the refractions index $n_o$ and $n_e$ respectively. They have been extensively researched in the last decades and the interest for such a technology is still increasing nowadays. The first demonstrations of an OPO process were made by Giordmaine and Miller (1965) [16-17]. Continuous-wave operation of an OPO was stated by Smith et al. (1968) [19]. The new materials such as BBO, LBO, and KTP, conducted to the achievement of efficiencies of nonlinear mixing in the OPO as large as 32% (Bosenberg el al. 1989, [11, 12, 18]) and to generation of femtosecond OPO lasers two decades after (Edelstein et al. 1989, [15]). One especial mention deserves R. Wallenstein et al. who have performed investigations of fundamental and applied non-linear optics. In particular their studies in OPO effects [5-10] had strong influence on the development of the InnoLas Laser-GmbH-OPO lasers [26]. The pumping laser of the new OPO laser system is a solid state Nd:YAG laser whose 3$^{rd}$ harmonic $(\omega, 355\ nm)$ radiation (triple harmonic generation, THG) is used to pump the OPO crystal. In the following the focus will fall on the processes responsible for OPO operation.

### 5.1.1. Optical parametric oscillation (OPO)

The description of the OPO effect is briefly presented here [2]. First of all one has to consider the dipole moment per unit volume, also called polarization $\tilde{P}(t)$. In the case of linear optics, the induced polarization depends linearly on the electric field strength $\tilde{E}(t)$. However in the case of a non-linear process the relation has to be described as follows,

$$\tilde{P}(t) = \chi^{(1)}\tilde{E}(t) + \chi^{(2)}\tilde{E}^2(t) + \chi^{(3)}\tilde{E}^3(t) + \cdots \equiv \tilde{P}^{(1)}(t) + \tilde{P}^{(2)}(t) + \tilde{P}^{(3)}(t) + \cdots \quad (5.1)$$

where the $\chi^{(2)}$ and the $\chi^{(3)}$ are the second- and third-order nonlinear optical susceptibilities, respectively. In eq. 5.1, it is assumed that the polarization at time $t$ depends only on the instantaneous value of the electric field strength. The fact that the medium responds instantaneously also implies that the medium must be lossless and dispersionless. Furthermore, in eq. 5.1, it is stated that the susceptibilities do not depend on the frequencies, instead they are

constant. The second-order nonlinear polarization processes are different from those which occur for the third-order. Only non-centrosymmetric crystals (no inversion symmetry) have features which may induce nonlinear optical effects.

The process known as difference-frequency generation (DFG) is a second-order nonlinear optical process. It can be described according to

$$P(\omega_1 - \omega_2) = 2\chi^{(2)} E_1 E_2^* \tag{5.2}$$

what is graphically shown in fig. 5.1. Amplification of one of the lower-frequency fields which enter the nonlinear crystal together with the pump beam is called optical parametric amplification (OPA). If amplification of one or both of the lower-frequency fields is performed by an adequate resonator then an optical parametric oscillator (OPO) is achieved. In the fig. 5.1 we can see a graphical description of the process.

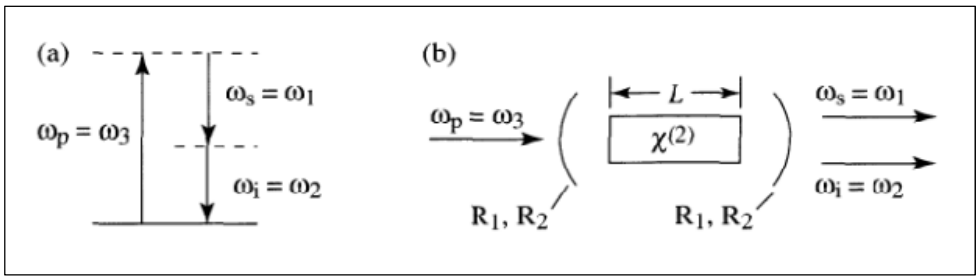


Figure 5.1. a) DFG process and b) OPA taking place within a (pseudo) Fabry-Perot cavity. This last is known as an optical parametric oscillator, OPO. In between of two high reflecting mirrors ($R_1, R_2$) an element with $\tilde{P}(t) \propto \chi^2$ is located.

In the DFG process three different wavelengths are involved. The physical effect can be written as, $\omega_i = \omega_p - \omega_s$, where $\omega_i$ is the idler frequency, $\omega_s$ is the signal frequency and $\omega_p$ is the pumping frequency (fig.5.1.a). The gain associated with the process of OPA can, in the presence of feedback, produce oscillation as shown in fig. 5.1.b. The OPOs have been extensively used to generate tunable radiation in the range of infrared, visible, and ultraviolet light. The laser can be continuous or generate pulses of nanoseconds, picoseconds and femtoseconds duration. We can distinguish two cases:

1. Both mirrors are highly reflected at both (signal and idler) frequencies: Doubly resonant oscillator.
2. The mirrors are highly reflected either to the signal or to the idler radiation: Singly resonant oscillator.

Let us consider briefly the threshold of a parametric oscillation. Considering a device equal to that one represented in fig. 5.1.b, one can define $R_1$and $R_2$ as the reflectivity of the mirrors which can be equal or not. Firstly we consider the approximation of that a fraction of the energy gain per pass must be the same as the fractional energy loss per pass. Assuming exact cavity resonance, of perfect phase matching ($\Delta k = k_1 + k_2 - k_3 = 0$) and that the cavity is double resonant with the same reflectivity for signal and idler frequencies, $R_1 = R_2 \equiv R$, $(1 - R) \ll 1$), we obtain

$$(e^{2gL} - 1) = 2(1 - R) \tag{5.3}$$

In a realistic condition that the single-pass exponential gain $2gL$ with $L$ being the length of crystal $g$ (defined below) is not large compared to unity, then 5.3. becomes

$$gL = 1 - R \tag{5.4}$$

which is the threshold condition [4]. More generally the threshold condition can be formulated as the fact that the fields within the resonator must replicate themselves each round trip. For arbitrary end-mirror reflectivity at signal and idler frequencies, the condition can be expressed by assuming perfect phase matching as,

$$A_1(0) = \left[A_1(0)\cosh gL + \frac{k_1}{g}A_2^*(0)\sinh gL\right](1 - l_1) \tag{5.5}$$

$$A_2^*(0) = \left[A_1(0)\cosh gL + \frac{k_2^*}{g}A_2^*(0)\sinh gL\right](1 - l_2) \tag{5.6}$$

where $l_i = 1 - R_i e^{-\alpha_i L}$ is the fractional amplitude loss per pass, $\alpha_i$ is the absorption coefficient of the crystal at frequency $\omega_i$, $A_i$ is the amplitude of the$i$ field and $g = [\kappa_1\kappa_2^* - (\Delta k/2)^2]^{1/2}$ ($\kappa = \frac{8\pi i\omega_i^2 dA_3}{k_j c^2}$). Now if we state that eq. 5.5 and 5.3 must be simultaneously satisfied, one can obtain

$$\cosh gL = 1 + \frac{l_1 l_2}{2 - l_1 - l_2} \tag{5.5}$$

which contains the threshold condition for both cases, singly and doubly resonant. For a singly resonant oscillator the equation becomes $g^2L^2 = 2l_1$ in which there is not feedback for the idler frequency ($l_2 = 1$).

The condition of energy conservation $\omega_s + \omega_i = \omega_p$ enables any frequency $\omega_s < \omega_p$ to be generated in an OPO. This is feasible because of the phase-matching condition $(\Delta k = 0)$ which could be reached for at most one pair of signal and idler frequencies for any angle between light propagation and crystal axis.

Several crystal materials can be used in a tunable nano-second (ns) OPO laser. However, the most widely used are type-I and type-II BBO crystals. Type-I and the type-II BBO crystals differ in the cutting angle between front surface and crystal axis which influences divergence and bandwidth. The resonator composition and configuration has been since long time investigated too. R. Wallenstein et al. have made several studies which are very useful for the development of the present laser. In the next two sections the type of crystal and the sort of resonator will be described following their studies.

#### *5.1.1.1.* ***β-Barium Borate (BBO) crystals as OPO generator***

During the development of the laser, both type-I $(\mathrm{e} \rightarrow \mathrm{o} + \mathrm{o})$ and type-II $(\mathrm{e} \rightarrow \mathrm{o} + \mathrm{e})$ BBO crystals were investigated. The use of one or the other depends on the compromise between the divergence, gain bandwidth and output energy. The advantage of using a very narrow bandwidth laser light in LIF which allows a huge selectivity can be set apart since selectivity is achieved in our case by integrating the PMT signal within two different time gates (chapter 7). In our case and due to a mathematical subtraction bandwidth is not as important as the other two factors. Figures 5.3 and 5.4 show the phase-matching curves of type I and II BBO crystal for both signal and idler waves. It is interesting to notice the different degeneracy angle which is defined as the one at which wavelength of signal and idler are the same. They are 33.2˚and 48.65˚ for type I and II respectively.

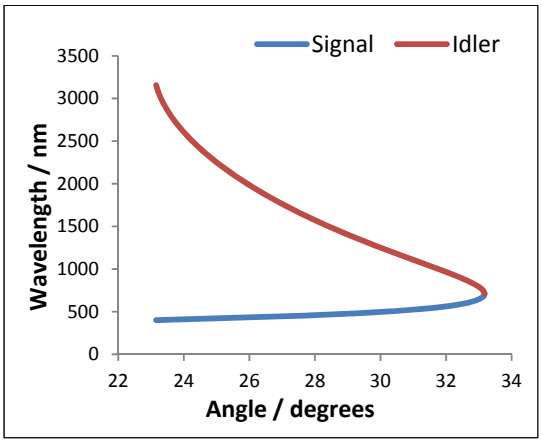


Figure 5.3. Type-I BBO crystals phase-matching curves [29] for a pumping of 355 nm.

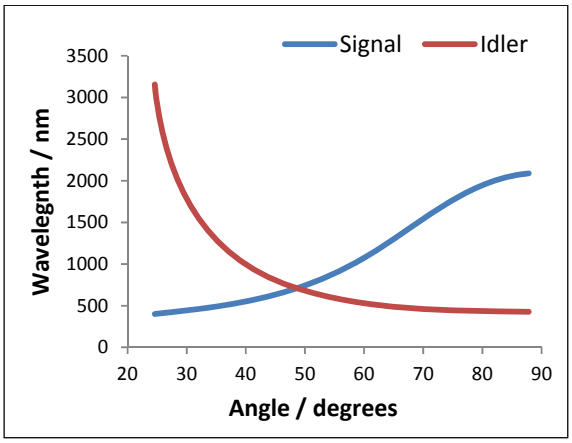


Figure 5.4. Type-II BBO crystals phase-matching curves [29] for a pumping of 355 nm.

The spatial and spectral (bandwidth of 5 $cm^{-1}$) properties of the output waves of a type-II BBO crystal are considerably improved, but can be improved even further with a double passing (section 5.1.1.2.) of the laser pump radiation. This lowers the divergence and reduces the oscillation threshold which improves the conversion efficiency) [3].

### *5.1.1.2.* ***Double pass of pump radiation (355 nm) and prism-mirror cavity.***

The design of the cavity in the OPO laser from InnoLas Laser-GmbH includes two features that contribute to improve divergence both in horizontal and in vertical plane for a type-II phase matched BBO crystal [3]. The horizontal divergence is reduced by a double-passing of the laser pump beam. This is achieved by reflecting back the transmitted pump radiation into the OPO. Due to the fact that the pump wave passes the BBO crystal in both directions, the pumping field strength within the OPO crystal is strongly enhanced. However, only the collinear rays undergo gain at the same wavelength when they bounce back and forth [3]. The reflection is performed with a 90˚ prism (cateye reflector) instead of a HR rear mirror. There are three advantages of a cateye reflector: 1) It is a self adjusting 180° reflection device, and 2) It mirror images the cross section of the laser beam giving rise to a more symmetric illumination of the crystal and thus a reduction of vertical divergence [3]. 3) No dielectric mirror layers are involved which tend to be destroyed by high laser power levels present at very different wavelengths. This prism is then aligned with an angle of 90° between the front plane and the resonator axis (figure 5.5). The pump

wave is coupled into the cavity by a 45˚ HR front mirror which is transparent for the OPO wavelength.

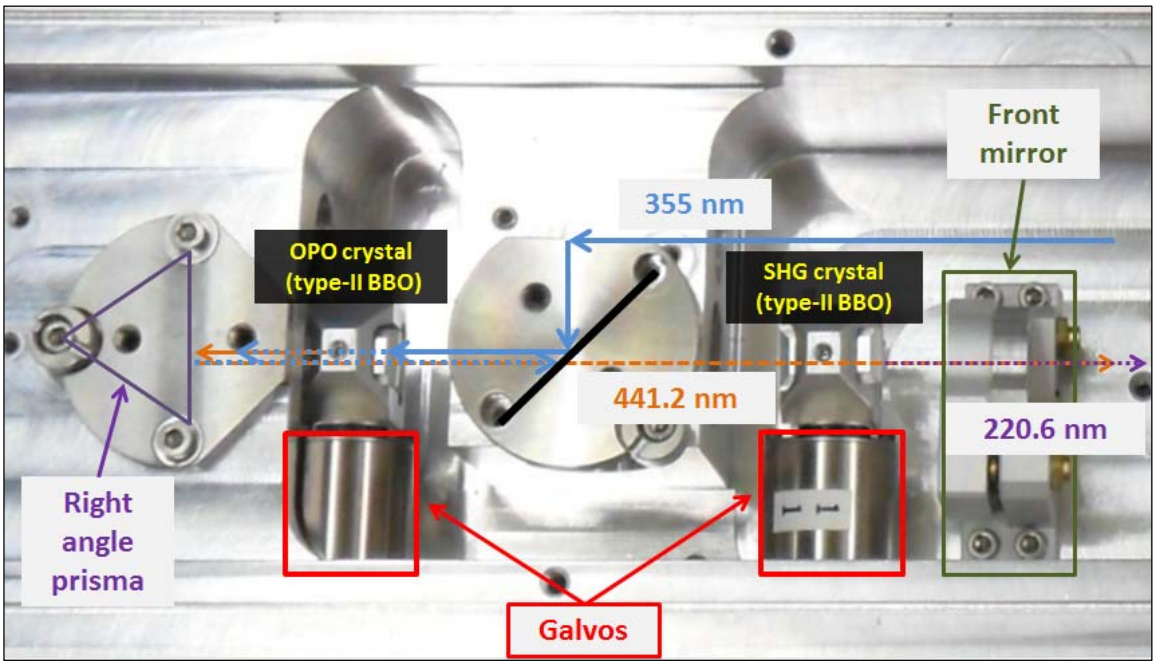


Figure 5.5. OPO cavity with intracavity BBO-SHG crystal. The red rectangle shapes mark the two galvanometer motors. The triangle mimics the prism. OPO and SHG (see chapter 5.2.1) crystals are labeled. The blue line indicates the pumping beam at, 355 nm. The orange lines indicate the OPO-signal (440 nm) and the purple ones the OPO-idler radiation, which is doubled at the SHG unit (220 nm).

InnoLas Laser-GmbH company decided to use a type-II crystal in our setup. Due to the narrower bandwidth and the reduced beam divergence, the type-II BBO crystal with the back reflection for the pump beam allows efficient OPO radiation and consequently efficient frequency doubling with quite long nonlinear crystals. In addition, in the OPO used in this work, the SHG process takes places intracavity for a further enhancement.

### 5.1.2. Intracavity second harmonic generation (ISHG)

The utility of an OPO laser can be increased with conversion of idler wave into a tunable UV. This is done by a process named second harmonic generation (SHG). In the case of a Nd:YAG laser, the fundamental wavelength (1064 nm, $\omega$) is in many occasions doubled giving rise to a 532 nm ($2\omega$), The SHG is a non-linear optical process which occurs due to the birefringence of a material too. If

the medium does not have any loss for both the fundamental $\omega_1$ and the second harmonic frequency $\omega_2$, the non-linear polarizability (proportional to $\chi^{(2)}$) can be expressed as

$$\tilde{P}_{NL}(z,t) = \tilde{P}_1(z,t) + \tilde{P}_2(z,t) \tag{5.6}$$

Where $\tilde{P}_1(z,t)$ is the polarizability due to $\omega_1$ and $\tilde{P}_2(z,t)$ is the one corresponding to $\omega_2$. Thus one can write

$$P_1(z) = 4d_{eff}E_2E_1^* = 4d_{eff}A_2A_1^*e^{i(k_1-k_2)z} \tag{5.7}$$

$$P_2(z) = 2d_{eff}E_1^2 = 2d_{eff}A_1^2e^{ik_1z} \tag{5.8}$$

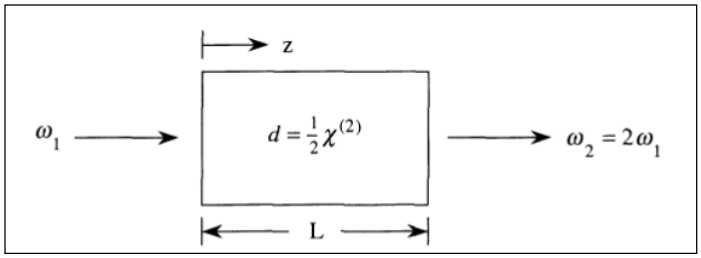


Figure 5.6. Sketch of the second harmonic generation process in a material of electrical susceptibility $\chi^{(2)}$ and length L. The resulting frequency $\omega_2$ is the double of the incoming one $\omega_1$.

After a mathematical treatment of 5.7 and 5.8 (Armstrong et al., [21]) the resulting SHG frequency efficiency can be described as

$$\eta = \frac{u_2^2(L)}{u_1^2(0)} \tag{5.9}$$

with $u_2(O) = \tanh(\zeta)$ , $u_1(O) = \mathrm{sech}(\zeta)$ and

$$\zeta = \left(\frac{(1024\pi^5 {d_{eff}}^2 LP)}{\lambda_1^2 c n_1 n_2}\right)^{1/2} \tag{5.19}$$

where $P$ is the power, $L$ is the length of the crystal, $n_1$and $n_2$are the refraction indexes of the crystal and surrounding, $\lambda_1^2$ is the square of the wavelength and ${d_{eff}}^2$ is the effective value of $d_{ijk} = \frac{1}{2}{\chi^{(2)}}_{ijk}$.

This efficiency can be improved if the second harmonic generation is performed intracavity. SHG intracavity processes have been theoretically described for the first time by J.A. Armstrong et al. [22] (1962) and the realization was demonstrated by Ashkin et al. [23]. The process was performed experimentally in a double resonant OPO cavity (Q-switched pumped) by A.J. Campillo [24] (1972). Besides, V. Berger [26] has derivated an expression for the efficiency of an intracavity up-conversion SHG process. The main conclusion drawn from mathematics and experiment is that, ISHG is potentially more efficient than extracavity up-conversion due to higher intensity of resonating signal in the cavity. Besides, nonlinear loss at signal wavelegnt in SHG yields favorable dynamics for efficient up-conversion over a large dynamic range in the pump power [25].

### 5.1.3. Galvanometric motors (galvo) and fast wavelength switching mode

The BBO crystals where OPO and SHG processes take place, are mounted onto holders turned by a galvanometric motor. This allows a very quick wavelength switching. This ultrafast wavelength shift developed by the company was especially designed for the analytic method uses at the beginning of this work [1, 30]. Both galvos have a range of 64000 steps (steps/nm). This indicates the high precision with which a certain value of wavelength can be reached and the energy optimized. In the figure 5.7 a typical calibration is shown. Neither the OPO (section 5.1.1) nor the ISHG (section 5.1.2) processes are linear. However, in the short range of wavelength that fig. 5.7 shows (432-448 nm / 216-224 nm) linearity may be assumed in a very good approximation. This region is optimal for excitation of $SO_2$ with maximal intensity.

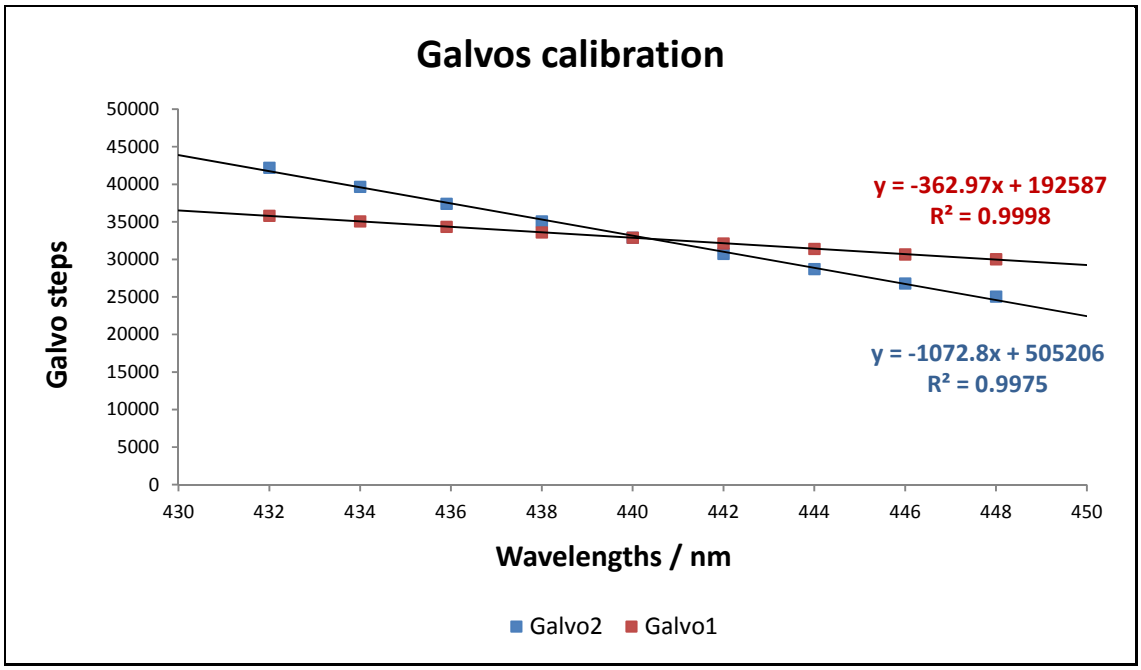


Figure 5.7 .Typical linearity of the galvo 1 (ISHG) and the galvo 2 (OPO) positions versus wavelengths. The range that the type-II BBO crystal can reach is from 400-700 nm (idler) and 710-2500 nm (signal). Wavelengths displayed are referred to fundamental OPO radiation.

## 5.2. InnoLas Laser-GmbH OPO laser

For the final realization of the new OPO several parts needed to be improved and many problems had to be solved. It was due to the fruitful cooperation between our group at TUM and InnoLas Laser-GmbH that finally a functional laser system was available. The final model which is suitable on the market consists of a laser head, a power supply and an optional cooling system.

### 5.2.1. **Laser head**

The laser head incorporates a Nd:YAG laser with second and third harmonic generation units, the OPO crystal and an intracavity SHG units. Besides, there are two telescopes. One serves to focus the OPO pumping laser, with 355 nm into the crystal which increases the OPO process efficiency. The second one is after the exit mirror of the OPO/SHG resonator and aims to improve the beam quality of the final UV laser radiation. The laser head is mounted in compartments machined out of a solid aluminum block. This has the advantage of giving a high mechanical and thermal stability to the whole system as well as it protects the entire laser from vibrations. The function of the different compartments is as follows: In the first, the Nd:YAG laser emitting its fundamental at 1064 nm is located, in the second the SHG and THG units of the Nd:YAG laser are placed, in the

third the OPO system with the intracavity SHG is set. The size of the laser head is 55x30x20 cm (LxWxH). Pockels cell and Nd:YAG rod are cooled by distilled water from an external source (lab cooling system) or as in our case from a mobile 19 inch compact chiller.

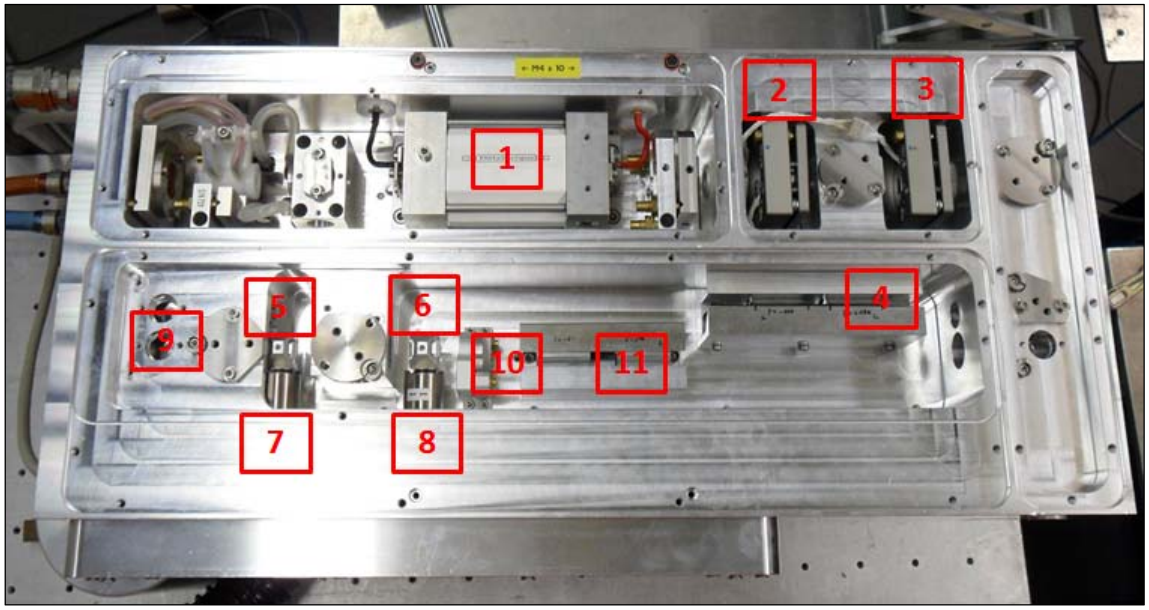


Figure 5.6. Top view of the InnoLas Laser-GmbH OPO ns-laser where the carbon-fiber covers removed. 1) Nd:YAG laser, 2) SHG unit, 3) THG unit, 4) First telescope to focus the 355 nm, 5) Type-II BBO crystal for the OPO process, 6) Type-II BBO crystal for the conversion of the OPO idler into UV, 7) and 8) Galvos, 9) Prism as rear reflector, 10) Front mirror and 11) Second telescope. (SHG crystal of the Nd:YAG is a BBO-type I, THG crystal of the Nd:YAG is BBO-type II)

### 5.2.2. **Power supply**

The power supply has the size of 50x50x20 cm (LxWxH) and it has all the necessary inputs and outputs connectors for both, triggering and controlling the laser. The communication between PC and laser can be made by LAN (TCP/IP protocol) and by LDL (optical fiber). Figure 5.7 shows a picture of it. The small size is particularly appropriate for mobile systems.

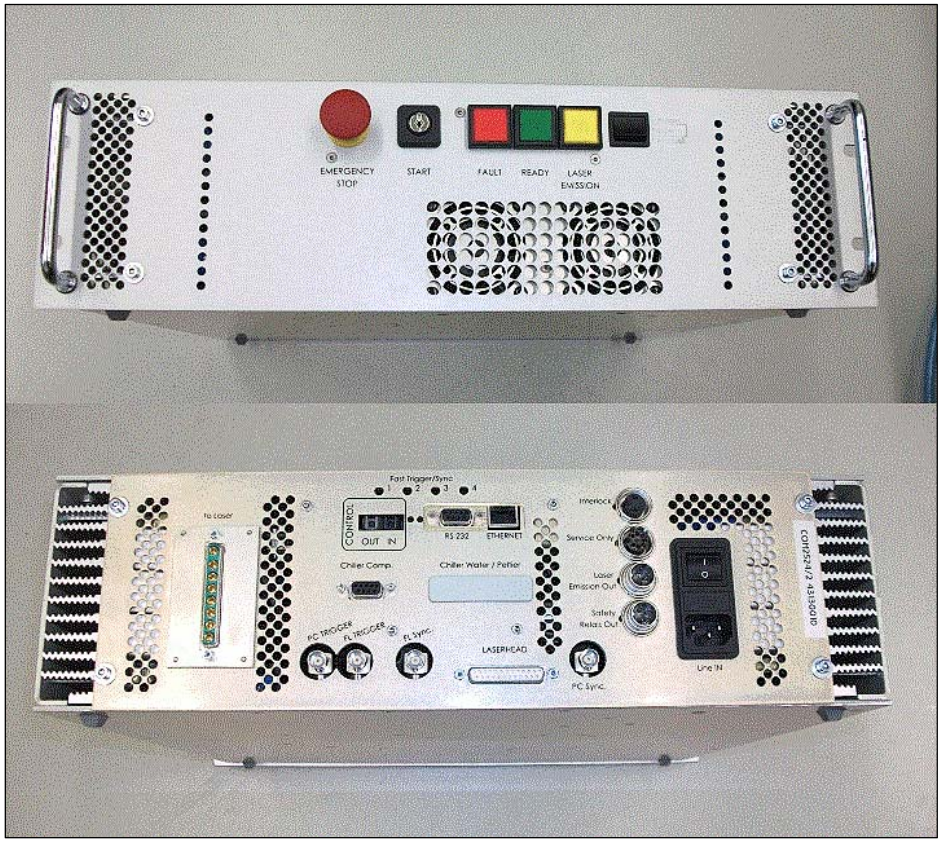


Figure 5.7.Front and back part of the OPO power supply.

### 5.2.3. **Cooling system**

Maintenance of Pockels cell and Nd:YAG rod temperatures are essential in order to attain steady laser operation mode. This means that the laser pulse energy does not decrease over the time. The cooling system includes two filters, one for avoiding small-medium size particles flowing into the laser system, and another to compensate feasible increments in the water conductivity. The water must be always of quality micro-Q. The conductivity should never be higher than 1 μS and the temperature must be kept below 25˚C. Figure 5.8 shows the internal cooling system used at prototype-III. Dimensions are 65x50x20 cm (LxWxH).


Figure 5.8. Internal cooling system utilized in prototype-III.

## 5.4. Literature.


1. Laserspektroskopische Spurenanalytik von Ölbestandteilen in Abgasen von Verbrennungsmotore, Stefan Sellmeier, (PhD Thesis), 19.07.2011.
2. R. W. Boyd, Non-linear optics, Chapter 2, 99-107, 2º Edition, Academic Press, 2003.
3. G. Anstett, G. Göritz, D.Kabs, R. Urschel, R.Wallenstein, A. Borsutzky, *Appl. Phys.* B 72, 583–589 (2001).
4. J.A. Giordmaine and R.C. Miller, *Phys. Rev. Lett.* 14, 973 (1965).
5. S. Burdulis, R. Grigonis, A. Piskarskas, G. Sinkevicius, V. Sirutkaitis, A. Fix, J. Nolting, R. Wallenstein, *Optics communications*, Vol. 74, No. 6, 15 January 1990, 393-402.
6. Y.X. Fan, R.C. Eckardt, R.L. Byer, J. Nolting, R. Wallenstein, *Appl. Phys. Lett.* 53 (21), 21 November 1988, 2014-2016.
7. A. Piskarskas, V. Smilgevicius, A. Umbrasas, A. Fix, R. Wallenstein, *Optics communications,* Vol. 77, No. 4, 1 July 1990, 335-338.
8. G. Nastett, A. Borsutzky, R. Wallenstein, *Appl. Phy.* B 76,541-545 (2003).
9. H., A. Lago, R. Wallenstein, *J. Opt. Soc. Am. B*, Vol. 4. No. 11, November 1987, 1753-1764.
10. A. Fix, T. Schröder, R. Wallestein, J.G. Haub, M.J. Johnson, B.J. Orr, *J. Opt. Soc. Am. B*
11. W. R. Bosenberg, W. S. Pelouch, and C. L. Tang, *Appl. Phys. Lett* 55, 1952 A989).
12. W. R. Bosenberg and C. L. Tang, *Appl. Phys*. Lett 56, 1819 A990).
13. R. L. Byer, H. Rabin, and C. L. Tang, eds., Treatise in Quantum Electronics, Academic

Press, New York, 1973.

14. M. Ebrahimzadeh and M. H. Dunn, in Handbook of Optics IV, 2nd ed., McGraw-Hill, New York, 2001.
15. D. C. Edelstein, E. S. Wachman, and C. L. Tang, *Appl. Phys. Lett* 54, 1728 A989).
16. J. A. Giordmaine and R. C. Miller, *Phys. Rev. Lett.* 14, 973 A965).
17. J. A. Giordmaine and R. C. Miller, *Appl. Phys. Lett.* 9, 298 A966).
18. L. E. Myers, R. C. Eckardt, M. M. Fejer, R. L. Byer, W. R. Bosenberg, and J. W. Pierce, *J. Opt Soc. Am. B* 12, 2102 A995).
19. R. G. Smith, J. E. Geusic, J. H. Levinstein, J. J. Rubin, S. Singh, and L. G. van Uitent, *Appl. Phys. Lett.* 12, 308 A968).
20. U. Simon and F. K. Tittel, in Methods of Experimental Physics, Vol. Ill, R. G. Hulet and F. B. Dunning, eds., *Academic Press*, San Diego, 1994.
21. J. A. Armstrong, N. Bloembergen, J. Duelling, and P. S. Pershan, *Phys. Rev.* 127, 1962.
22. J.A. Armstrong, N. Boembergen, J. Ducuing, P.S. Pershan, *Phys. Rev.* 127 (1962) 1918, R. A. Baumgartner, R.L. Byer, IEEE, J. Quantum Electron.QE-15, (1979) 432.
23. A. Ashkin, G.D. Boyd, J.M. Dziedzic, IEEE *J. Quantum Electron.* 2, 109-124 (1996).
24. A.J. Campillo, IEEE *J. QuantumElectron,* QE-8 (1972) 914.
25. G.T. Moore, K. Koch, E.C. Cheung, *Optics Commun.* 113, 1 January 1995, (1995) 463-470.
26. InnoLas Laser-GmbH Holding (Krailling, Germany)
27. http://www.pc.ch.tum.de/index.php?id=4
28. http://www.forschungsstiftung.de/
29. A. Smith , SNLO free software.
30. Y. Matsumi, H. Shigemori, K. Takahashi , *Atmospheric Environment* 39 (2005) 3177–3185.

# 6. Apparatus: Prototype-II & Prototype-III

## 6.1. General description

Herein components of the apparatus are described as well as prototype-II & III are shown. The mobile, robust and compact prototype-II & III contain several devices. A critical one is the OPO laser which has been described in the previous chapter. In general, the rest of the setup corresponds to a normal LIF setup as one can see in fig. 6.1. However, some parts are special developments and need to be explained. In appendix there are two tables containing all the main devices used to construct the prototypes II and III.

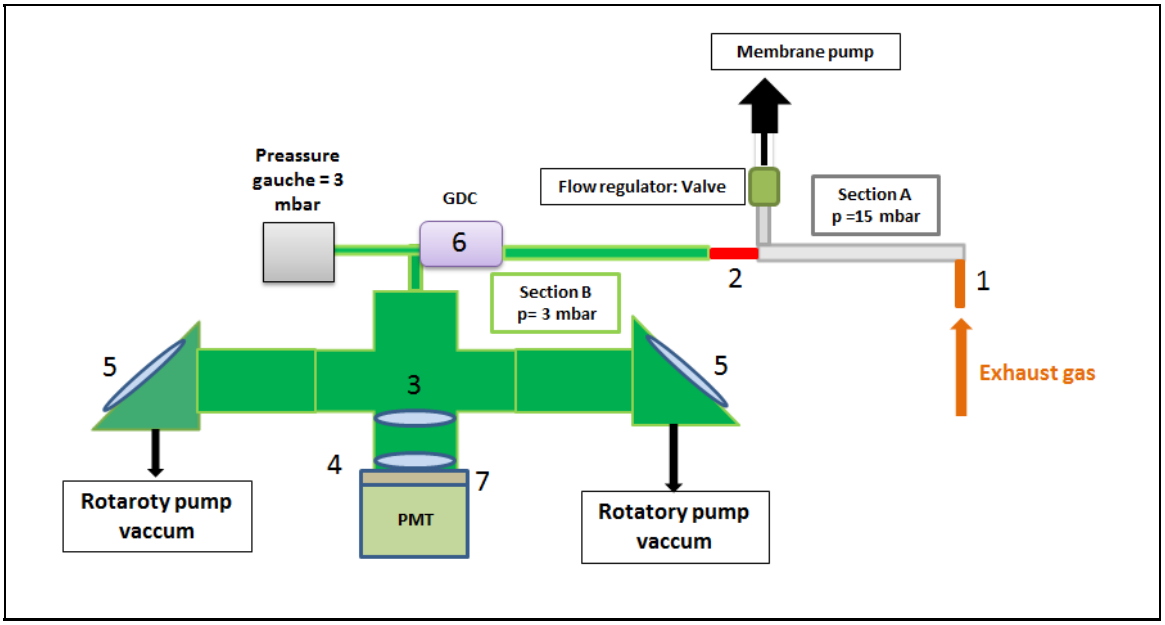


Figure 6.1. Scheme of LIF setup and piping. 1: Primary (sampling) nozzle, 2: Secondary nozzle, 3 & 4: Bi-convex lenses, 5: UV/VIS windows set at Brewster angle (~56˚), 6: Glow discharge cell (GDC), 7: Long-pass filter and photomultiplier (PMT).

Figure 6.1 shows a scheme of LIF setup with pipes and sampling system. Two sections are differentiated. Section A (grey) represents a pre-vacuum step where pressure is kept in a range from 15 to 30 mbar. This begins at sampling nozzle (orange, 1 in fig. 6.1) and finishes at the pressure reduction nozzle (red, 2 in fig. 6.1). Grey section represents a black hose which is necessarily heated up till 230 °C. Pressure in section B (green) is regulated via allowing more or fewer gas flow to enter the FC (section 6.2.3). A pressure gauge is connected in this section to

measure the pressure and keep it constant at 3 mbar. After plasma conversion the sample from the engine exhaust enters the fluoresce cell (FC) where laser light excites the formed $SO_2$. Two UV/VIS windows are fixed at the extremes of both fluorescence cell arms. At an angle of 90° to the laser beam the optical system and detector are located. These are formed by two bi-convex lenses, a long-pass filter and a photomultiplier (PMT). Below every window a Swagelok® adaptor is welded and a vacuum stainless steel pipe is connected. Those are finally connected to a zeolite filter in front of a rotatory pump. The pressure at this point is monitored also by a Penning gauge.

## 6.2. Vacuum system

The glow discharge cell worked best at a pressure of 3 mbar. This rough vacuum is obtained by using a rotatory pump and a membrane pump. For an on-line measuring instrument (as the presented prototypes) a well-controlled vacuum system is of particular importance. It is responsible for the gas flow as well as for regulating pressure in GDC and FC.

### 6.2.1. **Two step pressure reduction: Nozzles**

The apparatus works in a rough pressure regime. Several studies were made during setting up of the prototype-I [1]. Those led to the conclusion that the nonthermal plasma created in the GDC worked most efficiently at 3 mbar. To achieve that, a two-step pressure reduction is utilized. This is realized by two different pumps and two nozzles. The first one is the so called sampling nozzle and is located at the initial part of the black hose collinear to it. This nozzle is directly connected to an engine when measurements are carried out. A second one is located orthogonal to the sampling one. It allows that concentration of $O_2$ does not drop below 3 %. It has been proved [1] that 3% of $O_2$ is the necessary minimum amount to fully oxidize all the sulfur present in the oil compounds (efficiency ca. 99.5%). Together with the two nozzles a thermocouple is located (fig. 8.5). A third nozzle is fixed inside the apparatus, between the black hose (below explained) and the glow discharge cell. Previous to it the flow regulating valve is located. This is of particular importance and allows the user to adjust the pressure in the glow discharge cell. An optimum width of the nozzles was chosen to avoid soot deposition and to be able to reach the needed vacuum. Dimensions of nozzle are 250 μm of diameter and 1 mm of length. The nozzle is located at the end of a tube with a length of 45 mm and an inner diameter of 1.8 mm (3 mm outer diameter).

### 6.2.2. **Rotatory pump**

This pump creates the main vacuum in the FC (see table 6.1). Two different pressure regimes must be considered when membrane pump is not active. The first one concerns the pressure ($1.5 \cdot 10^{-2}$ mbar) reached by the pump (full speed) when the system is sealed from the atmosphere and no leakages are affecting to it. This is reached by two caps which seal both nozzles (sampling and extra air nozzle). Then, the pump can create a vacuum in the cell (fluorescence cell) of about $3 \cdot 10^{-2}$ mbar. A second pressure regime is that obtained when caps are removed. Thus pressure rises till 2.7 mbar. Those pressures (measured when the whole system is heated up to 230 °C) serve as a reference to check whether leakages exist at pipe unions or rotatory pump works inadequately.

| Nozzles | Membrane pump | Pressure section B (sensor 1) / mbar | Pressure in section A (sensor 2) / mbar | Temperature / ˚C |
|---|---|---|---|---|
| **Sealed** | OFF | $3.5 \cdot 10^{-2}$ | $4.4 \cdot 10^{-1}$ | room |
| **Sealed** | OFF | $1.5 \cdot 10^{-2}$ | $3.7 \cdot 10^{-1}$ | 230 |
| **Opened** | OFF | 2.7 | 5 | 230 |
| **Opened** | ON | 1.5 | 3 | 230 |

Table 6.1.Standard pressures in the section A and B (according fig. 6.1) obtained in ideal conditions (Optimum conditions: no leakages and nozzles not blocked by particles) at the different configurations.

### 6.2.3. **Membrane pump**

This pump allows the regulation of flow and in consequence, it controls pressure in the FC. For this purpose a Swagelok® valve was set. This connects the membrane pump and is used both as a by-pass and to create a differential vacuum. In section B the GDC is fixed and is heated up together with the stainless steel pipe (green in figure 6.1). The Swagelok® valve in section A is connected via a Swagelok® T piece and removes most of the gas stream. That enables to work with a rather constant value of pressure in section B. The optimum pressure inside the cell finally is 3 mbar (tab. 6.1) whereas that, in the pre-vacuum between the sampling and the secondary nozzle, is in range of 15 to 30 mbar.

## 6.3. Heating system

### 6.3.1. **Sampling and air nozzles**

Heating at this part avoids primary condensations of polyaromatic hydrocarbons (PAH), hydrocarbons (HC) or other volatile organic compounds (VOC). A block of metal, where the

sampling and the air nozzle are incorporated, is heated up to the temperature of 230 ˚C. A thermocouple was fixed inside of a drilled hole.

### 6.3.2. **Black hose**

Minimum distances between apparatus and engine must be kept to avoid that the laser is affected by engine temperature. For this purpose a black heated hose is utilized between apparatus and engine. It is about one meter long with an external diameter of 8 cm. This pipe contains inside a ¼ inch pipe made either of Teflon® or stainless steel. A heating wire is wrapped around. Temperature of 230 ˚C is adjusted and self-regulated from a temperature control set in the back (Prototype-II) or in the front (Prototype-III). Between this wire and the external black protective sheath (polyamide) an isolation material is set. The heating of this hose avoids subsequent concentration of both oil, PAH, HC and/or VOC from engine exhaust.

### 6.3.3. **Stainless steel flow pipes and GDC**

To connect the black hose with the GDC a pipe is needed. Stainless steel was chosen as material however, Teflon® can be used as well. This would avoid in a great manner memory effects and it can be heated up to 230 ˚C. Besides, flexibility of this polymer will avoid breaking of GDC when apparatus is moved or transported between engine test desks. Heat is given to GDC and pipe by using a heating wire wrapped all around the pipe. Temperature must be 230 ˚C as well. To avoid heat losses an aluminum paper was covering the wire. A thermocouple is located between the pipe and the heating wire to enable temperature control.

## 6.4. Laser and optical path

The new developed laser was described in chapter 5. The output of the laser is a combination of the OPO idler (440 nm) and its second harmonic (220nm). Both of them are separated with the use of a Pellin-Broca prism which deflects the 220 nm laser beam by 90°. Then it is reflected into the fluorescence cell by using a dichroic 45˚ mirror. The visible wavelength is led into an optical fiber which is connected to a spectrometer. An iris is located just in front of the entrance window of the fluorescence cell. This allows the user to control the size of the laser spot and in consequence the stray light.

## 6.5. Fluorescence cell

The fluorescence cell was specifically designed for the prototypes of the oil consumption measuring system. It consists of a cylindrical body with two arms. In the extremes of the arms

window holders in Brewster angle position for the interface glass-air (~ 56˚) were welded. In the bottom part of the cylindrical body a holder containing the two bi-convex lenses is mounted (fig. 6.1). Below them a photomultiplier is located and before it the long-pass filter.

The exhaust gas, once it has passed through the GDC, comes into the cell from the top part of the cylindrical body. A Swagelok® connector is used there, as well as for the output gas system which is below both window holders. Connected to them, two vacuum pipes allow the rotatory pump to create the necessary vacuum. The fluorescence cell was made of anodized aluminum. A plot of it is included in the appendix.

## 6.6. Spectrometer

It is necessary for two reasons to have a wavelength measurement device in the apparatus, namely to calibrate the laser and monitor continuously wavelengths during the measurements. As for the second utility, it is necessary to know during measurements, if the value of the wavelength changes. The wavelength is recorded by the LabView program. The features of the spectrometer are described in table of devices. The model was selected with respect of a good enough resolution (bandwidth) and at the same time of a small size and high stability. This latter is important since the whole apparatus has to be moved from the storage room to the laboratory test rig and from there to the engine test bench.

## 6.7. Power meter

The measurement of the laser pulse energy is as essential as the wavelength recording. The power meter is set behind the output window of fluorescence cell. A pyroelectric power meter was employed. These sorts of detector are based on materials which possess an internal macroscopic electric-dipole moment which is depending on the temperature. In them, the electric field of this dielectric polarization is neutralized by a crystal due to surface-charge distribution. Changes in internal polarization as consequence of a temperature increment produce alterations in surface charge which can be measured by two electrodes. Pyroelectric detectors work only for pulsed laser. They are more robust and have a time resolution to the nanosecond range [2].

The value of the energy is utilized with two critical aims.

1. The energy is a value needed to correct integrated signal (see eq. 9.1 chapter 9).
2. To observe energy trend over time. A decrease or an increase sheds light on problems that could have occurred during the measurement.

Thus it is recommendable to rule out a measurement,

a. If the laser energy trend shows a strong nonlinear dependency, that is to say when the average (smoothed energy trend) cannot be fitted to a linear equation.
b. If in a linear dependency, the difference between the initial and the final value is bigger than 30 %.

Both indicate that there is a wrong functioning of the laser. In figure 6.2 and 6.3 two different energy measurements are shown. Both were acquired to $SO_2$ calibrations. In the first, the trend is linear but decreases slightly, whereas the second one shows an increase ending in a flat top. In the first case it is due to laser energy loss. This effect can occur always when there exists a temperature increment. The second one is the typical behavior of a laser turned on at the same time that a measurement was started. This occurs when a laser has not been previously warmed up.

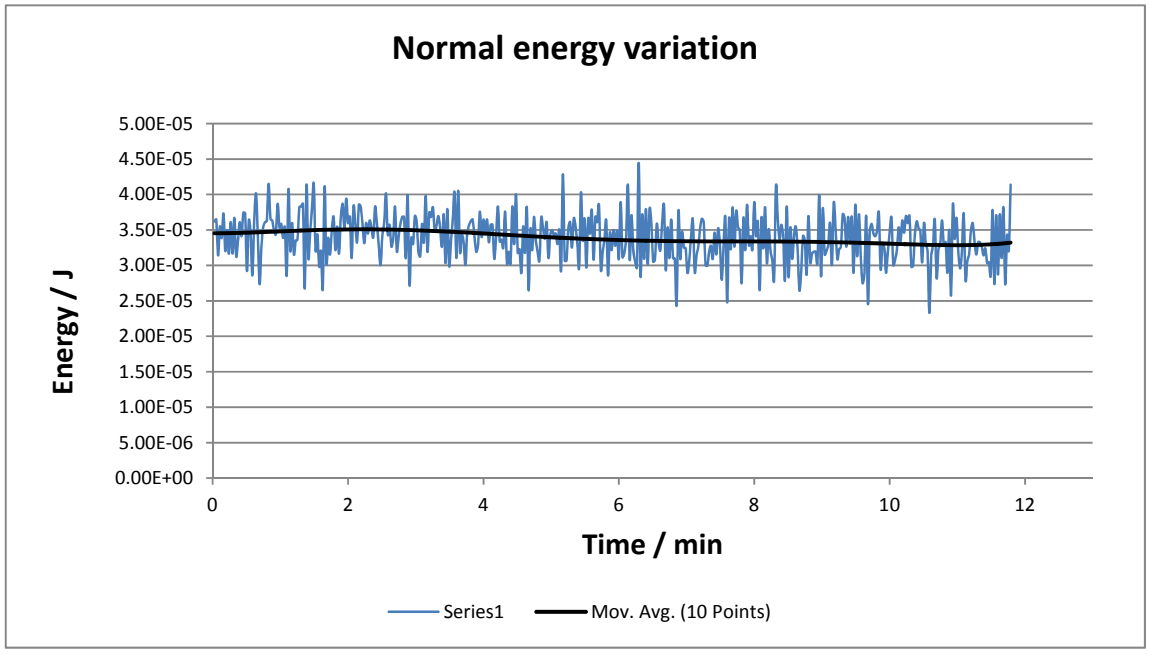


Figure 6.2. Slight decrease of laser energy over the time.

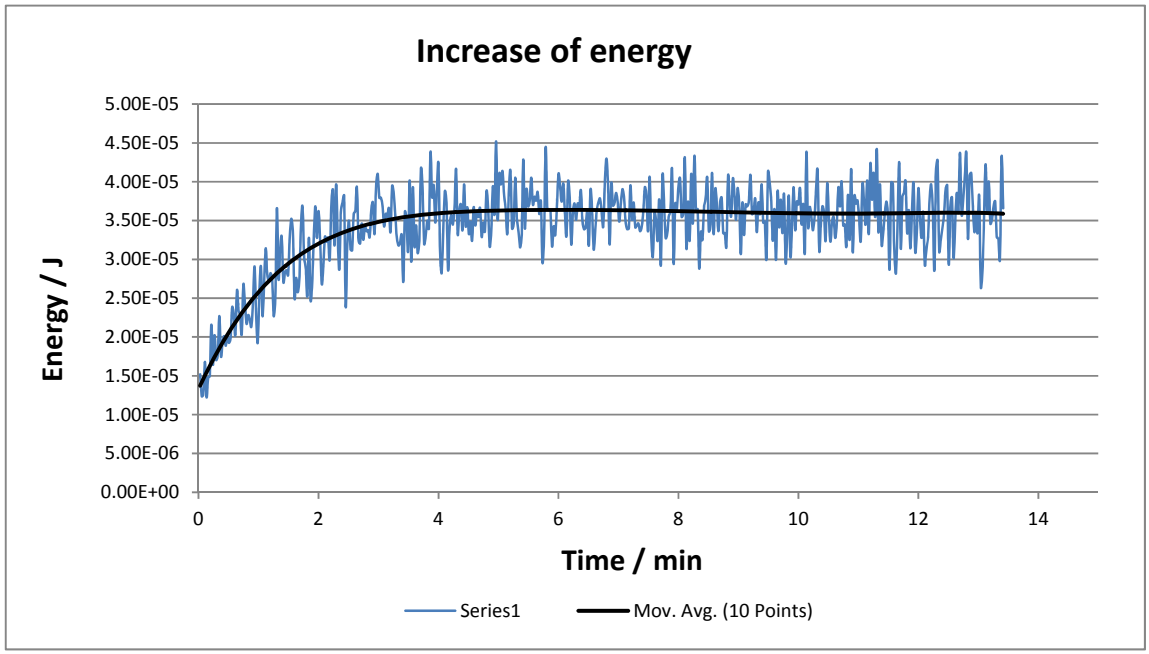


Figure 6.3. Increasing energy behavior till energy is stabilized.

## 6.8. Prototype-II

The first OPO-LIF apparatus was set up during the year of 2012 and tested, at the analysis in-situ laboratory (Lehrstuhl für Physikalische-Chemie, TUM) and at BMW-AG facilities. Several tests including $SO_2$ & NO wavelength scans, $SO_2$ calibration, NO concentration variation measurements, as well as HC and water interference measurements were performed. All these are presented in the chapters 8 and 9 together with the ones taken with the prototype-III. In the following a explanation of the physical set-up is included.

The prototype-II viewed from the upper part is depicted in fig. 6.2. It is interesting to notice that despite the compactness of the whole system and the number of devices into it, there are still possibilities to handle every element independently. External optics (Pellin-Broca, iris or pin-hole and dichroic mirror) were mounted in an optical rail to facilitate the alignment of the laser light along the fluorescence cell arms. The OPO-laser is located parallel to the fluorescence cell. Heating system (with aluminum foil wrapped around) is far enough from the laser. Nevertheless, laser heating tests were made to probe the behavior of it up to temperatures of 38˚C. Losses of mismatching angle or decrease in the energy were not noticed.

The prototype-II had only two floors, the one shown in the figure 6.2 and the other situated below. In this last power supplies (for laser, PMT and GDC), temperature controllers, pressure reader and both pumps were located. This could be done in this way since no space was needed for a laser cooling system. Refrigeration of laser power supply, Pockels cell and flash lamps were performed by an external chiller provided by BMW-AG. The prototype-III incorporated a cooling system delivered by InnoLas Laser-GmbH and for this reason this apparatus version had an extra floor.

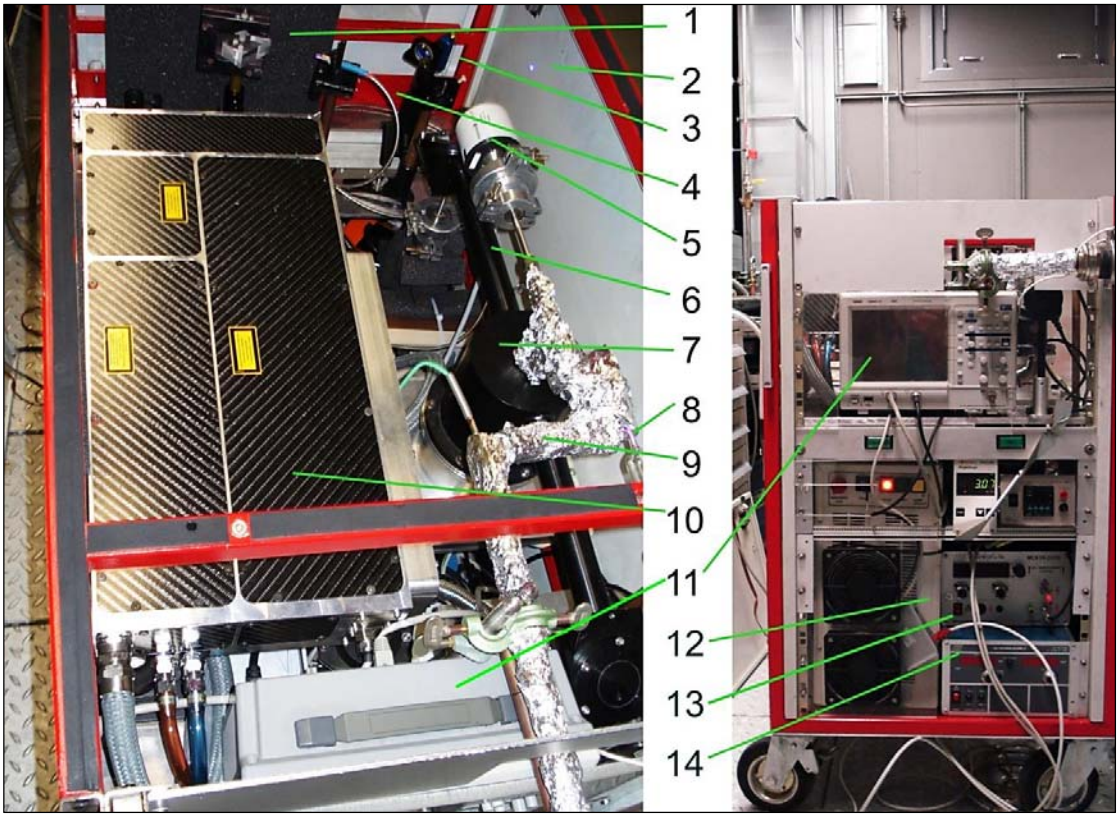


Figure 6.4. 1) Pellin-Broca, 2) 440 nm reflection, 3) Dichroic mirror, 4) Optical fiber, 5) Full range pressure gauge, 6 & 7) Fluorescence cell, 8) Glow discharge cell, 9) Heated stainless steel pipe, 10) OPO-laser, 11) Scope, 12) OPO power supply, 13) PMT power supply, 14) GDC power supply.

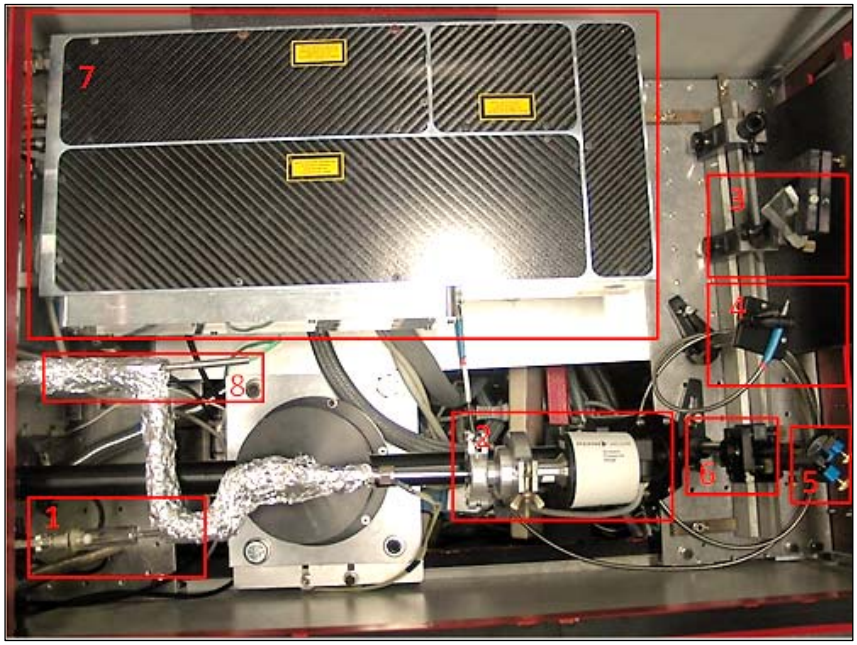


Figure 6.2. Top view of the Prototype-II upper part (protecting cover was removed). 1. Glow discharge cell, 2. Full range pressure gauge, 3. Pellin-Broca, 4. Optical fiber, 5. Dichroic mirror, 6. Iris, 7. OPO-laser and 8. Thermocouple wrapped around together with the heating wire.

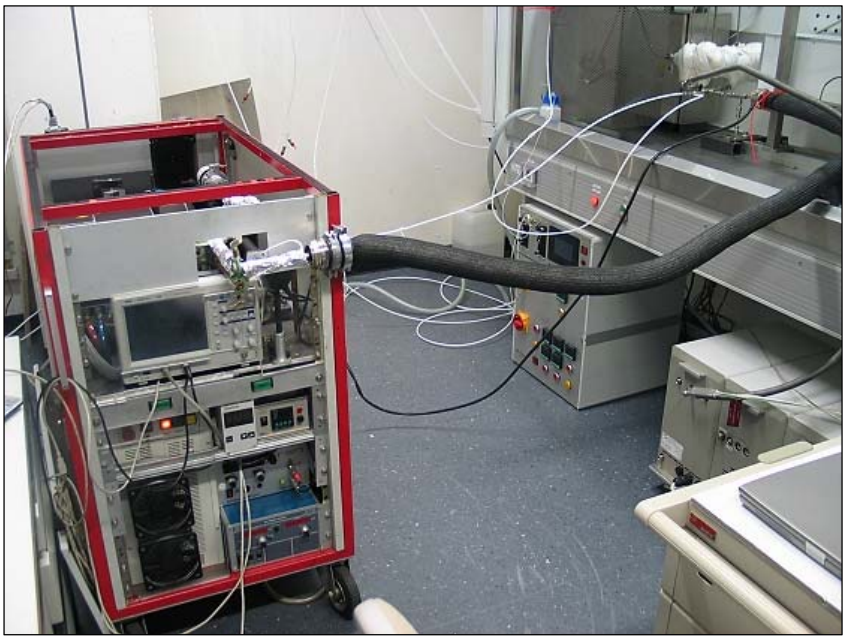

Figure 6.3. Setup at chemistry lab of BMW-AG. On the right part of the image is visible gas test rig. In it different kinds of gases and water can be added and their concentration regulated.

## 6.9. Prototype-III

The second OPO-LIF apparatus was fixed and set up during the year of 2013. This is the so called prototype-III and it was destined for use at motor test facilities of the BMW-AG with the aim to measure oil consumption of combustion engines. The apparatus is an improved version of the prototype-II. In particular, a new design of the levels (three) and a new arrangement of every component resulted in a more compact and mobile instrument. An important change was the incorporation of a cooling system (fig. 5.8). This was connected to laser and contained deionized water. The incorporation of the cooling system resulted in an enlargement of system height. This was quite convenient since the laser and the fluorescence cell (upper floor) were now more accessible for the user. Furthermore, the pumps of this model are fixed in two different floors which avoid overheating. The rotatory pump is located in the lower floor and the membrane in the medium. In the prototype-III the software (LabView, program) was highly improved and a new oscilloscope was used. This is a PicoScope (6402A) with a reduced space. Besides, all the COM and LAN connections were made by the employment of a USB-port HUB. Two flow regulator and one flow controller were included as well. They enable a fast calibration with $SO_2$ or $H_2S$ diluted in pressurized air in any necessary moment. Connection between black hose and stainless steel pipe was improved. The new fixing avoids the transmission of torque force and forces due to the movement in any other direction to the stainless steel pipe, and in consequence to the GDC (glass made). A new membrane pump is mounted to avoid bad functioning during water or real engine measurements. Water which either has been added to the sample gas for the purpose of in calibration or is produced in the combustion can create a decrease in the power and speed of the membrane pump. High percent of water can give rise to condensation within the pump. The new model incorporates a function with many optional programs whose purpose is to get rid of the water condensed in the internal brushes.

Figure 6.4. Picture of the prototype-III destined for use at BMW-AG. **Upper floor contains:** OPO laser, FC, power meter, spectrometer, optical path, gas inlet system with the GDC and the heated stainless steel pipe. **Medium floor contains:** the optical collection system, filter, PMT, membrane pump, two power supplies (GDC and PMT), two heating controllers, pressure reader and flow meter. **Lower floor contains:** laser power supply, laser cooling unit, penning, rotatory pump with zeolite filter and several multi-sockets.

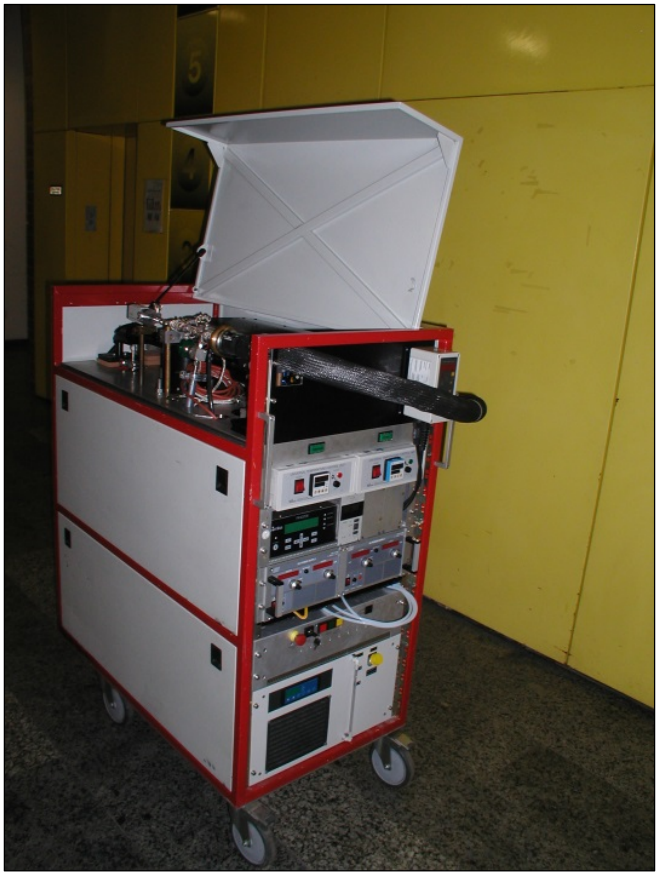

Figure 6.5. View of prototype-III including frontal panel and showing the easy accessibility that allows the cover.

Figure 6.6. Transportation of prototype-III to BMW-AG engine facilities.

## 6.10. Literature

1. Laserspektroskopische Spurenanalytik von Ölbestandteilen in Abgasen von Verbrennungsmotore, Stefan Sellmeie r, (PhD Thesis), 19.07.2011.
2. W. Demtröder, Laser Spectroscopy: Experimental techniques, Vol. 1, pag. 197, Fourth edition, Springer (2008).

# 7. Description of two temporal gate integration method (TTGIM)

Selective laser induced fluorescence has been thought to selectively excite vibronic transitions of molecules. If two different molecules show excitation spectra with several overlapped transitions, one should be able with a low bandwidth light source, to excite one or another. However the use of an OPO laser with a bandwidth of 5 $cm^{-1}$ makes impossible this. $SO_2$ robivronic lines are very close in wavelengths to the NO ones. Thereby with the before mentioned laser both molecules are excited. The OPO laser could provide a small and compact enough excitation source which allows the commercialization of the system, but due to the bandwidth the selectivity were put on risk. The broad enough bandwidth of InnoLas Laser-GmbH OPO (0.025 nm at 220 nm) led us to figure out an additional method to discriminate between $SO_2$ and NO.

## 7.1. Fundament and explanation of α factor

Engine exhaust is a complex mixture of gases containing several organic molecules from both oil and gasoline, simple gases such as e.g. $SO_2$ and $CO_2$ and soot. After sucking a fraction of this into the system and its treatment by a NTP, the composition becomes much simpler. Only molecules containing few atoms are formed and led to the FC afterwards. Nitric monoxide (NO) constitutes one of the most abundant molecules. The lifetime of excited NO is much longer than the $SO_2$ one which results in a fluorescence exhibiting a tri-exponential. In case of having only $SO_2$ and scattering, a bi-exponential would be recorded at a scope after detection in a photomultiplier. This signal is the sum of two processes which start nearly at the same time but last differently. The first is the elastic scattering (stray light) which comes from the laser pulse and the second is the $SO_2$ fluorescence itself. The addition of both resulted in a bi-exponential decay.

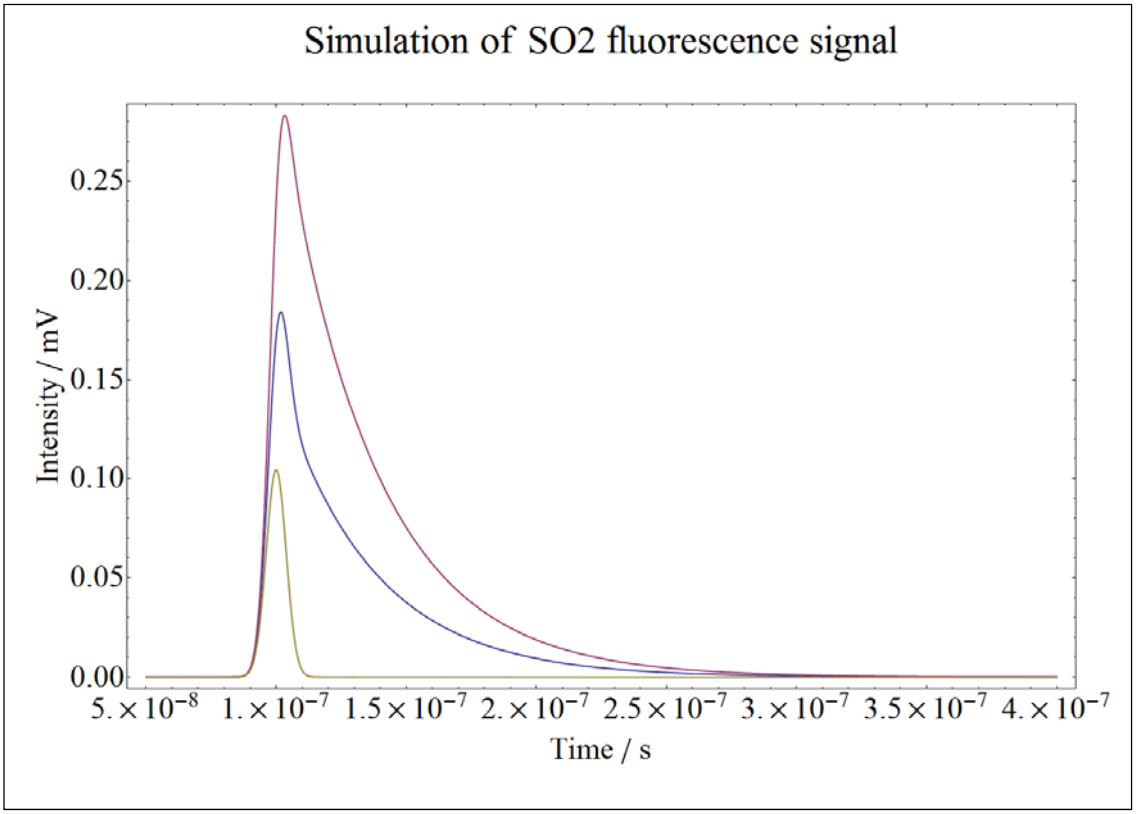


Figure 7.1. Simulation of signal displayed at a scope when fluorescence from two different $SO_2$ concentrations (red and blue lines) are recorded together with scattering light (brown).

Figure 7.1 shows a simulated scope signal for two different concentrations of $SO_2$ and where a contribution of scattering has been added. In presence of NO and at the wavelengths of excitation used; 220.6 nm and 220.2 nm, a tri-exponential decay is obtained (fig. 7.4). The third decay is produced by NO. To suppress the NO contribution two different time gates are set and the integral of them recorded [1]. The first one contains the sum of scattering, $SO_2$ and NO signals, whereas the second one contains only the NO signal. If the second integrated signal is subtracted from the first one, a $SO_2$ fluorescence integral is obtained. This is still containing scattering. The following considerations must be taken into account at this point; the fluorescence signal of NO does not have the same value in both gates: NO lifetime (2 μs) is not long enough in comparison with the $SO_2$ one. Therefore the integral measured at the second gate must be corrected by a factor before its value is subtracted from the first gate. This correction factor is named in the following as “alfa factor” or simply “alfa” or written with letter α. Equation 7.1 expresses this simple mathematical procedure.

$$Integral_{Sulfur} = Integral_{Gate\,1} - Integral_{Gate\,2} \cdot \alpha \quad (7.1)$$

This factor corrects the proportional NO signal which is measured in the gate one and it is necessary for two different reasons. During the development of the first prototype [1] the value of alfa was empirically calculated. Determination of this factor implied the measurement of a $SO_2$ wavelength spectrum, normally in the range of 216-222 nm. The a value for alfa factor was calculated by try an error up to the $SO_2$ spectrum was obtained. This process is illustrated in figure 7.2. Several alfa values were utilized here. The chosen optimum value (1.15) resulted in a $SO_2$ excitation spectrum which is the most similar to one either recorded by having only $SO_2$ in a stream where GDC is switched off, or to one in literature (fig. 9.2). This way to find the appropriate alfa is time consuming as well as it has a lack of both precision and accuracy.

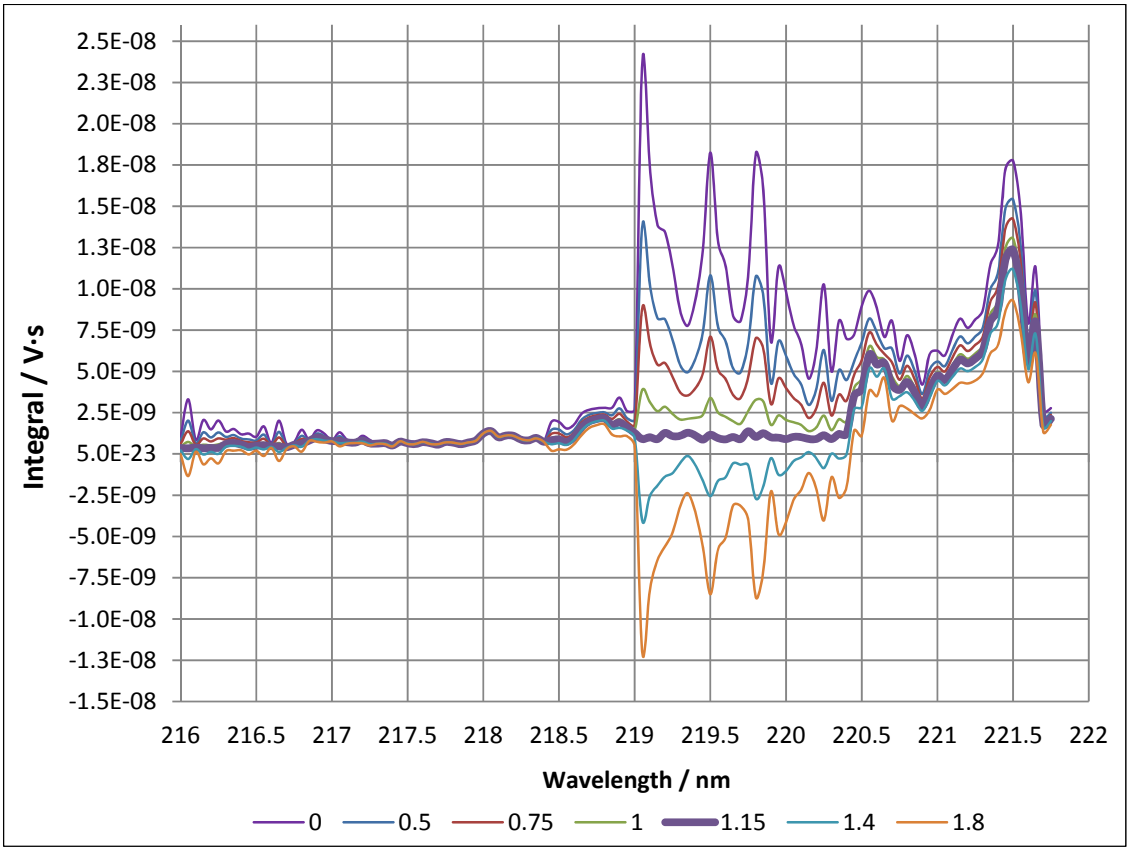


Figure 7.1. Empirical estimation of α factor. Wavelength spectra recorded setting a $H_2S$ (400- 800 ppb) and with GDC turned on. When α is different than 1.15, NO spectra is visible.

The value of α depends on gate width (discussed in section 7.3) and on NO life time. The latter should not change if the excitation wavelength does not change. At the wavelength of 220.6 nm this is equal to 2 μs. However, lifetimes are different for different vibronic transitions (bands) [3, 4 5, 7]. Thereby a $SO_2$ spectra correction based on a second integration gate must in principle take into account the life time of NO for every excitation wavelength.

Due to reasons of increment in accurateness as well as simplification of the measurement, another procedure was developed. The new one involves mathematical calculation of alfa by signal simulations. This is a semi-empirical method since is based on mathematical convolution and employees data from literature.

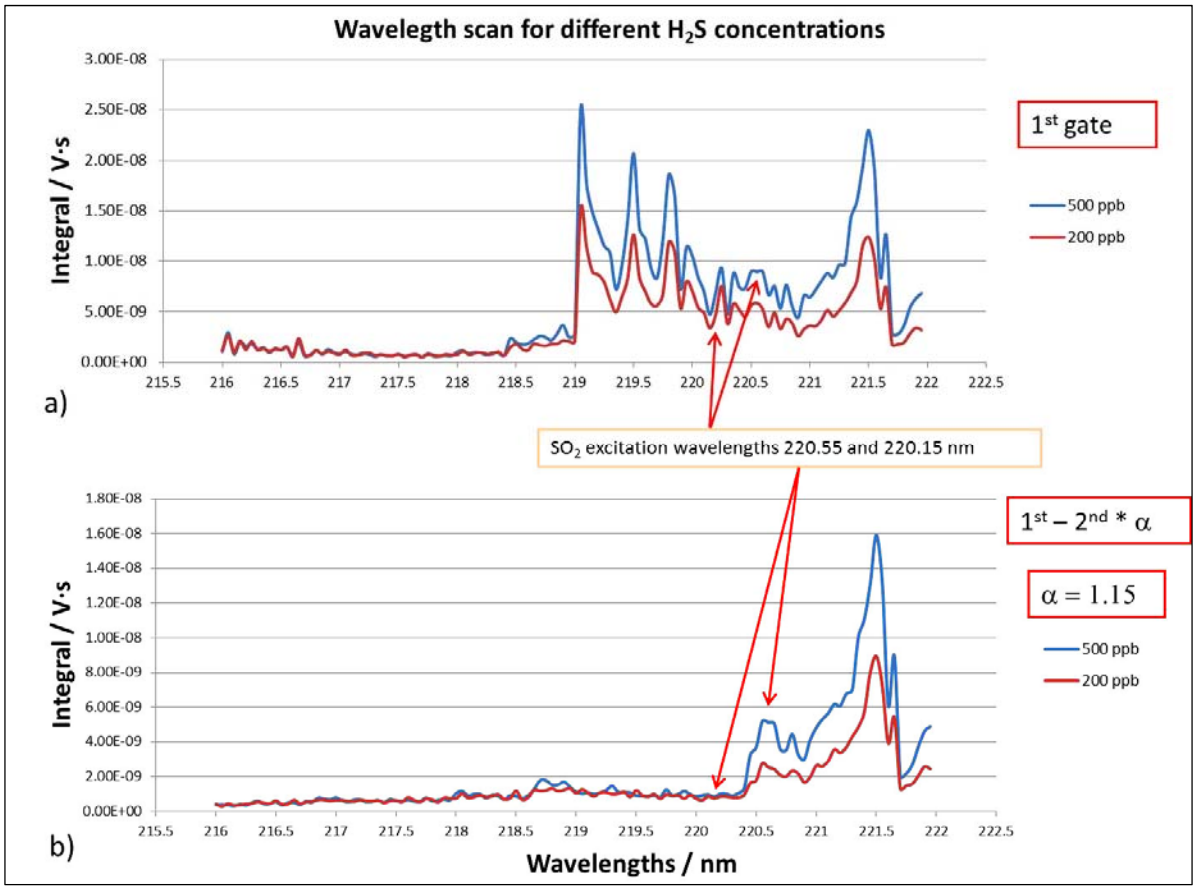


Figure 7.2 Wavelength scans obtained for two different $H_2S$ concentrations. A) Both $SO_2$ and NO excitation spectra are observed. B) Corrected spectra after application of a value of 1.15 for the $\alpha$ factor.

## 7.2. Simulation of fluorescence signal: Convolution

Simulations of typical response signals delivered by PMT and displayed at a scope in a LIF setup can be made by the use of convolution (faltung or folding). This mathematical operation transforms two functions into a third one according to,

$$f(x) \otimes g(x) = \int_{-\infty}^{\infty} f(t)g(x-t)dt \tag{7.2}$$

The result is often a "broadening" of the first by the second (or conversely). A detailed description of the properties and utilities of this operation can be found elsewhere [2] which is far beyond the scope of this work. Herein equation 7.2 (special formulation derived from Fourier theorem) is directly applied to our particular purposes. Equations 7.3 and 7.4 are the two functions $f(x)$ and $g(x)$ employed during the simulation of our fluorescence response.

$$f(x) = f(x_0) + \mathrm{A1}\, e^{\frac{-(x)}{\tau}} \tag{7.3}$$

$$g(x) = g(x_0) + \mathrm{A2}\frac{e^{\frac{-(x-\mu 1)^2}{2\sigma 1^2}}}{\sigma 1\sqrt{2\pi}} \tag{7.4}$$

Equation 7.3 is the expression of a mono-exponential decay where $\tau$ is the life time, $A1$ the amplitude and $f(x_0)$ is the value of the function at infinite. The second represents the laser pulse which is simulated by a Gaussian function centered at $\mu$, where $A2$ is the amplitude, $\sigma 1$ is the standard deviation and $g(x_0)$ is the height over the $x$ axe.

Convolution occurs between two defined limits $B$ and $C$ where the new function has to be defined. The result in our particular case is the product of an exponential and an Erf function (integral of the Gaussian distribution). This latter is a special sigmoid function which can be defined as,

$$\mathrm{Erf\,(y)} = \mathrm{T}\,\frac{2}{\sqrt{\pi}}\int_0^y e^{-x^2}dx \tag{7.5}$$

and finally

$$f(x) \otimes g(x) = \int_C^B f(x)\, g(x-y)dx \propto H \cdot e^{-y} \cdot T \cdot Erf(y) \tag{7.6}$$

with $H$ and $T$ being the new amplitudes. It must be noticed the fact that a new convoluted function is dependent on another variable which in our case is $y$. In all effects $y$ and $x$ are variables whose representation is performed in time.

Figure 7.3 shows the result of two convoluted exponentials with a Gaussian function (NO and $SO_2$ fluorescence), a Gaussian peak (scattering) and the sum of all these three. These different signals are explained in the following.

1) **Gaussian pulse.** This is a function describing scattered light. In a LIF setup scattering is a frequent contribution to the final response. Scattering can be elastic (Rayleigh) or inelastic (Raman). Molecular inelastic scattering is a rather improbable effect with a weak intensity occurring both at lower and higher wavelengths than the excitation one. Due to its low intensity contribution to stray light has to be very small. Therefore scattering at surfaces is the most probable effect. The signal of a scattering is represented as a Gaussian with full width half maximum ($\sigma 1 = \mathrm{FWHM}/2\sqrt{2ln2}$) of 6 ns (laser pulse duration).

2) **Gaussian pulse followed by a mono-exponential decay.** This is the typical response signal of fluorescence. With this regard two of those functions have to be simulated, one due to $SO_2$ decay ($\tau$ = 36 ns, [4]) and another due to NO ($\tau$ = 2 $\mu$s, [5]). In figure 7.3 purple curve corresponds to $SO_2$ and brown to NO.

3) **Total signal.** It is obtained by summing up 1) and 2) (blue in fig. 7.3).

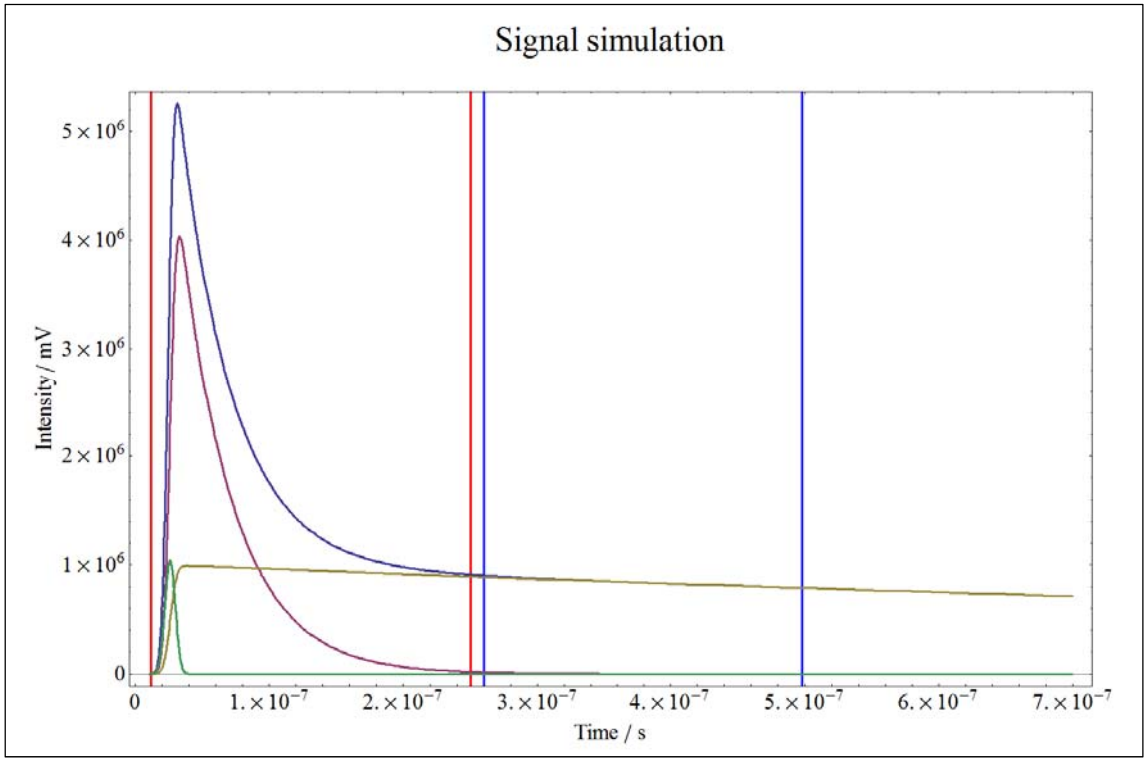


Figure 7.3. Simulation of a signal recorded on the scope using a program written with Mathematica (Program 2). **Green:** scattering. **Purple:** $SO_2$ fluorescence signal. **Brown:** NO fluorescence signal. **Blue:** the sum of all three contributions. In this particular case first gate (red lines) is set between $1.2\cdot10^{-8}$-$2.5\cdot10^{-7}$ s and second one (blue lines) in $2.6\cdot10^{-7}$-$4.98\cdot10^{-7}$ s ($\alpha$ = 1.0611).

To calculate the $\alpha$ factor only the NO signal must be integrated. First gate is set between two times: limit 1 and limit 2 and second between two further ones: limit 3 and limit 4. The limit at higher time in first gate(limit 2) can be set equal to lower limit in second gate (limit 3). For visualization reasons a short time delay was let between them for visualization. Thus solving equation 7.7 alfa is obtained.

$$\int_{limit\ 1}^{limit\ 2} Convolution_{NO} - \left(\int_{limit\ 3}^{limit\ 4} Convolution_{NO}\right) * \alpha = 0 \qquad (7.7)$$

One can proof the accurateness of this value by using equation 7.8 where the whole signal resulting from the convolution plus the contribution of the stray light is integrated, and the calculated value of alfa used.

$$\int_{limit\ 1}^{limit\ 2} Gate_1 - \left(\int_{limit\ 3}^{limit\ 4} Gate_2\right) * \alpha = I_{Total} \quad (7.8)$$

The result of equation 7.8 must be compared to the one which corresponds to equation 7.9. which is the integral of $SO_2$ and scattering at first gate.

$$\int_{limit\ 1}^{limit\ 2} \{Convolution_{SO2} + Scattering\} = I_{SS} \quad (7.9)$$

Results from equations 7.8, $I_{Total}$ and 7.9, $I_{SS}$ must be identical to confirm the validity of the calculation. The value of them depends on the time width of gates. The α factor grows proportional to the time width since the NO signal decreases in the second gate and this turns out in a higher overestimation of the first gate. Thereby, if time width of gates is kept constant and alfa is calculated versus different values of limit 2, a parabolic relation is obtained. Figure 7.4 shows the result of this with equation that can be employed to calculate alfa according to time location of limit 2.

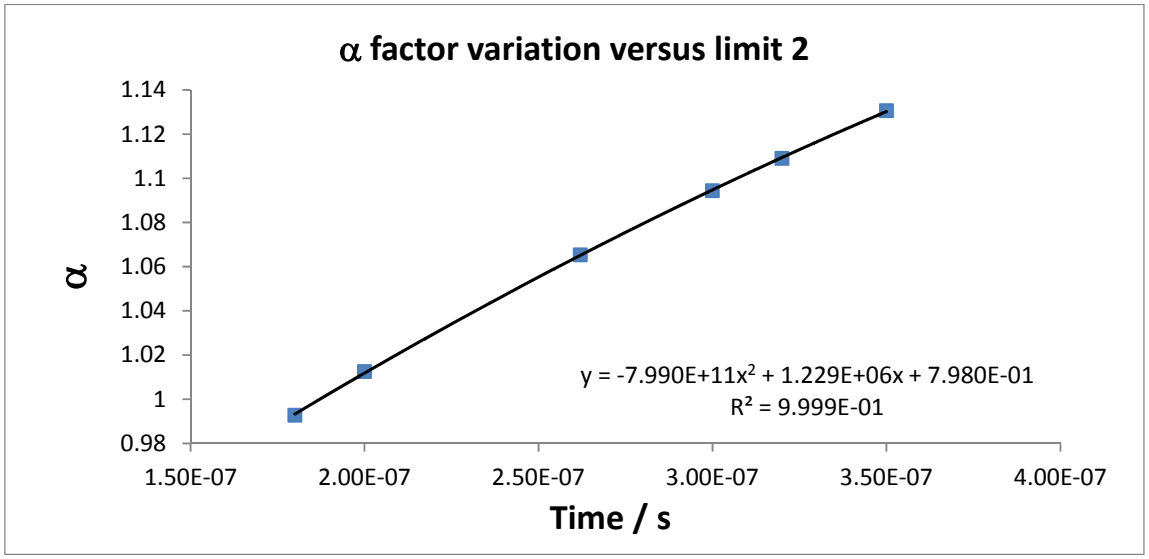


Figure 7.4. Limit 1 is always $1.2 \cdot 10^{-8}$, limit 2 could vary, limit 3 is defined as $0.1 \cdot 10^{-7}$ s + limit 2 and limit 4 is equal to $0.1 \cdot 10^{-7}$ s + limit 2 + (limit 2-limit 1). Therefore the equation plotted in fig. 7.4 could be used to calculate the α value for any value of limit 2. The calculation is made for scattering signal centered at 2.6 x $10^{-8}$ s according to experiment.

## 7.3. Results of simulations

In this section some simulations were made to clarify the double wavelength switching mode. Figure 7.5 (both parts) were obtained with program 2 (appendix). Life times for $SO_2$ and NO are $\tau$ = 36 ns [4] and $\tau$ = 2 $\mu$s [5] respectively. Two relative amplitude ratios were calculated for every wavelength according intensity values displayed in spectrum of figure 7.2. For 220.6 nm a ratio $SO_2$/NO = 3, for 220.2 a ratio NO/$SO_2$ = 15 were used. Besides, a ratio for every molecule at the two wavelengths can be calculated: $NO_{220.6nm}/NO_{220.2\ nm}$ ratio (2.1) and $SO_{2\ (220.6nm)}/ SO_{2\ (220.2\ nm)}$ ratio (21). Scattering amplitudes can be as high as 100 mV. In figure 7.5 it surpasses for both wavelengths the NO and $SO_2$ contribution. This is due to simulations based on lower $SO_2$ concentrations as well as the low amount of NO excited at these two wavelengths (chapter 8). This results in a particular shape of PMT response showing a pronounced peak at the begginning. This shape is clearly observed within the first 12 ns of signal. At the lower excitation wavelength scattering is almost higher than the $SO_2$ signal which turns out in a nearly constant integral value up to high $SO_2$ concentrations. Besides, noise, and energy or flow fluctuations affect much more to the signal at this lower wavelength. This was frequently seen during calibrations measurements (fig. 9.6). Together with the time cost these are two reasons which explain why the double wavelength switching mode was definitely ruled out (discussed in chapter 9).

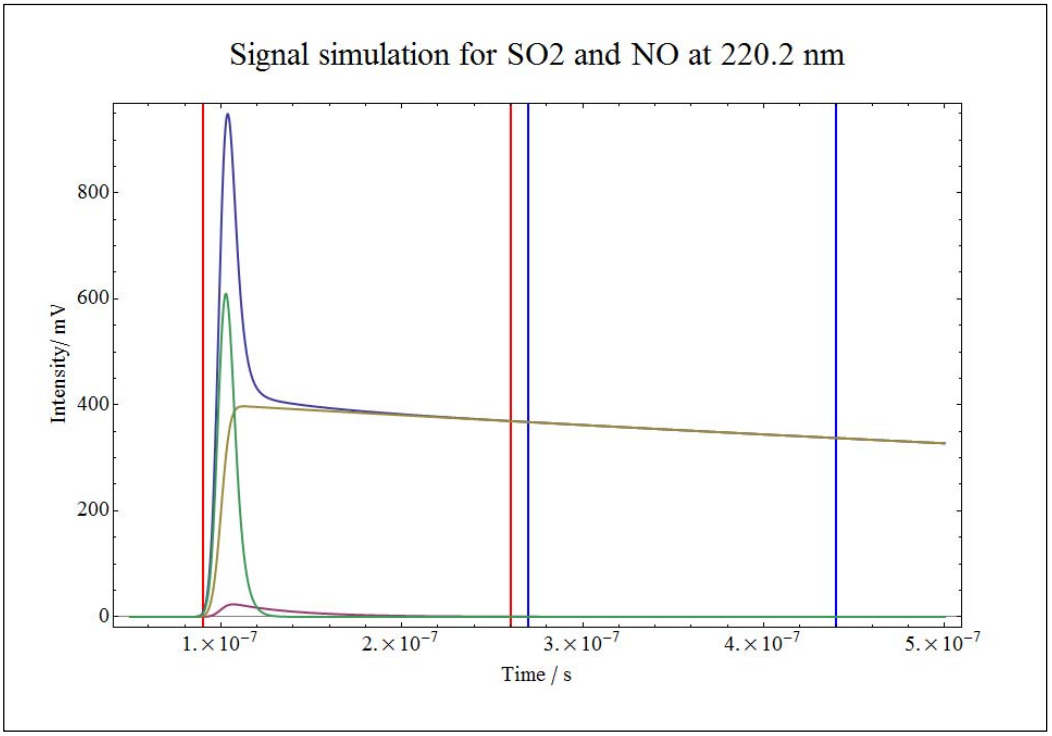


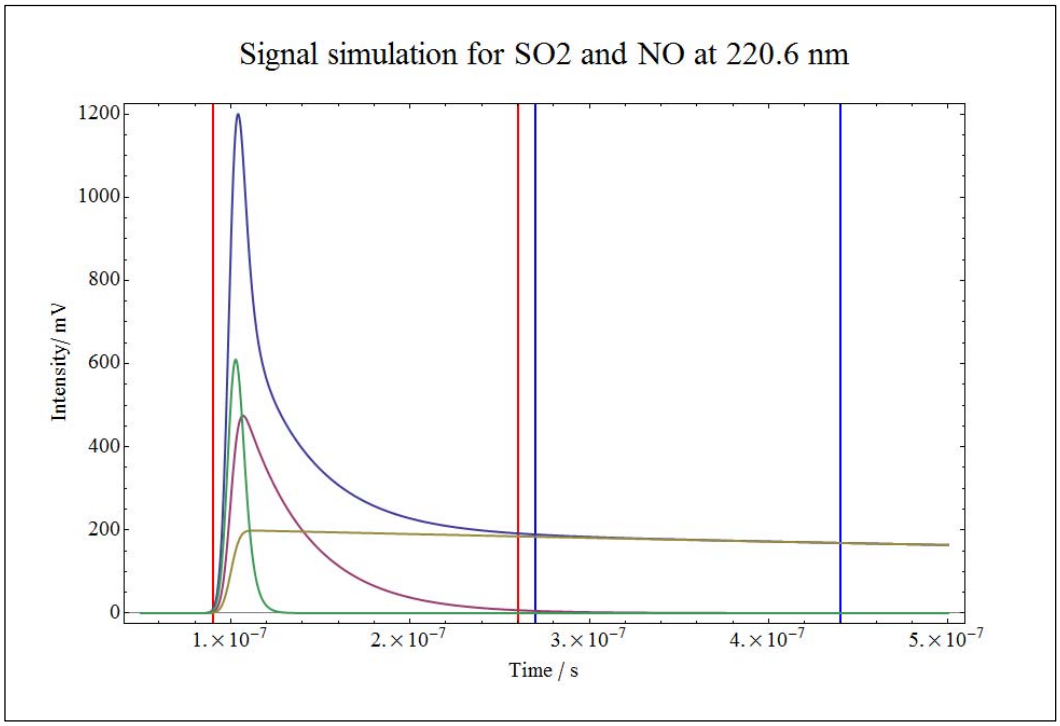


Figure 7.5. Simulation of PMT response at wavelengths 220.2 and 220.6 nm. **Brown:** NO, **purple:** $SO_2$, **green:** scattering, and **blue:** total. Amplitudes are according figure 7.2 at 220.2 NO signal is higher than $SO_2$ (15 times) whereas at 220.6 nm $SO_2$ is higher (3 times) than NO. Scattering is assumed equal for both and with amplitude bigger than $SO_2$ and NO one.

## 7.4. Literature


1. Laserspektroskopische Spurenanalytik von Ölbestandteilen in Abgasen von Verbrennungsmotore, Stefan Sellmeier, (PhD Thesis), 19.07.2011
2. Fourier transforms and their physical application, D. C. Champeney, Academic Press, 1973
3. J. Luque, D. R. Crosley, *J. Chem. Phys.* 111, 7405 (1999).
4. T. Ebata, O. Nakazawa, M. Ito, *Chem. Phys. Lett.* 1988, 143, 31.
5. G.E.Gadd, T.G.Slanger, *J. Chem. Phys.* 1990, 92, 2194.
6. Mathematica 9.0.1, Wolfram Research.
7. Man-Him Hui and S. A. Rice, *Chem. Phys. Lett.* 17, 474 (1972).

# 8. Interferences

## 8.1. Volatile organic compounds (VOCs) and polycyclic aromatic hydrocarbons (PAHs)

Volatile organic compounds (VOCs) such as alkanes, alkenes, alcohols, aldehydes, ketones and aromatics or halogenated organic molecules can be present in the exhaust. Poli-aromatic hydrocarbons (PAH) could be either generated during combustion processes or be unburnt components of gasoline. These compounds are constituted by condensed benzene rings and their molecular weights are higher than 200 amu. Some examples of them are pyrene, anthracene, pentacene, benzo[a]pyrene, corannulene and ovalene. Although many VOCs and PAHs exhibit fluorescence at the UV range at which $SO_2$ also does, they do not give rise to any interference when $SO_2$ is measured. This is due to the fact that they are totally oxidized ($CO_2$ and $H_2O$) into the glow discharge cell due to nonthermal plasma. Tests of fragmentation and oxidation within our glow discharge cell have been performed during this work for molecules such as butane, benzene and toluene (chapter 3). Nowadays NTPs are utilized as a tool to remove pollutants: VOCs ([8]-[13]) and odors ([1]-[7]). Despite the fact that our glow discharge cell differs from those described in literature (pulsed corona streamer and silent discharge reactors), all are based on nonthermal plasma. This sort of plasma contains in any case same radical species (chapter 3). Thus one can with no doubt assume that reactions and results are equivalent.

## 8.2. Nitric oxide (NO)

The presence of molecular nitrogen in NTPs produces several oxides. The way they are formed has been explained in detail in chapter 3. In here the focus falls on the most abundant one, the nitric oxide (NO).

### 8.2.1. NO life time and fluorescence spectrum

The lifetime of the NO depends on the rovibronic level that is excited and on the surrounding conditions [16-25] such as pressure. In figure 8.1 the NO Morse potentials for every electronic level are drawn [14]. In the case of the present work excitation of NO takes places at the same UV region where the $SO_2$ fluorescence occurs. That is to say, NO is excited at the so-called peak and bottom wavelengths 220.6 and 220.2 nm. The relevant transitions of NO correspond to the rovibronic transition in one of the *β-bands,* $NO(B^2\Pi)(\upsilon' = 0, 1, 2, 3, 4, \dots) \rightarrow NO(X^2\Pi)(\upsilon'' = 6)$ [14, 18]. According to the study of G.E. Gadd et al. [14] all these exhibit lifetimes in a range of 0.85

to 2 μs. These lifetimes depend strongly on the pressure. Under our experimental conditions a life time, $\tau$ of 2 μs has been observed.

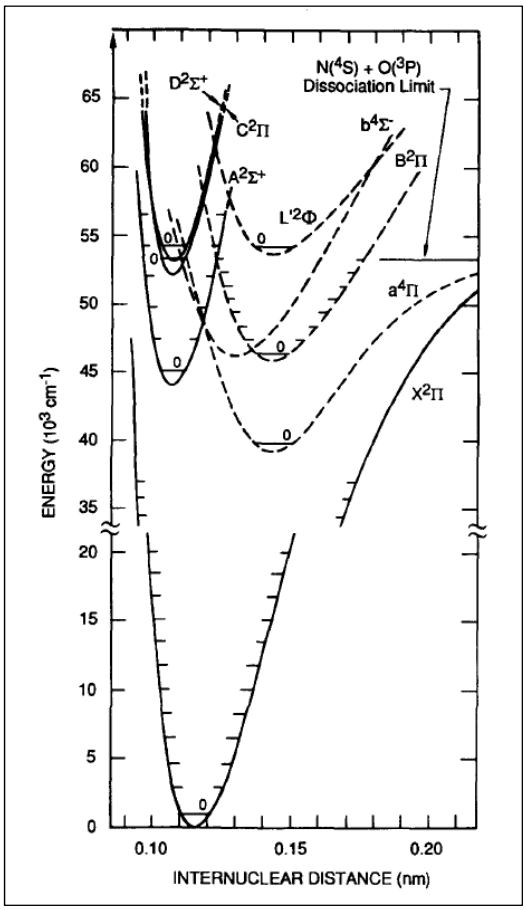


Figure 8.1. NO potentials [14].

An excitation spectrum of NO can be recorded with an OPO laser. Figure 8.2 depicts a NO and a $SO_2$ excitation wavelength spectrum. A concentration of 800 ppb $H_2S$ was set in the flow controller and GDC was turned on. The NO spectrum can be seen in blue and the $SO_2$ spectrum in red. Contributions to the $SO_2$ spectrum at higher wavelengths than 221 nm correspond to NO produced after $NO_2$ dissociation. This NO has a totally different lifetime than the one excited by the laser. This is basically the reason why the subtraction method and "alfa" correction optimized for a 2 μs life time does not work out there (section 9.1).

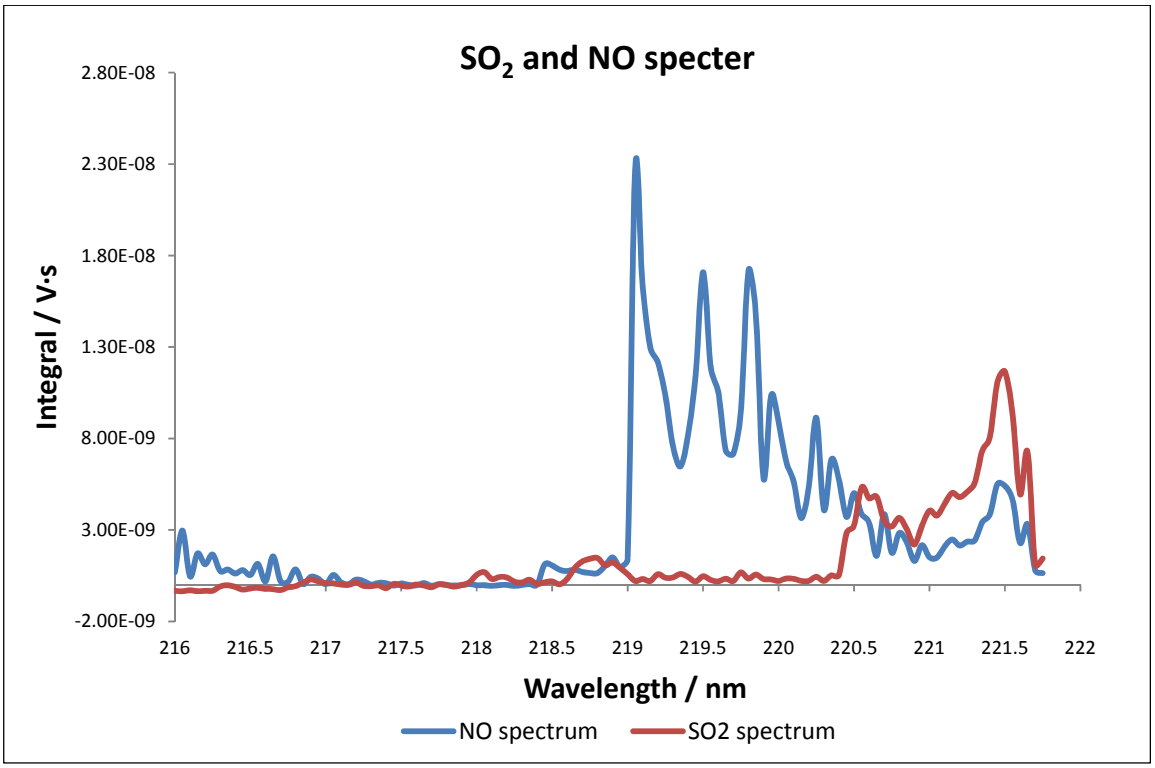


Figure 8.2. Excitation fluorescence spectra of $SO_2$ (800 ppb) and NO (unknown amount produced in the GDC). Background (scattering contribution) has been subtracted from both species.

Rovibronic transitions of NO are clearly visible between 219 and 221 nm. $SO_2$ shows a maximum at 220.6 nm and another at 218.85 nm. The first band corresponds to the combination band (132) and the second to (142).

### 8.2.2. **Results**

The main problem of having huge NO amounts present in gas stream (behind the GDC) is based on the fact that it exhibits fluorescence at the same region as the $SO_2$ does. NO is produced internally during engine combustion and in NTP. The amount of NO coming from the engine (ca. 5000 ppm) is negligible in comparison with the one produced when the GDC is switched on. This fact is shown in figure 8.3. In there, an increasing concentration of NO in the range from 0 to 3200 ppm was added together with dried air. In addition after each change of concentration, the GDC was turned on and off. The clearest observation of such measurement is that by far the amount of NO produced by the NTP is much higher than the one existing in the gas stream.

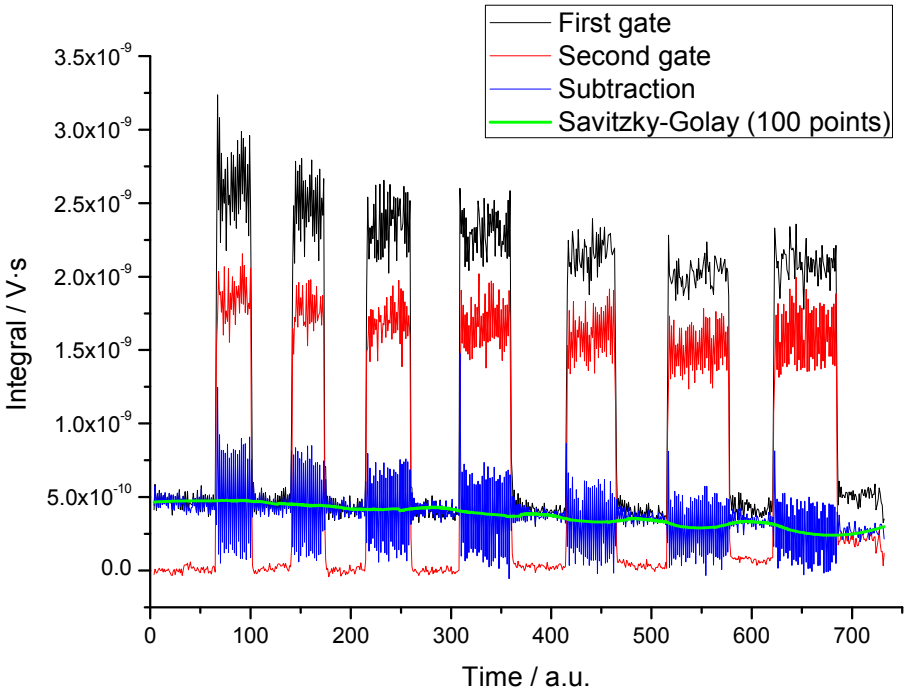


Figure 8.3. NO detected by SLIF (excitation at 220.6 nm).

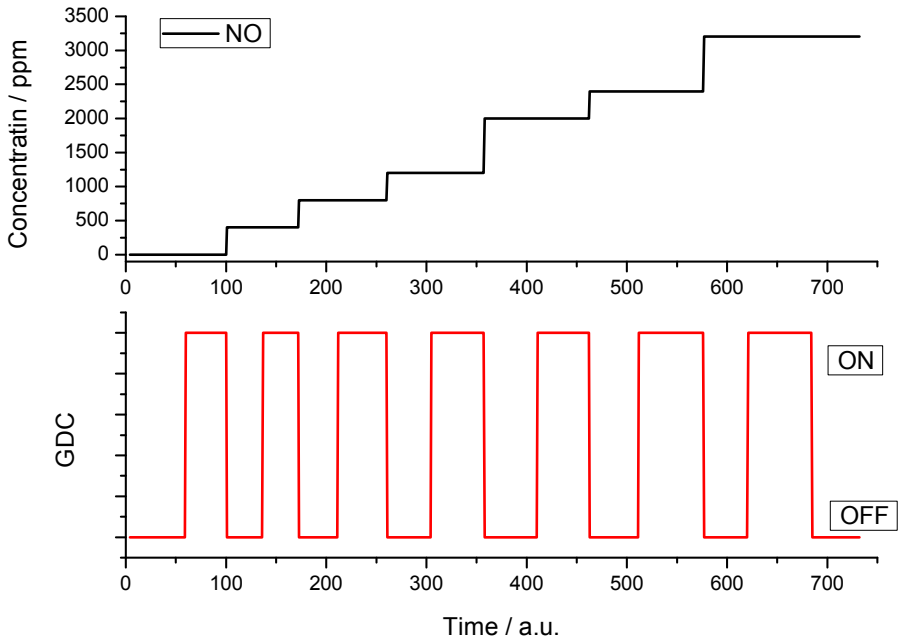


Figure 8.4. Concentration increment of NO (ppm) and GDC ON-OFF cycles for measurements shown in figure 8.3.

In figure 8.3 the black signal is the first integration gate and the red line the second one. Blue is the result of subtraction (applied α factor). The thick green line is the average of subtracted value ($\alpha$ = 1.15). Higher black and red integral signals belongs to a cycles were the GDC was switched on (fig. 8.4). Black integral contains contribution of scattering light (chapter 7). This is the reason why its integral value is always higher that the red one. When subtraction is applied (green smoothed line) only NO contribution is ruled out and final signal is higher than zero since integral of scattering is not deleted.

Another important observation is the signal intensity of the NO. Despite the large amounts of NO coming from the exhaust or are produced in the NTP, the intensity of the signal is not as intense as it was expected. This is observable in figure 8.3. The steps from 0 to 750 cycles where the GDC is turned off (lower integral values), correspond to increasing amounts of NO. However, the cycle starting at 575 is the first where NO was detected. NO concentration was 2400 ppm at this point. The baseline increased from its constant value to a higher value. The explanation of this very interesting effect is supported in the fact that the laser pulse energy is distributed in a broad range of wavelength because of OPO´s bandwidth. NO has sharp single rotational lines with wide slots of non-absorption between them. For this reason overlap of the narrow NO-lines and the large laser bandwidth is small. In consequence a large part of light is not absorbed by NO. On the other hand, the considerably broad vibronic bands of $SO_2$ have a good overlap with the laser bandwidth.

## 8.3. Water ($H_2O$)

Combustion reactions occurring within an engine produce a considerable amount of water. Gasoline is mainly composed of several organic molecules which after reaction with oxygen give rise to carbon dioxide and water according to,

$$C_nH_{2n} + \frac{3}{2}nO_2 \leftrightarrow nCO_2 + nH_2O \tag{8.1}$$

The yield of this reaction is not always the highest ($\eta = 100\ \%$) and other products such as carbon monoxide or soots (particles with size in the range of 20 to 5000 nm) are formed. Those soot particles are carbonaceous molecules containing hydrogen and they are produced by aggregation or reactions of partially transformed gasoline molecules.

Eq. 8.1 assumes that most of organic molecules in gasoline are alkenes ($C_nH_{2n}$). If they are 100 % burnt the amount of water can be as high as 16.65 % in volume (considering density of $CO_2$ equal to 1.84 g/cm$^3$). To check the influence of water on the $SO_2$ fluorescence signal, measurements in the presence of water were performed. Experiments with $H_2S$ oxidized in plasma by humid air and fluorescence measurements of resulting $SO_2$ were performed in the chemistry laboratory located at BMW-AG (Munich). There exists a gas test rig (fig. 8.5 & 6.3) for mixing and heating substances in well-defined and controlled concentrations.

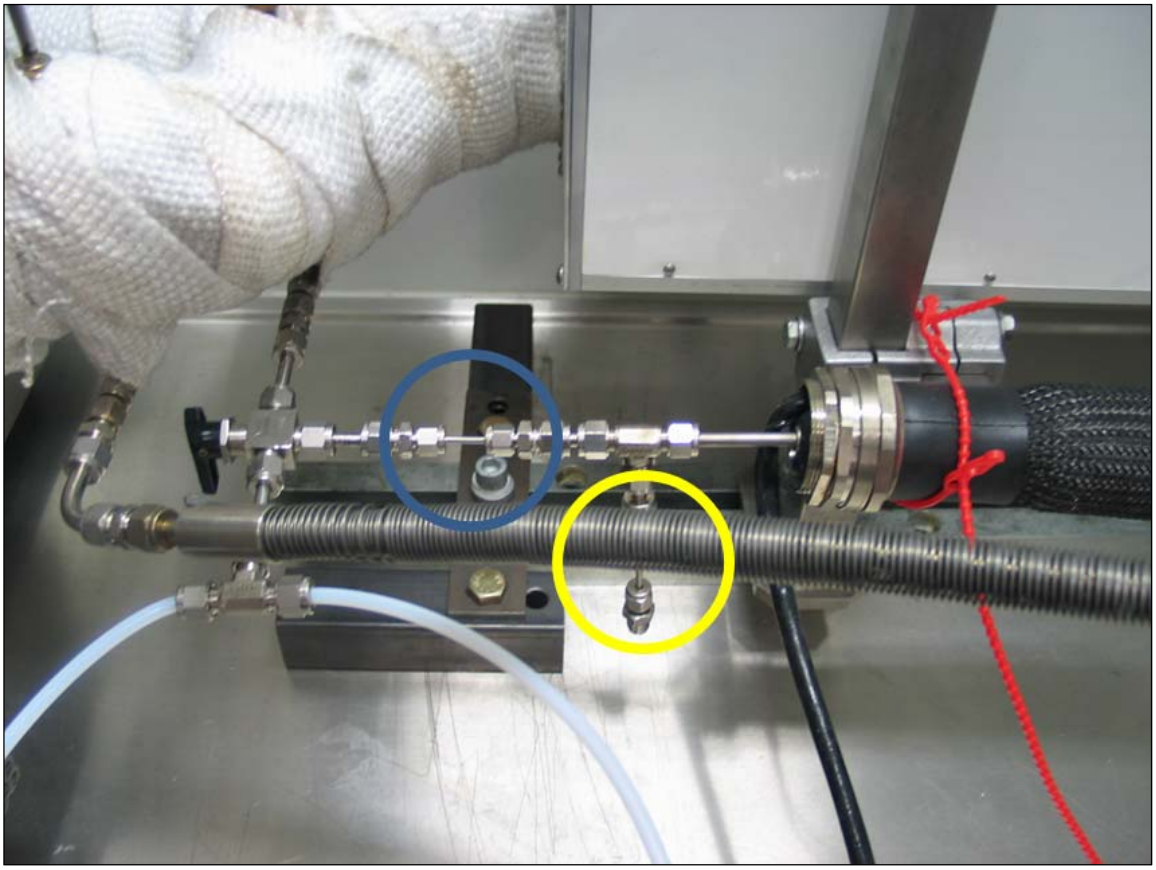

Figure 8.5. Test rig facility for gas mixtures. In the heated white box flow of different gases, in a very specific concentration are added. Water can be added up to 14 % of the total volume. Sampling (blue circle) and air (yellow) nozzles are visible. The heated black hose leading the exhaust to the apparatus is visible as well. An external Teflon® pipe was added to carry out external measurements or calibration with the aim to check the functioning of the test rig.

The test gas rig is a heated mixing unit, where several gases, in different concentration, can be added. Moreover, a very precise amount of water can be included in the gas stream simulating engine exhausts. The test rig is open to the atmosphere and residual non-probed exhaust is pumped away by a fume hood. A very small portion of the exhaust is only extracted by the apparatus due to the much lower vacuum existing in the black hose (30 mbar). The test rig is designed to have three different probe connectors. This allowed the monitoring of the gases coming out of it by a FT-IR. Water was monitored to verify its concentration. Due to the lack of sensibility to $SO_2$ and poor absorbance in the IR region, the FT-IR was useless for a comparison with measured values of $SO_2$ fluorescence.

### 8.3.1. Reaction of $SO_2$ with water ($SO_2 + H_2O \neq H_2SO_3$)

One possible problem which could occur when measuring $SO_2$ fluorescence in humid air is a reaction yielding $H_2SO_4$. The oxidation of $H_2S$ or any other molecule containing sulfur could in principle lead to formation of sulfurous/sulfuric acid in presence of high amounts of OH radical (chapter 3). Jarrige et al. [3] observed $H_2SO_4$ formation, and in consequence $SO_2$ depletion, at atmospheric pressure with the addition of only 2.3 % of water. However, in the apparatus herein described and under the working conditions this effect was never observed. The stability of the sulfurous/sulfuric acid at the temperature of 525 K and 3 mbar is low. In case that substance is formed, the result due the conditions would be a fast reconversion into $SO_2$.

### 8.3.2. Collisional quenching of $SO_2$ fluorescence by water

The existence of water in the stream could also result in a high probability of signal decrement due to collisional quenching. This effect has been observed at atmospheric pressures as well [16]. However, this is not an effect that has been noticed at 3 mbar.

### 8.3.3. Depletion of total fluorescence signal

Although the quenching of the $SO_2$ signal due to water and reactions with it to form sulfurous/sulfuric acid have been discarded, there is another phenomenon that has been observed only when water is added which is the decrease of in the integrated signal from the first and the second time gate. Several measurements were performed. Figure 8.6 shows an instance of them.

The measurement starts with glow discharge cell turned on and zero concentration of $H_2S$. Then at time 28, 80 ppb of $H_2S$ are set and after, at time 55 addition of water started (1.32 % v). From this time on water is increased in steps of 2.69, 4.08, 6.10, and 8.51 % v. It must be noticed that

integrals of both gates decreased from time 55 even below the value corresponding to 0 ppb of $H_2S$. The unique feasible explanation for this fact is that extra water or sub-products formed in a NTP ($O^{\cdot}$, $O_3$, $H_2O_2$, $O_2H^{\cdot}$) react with NO, $SO_2$ or both. If $SO_2$ reacts with water, the signal of the first time gate should decrease only till its initial value (0 ppb). However, this does not occur. The integral diminishes even below its initial value when high water concentrations are added. What is more important, if $SO_2$ would be involved in a reaction, the signal from the second gate should remain constant. Therefore this effect must be related to NO since its fluorescence contributes to first and second gate. The final confirmation is the fact that subtracted signal of 80 ppb ($H_2S$) remains constant over the whole water measurement when correction by α factor is made (blue and green in fig. 8.6). This leads to the conclusion that the only product under reaction is NO.

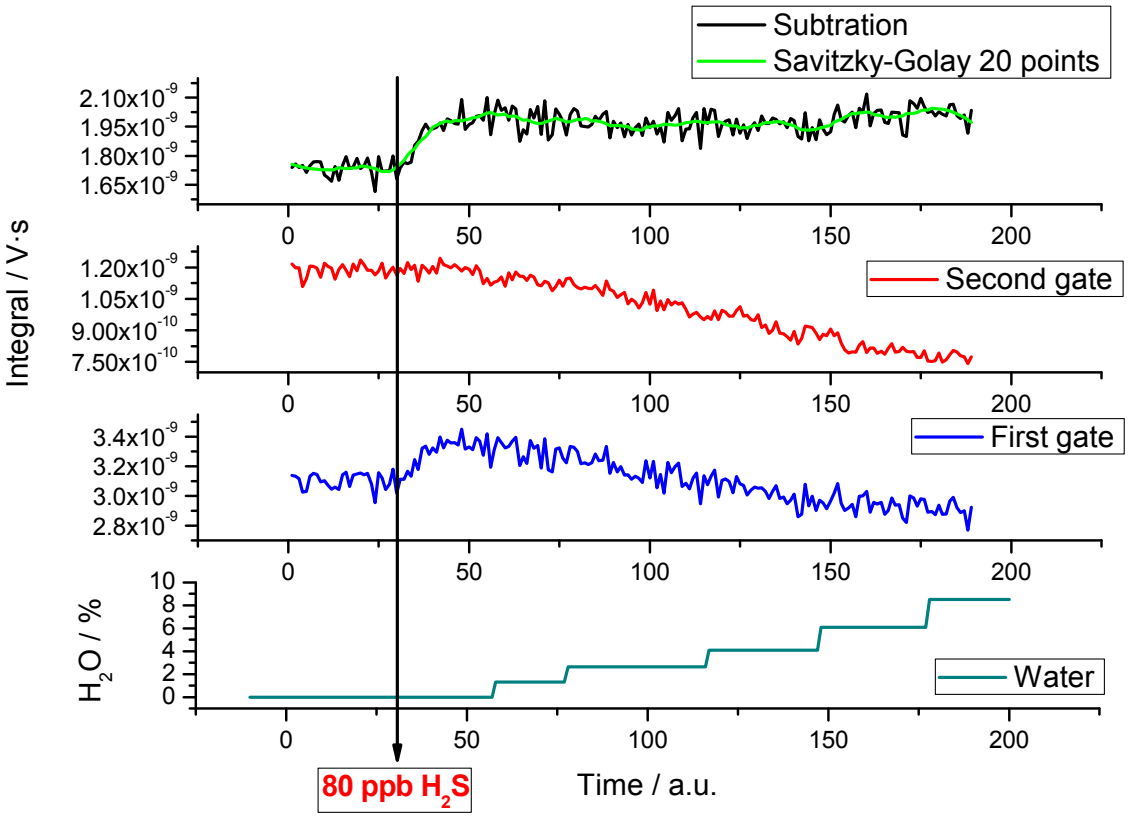


Figure 8.6. Integrated signals from first and second gate for a concentration of 80 ppb $H_2S$ (added from time 28) and water increasing water per cents (added from time 55).

## 8.4. Literature


1. MB. Chang, TD. Tseng, *J Environ Eng* 1996, 122(1):41-46.
2. A. Fateev, F. Leipold, Y. Kusano, B. Stenum, E. Tsakadze, H. Bindslev, *Plasma Process Polym* 2005, 2(3):193-200.
3. J. Jarrige, P. Vervisch, *Plasma Chem Plasma Process*, 2007, 27(3):241-255.
4. ER. Lovejoy, TP. Murreslls, AR. Ravishankara, CJ. Howard, *J PhysChem*, 1990, 94(6)2386-2393.
5. H. Ma, P. Cen, R. Ruan, *Plasma Chem Pasma Process,* 2001, 21(4):611-624.
6. BS. Nicole, T. Pierre, R. Aurore, J. François, P. Stéphane, *Plasma Process Polym*, 2005, 2(3):256-262.
7. Y. Shi, JJ. Ruan, X. Wang, W. Li, TE. Tan, *Plasma Chem Plasma Process* ,2006, 26(2):187-196.
8. EW. Anna, JC. Withehead, K. Zhang, *ApplCatal B Environ*, 2007, 72(3-4):282-288.
9. LT. Hsieh, WJ. Lee, CY. Chen, YPG. Wu, SJ. Chen, YF. Wang, *J Hazard Mater*, 1998, 63(1):69-90.
10. S. Futamura, M. Sugasawa, IEEE *Trans IndAppl*, 2008, 44(1):40-45.
11. S. Futamura, A. Zhang, G. Prieto, T. Yamamoto, 1998, IEEE *Trans IndAppl* 34(5(:967-974
12. S. Futamura, H. Einaga, H. Kabashima, LY. Hwan, 2004, *Catal Today* 89(1):89-95.
13. F. Thevenet, O. Guaitella, E. Puzenat, 2007, *Catal Today* 122(1-2):186-194.
14. A. Zhang, S. Futamura, T. Yamamoto, 1999, *J Air Waste Manage Assoc* 49(12):1442-1448.
15. G.E. Gadd, T. G. Slanger, *J. Chem. Phys.* 92 (4), 15 February 1990.
16. Luke, W. T., *J. Geoph. Res.*, **1997,** 102, pp. 16255-16265.
17. M.J. Dyer, G.W. Faris, P.C. Cosby, D.L. Huestis, T.G. Slanger, *Chem. Phys.* 171, (19939237-252.
18. T.B. Settersten, B.D. Patterson, W.H. Humphries IV, *J. Chem. Phys.*, 131, 104309 (2009)
19. R.P. Frosch, G.W. Robinson, J. Chem. Phys., Vol. 41, No. 2, 15 July 1964, 367-674.
20. H. Rottke, H. Zacharias, *J. Chem. Phys.* Vol. 83, No. 10, 15 November 1985, 4831-4844.
21. J. Brozozowski, P. Erman, M. Lyyra, *PhysicaScripta*. Vol. 14, 290-297, 1976.
22. J.R. Banic, R.H. Lipson, T. Efthimiophoulos, B. Stoicheff, *Optics letters,* Vol. 16, No. 10, October 1981, 461-463.
23. I. Stuart McDermid, J. B. Laudenslager, *J. Quant. Spectrosc. Radiat. Transfer,* Vol. 27, No. 5, 8 October 1981, 483-492.

24. J.A. Gray, P.H. Paul, J.L. Durant, *Chemical Physics Letters*, Vol.190, No. 3,4, 6 March 1992, 266-270.
25. G.R. Möhlmann, H.A. Van Sprang, E. Bloemen, F. J. deHeer, *Chem. Phys*. 32 (1978) 239-246.
26. P. Erman, A. Iwamae, *Chemical Physic Letters* 234, 3 March 1995, 123-126.

# 9. Measurements of $SO_2$ fluorescence

Data shown in this chapter are referred to measurements of $SO_2$ fluorescence recorded either at different wavelengths (excitation spectra) or related to calibrations. In some cases $SO_2$ has been used, but in the mostly $H_2S$ was employed and converted to sulfur dioxide with the use of the GDC. The hydrogen sulphide is one of the best calibration gases since the apparatus has to work with the glow discharge cell which implies the creation of NO and the test of temporal gate correction via alfa factor.

## 9.1. Wavelength scans

Wavelength scans are necessary to prove the calibration of the OPO laser as well as the good functioning of the whole set-up. Figure 9.1 shows two $SO_2$ fluorescence wavelength spectra at the concentration of 500 ppb. Both were corrected with the alfa method to discard NO contribution. Intensities are nearly equal for all bands. Figure 9.2 shows two $SO_2$ spectra from literature [4]. The upper one was taken at room temperature and shows a typical resolution of a hot molecule whereas the lower one was measured for $SO_2$ cooled in a supersonic jet. The spectrum recorded with an excitation source (laser) of medium bandwidth (5 $cm^{-1}$) at 3 mbar (fig. 9.1) is in agreement with the upper one in figure 9.2. Different bands (132, 142, 152, 300 & 310) are labeled for clarification.

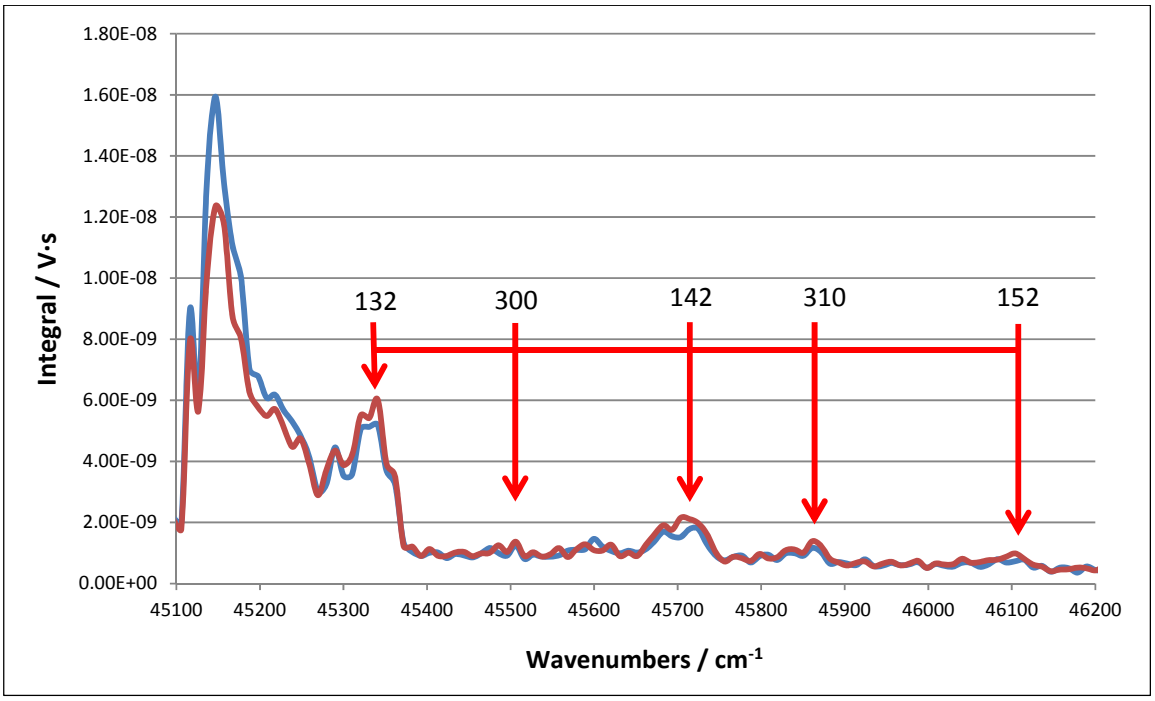


Figure 9.1. Wavelength scans of 500 ppb of $H_2S$ oxydized in a NTP (blue curve) and the same concentration of $SO_2$ (red curve).

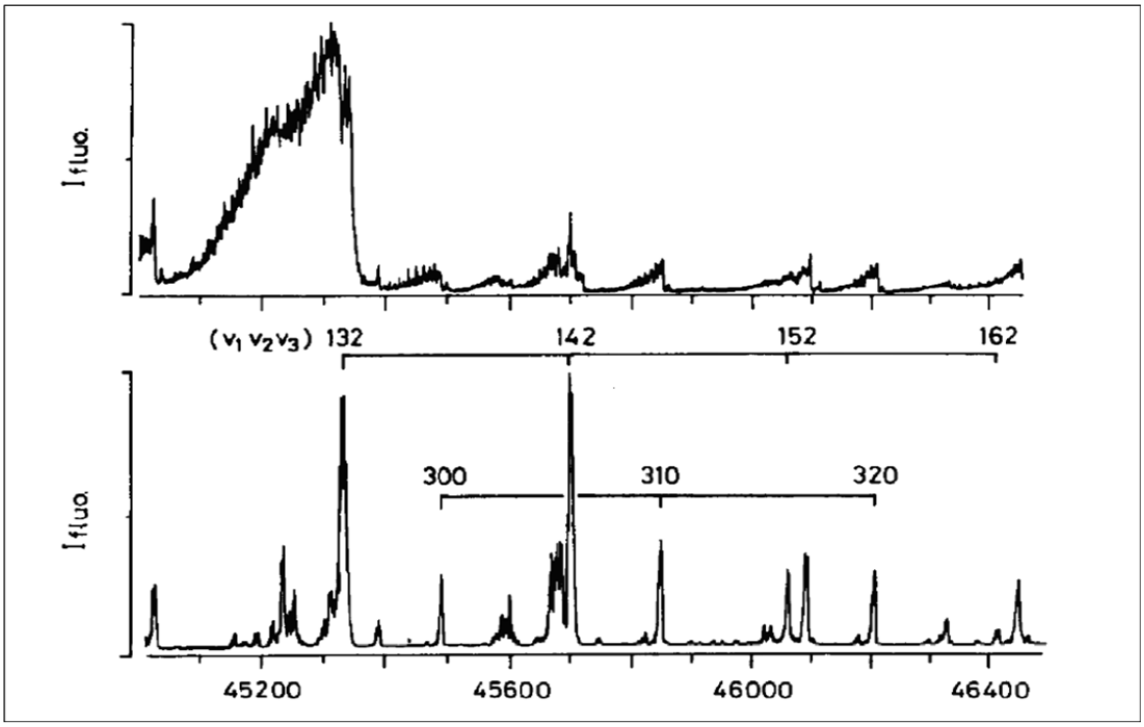


Figure 9.2. $SO_2$ spectra at room temperature and supersonic free jet [4].

The features at lower wavenumbers than 45280 $cm^{-1}$ in figure 9.1 can be explained taking into account species, others than $SO_2$, which are present in the gas mixture after a NTP and can be excited in the wavelength range where the spectrum is recorded, namely NO and $NO_2$. Dissociation of $NO_2$ takes place below 25000 $cm^{-1}$ giving rise to NO ($B^2\Pi$, $\nu'$ = 0, 1, 2, 3, ...) and to O. The electronic state of the latter depends on the dissociating wavenumbers [5]: $O^3P_J$ for 41000.41 < $\lambda$ < 25131.94 $cm^{-1}$ and $O^1D_2$ for < 41000.41 $cm^{-1}$. The NO($B^2\Pi$) formed can emit fluorescence from different rovibronic states whose fluorescence lifetimes are in the range of 850 to 2000 ns ($\nu'' = 6 - 0 \leftarrow \nu' = 0$). Besides, in gas mixture resulting of the nonthermal plasma, NO exists in its ground electronic ($X^2\Pi$) state. Excitation of NO($B^2\Pi$) levels is feasible from cold NO($X^2\Pi$) in the range of 45454.54 to 51813.47 nm [8], but also to higher levels if NO is hot. On the other hand, transitions between the ground state and the first excited state $A^2\Sigma^+$ occur at the following wavenumbers: 40453.07 and 40355.12 $cm^{-1}$ for $A^2\Sigma^+$ ($\nu'$ = 0) ← $X^2\Pi$ ($\nu''$ = 2), 42319.08 $cm^{-1}$ for $A^2\Sigma^+$ ($\nu'$ = 0) ← $X^2\Pi$ ($\nu''$ = 1), 44189.13 $cm^{-1}$ for $A^2\Sigma^+$ ($\nu'$ = 0) ← $X^2\Pi$ ($\nu''$ = 0) [5], 46418.79 $cm^{-1}$ for $A^2\Sigma^+$ ($\nu'$ = 1) ← $X^2\Pi$ ($\nu''$ = 0) and 48728.19 $cm^{-1}$ for $A^2\Sigma^+$ ($\nu'$ = 2) ← $X^2\Pi$ ($\nu''$ = 0) [6]. Hence one should discard those transitions since none of them occur in the wavenumber range were the spectrum was recorded, namely 46296-45045 $cm^{-1}$. Life times of NO($A^2\Sigma^+$) rovibronic states are all in the range of 150 to 200 ns [7]. Excitation of hot NO($X^2\Pi$) to NO($A^2\Sigma^+$) could occur at wavelengths different than those above mentioned (lower than 45280 $cm^{-1}$) giving rise to fluorescence decays which would not be corrected by $\alpha$ optimized for a 2 $\mu$s decay. In fact, three different species (with different lifetimes) might contribute to the uncorrected excitation spectrum: NO from dissociated $NO_2$ (produced in GDC), NO produced in GDC and $SO_2$. In order to shed light onto this issue a simulation of a fluorescence signals with contribution of three lifetimes was made. The result is plotted in figure 9.3. Decays of 2 $\mu$s (NO), 36 ns ($SO_2$, 132 band) and 200 ns (hot NO($X^2\Pi$) → NO($A^2\Sigma^+$)) was convoluted with a Gaussian function. All the three were summed to a scattering contribution and the result is the black curve. As one can deduce from where the integration gates are set, correction of signal with decays lower than 2 $\mu$s is not feasible. Therefore the contribution to signal intensity for wavenumbers lower than 45280 $cm^{-1}$ is in opinion of the author due to hot NO($X^2\Pi$) ← NO($A^2\Sigma^+$) transitions after excitation.

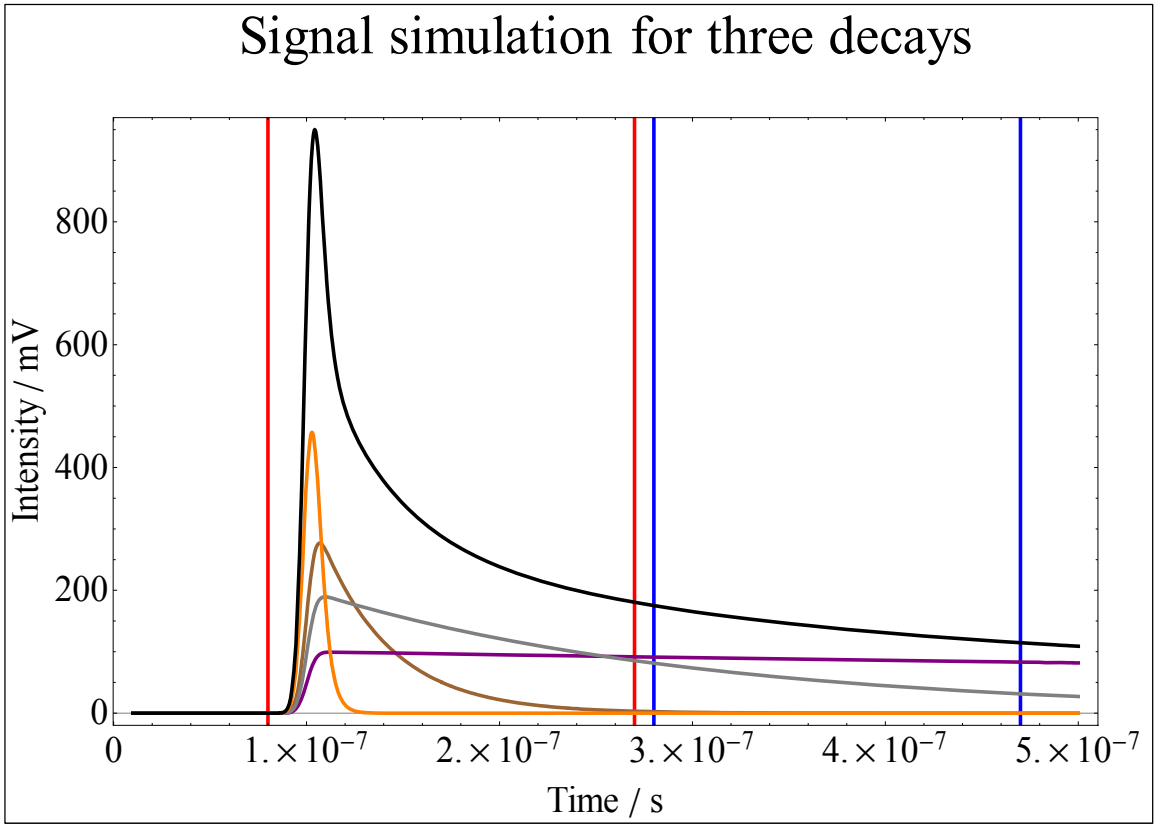


Figure 9.3 Signal produced by the sum of scattering and convolutions of three different exponentials decays (2000, 200 and 36 ns) with a laser pulse function (Gaussian).

## 9.2. Calibrations

A definitive proof of apparatus can be made by measuring $SO_2$ fluorescence at different concentrations where at the same time wavelength and laser energy are monitored. It is also recommendable to perform a calibration every time when a long engine oil consumption test is going to be made. Moreover, calibration is necessary for calculating oil consumption (section 9.3).

To carry out a calibration one has to consider firstly important characteristics such as the signal to noise ratio (SNR). The bigger this ratio the lower the detection limit (chapter 10). Therefore, it is essential to not record individual signals every laser shot. Modern scopes display already an averaged signal composed of several response signals that the PMT delivers over time. In our case measurements have been made always with averaging over 32 or 64 laser pulses. For a laser repetition rate of 20 Hz, this means 1.6 and 3.2 seconds per point, respectively. Herein it is important to know that $n$ is a number quantifying the scope averages.

The whole calibration procedure takes into account the following equations. Firstly two gates must be set and the integral of the signal inside them is made. Besides, alfa correction must be performed. An unique final value, $I$ is obtained for $n$ averaged scope signals.

$$I = \left(\int_{lim1}^{lim2} \sum_i^n n\ times\ averaged\ signal\right) - \left(\int_{lim3}^{lim4} \sum_i^n n\ times\ averaged\ signal\right) * \alpha\ \ [V \cdot s] \tag{9.1}$$

This value is corrected by the laser pulse energy according to,

$$I_{EC} = \frac{I \cdot n}{\sum_i^n E_i}\ [V \cdot s \cdot J^{-1}] \tag{9.2}$$

where $\sum_i^n E_i$ being the average over $n$ laser pulses (Joules).

The $I_{EC}$ value must be measured 10 or more times to determine a correct integral signal for a given $SO_2$ concentration. Thus a value is calculated according to,

$$\bar{I} = \frac{\sum_i^m I_{ECi}}{m}\ [V \cdot s \cdot J^{-1}] \tag{9.3}$$

with $m$ (10, 15, 20, etc.) being the number of times the same concentration is measured. $\bar{I}$ is a function of the concentration $x$. The standard deviation (STD) for every concentration can be calculated by using,

$$\sigma_{\bar{I}} = \sqrt{\sum_i^m \frac{(I_i - \bar{I})^2}{m-1}}\ [V \cdot s \cdot J^{-1}] \tag{9.4}$$

Final equation of calibration is obtained when a linear regression (minimum squared method) is performed with different pairs of mean integral and concentration: $(\overline{I_1}, x_1)$, $(\overline{I_2}, x_2)$, $(\overline{I_3}, x_3)$, etc.

$$\bar{I} = m \cdot x + b\ \ or\ (\bar{I} = m \cdot [SO_2] + b) \tag{9.5}$$

with $m$ being a slope and $b$ an intercept.

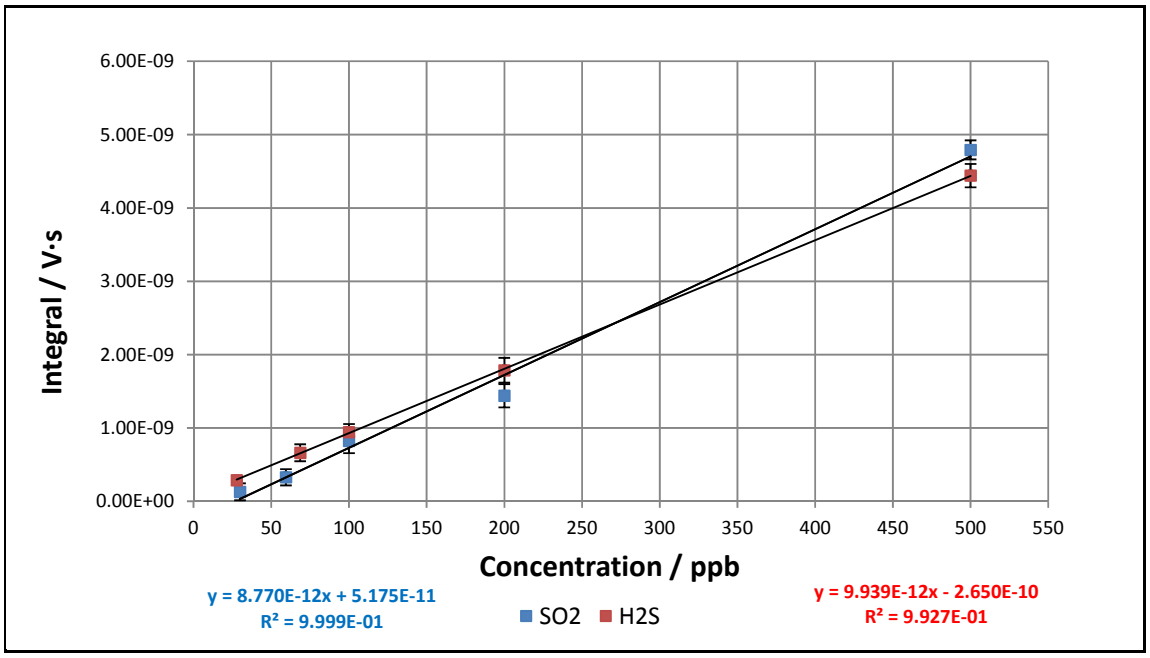


Figure 9.3. Comparison between calibrations made with $H_2S$ and $SO_2$.

Figure 9.3 shows a comparison between a calibration made with $H_2S$ (GDC-on) and another with $SO_2$ (GDC-off). Data follows in both cases a linear model what can be seen in value of $R^2$ (0.9999 for $SO_2$ and 0.9927 for $H_2S$). Slopes vary slightly with the one for $H_2S$ being 12% bigger. Intercepts are much more different; the one for $H_2S$ is 80 % bigger than that for $SO_2$. Evaluation of accuracy and precision will be made in chapter 10.

Figure 9.4 shows an ideal calibration measurement with several $SO_2$ concentrations. It was made in a way that imitates a typical measurement of oil consumption of a combustion engine. Concentrations were changed from low to high values: from 0 to 500 ppb and 27.8 to 1000 ppb. Repeatability of measurement was tested at 0, 27.8 and 500 ppb. Those three concentrations were set twice each. In figure 9.5 the agreement of data with a liner model ($R^2$ = 0.99996) is shown. Although the intercept (4.435E-11) is quite similar to that of the $SO_2$ calibration in fig. 9.3 (5.175E-11), the slope is quite different (1.3338E-11 in fig. 9.4 versus 8.770E-10 in fig. 9.3). Relation between slope and intercept and parameters having an influence on them will be explained in chapter 10.

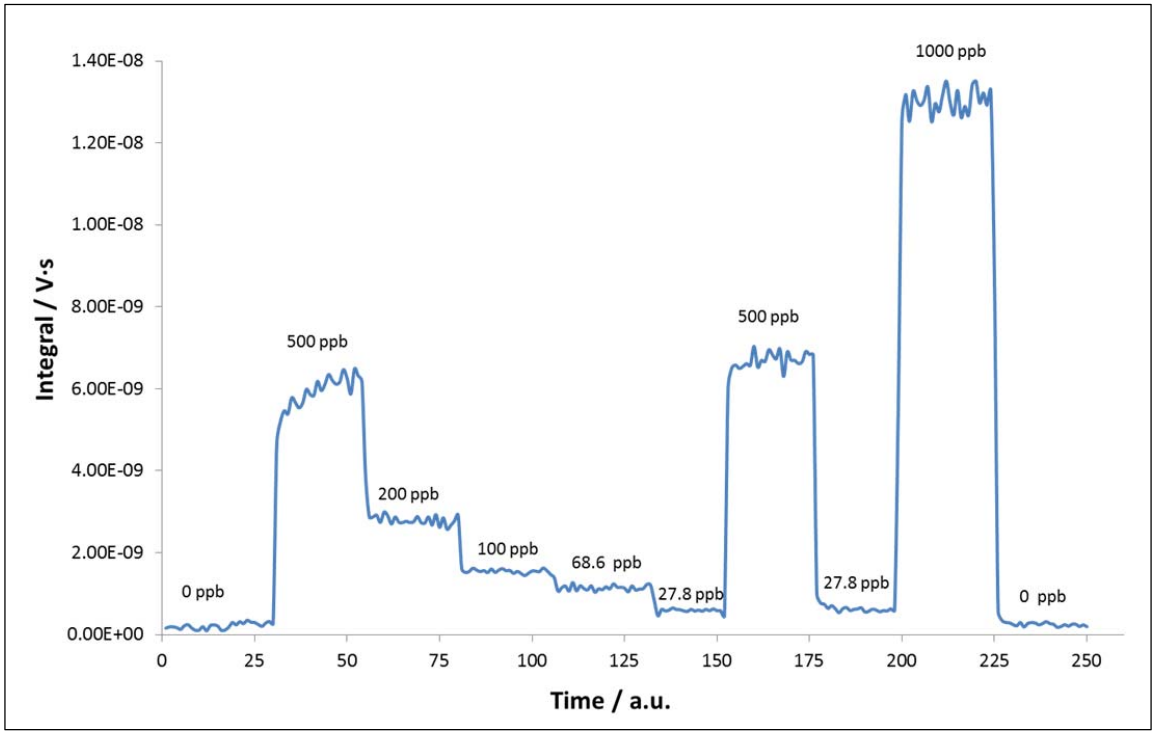


Figure 9.4. Typical calibration cycle (raw data) measured at the test rig (BMW-AG) for different concentration of $SO_2$ (diluted in air) with GDC turned on.

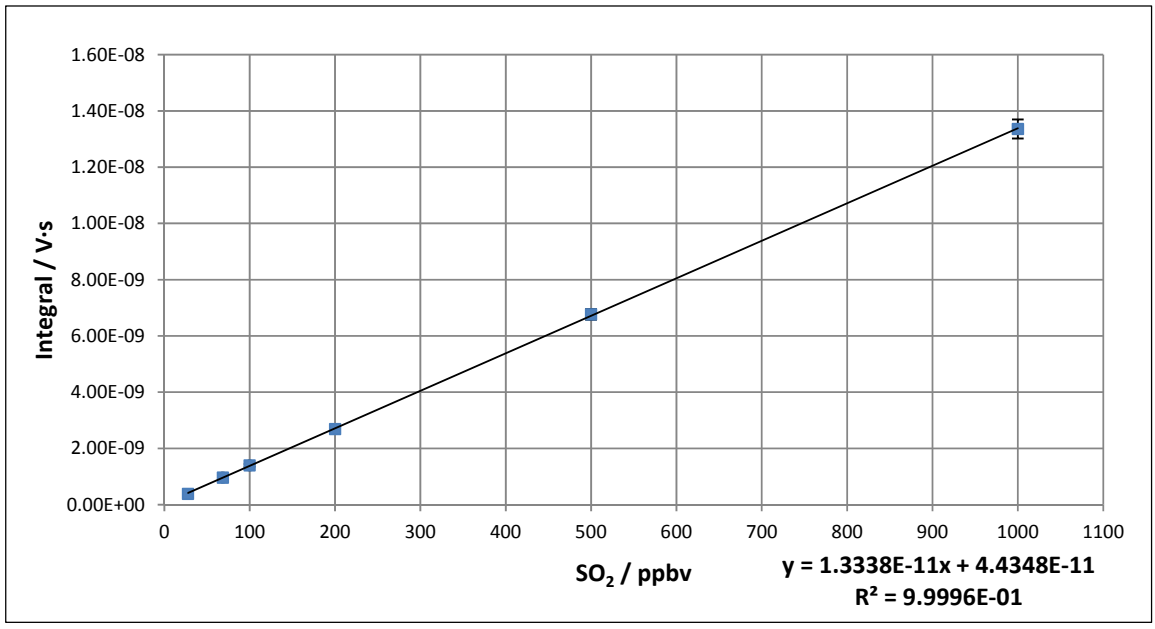


Figure 9.5. Calibration obtained from measurement plotted in 9.4. Standard deviation (STD) is only noticeable at the highest concentration (1000 ppb). Linearity covers almost two orders of magnitude with an $R^2$ equal to 0.99996.

Despite the several calibrations made with the wavelength switching mode [1] during the performance of this work, it is found that this method is not necessary. Originally it was developed to get rid off fluorescence signals from any other molecule different than $SO_2$. In chapter 8 all feasible interferences were described in detailed. Thus it is clear that only NO can be a problem. However, the TTGIM (section 7) can be used to avoid fluorescence from NO. Therefore, herein it is proposed that one single wavelength, namely 220.6 nm must be utilized. In addition as it was mentioned usually scattering is so intense that $SO_2$ signal at bottom wavelength becomes nearly constant for lower concentrations. This results in lower SNR, higher standard STD and in consequence in a worse linear fitting.

Figure 9.6 shows a measurement where $SO_2$ concentration was changed over time along three orders of magnitude. In figure 9.6.b the integral of the peak wavelength is shown whereas in figure 9.6.b the bottom one is plotted. Correction obtained after subtracting the second from the first one is drawn in figure 9.6.c. Figure 9.6.d shows how concentration was varied.

In figure 9.7 calibration from one and two wavelengths are drawn. The subtracted signal contained more “noise” since integral from bottom signal is affected for more noise (lower SNR). This effect results in a slightly decrease of $R^2$. In case of a single wavelength, intercept is bigger which turns out in a better sensitivity (slope is the ability to detect changes in integral with regard to concentration, see chapter 10).

Figure 9.8 shows the use of one or two wavelengths when water is added to 80 ppb of $SO_2$. Both results are equivalent. Therefore it is recommendable for the author to use a single wavelength together with the TTGIM.

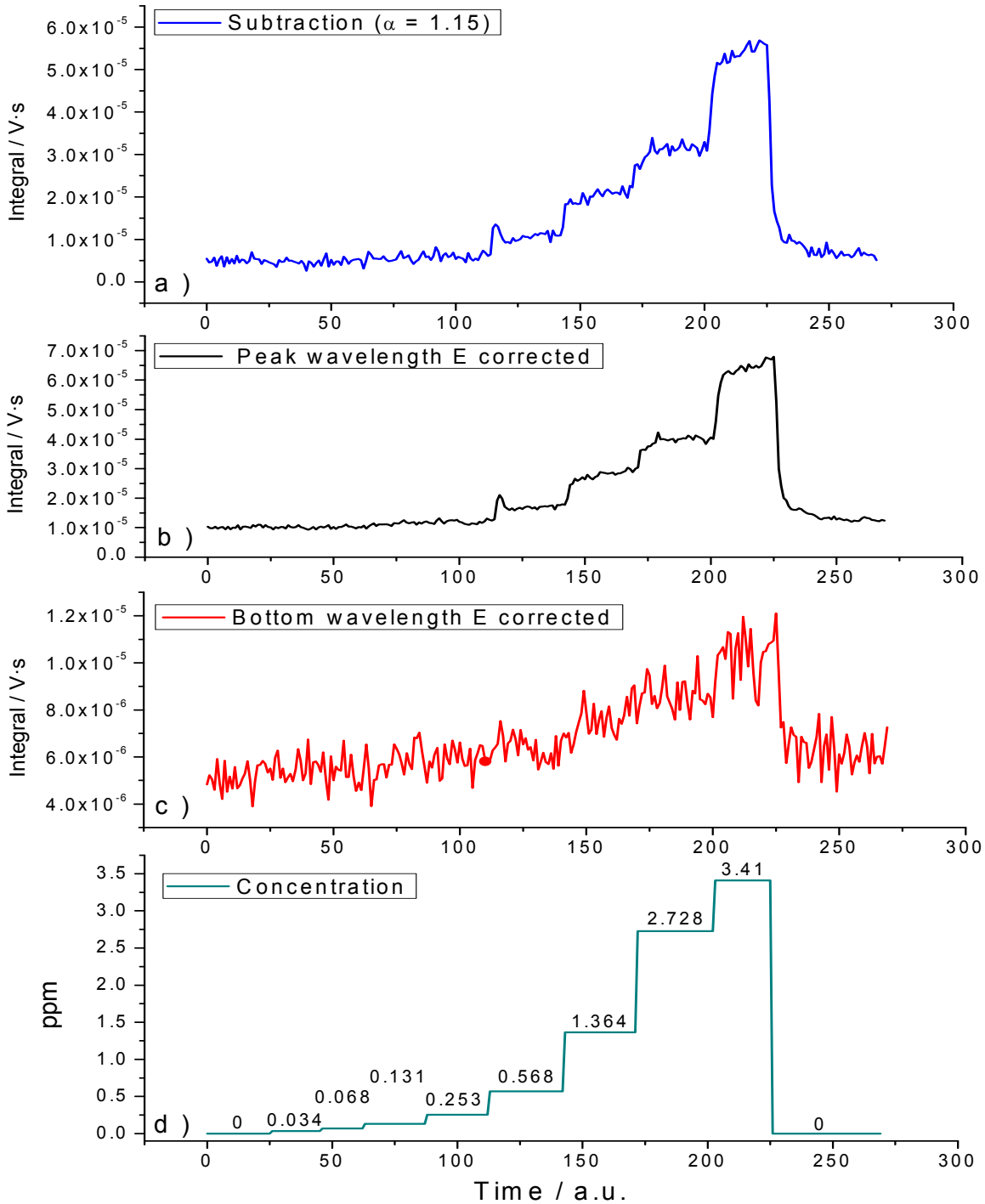


Figure 9.6. Measurement of $SO_2$ fluorescence integral at different concentration and corrected by α = 1.15. a) Signal obtained by subtracting integrals measured at peak and bottom wavelength. b) Integral of peak wavelength. c) Integral of bottom wavelength, and d) Concentrations of $H_2S$ in gas stream.

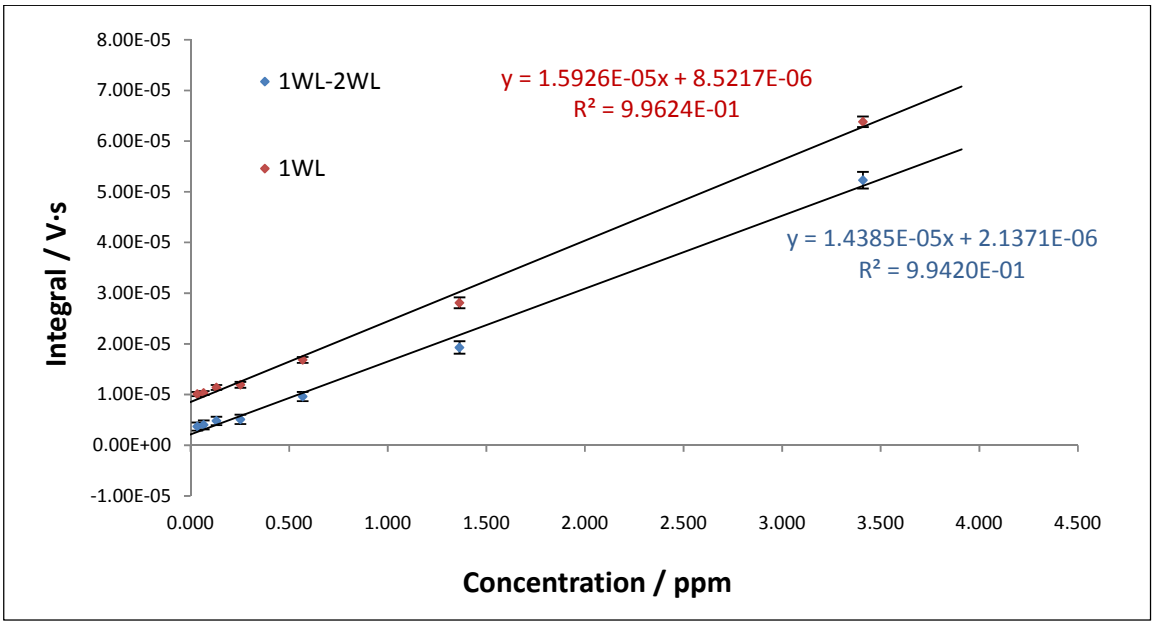


Figure 9.7. Calibration of $SO_2$ with two (1WL-2WL) and one (1WL) wavelengths. $R^2$ and individual STD of concentrations are better for 1WL method.

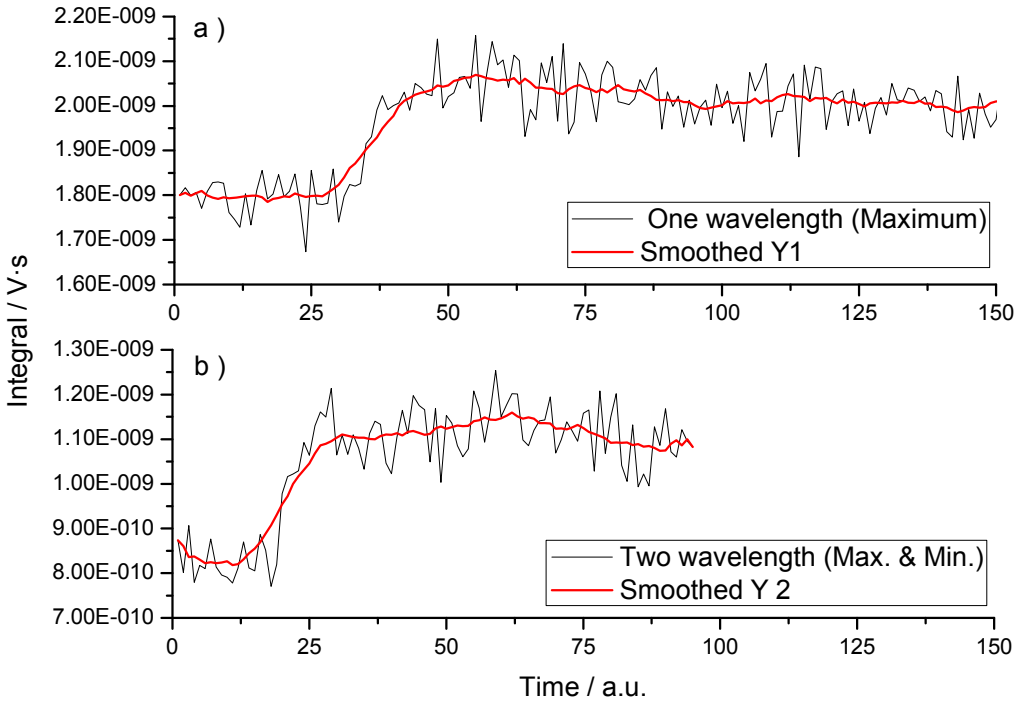


Figure 9.8. Fluorescence integral for 80 ppb of $SO_2$ measured in humid air (similar water increment as in fig. 8.6) with one (a) and two wavelengths (b).

## 9.3. Measurements at the engine

Finally the oil consumption can be calculated as follows [2];

$$\dot{m}_{\ddot{O}l} = \left[\frac{y-b}{m} \cdot \frac{\rho_A}{\rho_{SO}} \cdot \frac{\dot{V}_M}{1000} \cdot 60 \cdot \frac{U}{2} \cdot Z \cdot \rho_L \cdot \frac{M_S}{M_{SO}} - \dot{m}_{KS} \cdot 1000 \cdot c_S^{KS}\right] / c_S^{\ddot{O}l} \; [g \cdot h^{-1}] \qquad (9.6)$$

where $\rho_A$ is the density of the exhaust (g/L), $\rho_{SO}$ is the density of the SO (g/L), $\dot{V}_M$ is the volume flow of the engine, $U$ are the revolutions per minute (r.p.m.), $M_{SO}$ is the $SO_2$ molecular mass, $M_S$ is the sulfur atomic mass, $\dot{m}_{KS}$ is the mass flow of the exhaust, $c_S^{\ddot{O}l}$ is the concentration of sulfur in the oil in %, $c_S^{KS}$ is the concentration of sulfur in the gasoline in ppmv, $\rho_L$ is the density of air, $Z$ is the number of cylinders, $b$ is the intercept of our calibration, $y$ is the averaged signal ($\bar{I}$) and $m$ is the slope.

Figure 9.9 shows an oil consumption measurement performed in a BMW engine. It shows four different cycles where values of r.p.m and load were varied. Due to the speed in data acquisition some particular effect can be seen e.g. short oil consumption decrements before each maximum consume (local minimums). This is of course a promising measurement which demonstrates the capability of the set-up concerning on-line and in-situ measurements.

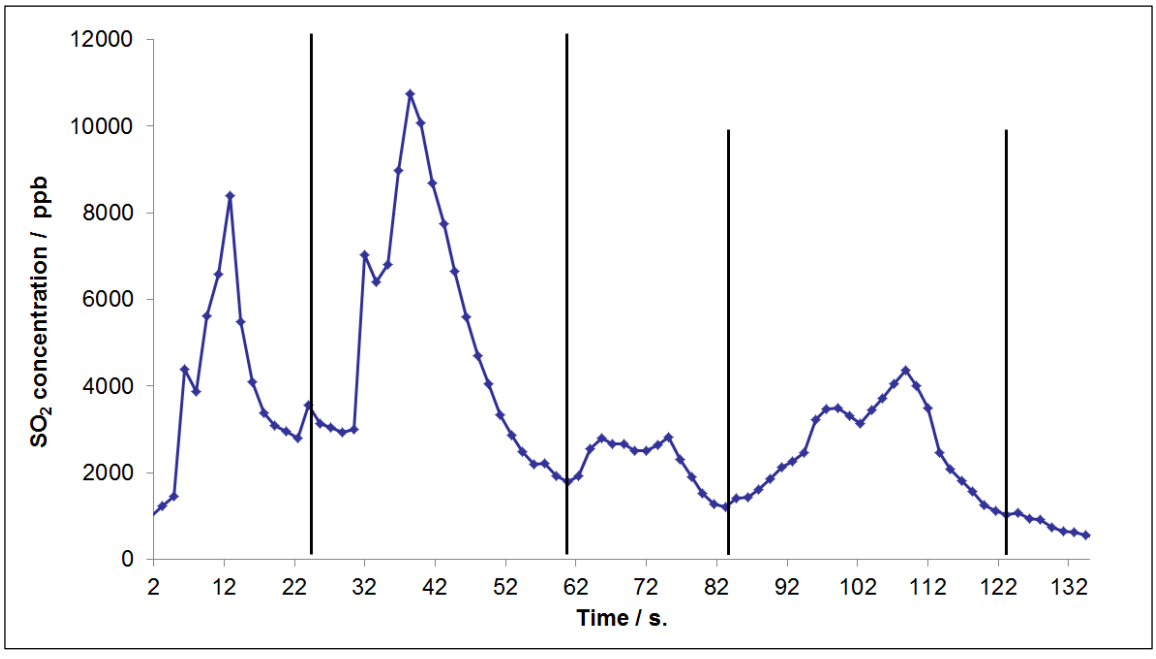


Figure 9.9. Oil consumption measurement taken at the BMW-AG facilities (prototype-II). This was a test measurement and the speed (r.p.m.) and loads (Nm) were not supplied by BMW.

## 9.4. Literature


1. Yutaka Matsumi, Hiroyuki Shigemori, KenshiTakahashi , *Atmospheric Environment* 39 (2005) 3177–3185.
2. Laserspektroskopische Spurenanalytik von Ölbestandteilen in Abgasen von Verbrennungsmotoren, Stefan Sellmeier, (PhD Thesis) 19.07.2011.
3. S. Sellmeier, E. Alonso, U. Boesl, *Anal. Chem.*, 2014, 86 (1), pp 380–389.
4. T. Ebata, O. Nakazawa, M. Ito, *Chem. Phys. Lett.* 1988, 143, 31.
5. A. Clark, K. W. D. Ledingham, A. Marshall, J. Sander, R. P. Singhal, *Analyst*, June 1993, VOL. 118.
6. T. B. Settersten, B. D. Patterson, W. H. Humphries IV, *The Journ. Of Chem. Phys*. 131, 104309 (2009).
7. J. Luque, D. R. Crosley, *J. Chem. Phys*. 111, 7405 (1999).
8. G.E. Gadd, T. G. Slanger, *J. Chem. Phys.* 92 (4), 15 February 1990.

# 10. Evaluation of the method

## 10.1. Noise

Noise is a critical factor when low concentrations have to be measured with any analytical technique. A detection limit as low as 5 ppb can be achieved when laser induced fluorescence techniques are employed. With this regard it is essential to consider the improvement of the signal to noise ratio (SNR). This factor is proportional to the squared root of the accumulated signals $n$, $(\propto \sqrt{n})$. In figure 10.1 average values are 1, 8 and 64. It is clearly visible that an improvement is obtained when $n$ is increased from 1 to 8 and to 64 which means an increment of 2.8 and 8 respectively. Steps for different $SO_2$ concentrations are only perfectly distinguishable in case of 64.

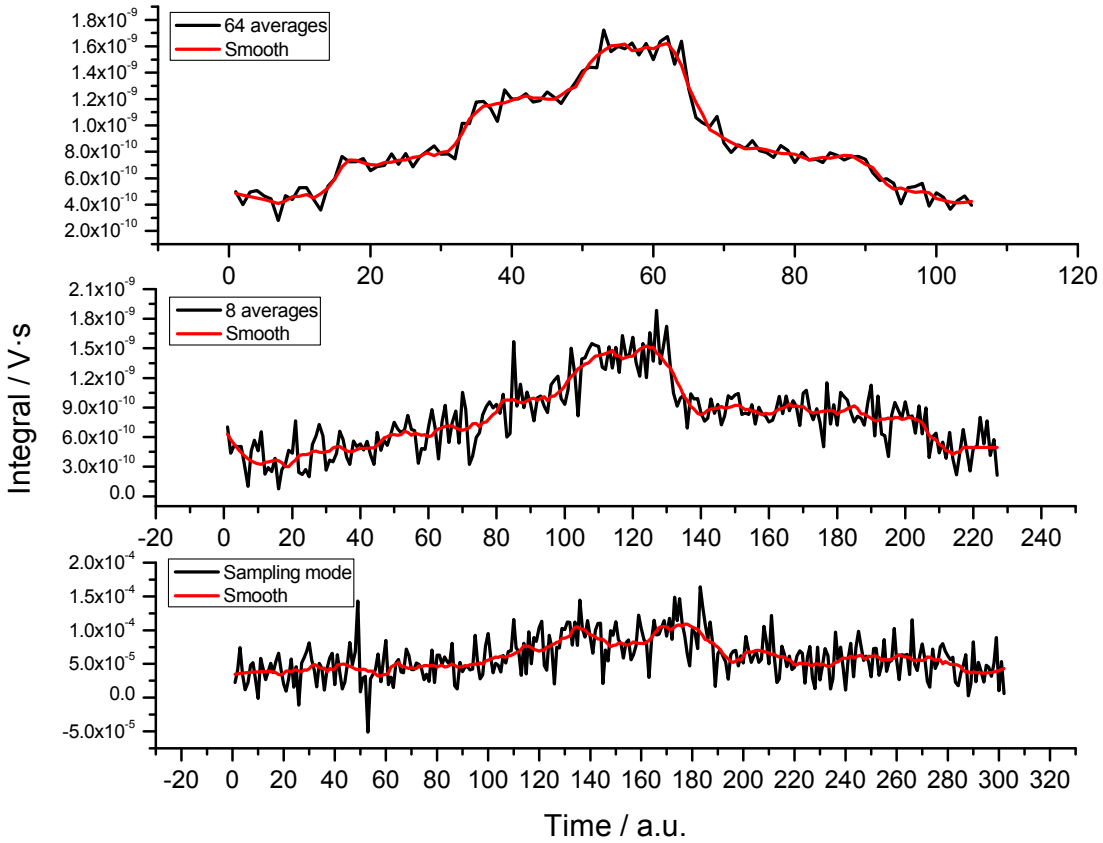


Figure 10.1. Increment in the SNR. A concentration cycle of 0, 80, 150, 250, 80, 70 and 0 ppb of $SO_2$ was measured for three different signal acquiring modes.

Thus it is necessary to accumulate signals over $n$ equal 32 or 64 which for a 20 Hz laser means a time of only 1.6 or 3.2 seconds per measured point. In the following different sorts of noise or contributions to it are shortly explained.

## 10.2. Sorts of noise

### 10.2.1. **Dark current**

Due to dark current which arises from the thermal emission of the electrons and from the photocathode (leakage current between dynodes), a PMT can produce signal even in the absence of light. This is due to the thermionic emission of electrons and is only partly caused by cosmic radiation or by radioactive decay of spurious radioactive isotopes in the materials. This noise depends largely on the temperature and on the work function ($\phi$). A decrease in temperature can dramatically reduce this noise although the optimal point is related to the cathode composition. However, the cooling of the system can produce undesirable effects, for instance the reduction of the signal photocurrent or voltage drops across the cathode [4].

### 10.2.2. **Shot noise**

This noise is associated with the particle nature of the light. With regard to the optical processes, it describes the fluctuation in the number of photons detected. The origin is essentially the discrete origin of the matter. It is very important within a PMT because the relevancy of a random conversion of photons into photo-electrons. Huge fluctuations in the velocity of the flow and recombination of electrons and hollows e.g. in a p-n semiconductor (never in a conductor), increases this noise [4].

### 10.2.3. **Johnson noise**

Electronic noise contributes to the dark current as well. This so-called Johnson noise is caused by fluctuations of the amplification and by noise of the load resistor. Those last are often included in the dark-current value. This noise comes from the load resistor at a certain temperature. This and the shot noise can be treated together. With a gain of $10^6$ and a load resistor of $10^5$ Ω the anode current due to the Johnson noise should be larger than $10^{-13}$ A. The noise due to the shot is bigger than this one (ca. 5 nA), therefore the Johnson noise is negligible within a PMT. This noise represents the lower limit in a device [4].

### 10.2.4. **Electronic noise in electric cables**

Magnetic fields can create inductive effects in cables and this can be seen in a signal displayed at scope. In addition electrical fields from power supplies affect cables in the apparatus. During this work it was observed that the shielding of the cable connecting PMT and scope reduces the noise. For this purpose a simple copper mesh was set around the BNC cable.

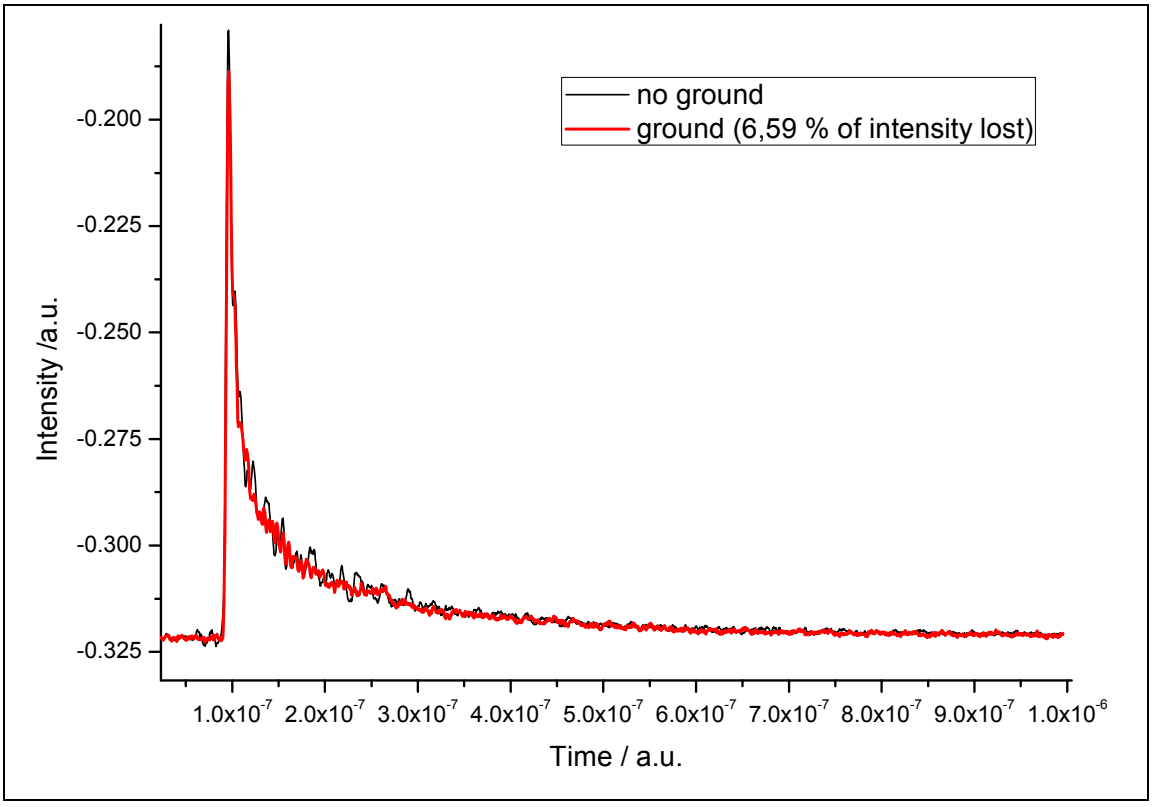


Figure 10.2. Shape of a scope signal owing to $SO_2$ fluorescence with electronic noise (black curve) and without (red curve).

Figure 10.2 shows oscilloscope signal with and without shielding. Many ripples which disturb especially the determination of the decay time of the fluorescence signal are deleted.

### 10.2.5. **Scattering**

Despite all three previous types of electronic noises, most important contribution to signal disturbance and in consequence to decrement of detection limit, is scattering of light (chapter 7). Scattering within a LIF apparatus can be produced by molecules. The most abundant one in engine

exhaust is $N_2$. Scattering coefficient for it at 220.6 nm is $2.26 \cdot 10^{-25} cm^2$ which turns out in a negligible scattering at the calculated solid angle (chapter 4). Scattering at solid inner surfaces occurs within the FC. This is considered to be the main source of scattering and it is constant meantime the alignment does not change. This physical effect is mathematically described by a Gaussian peak with the FWHM of the laser pulse divided by $2\sqrt{(2ln2)}$ and having certain amplitude $A$ (eq. 7.3). This amplitude is very difficult to determine. However, it is taken into account during the signal strength calculations and it is clearly dependent on both, laser pulse energy and beam diameter. The value of the amplitude is expressed in mV which corresponds to the peak height observed in the scope. Thus one can simulate the signal corresponding to this effect for a certain diameter and energy of the laser pulse. Thereby, it can be included in the final signal strength contribution. The value of scattering integral when no $SO_2$ or NO are excited is the intercept of the linear calibration curves (see chapter 9.2).

## 10.3. Signal strength

The so called signal strength of a single-photon LIF signal is a mathematical expression obtained taking into account all physical and electronic processes occurring in molecules and in PMT respectively. With it one can predict how high is a signal on a scope or in other terms which is the amplitude of it. Thus the aim is to be able to study in detail how the apparatus responses and depends on the many parameters affecting fluorescence. Beside, signal strength is used to predict trends of fluorescence versus concentration. To attain this firstly the signal strength is calculated as amplitude, and then an artificial response signal is plotted. The expression of it is basically the convolution of a Gaussian and an exponential function. In the following a procedure to calculate the amplitude is performed according to J. D. Bradshaw el al [1]. A program in Mathematica (appendix) was written to compute final equations.

Signal strength depends on total number of photons emitted $P_{\lambda 2}$ at the fluorescence wavelength $\lambda_2$ $(240 - 420\ \mathrm{nm})$, optical detection efficiency $E_d$ and electric detection efficiency $E_e$. That is,

$$D_{\lambda 2} = P_{\lambda 2} E_d E_e \tag{10.1}$$

After mathematical deductions based on the physical and electrical effects that take place during the whole process [1], equation 10.1 becomes

$$D_{\lambda 2} = (AB)VE_{\lambda 1}\eta_k E_d E_e \tag{10.2}$$

where $\eta_k$ being the quantum yield ( $0.817$ [3, 4], calculated in program) and $AB$ being the concentration of the molecule in study. Equation 10.2 includes some terms that are discussed below.

*The optical pumping,*

$$E_{\lambda 1} = \left[1 - exp\left(-\frac{P_{\lambda 1} \cdot \sigma_{\lambda 1}}{a_{\lambda 1}}\right)\right] f_i S_{\lambda 1} \tag{10.3}$$

with $f_i$ being molecular population of $SO_2$ in 000 state and $S_{\lambda 1}$ is the optical saturation parameter, $P_{\lambda 1}$is the number of photons at the excitation wavelength $\lambda_1$ $(220.6\, nm)$, $a_{\lambda 1}$ is the cross sectional area of the $\lambda_1$ laser beam (CSALB), and $\sigma_{\lambda 1}$ is the absorption cross section of $SO_2$ at 220.6 nm [5].

*The optical detection efficiency*

$$E_d = \delta_{\lambda 2} Y_{\lambda 2} Z_{\lambda 2} \eta_{ph_{\lambda 2}} \tag{10.4}$$

where $\delta_{\lambda 2}$ is the fraction of total fluorescence within the optical sampling window (section 4), $Y_{\lambda 2}$ is the collection optics efficiency factor at $\lambda_2$, $Z_{\lambda 2}$ is the filter transmission factor at $\lambda_2$ and $\eta_{ph_{\lambda 2}}$ is the quantum efficiency of the photocathode at $\lambda_2$.

*The electronic detection efficiency (equal to 1 [2])*

$$E_e = \frac{PMT\ signal\ pulses\ counted}{PMT\ signal\ pulses\ emitted} \tag{10.5}$$

*And the effective volume of sampling region,*

$$V = a_{\lambda 1} l \tag{10.6}$$

with $l$ being the probe distance. The latter can be calculated as; $l/2 = D/2 = f \cdot \theta$ (with $f$ the focal length and $\theta$ being the half angle defined by the NA. However and due to the length of the photocathode $l$ becomes 2.4 cm. The signal generated in the PMT output BNC must be then converted to voltage (amplitude) by using the total impedance (1MΩ) of the scope-input channel resulting in a pulse rise time of 4 ns. The voltage amplitude resulted from these calculations agreed very well with the one of the scope signal. It is necessary to highlight which are the assumptions, calculation specifications and the utility of the program displaying all signal strength ($SO_2$ fluorescence) dependencies.

### *Assumptions*

- Calculated signal strength in voltage (V) is used as the amplitude to simulate the corresponding fluorescence signal. This last is the result of the convolution of a Gaussian and an exponential. The latter represents $SO_2$ fluorescence with a decay of 36 ns.
- For $SO_2$-PMT response signal, a correction to the amplitude of the convolution through the signal strength must be applied. This is due to the fact that the amplitude of a convolution is not equal to the amplitudes of the scattering or fluorescence signals. These parameters called RatioA and RatioB are constant for each concentration. They are calculated in program either.
- The simulation of the signal strength does not take into account the NO signal. In the signal simulated by the program only scattering and $SO_2$ signal are plotted. The NO signal is not included as the alfa factor correction cancels it.
- The population of the $SO_2$ ($f_i$) is assumed to be 1. All $SO_2$ molecules are in the vibrational ground state.
- Cross sectional area ($a_{\lambda 1}$) of the $\lambda_1$ laser beam (CSALB) is corrected by a parameter ($btz$, in program) which accounts for laser divergence.

### *Calculation*

- Several parameters must be used during computation. They are written in the first lines of the program. The values were taken from the literature, data sheets of devices or calculated in the program. Every parameter, its name and its units are written between the curved brackets with two * symbols next to them.

- The calculations within the program run several times for the same convolution. This is done for different purposes: displaying of the response signal, calculation of the predicted integral values of the response signal or simply for some parameter calculation such as RatioA and RatioB.
- The amplitude of scattering can be varied according the value observed at the scope. This depends as expected from the laser energy and the laser beam diameter. Normal values vary from 50 to 100 mV and program does not include its calculation.

### *Dependencies*

- Signal strength and consequently the fluorescence recorded depend mainly on the optical collection system. The capability of this was taken into account in the calculations. It is based on the solid angle calculated in the chapter 4. The reflections of the four lenses surface were taken into account (R < 1.5%).
- In program it is considered an isotropic emission of fluorescence. This means that light of $\lambda_2$ $(240 - 420\ \mathrm{nm})$, is emitted isotropically around the excitation volume.
- The signal is highly dependent on the number of photons and on the size of the laser beam.

Equation 10.4 is utilized in the following section to demonstrate the variation of the slope (sensitivity) and intercept when laser energy and scattering amplitudes are different.

## 10.4. Sensitivity

In analytical chemistry the sensibility of an instrument or method is the capacity to differentiate small variations of the substances that cause the signal. There are two factors which limit the sensibility: slope of the calibration curve and the precision of the method. This latter is discussed in chapter 10.5 below. With regard of the first, it is most common that analytical instruments have a linear dependency of response versus amount of substance, or concentration. Thus one can define in an ideal case an equation with a dependent variable $y$, and an independent variable $x$, as $y = m \cdot x$ where $m$ is the slope. However, in reality one should consider an intercept $b$, since the instrument delivers a response also in absence of substance. In our particular case scattering has the major influence onto the final value of $b$. This then gives $y = m \cdot x + b$ where $x$ is

referred to the concentration of $SO_2$. With regard of the slope it must be clarified that for equal intercepts the steeper the slope the better is the sensitivity.

Calculation of signal strength has been herein applied to study how different parameters affect the values of the slope and intercepts. The most important ones namely energy per pulse (number of photons) and cross sectional area of laser beam (CSALB), are included in the before mentioned optical pumping. Those two variables can be varied together with the concentration of $SO_2$ in order to study the linearity and the slope of a calibration. However, one problem comes out when calculations are carried out, namely the scattering. It has been mentioned (chapter 7) that scattering contributes highly to the PMT signal but no equation or way to quantify this effect can be given. It is clear that there must be a relation between laser beam cross sectional area and scattering as well as between the latter and the laser pulse energy. An increment in any of those conditions makes that scattering rise up. However, neither a theoretical equation was derived nor experimental relation was found accounting for this effect. During measurements, the scattering amplitudes (SA) with no fluorescent substance in the gas stream had values in the range from 50 to 100 mV. With a program written in Mathematica shapes of PMT signals can be simulated if the value of SA is known as well as calibration can be predicted. In fig. 10.3 four different regression lines were predicted according to different values of SA and laser energy. Figure 10.3 shows the influence of SA in the intercept whereas the laser pulse energy affects the slope. In both cases of a SA of 100 mV the integral over scattering is equal. However when different mean laser energy values are employed in calculation, slopes change notably. Thus for energies of 1000 μJ the slopes are bigger than in case of 600 μJ. The difference between these regressions is intercept value. Besides, it is interesting to notice that for a same value of SA (same intercept) the slopes varies dramatically when 600 or 1000 μJ are used.

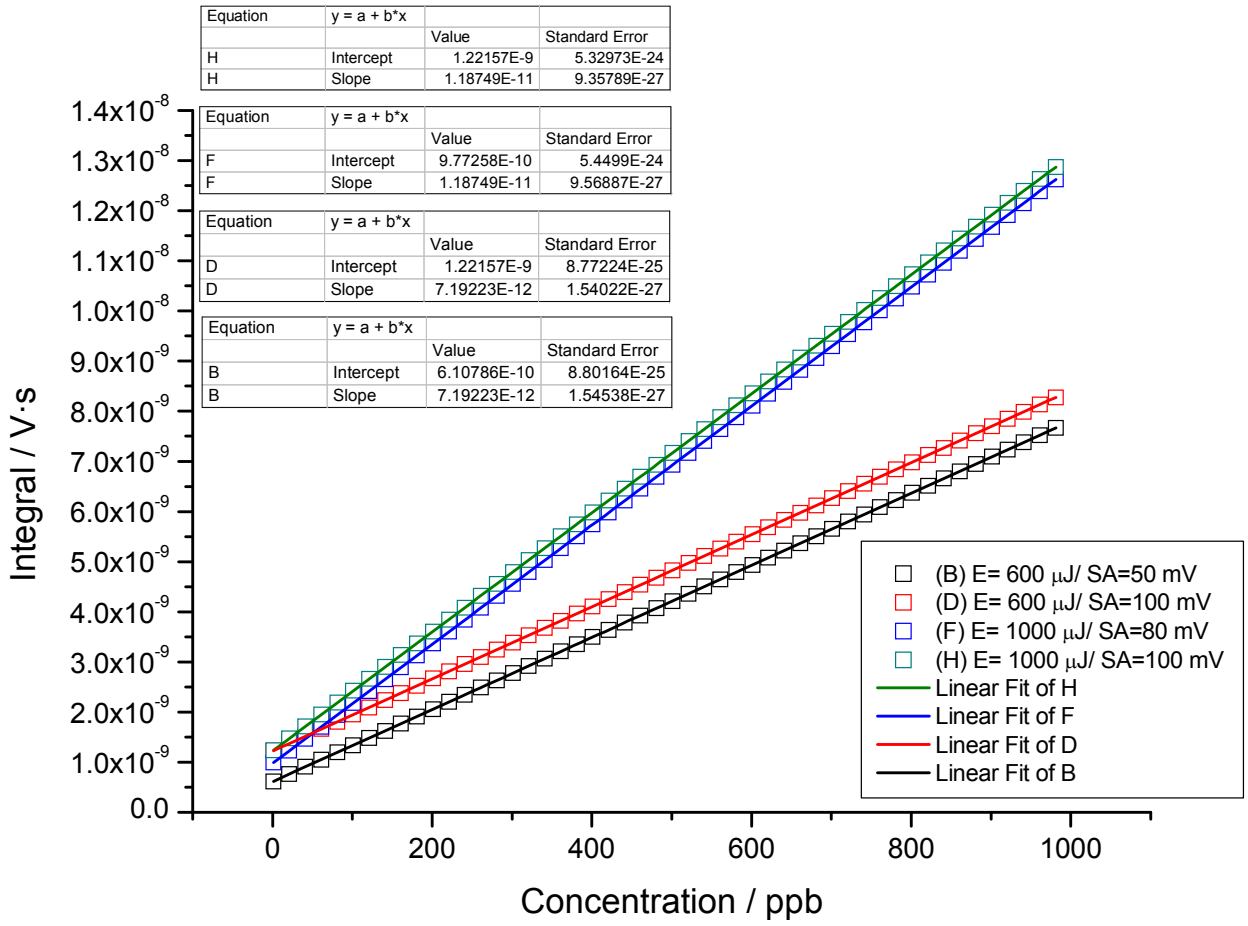


Figure 10.3. Predictions of a calibration for different scattering amplitudes and laser pulse energies.

It can be seen in figure 10.3 that predicted slopes are similar to those of measured curves shown in figures 9.3, 9.5 and 9.7. Finally figure 10.4 shows the experimental proof of what has been explained for figure 10.3. Energies of laser are displayed in figure 10.5 with a polynomial of sixth order to show the trend. In case of calibration H2S-20/06 energy is high which results in a higher SA and in consequence in a bigger intercept value. On the contrary intercept values are nearly similar for SO2 and H2S-18/06 since laser energy at the beginning of the sample was similar. The slopes increase together with the laser pulse energy. Thus the largest slope corresponding to measurement H2S-20/06 is due to a mean energy of about 30 µJ measured after the FC (500 µJ of laser pulse). The laser pulse energy at measurement SO2-18/06 was slightly higher (13 µJ, 300 µJ laser pulse) than that for measurement H2S-18/06 (10 µJ, 250 µJ laser pulse). However, this

turned out in a value of the slope which was two times bigger. This indicates how important individual calibrations before and after a serious of measurements is. Obviously, other factors besides laser scattering and laser pulse energy influence the measured signal. Frequent calibration may cope with this problem, but it will be the task of further investigations to find out these further effects.

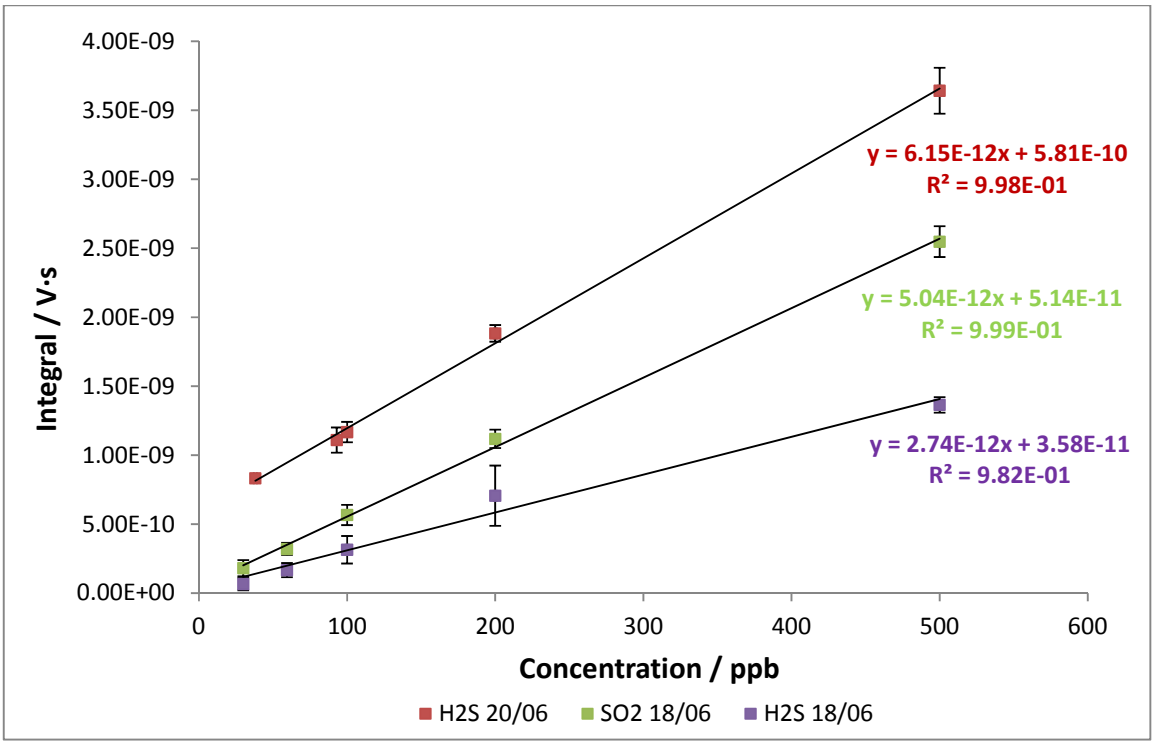


Figure 10.4 Three different calibrations where $SO_2$ and $H_2S$ have been utilized. Slope and intercept are all different due to the different scattering intensities.

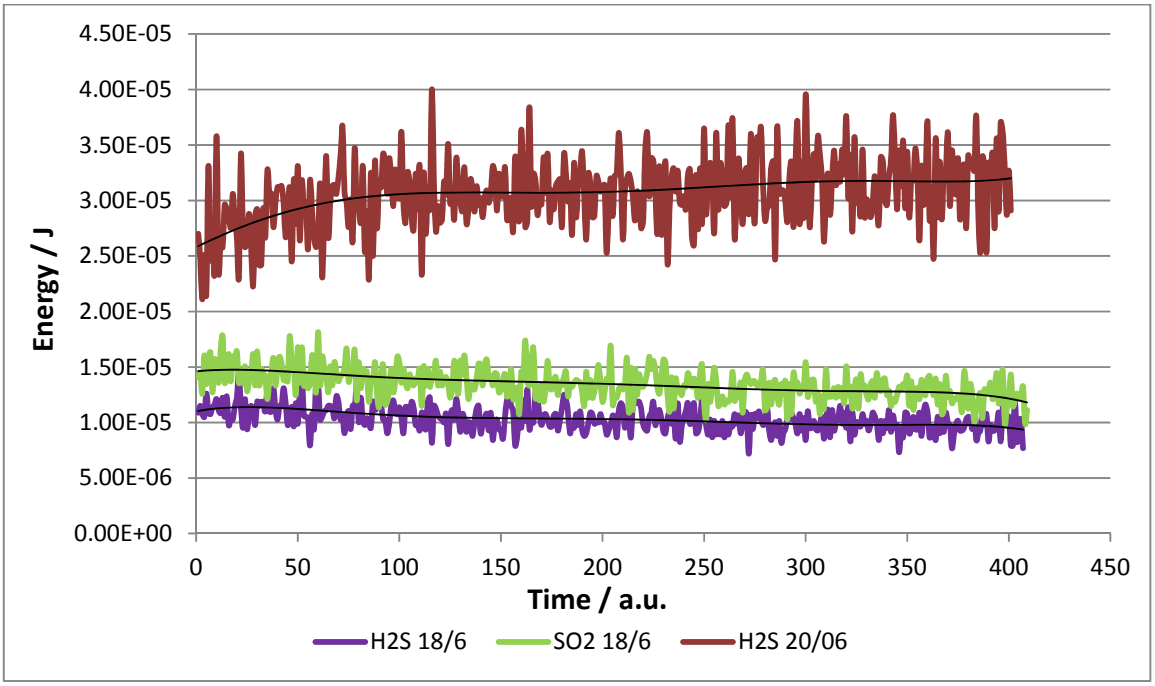


Figure 10.5. Laser pulse energy variation for the three calibrations in figure 10.4. Black line is a fit using a polynomial of 6$^{th}$ order.

## 10.5. Statistical analysis

### 10.6.1. **Correlation**

Correlation is a way to measure the relation between two variables that is to say if these are associated in a way so that one can contain information about one variable from the other. The connection between them can be estimated by calculating the covariance and the coefficient of linear correlation of Person, $r$. Since covariance depends only on the scale and it is not delimited, with its value one cannot know if two variables e.g. $x$ and $y$ are strongly or weakly associated. Therefore it is convenient to use the coefficient $r$. This coefficient has no dimension or in other words it is independent on the scale. Its value oscillates between -1 and 1. If $r$ is closer to those the correlation is strong whereas zero indicates no correlation at all. $r$ gives information only about linear relations.

### 10.6.2. **Simple linear regression**

Most of the regression problems in analytics are of type-I, which means that the experimentalist knows with high precision the values of one variable whereas he has no control about the other. Calibration is a process of this type. The most simple relation between two variables e.g. concentration and instrumental signal $(x\ and\ y)$, is linear,

$$\hat{y} = b_0 + b_1 x \tag{10.7}$$

With $b_0$ and $b_1$ being the estimations of intercept and slope respectively. When data have been adjusted to equation 10.7 a parameter named determination coefficient $r^2$, can be calculated on basis of three different variances; the one which is explained by the model, the residual one and the total one. Thus values of $r^2$ =1 means a perfect fitting to a linear model (eq. 10.7) whereas zero indicates the contrary. When the number of parameters of a chosen model is two ($b_0$ , $b_1$) $r^2$ can be written as $R^2$. The value of this is interpreted in the same way as $r^2$ : the closer its value to 1 the better the fitting and the lesser the error committed. It is calculated by the least square regression method. For every calibration shown in this work $R^2$ is given.

### 10.6.3. **Uncertainty of regression coefficients and confidence bands**

It must be noticed that uncertainty in regression coefficients are as important as $R^2$ value. These statistical errors are easily computed in any program having statistical analysis (Excel, Origin). The

errors (standard deviations) associated to parameters $b_0$ and $b_1$ are used to calculate the confidence limit. Thus one can plot for every linear regression (calibration) a confidence band. This is a region existing between hyperbolic graph which is plotted having origin at the centroid. With this, predictions of an instrumental response for a precise concentration are given (interpolation). If a prediction of concentration must be done, the uncertainty of response must be calculated in a different way. For a measured response with an associated error the steeper the slope is the smaller is the uncertainty. Figure 10.6 shows statistical analysis for calibrations plotted in figure 9.3. In this figure two different confidence bands are visible. The calibration for $SO_2$ exhibits a bigger hyperbolic region whereas the one for $H_2S$ is almost not distinguishable. This latter has an $R^2$ equal to 0.99991 and it represents an ideal calibration.

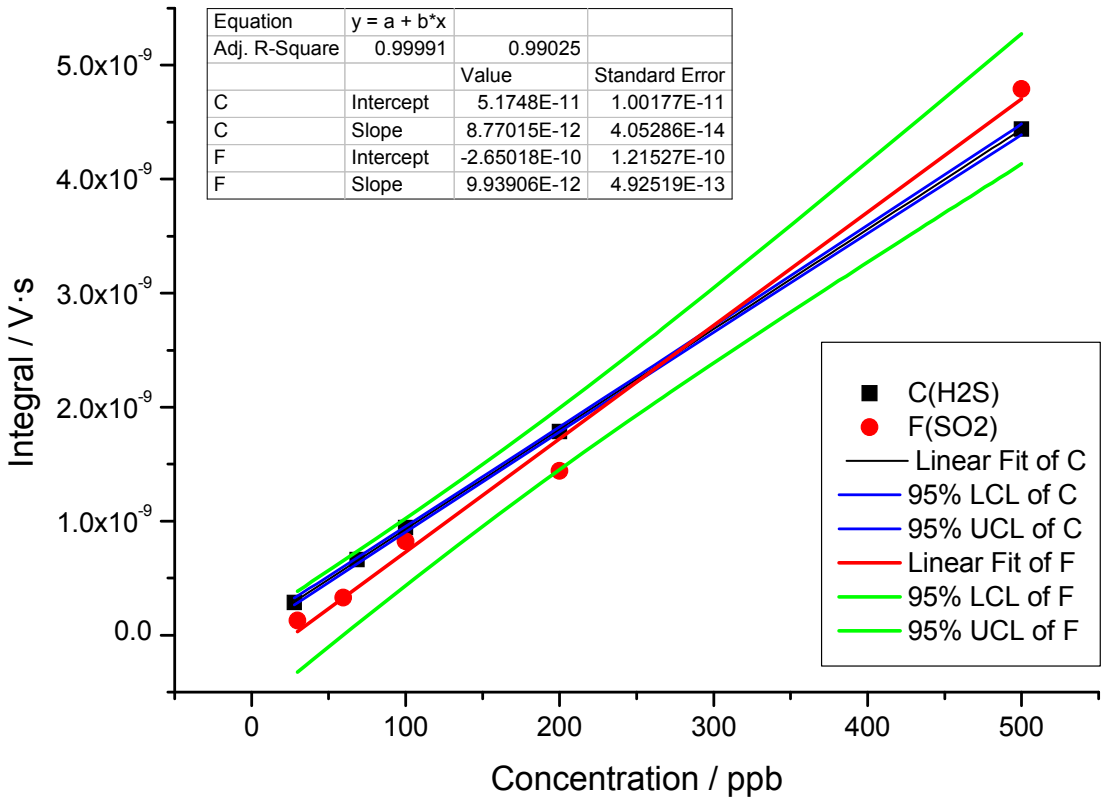


Figure 10.6. Confidence bands for calibrations made with $SO_2$ and $H_2S$ (fig. 9.2). (LCL: lower confidence limit, UCL: upper confidence limit)

Figure 10.7 shows the statistical analysis of calibrations plotted in figure 10.4. In this the $SO_2$ (18/06) calibration has the highest $R^2$ $(0.99803)$ and the lowest uncertainty for $b_0$ and $b_1$. Their confidence region is the narrowest as well. Calibration $H_2S$ has similar values for $R^2$ and $b_0$ , $b_1$ uncertainties, and similar confidence region. Slope of both are nearly equal. Nevertheless, the intercept of $SO_2$-18/06 is lower and it results in a better detection limit (section 10.5). If now, the intercept of the latter one is compared with that for $H_2S$-18/06 both are similar. However, the slope is steeper for $SO_2$-18/06 which results in a much lower error of a predicted concentration.

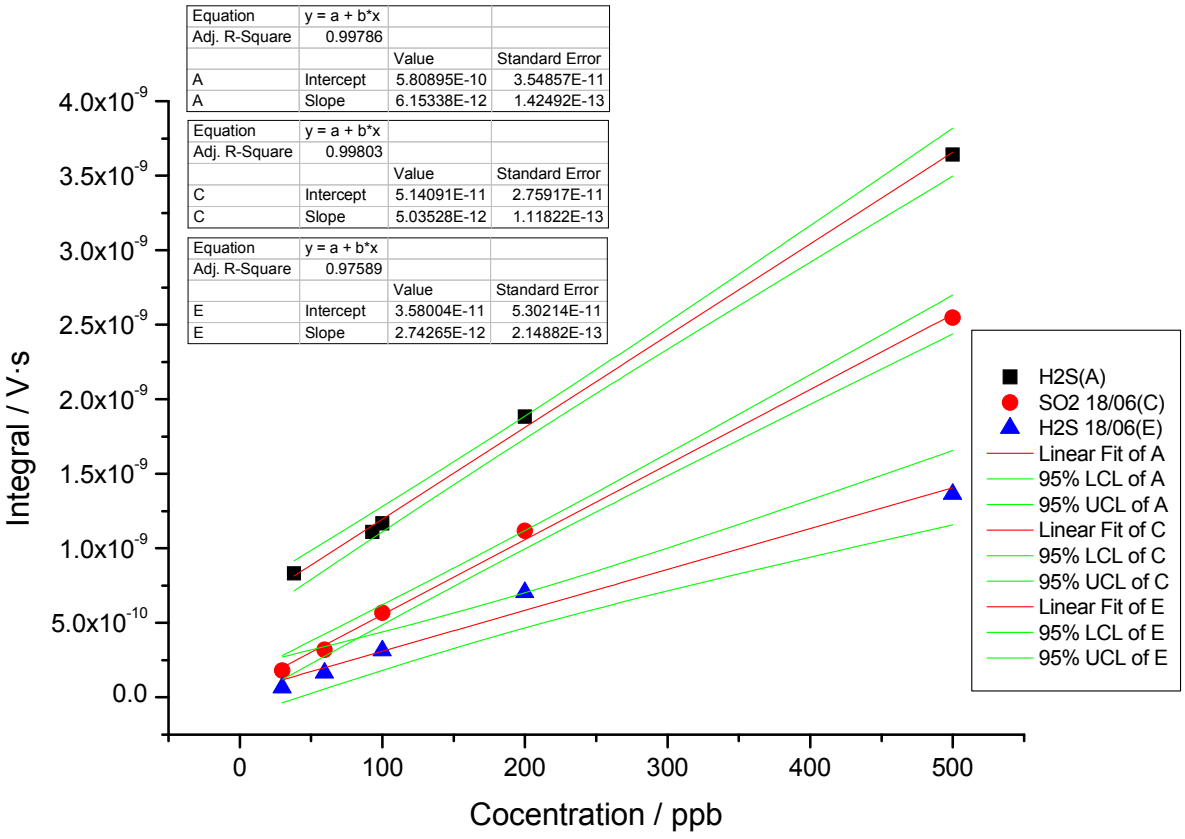


Figure 10.7. Confidence band for calibrations shown in figure 10.4.

### 10.6.4. **Prediction bands**

Prediction bands are defined as the hyperbolic region as well as for confidence bands. Those bands represent the interval of uncertainty in the response for a given concentration. This means that they give a certain range in which the instrumental response must occur. Figure 10.8 shows prediction bands (and confidence bands) for the calibration plotted in figure 9.5. In this case both

bands are nearly equal (differences are not distinguishable). This represents the perfect result, minimum uncertainty for both interpolation and response prediction, and it is considered an ideal calibration.

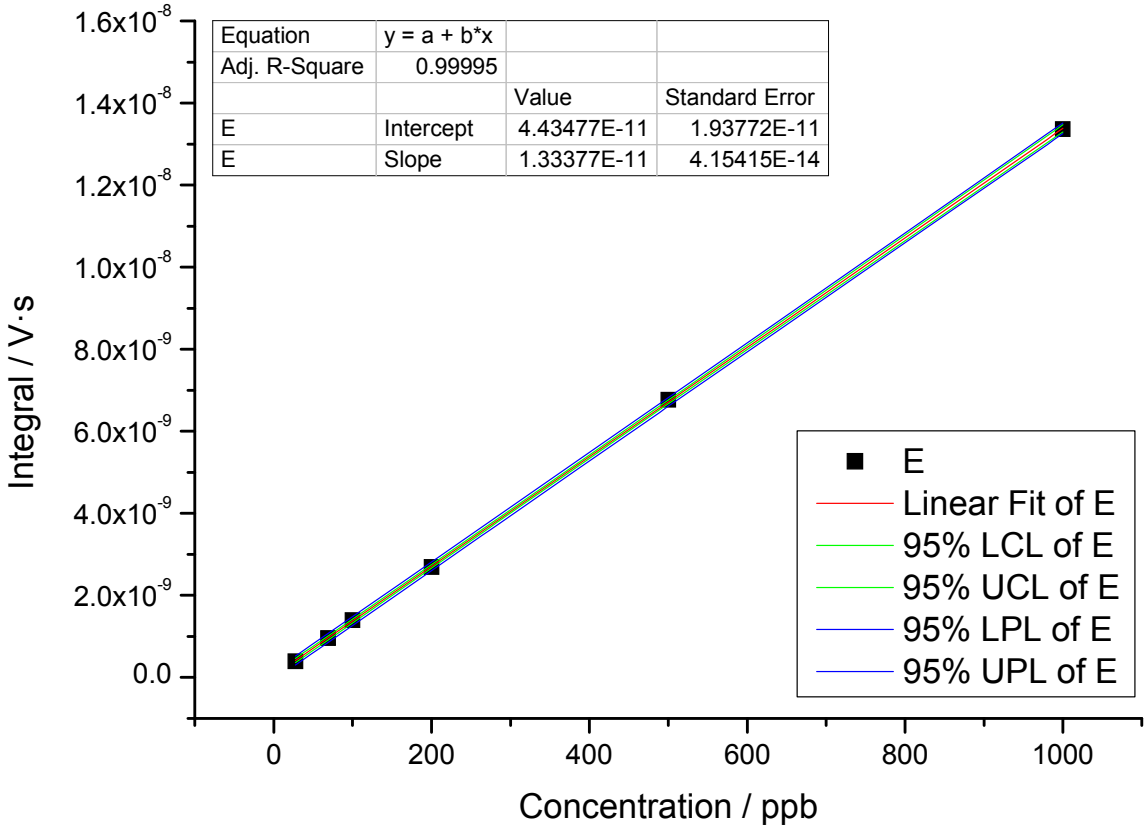


Figure 10.8 Confidence and predictions band are equal in this particular case which represent an ideal calibration. (LCL: lower confidence limit, UCL: upper confidence limit, LPL: lower prediction limit, UPL: upper prediction limit)

## 10.6. Limits of technique

Three different definition of limits can be used for every instrumental technique. The first is the decision limit and it is related to the statistical $\alpha$ error and it has been defined by IUPAC (1978), as the limit to which a signal is three times the standard deviation of a blank $s_b$,

$$LD = \frac{y_c - \bar{y}_b}{b_1} = \frac{3\, s_b}{b_1} \tag{10.8}$$

Division through the slope is made to obtain concentration units. However, this criterion does not include the probability to commit a statistical error of the type $\beta$. This leads to the use of a second limit called detection limit. It is defined by the same equation than 10.8 where the factor 3.29 is used instead of 3. The third limit used in the aim to determine the statistical quality of measurements is the quantification limit. This is defined as the concentration for which SNR is equal to 10. The SNR is calculated according to

$$\frac{S}{R} = \frac{y - \bar{y}_b}{s} \tag{10.9}$$

With $y - \bar{y}_b$ being the signal rested to the blank and $s$ is the standard deviation of a signal. Quantification limit can be estimated by $10 s_b / b_1$ if the noise does not increase to low values of signal. Calculation of all limits as well as SNR were made for the calibration plotted in figure 9.5. Table 10.1 shows the values for all.

| Conc. /ppb | Int. / V·s | Int. – blank / V·s | STD | SNR | Dec. L | Det. L |
|---|---|---|---|---|---|---|
| ***1000.00*** | *1.36E-08* | 1.336E-08 | 3.380E-10 | 39.53 | **24.44** | **26.80** |
| ***500.00*** | *6.99E-09* | 6.765E-09 | 1.882E-10 | 35.95 | | |
| ***200.00*** | *2.91E-09* | 2.689E-09 | 1.182E-10 | 22.76 | | |
| ***100.00*** | *1.62E-09* | 1.398E-09 | 4.900E-11 | 28.52 | | |
| ***68.63*** | *1.18E-09* | 9.604E-10 | 6.907E-11 | 13.90 | | |
| ***27.78*** | *6.12E-10* | 3.879E-10 | 5.607E-11 | 6.92 | | |
| ***0.00*** | 2.24E-10 | | 1.131E-10 | | | |

Table 10.1 Decision, detection and quantification limits for calibration in figure 9.5.

In table 10.1 one can see that the lowest concentration set during calibration is just a bit bigger than the detection limit 26.80 ppb. For this particular case where the standard deviation increases to low concentration, the calculation of quantification method takes into account the SNR criterion. The SNR ratio is bigger than 10 at the concentration of 68.63 ppb, but it is much lower

for 27.78. Thus quantification limit is between these two values. If a linear relation is assumed between the SNR and the concentration, the quantification limit is at 48 ppb.

## 10.7. Literature


1. J.D. Brandshaw, M.O. Morgens, D.D. Davis, *Applied Optics*, Vol. 21., No.14, 15 July1982, 2493-2500.
2. D. D. Davis *et* al., *Rev. Sci. Instrum*., 50, 1505 (1979).
3. J. Heicklen, N. Kellyand K. Partymillert 1980, Verlag Chemie International, Inc. Reviews of Chemical Intermediates 3, 315-404 (I 980).
4. W. Demtröder, Laser Spectroscopy: Experimental techniques, 4th Edition, Vol. 1, pag. 217-220, Springer 2008.
5. Y. Matsumi, H. Shigemori, K. Takahashi , *Atmospheric Environment* 39 (2005) 3177–3185.

# 11. Summary of part A

The first part (A) of the present work has been performed during two years. The main goal of this was the development, building up and testing of an apparatus capable to measure in-situ and on-line oil consumption. The initial idea was to obtain a prototype with all the characteristics necessary to be a commercial instrument. In previous works another similar set-up based on the approach of measuring laser induced fluorescence of molecular traces at rough vacuum was built and tested. Sulfur was chosen as tracer since this is contained in the oil and must not be ever added. The problem of its conversion to $SO_2$ was solved by using a glow discharge cell (GDC) which creates nonthermal plasma (NTP). With this regard the author further developed the existing GDC design by improving the security of it. The GDC can be now activated by a connection through a SHV-BNC connector. Moreover, several studies of the NTP were carried out by monitoring reaction products in a QMS. Formation of ozone ($O_3$) and reactive species such as hydroxyl (OH) or water ($H_2O$) were related to oxygen concentration. Formation of nitrogen compounds ($N_2O$, NO and $NO_2$) were related to nitrogen and oxygen concentration. Total conversion of hydrocarbons to $CO_2$ was tested. Besides reaction occurring in the complex NTP were described.

Laser induced fluorescence of $SO_2$ is used to measure the amount of converted sulfur existing in engine exhaust. The first prototype based on sulfur as tracer including a dye laser was set up by Sellmeieret al. Despite the fact that it was employed as proof of principle, the use of a dye laser had several inconveniencies e.g. difficulties of handling, content of hazardous substances (dyes) and big size. An apparatus for measuring oil consumption must of course be easy to handle, mobile, robust, compact, computer controlled and should not produce wastes (dyes). This cannot be accomplished by using a dye laser and an optical parametric oscillator (OPO) is employed instead. These lasers are normally smaller, more robust and much easier to handle. All this is indispensable to perform a set-up which can be used for non-expert technicians at engine test facilities. However, no lasers on the market delivering tunable UV radiation had the needed features. Before the beginning of this work cooperation with the laser company InnoLas Laser-GmbH- was established. The last development and optimization steps were all carried out together with the author during a whole year. The OPO laser was improved after several tests and the feedback of many experiments sent to the company. Cooperation succeeded and led to the commercialization of the first InnoLas OPO. An apparatus containing the final OPO version was fixed and herein it is named as prototype-II. This was tested in combustion engines at BMW-AG.

The highly satisfactory results convinced BMW-AG to finance an improved and more automatic apparatus. The so called prototype-III was built at TUM and transported to BMW-AG. Several $SO_2$ calibrations were recorded and gas mixture containing $SO_2$ were analyzed. Furthermore influences of water to the $SO_2$ fluorescence quenching or the $H_2SO_4$ formation were tested under the working conditions of pressure (3 mbar) and temperature (230 °C). Both effects have not been studied before. Prototype-III is fully controlled by Laptop and incorporates an internal cooling system (chiller). The prototype-III is currently being used by BMW-AG to measure oil consumption at engine test facilities.

The prototype-I (Sellmeier) worked with two different wavelengths to avoid interferences of other fluorescent molecules different than $SO_2$. It has been proven that the only molecule showing fluorescence at the excitation range is NO. Herein, the author states, recommends and proves the use of only one, namely the peak wavelength (maximum excitation). This one is much less influenced by electrical noise or flow fluctuations (increase of standard deviation). However, there is still the need to use a method to delete the interference of the NO signal onto the $SO_2$ one. Sellmeier et al. found a solution based on a double temporal integration gate of the fluorescence signal. This is possible due to different time decays of NO and $SO_2$ signals, but a factor ($\alpha$) must be used to correct the decrease of NO contribution in the second gate with respect to the first one. The author has developed a method based on mathematical simulations to calculate the value of $\alpha$. This supposes a meaningful advance in terms of speed and accuracy since the old calculation was empirically performed and based on the correction of the excitation fluorescence scan. The method described uses literature (life times) and experimental data (stray light and laser pulse length) to obtain the value of $\alpha$ with regard to the time width of the integration gates.

Finally it is worth to mention that the publication of two international papers (*LaserFocusWorld*& *Analytical Chemistry*) attracted the interest of several companies which develop, build and sell analytical instruments. Further detailed tests at motor-test facilities are planned during 2015 to evaluate the possibilities of a commercialization.

# Part B: Laser Desorption Source for Studies of Soot Formation

# 12. Introduction to laser desorption time of flight mass spectrometry

## 12.1. Laser ablation (LA), laser desorption (LD) and MALDI

Investigations of metals, organic compounds or biomolecules in gas phase have acquired an increasingly importance in the last decades. There are several techniques which can be used to introduce such samples in gas phase. It is not the goal of this work to deeply discuss and differentiate among all of them. However, three of them which work using lasers and must be shortly presented.

### 12.2.1. **Laser ablation**

This is a vaporization technique where a continuous or a pulsed laser hits a raw sample (metal, rock, etc.) and brings it into gas phase. The result is normally the creation of a plasma plume at first and then the expansion of neutrals, ions or bare molecules (also fragments) from the material surface. In the case of direct ablation on metals both cations and anions are formed. When molecules are ablated the interest is often focused in the molecular ion, that is to say the bare molecule. Depending on the fluence (Energy/area) neutral fragments (radicals) are produced. The ionization of them is performed normally via electron impact (EI) or by using laser radiation based on multiphoton ionization (MPI) or resonance enhanced multiphoton ionization (REMPI) schemes.

The very first laser ablation studies carried out by R.E. Smalley (1982) [1-6] and Bondybey (1981) [7-11] were focused in metallic clusters. Besides, in 1985 Smalley and al. shot a sample of char coal with the second harmonic of a Nd:YAG laser (5ns, 10-30 mJ per pulse). Within the composition of the vaporized complex mixture, the fullerene C60 was found [15]. This was the first time that C60 was created and measured in a laboratory. The importance of this experiment is based on the fact that within an ablation processes new molecular structures can be obtained to be studied afterwards. R.E. Samalley, H.W. Kroto and R.F. Curl to obtained in 1996 the Nobel Prize in chemistry. Another exceptional instance of laser ablation was carried out by R. Zenobi el al. (1989) [17] to analyze the content of PAH in the Allende meteorite. The study demonstrated the high capability of laser desorption-postionization techniques, to detect several compounds, in a concentration range as low as 0.05 ppm. This study is especially interesting from three points of view; it was only necessary a low amount of sample, there was no need to perform pre-treatment and it demonstrated the feasibility of carrying on spatial analysis, due to the small size of the laser

spot (focusing). Finally gas metallic clusters and studies of their activity in reactions are becoming indispensable. The purpose of such researches are, both to decipher physic-chemical processes and to develop better catalyzers capable of increase reaction yields.

### 12.2.2. **Laser desorption**

In laser desorption the sample is deposited on a surface or substrate which is different in nature than the sample. Substrate has the only goal of holding the sample. Sometimes and depending on the fluencies and wavelengths, the substrate can be involved in the desorption process. The mechanisms are complicated and theoretically difficult to describe. However, it is worth to mention that different substrates can bind or interact more or less with the sample depending on its composition, and that they can be involved in photochemical and heat transfer processes.

At the end of the 80´s H.R. Wendt et al. begun to develop new desorption sources [18] and to study the behavior of the molecular concentration profile within the jet, after molecules were vaporized. Other groups all around the world investigated vaporized molecules in the gas phase. Several sorts of laser desorption sources were developed and applied to molecules with biological importance. With this regard it is interesting the study of angiotensine I and chloropyll carried out by U. Boesl and al. (1986) [16]. Fragmentation patterns of the two molecules were studied for different ionization peak intensity (soft $10^6$ W/cm$^2$ and hard $10^7$ W/cm$^2$) through a scheme based on resonance enhanced multiphoton ionization (REMPI) and mass detection via reflectron time of flight mass spectrometry (Re-TOF).

At the beginning of the 90´s again Wendt together with G. Meijer, M.S. De Vries and H.E. Hunziker [19] designed a new desorption source. The new design consisted of a graphite plate which is held right below the nozzle of a pulsed valve. On the upper part of it, the sample is deposited. Then, the laser is shot from above and after that the holder is moved to the left or the right. This facilitates that laser hits new fresh sample every shot. This sampling rod differs from the one used by Smalley which was a rotating cylinder of small dimensions located just aside the nozzle. However, the greatest success of Meijer et al. and D.H. Levy were the applications of the LD techniques in combination with jet-cooling and high resolution spectroscopy (tunable lasers).

Many groups have are still applying LD-TOF-MS with spectroscopy (UV/UV, UV/IR, etc) nowadays in combination with quantum calculations. Nucleobases and their hydrates (water clusters) have been probed in gas phase by H. Saigusa [20, 21]. During his researches a channel-type desorption source was designed and built. In this sort of device the molecules are desorbed from a sampling

rod sitting next to the nozzle. Then the molecules are ejected in a channel which is in front of the nozzle. This design was compared with one of the before mentioned sources, called open-type (Meijer et al.). It was demonstrated that in the channel-type the formation of both guanine-water and guanine-guanine cluster was more probable. The long-time stability and low shot-to-shot fluctuation of the ion intensity were, in the case of a channel-type source, much better. Furthermore, the SNR during wavelengths scans was the best in the channel-type as well.

Studies with the aim of elucidating the conformational structure of biomolecules have shed light into interesting chemical effects. Analysis of conformers or optical properties of thermolabile molecules (sugars, amino acids, medicaments) can be done with laser desorption. Gas phase studies normally shed light about non-covalent interplays (Van der Waals). Furthermore, interesting biochemical processes such the anomeric effect in sugars as well as the turns of secondary structure in proteins can be observed.

M. Mons [22] has investigated chains of amino-acids up to five units. The UV/IR (infrared ion depletion spectroscopy, IRIDS) spectra recorded and their comparison with quantum calculations elucidated the formation of a $\beta$ turn in the gas phase. This is one of the numerous bonds that occurred in proteins and it is formed by the interaction of the end residues in a chain of three amino acids [23]. This has been the first demonstration of the transit from primary to secondary structure in poly amino acid chains. For such a purpose W. Chin et al. [24] developed a simple but useful laser-desorption source based on laser light coupled into an optical fiber.

In the same way, sugars can be vaporized and brought into gas phase. E. Cocinero et al. has demonstrated recently the interesting and long unknown anomeric effect in the solvent-free environment glucose [25]. This abundant and one of the most consumed sugars worldwide was brought into gas phase via laser-desorption. IR spectra (IRISD) of a part of finger print region (3300-3700 $cm^{-1}$) were recorded for $\alpha$ and $\beta$ forms. The stretching transitions corresponding to OH and NH bonds were shifted for the $\alpha$ with regard to the $\beta$ (O-H to the red and N-H to the blue). N. Mayorkas et al. [26] elucidated a few time later this same effect for the mannose in the presence of water.

### 12.2.3. **Soft laser desorption (SLD) or matrix assisted laser desorption ionization (MALDI)**

Again during the 80´s another technique based on laser desorption was developed. This technique employs a matrix where the sample is embedded. The laser is shot onto the matrix containing the

sample. This is desorbed and both positive and negative ion are formed during the desorption process. Desorption is much softer than the normal desorption and this is because the matrix, commonly an organic molecule, absorbs part of the radiation (soft laser desorption, SLD). The ionization of the compound within the plasma plume makes feasible the analysis via mass/charge ratio (mass spectrometry). This technique is known as matrix assisted laser desorption ionization. It is a highly developed technique and during long time it has been utilized in a wide range of applications. Biomolecules from medium ($10^3$ Da) to ultra-high ($10^5$ Da) molecular weights are analyzed with it. Nowadays composition of cell and tissues are feasible to be studied in detail and imaging technique is currently one of the most powerful tools.

MALDI was firstly discovered by D. Bachmann, F. Hillenkamp and M. Karas, 1984) [12]. It had a huge group of contributors and developers. On the contrary SLD was developed by K. Tanakawa (1987, [14]) who received the novel prize in chemistry in 2002.

## 12.2. Application of the technique

Laser desorption was utilized during the period of this work with the aim to investigate soot. Generation, structure and composition of the soot produced in combustion engine or processes are still not fully understood. In addition, analysis of soot concerning for instance distribution of particle size, type of adsorbed organic molecules, sulfur content etc. may deliver information about the combustion process of fuel as well as of motor oil. For this reason a laser desorption time of flight mass spectrometer was set up and desorption of decacyclene ($C_{36}H_{18}$) [27] as a model system was carried out. This is a relevant polyaromatic hydrocarbon (PAH) which allows to study the different situations depending on the desorption conditions [28]. Other possibilities would be to study the aerosols coming out of the engine exhaust. With this regard it can be studied the formation of clusters derived from molecules containing sulfur and those which have a main carbonaceous structure (decacyclene, char coal and soot). The final goal of this part of the work was to develop a first prototype of set-up which is able to analyze soot from the exhaust of combustion engines. The technique of laser desorption combined with secondary laser ionization and time-of-flight mass spectrometry has been chosen to achieve fast analysis without the necessity of chemical pretreatment. The method presented here may even be the basis for a short-term (in the minute time scale) and thus quasi-online soot analysis.

## 12.3. Literature


1. T. G. Dietz, M. A. Duncan, D. E. Powers and R. E. Smalley, *J. Chem. Phys.* 74, 6511 (1981).
2. D. E. Powers, S. G. Hansen, M. E. Geusic, A. C. Puiu, J. B. Hopkins, T. G. Dietz, M. A. Duncan, P. R. R. Langridge-Smith and R. E. Smalley, *J. Phys. Chem.* 86 2556 (1982).
3. D. L. Michalopoulos, B. E. Geusic, S. G. Hansen, D. E. Powers and R. E. Smalley, *J. Phys. Chem.* 86 3914 (1982).
4. D.E. Powers, S. G. Hansen, M. E. Geusic, D. L. Michalopoulos and R. E. Smalley, *J. Chem. Phys*. 78 2866 (1983).
5. J. B. Hopkins, P. R. R. Langridge-Smith, M. D. Morse and R. E. Smalley, *J. Chem. Phys.* 78, 1627 (1983).
6. R. E. Smalley, *Laser Chem.* 1983, Vol. 2, pp. 167-184.
7. V. E. Bondybey and J. H. English, *J. Chem. Phys.* 74, 6978 (1981).
8. V. E. Bondybey and J. H. English, *J. Chem. Phys.* 76, 2165 (1982).
9. V. E. Bondybey, *J. Chem. Phys.* 77, 3771 (1982).
10. V. E. Bondybey, *J. Phys. Chem.* $6, 3396 (1982).
11. M. Heaven, T. A. Miller, J. H. English and V. E. Bondybey, *Chem. Phys. Lett*.91, 251 (1982).
12. Karas, M.; Bachmann, D.; Hillenkamp, F. (1985). *Anal. Chem.*57 (14): 2935–9.
13. K. Tanaka, K H. Waki, Y. Ido, S. Akita, Y. Yoshida, T. Yoshida, *Rapid Commun Mass Spectrom* 2 Volume 2, Issue 8, pages 151–153, August 1988
14. http://www.nobelprize.org/nobel_prizes/chemistry/laureates/2002/index.html.
15. H.W. Kroto, J. R. Heath, S. C. O'Brien, R. F. Curl & R. E. Smalley, *Nature* 318, 162-163 (1985)
16. U. Boesl, J.Grotemeyer, K. Walter, E.W. Schlag, *Analytical Instrumentation*, 16(1), 151-171 (1987).
17. R. Zenobi, J. M. Philippoz, P.R. Buseck, and R. N. Zare, *Science* 246, 1026-1029 (1989).
18. Arrowsmith, M. S. de Vries, H. E. Hunziker, and H. R. Wendt, IBM *Research AppL Phys. B* 46, i65-173 (1988).
19. G. Meijer, M.S. De Vries and H.E. Hunziker, H.R. Wendt, *Appl. Phys.* B51, 395 (1990).
20. H. Saigusa, A. Tomioka, T. Katayama, E. Iwase, *Chemical Physics Letters* 418 (2006) 119–125.
21. Hiroyuki Saigusa, *Journal of Photochemistry and Photobiology C: Photochemistry Reviews* 7 (2006) 197–210.

22. M. Mons, I.Dimicoli, F.Piuzzi, Chapter 13, M. K. Shukla, J. Leszczynski (eds.), *Radiation Induced Molecular Phenomena in Nucleic Acids*, 343–367.
23. W. Chin,I. Compagnon,J. P. Dognon,C. Canuel,F. Piuzzi,I. Dimicoli,G. von Helden,G. Meijer,M. Mons , *J. Am. Chem. Soc.*, 2005, 127 (5), pp 1388–1389.
24. F.Piuzzi, I. Dimicoli, M. Mons, B. Tardivel, Q. Zhao, *Chemical Physics Letters* 320 (2000), 282–288.
25. Emilio J. Cocinero, Pierre Çarçabal, Timothy D. Vaden, John P. Simons & Benjamin G. Davis, *Nature*, Vol 469, 6 January 2011 (76-79).
26. N. Mayorkas, S. Rudi, B. G. Davis and J. P. Simons, *Chem. Sci.*, 2011, 2, 1128–1134
27. http://webbook.nist.gov/cgi/cbook.cgi?Formula=c36h18&NoIon=on&Units=SI.
28. H. Böll, P. Püffell, C. Weickhardt, U. Boesl, *American Institure of Physics*, 1995, 68-71.

# 13. Experimental set-up

## 13.1. Time of flight mass spectrometer: Theory

### 13.1.1. **Linear time of flight mass spectrometer**

Separation of ions according to their mass charge ratio (m/z) has been applied over almost a century. Several different set-ups have been designed and fixed with this purpose, and an uncountable number of researches, with almost infinite applications, have been performed. However, the fundament and the basis for all it is as simple as the application of an electrostatic field to a charged particle (atom or molecule) to accelerate it into a field free region (drift region), and to detect it at the end. Thus, the charged particle which has in origin a certain potential energy gains a velocity which can be defined by the electrostatic potential (U). According to this we can derivate the relation of the velocity or more useful the time (t), with regard of the m/z ratio. (eq. 13.1)

$$z \cdot U = \frac{1}{2}\, m \cdot v^2 \;\rightarrow\; t = \sqrt{\frac{c^2}{2U} \cdot \frac{m}{z}} \tag{13.1}$$

where c is the space of the so called drift region and z is the charge of the molecule. Equation 13.1 defines the dependency of the flight time versus the m/z ratio. The electrostatic potential U, can include one or two contributions depending on the sort of ion source. Thus, we can talk about one or two step ion sources. In the first case only one repulsion region is utilized, and in the second one, an extra acceleration is given to the molecule. The space existing in the TOF after the ground plate (c, in fig. 13.1) is called the field free region. No potential is applied in this region and the molecule only has speed due to the previous acceleration. The ion source built during this work was of the second type and it is sketched in figure 13.1.

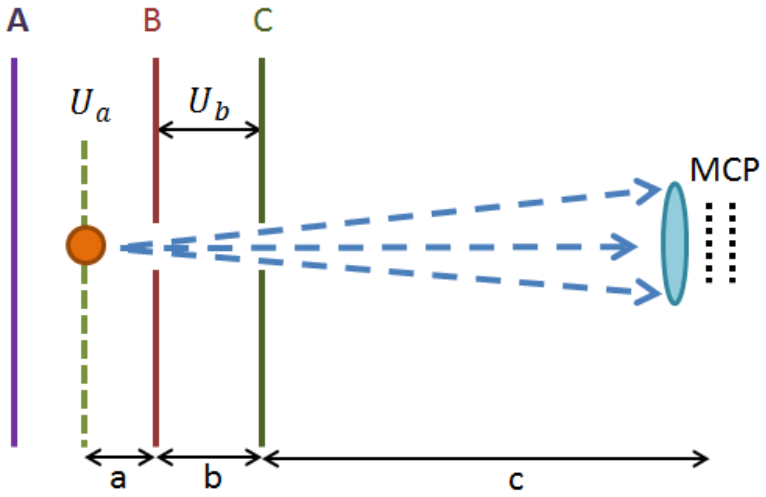


Figure 13.1. Scheme of a time of flight mass spectrometer based on a two steps ion source. A is the repeller plate (ionization region), B is the accelerator plate (extraction region), C is the grounding and MCP is the ion detector (multichannel plate).

Thus, one can define U according to $U = U_a + U_b$ , where $U_a$ is the potential where the molecule is ionized within the acceleration step, and $U_b$ is the one which is responsible of the secondary acceleration. The following distances are of importance: the distance $a$ between the ion and the attracting electrode B, the distance $b$ (= 1 cm) between electrode B and grounded electrode C, and $c$ is the distance between this last and the detector $(58.6\ cm)$. Using these numbers one may calculate the conditions (i.e. ratio of $U_a$ to $U_b$) where so-called first and/or second order focusing occurs. That means a compression of the ion clouds of one mass at the surface of the detector. This results in optimum mass resolution. First order focusing is part of the so-called Wiley-McLaren approach for time-of-flight mass analyzers [1]. Equations 13.2 and 13.3 are valid for two-order focusing.

$$U_a = U\ \frac{2c+2b}{3c} \tag{13.2}$$

and

$$a = \frac{c-2b}{2c+2b}\left\{b + c\ \left(\frac{c-2b}{3c}\right)^{\frac{3}{2}}\right\} \tag{13.3}$$

For the most usual case $b << c$ equation 13.3 results in: $c\ \approx 10.5 \cdot a$. Second-order space focusing mainly plays a role for high-sophisticated so-called reflectron time of flight (Re-TOF) instruments [2]. For usual linear time-of-flight analyzers (with $a$ of about 1 cm) this would allow only very short

drift regions $c$. This results in small separation times and therefore resolution of neighbored masses. The time of flight spectrometer built during this work accomplishes the first order space focusing. Equation 13.4 is valid for first order space focusing ($R = U/U_a$) and is employed to calculate the potentials $U_a$ and $U_b$. In table 1 those potential are shown for three different a values (1.5, 1.65 and 1.8) and b equal to 1.

$$c = 2R^{\frac{3}{2}}\left(a - \frac{b}{R+\sqrt{R}}\right) \tag{2.4}$$

| a / cm | c / cm | Accelerator | Repeller | Flight time / µs |
|---|---|---|---|---|
| 1.5 | 58.6 | 1736.3 | 2087.9 | 23.3 |
| 1.5 | 58.6 | 1910.0 | 2296.7 | 22.3 |
| 1.5 | 58.6 | 2083.6 | 2505.5 | 21.3 |
| 1.5 | 58.6 | 2257.2 | 2714.3 | 20.5 |
| 1.65 | 58.6 | 1546.7 | 1876.8 | 24.8 |
| 1.65 | 58.6 | 1718.5 | 2085.3 | 23.5 |
| 1.65 | 58.6 | 1890.4 | 2293.8 | 22.4 |
| 1.65 | 58.6 | 2062.2 | 2502.4 | 21.5 |
| 1.65 | 58.6 | 2234.1 | 2710.9 | 20.6 |
| 1.8 | 58.6 | 1531.1 | 1874.7 | 25.0 |
| 1.8 | 58.6 | 1701.3 | 2083.0 | 23.7 |
| 1.8 | 58.6 | 1871.4 | 2291.3 | 22.6 |
| 1.8 | 58.6 | 2041.5 | 2499.6 | 21.6 |
| 1.8 | 58.6 | 2211.7 | 2707.9 | 20.8 |
| 1.8 | 58.6 | 2381.8 | 2916.2 | 20.0 |

Table 13.1. Exemplary values of the accelerator and repeller plate potentials for different ionization regions. It is included the flight time for the decacyclene (450 amu).

To calculate the total flight time (table 13.1) one should consider the flight times in the ionization, acceleration and field free (drift) regions. Those are in this order the three sums written in equation 13.5,

$$t_{TOTAL} = a \cdot 2 \cdot C \cdot \sqrt{\frac{M}{U_a}} + 2 \cdot C \cdot \left(\sqrt{U} - \sqrt{U_a}\right) \cdot \sqrt{M} \cdot \frac{a}{U_a} + c \cdot C \cdot \sqrt{\frac{M}{U}} [=]\ \mu s \tag{13.5}$$

where $C$ is a constant equal to 0.72 $\mu s \cdot cm^{-1} \cdot V^{0.5}$. To know which mass corresponds to what flight time (detected in a scope), a calibration is needed. If the masses of two signals (peaks) observed on a scope, the following equation can be applied

$$m = K \cdot (t_{TOTAL} - \mathrm{t_0})^2 \; [=] \; amu \tag{13.6}$$

This is equivalent to eq. 13.1 and describes a quadratic relation between the mass and time. In the equation $K$ is a factor which includes several parameters (a, b, c, $U_a$, $U_b$, etc) and $\mathrm{t_0}$ is a time constant which accounts for scope trigger and electronic delays in cables, etc.

The resolution of a TOF-MS is defined as the smallest difference $(\Delta \mathrm{m/z})$ that can be separated for a given $m/z$ is equal to $R = \frac{\mathrm{m}}{\Delta \mathrm{m}} = \frac{\mathrm{m/z}}{\Delta \mathrm{m/z}}$. The separation between neighboring peaks is called resolving power and it is obtained from the peak width at a specific percentage of the peak height as a function of the mass.

### 13.1.2. **Einzel lens**

The charged molecules created in the ionization region (AB space in fig. 13.1) can follow several trajectories along the field free region. If this effect is not compensated the ions will spread out more and more during their flight. Such a behavior results in a decrease of the ion signal. To avoid this problem the so-called einzel lens device can be utilized. It consists of an array of three cylindrical electrodes or round plates with an aperture in the middle. The main goal of such a set of metal electrodes is to focus the ions. The electrostatic potential applied in them is symmetric, which makes that the initial and final energy of the ions be the same. The energy only changes within the einzel lens the central electrode of which can be set either at positive or at negative potential. Figure 13.2 depicts a normal einzel lens and shows qualitatively the effect that ions suffer when they travel through it.

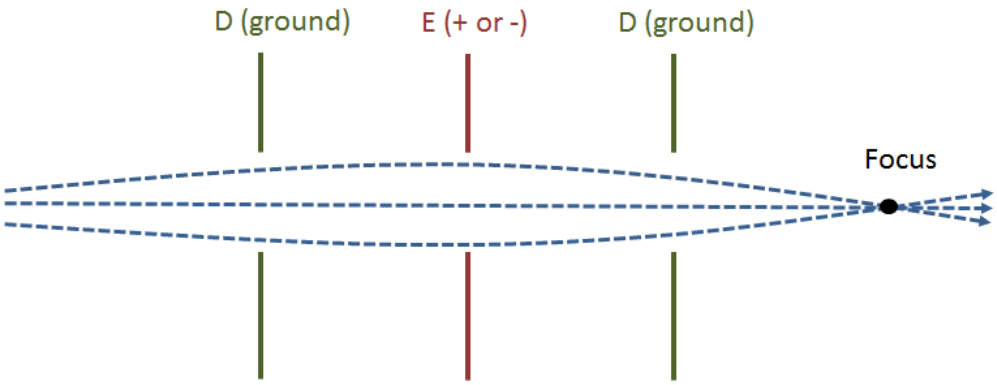


Figure 13.2. Einzel lens set showing the trajectories of the ions passing through, and the focal point.

An einzel lens arrangement contributes to increase the number of ions that reach the detector, and due to this the signals on the scope rises (fig. 13.3).

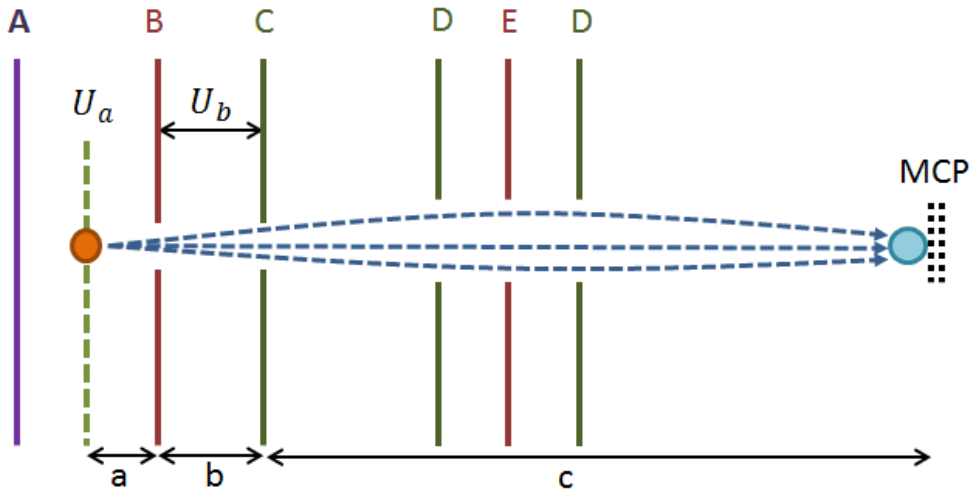


Figure 13.3. Trajectory of the ions corrected by an einzel lens set (D, E, D) and focused onto the detector (MCP).

## 13.2. Time of flight mass spectrometer: Experiment

The time of flight mass spectrometer consisted in a tube of 85 cm long. When sample is introduced into the ion source via pulsed valve or desorption the pressure in the tube increases. For this reason and at a distance of 23 cm from one extreme, a circular plate with a hole (6 cm

diameter) was fixed. This plate separates the ion source from the field free region and allows the creation of a differential vacuum between the ion source and the drift region. The ion source region is pumped by a turbo pump whereas in the field free region another one is set up. At the end of the tube a flange containing a MCP detector is fixed. Two CF flanges of where viewports can be screwed are orthogonally set with regard. They are welded to a distance of 9 cm from the initial part of the tube. They windows set onto them allow both desorption and the ionization laser to pass through. Besides, perpendicular to the windows and another CF flange exists where the manipulator and the sampling rod are located. Two more CF flanges are welded to install pressure gauges (full range) right above the turbo pups (CF). Copper gaskets were utilized in all the CF connections (viewport, pressure gauge, turbo pumps, et cetera).

A new ion source was entirely designed and constructed. This incorporates a pulsed valve and a desorption source. The first one is essential to create a pulsed gas beam which serves to transport the desorbed molecules into the ion source and to supply room temperature equilibrium. The total size of it is about 21.5 cm large and 5 cm of diameter. It can be seen with detail in figure 13.4.

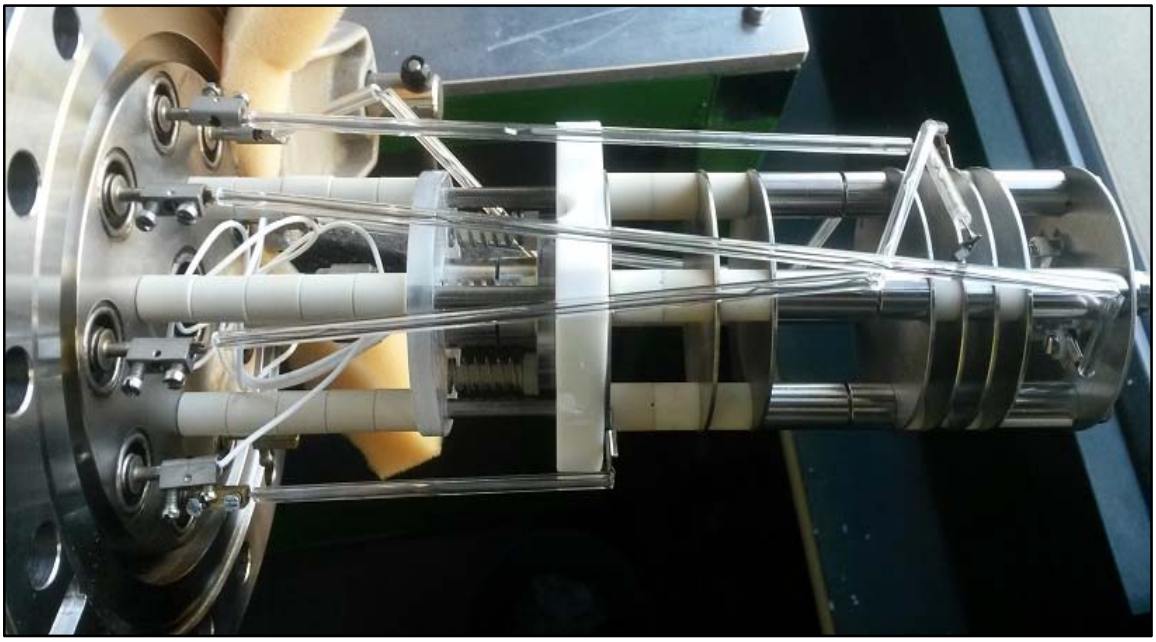

Figure 13.4. Compact ion source with a Parker valve, a Teflon® block where desorption takes place, repeller, accelerator plate, and einzel lens.

Figure 3.15 shows a schematic view of the ion source. The valve-gas pipe connection was designed in a way that the distance between valve and the body containing a nozzle can be adjusted from outside. An o-ring was set between and a CF flange. A simple movement to the left or the right turns only the valve without affecting to the plates of the ion source. This is because the nozzle is fixed to a Teflon® piece and this to the ion source as well. The slot between valve and nozzle affects the pulsing of the valve, and in consequence the pressure reached in the chamber. Although the optimization of such distance is often made before setting the ion source into vacuum, an external fine adjustment is favorable. This can be done in the current system during monitoring pressure and ion signal. The pipe for the carrier gas (He, Ne, Ar) passes through a CF flange and it is isolated from inside with an o-ring or a copper gasket (fig.13.5).

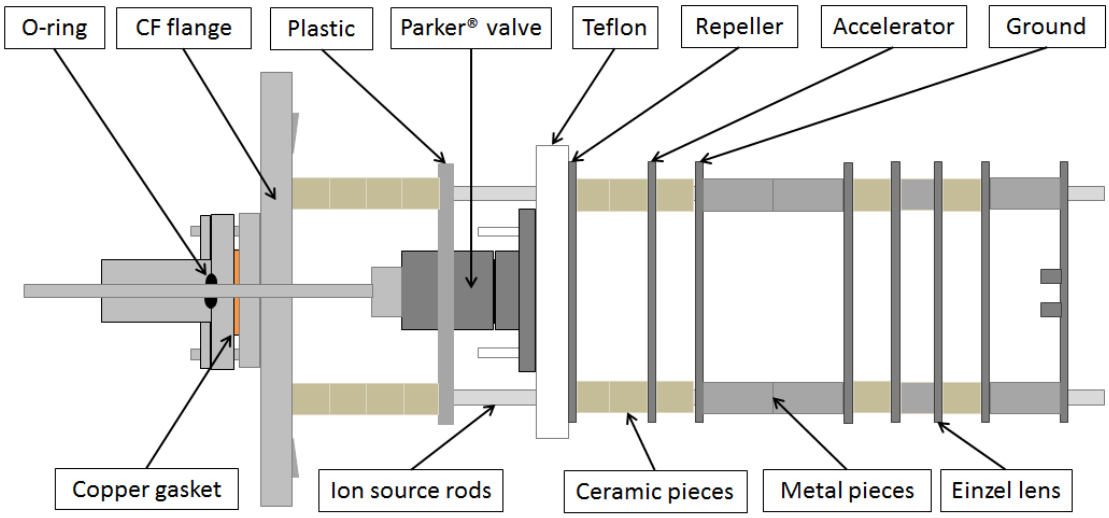


Figure 13.5. Sketch of the ion source.

The source includes a Teflon® piece right in front of the nozzle body which main goal is to hold the sampling rod and to contain a lens (section 13.1.1).

The CF flange contains nine welded SHV feedthroughs which are necessary for connect both valve and metal plates of the ion source to power supplies. An Ultra-Torr fitting (Swagelok®) was welded next to the feedthroughs and a hole was drilled through the CF flange. The idea behind this is the possibility to carry out laser desorption via an optical fiber.

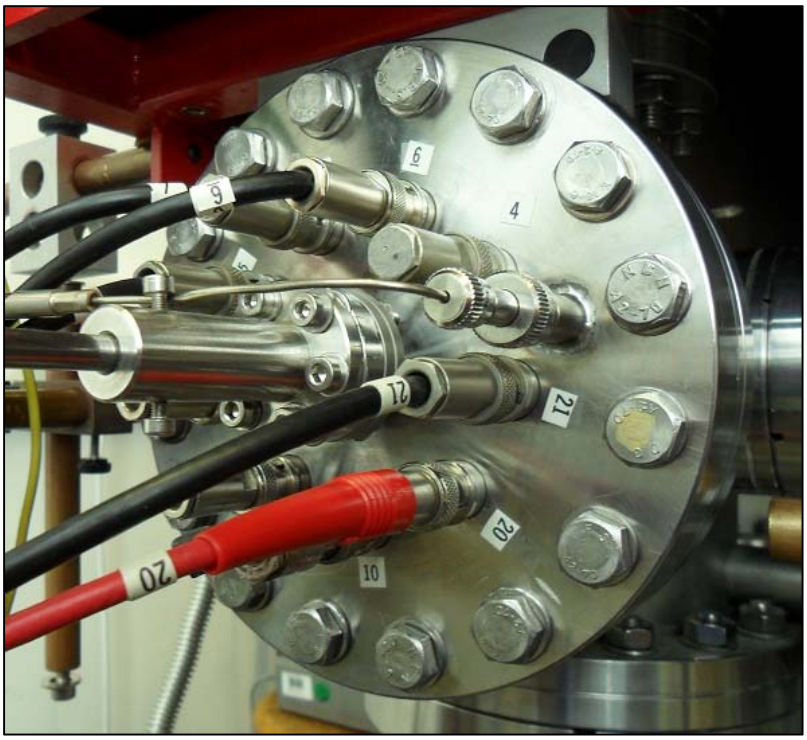


Figure 13.3. External view of the ion source.

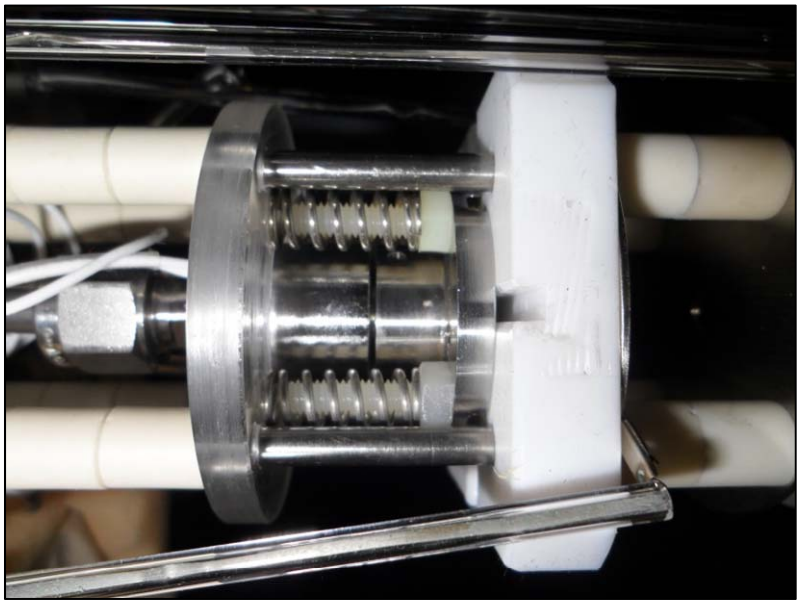

Figure 13.4. Detail of the Parker® valve and the Teflon® block.

## 13.3. Desorption source

In the following the two main parts of the laser desorption source are explained. The main characteristic of the source is that there exists a channel in front of the nozzle which guides the gas beam. This channel is drilled in a piece of Teflon® whose aim is to hold sample as well as to contain a cylindrical lens to focus the desorption laser. The nozzle body is screwed to this Teflon® block. This sort of desorption source is known as channel-type [5]. In tis vaporized molecules are led into the chamber due to a gas pulse (80-150 μs) emitted from the pulsed valve. The sample is deposited on a tip with several slots (fig. 13.9.). This tip is introduced into the chamber, and slit into the Teflon® block from the upper CF flange. The sampling rod with the tip screwed at the end is easily introduced into the vacuum chamber. This is possible due to the manipulator designed (section 13.5.2). Furthermore, it is necessary a short time to create the necessary vacuum opening the valve which connect the manipulator with the ion source of the TOF. A small rotatory pump is employed for pumping the volume of manipulator. Total operation time including introduction of sample does not overcome 15 min. This enables a quick change and the measurement of several samples in a short time without the need to break the high vacuum. Other groups have designed similar sorts of blocks with the sample (cylindrical) rotated and translated by an electrical motor [3]. The main advantage of such devices is that desorption laser hits every shot a new fresh and intact slot of sample. This contributes to the signal stability as well as to the duration of the sample over a long period of measurements e.g. wavelength scans.

### 13.3.1. **Teflon block**

Laser desorption devices are based on a three axes configuration. The laser for desorption, the pulsed valve and the sample are set up orthogonal to each other. The laser comes into the chamber from one side and hits the sample located in a perpendicular position to it. After some time the pulsed valve, fixed perpendicular to both of them, blows desorbed molecules into the chamber. For this aim a carrier gas is utilized (Helium, Neon, Argon). To hold the sampling rod and a focusing lens, a compact block was redesigned and attached to the valve nozzle (fig. 13.5).

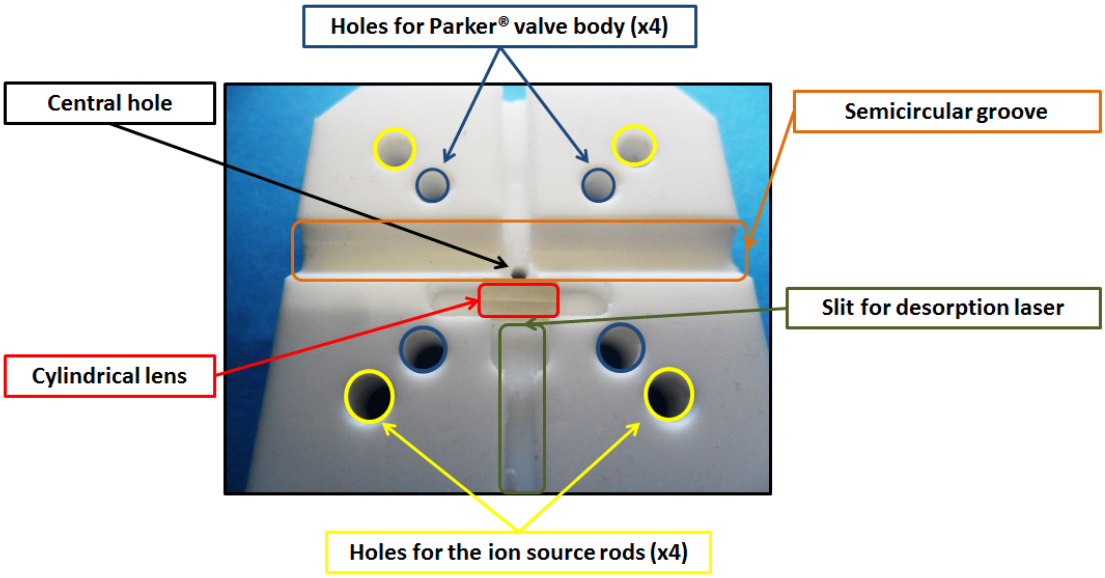


Figure 13.5. Teflon® block containing the cylindrical lens. Holes for nozzle body of valve and ion source rods are visible in the diagonals.

Teflon® material was chosen for this critical and specific piece. This material avoids memory effects as well as it acts as an electrical insulator between the nozzle body of the valve and the repeller plate. This nozzle body is screwed to the block (fig. 13.4). The thickness of the channel and the angle of it are 1 cm long and 30 ° respectively. Four holes were to hold the stainless steel rods which act as holder for the ion source. Cylindrical lens (fig. 13.5, Thorlabs, NBK-7, Uncoated, 3.8 x 4 x 8 mm, f = 3.8 mm) has the perfect size to close a slit which desorption laser follows to hit the sample (fig. 13.5). The block contains a groove with a semicircular shaped cross section (fig. 13.5 middle, left to right) to allow the sliding of the sample rod tip.

### 13.3.2. **Manipulator**

The tip containing the sample slots is screwed to a large solid rod of ¼ inch. This allows the introduction of the tip into the chamber as well as the movement up and down of the slots containing different substances. It was important to design a manipulator to hold the rod and which could allow the change of the tip without opening the chamber. The idea behind was always to keep the constant the background vacuum ($2 \cdot 10^{-7}$mbar) unaltered. Besides, this makes faster the analysis of different samples.

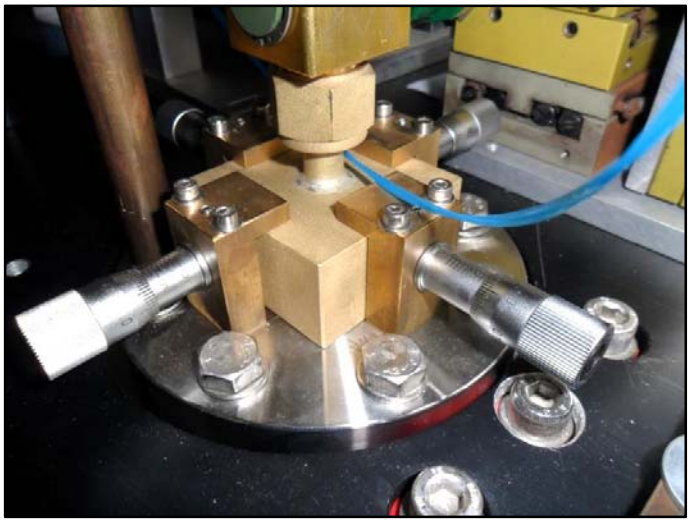

Figure 13.6. Block made of brass and the four micrometer screws.

The manipulator consisted in a block of brass which could be moved in x and y directions. With this aim, four micrometric screws were fixed as it is depicted in figure 13.6. The adjustment of these positions is essential to be able to slide the tip along the groove with the semicircular shaped cross section located at one surface of the Teflon® block (fig. 3.15). On the top of the brass block, a Swagelok® brass valve (½ inch) was fixed, and connected to it brass tube was screwed. This last has an Ultra-Torr fitting (Swagelok®) at the end which seals the sampling rod and the chamber (fig. 13.8).

A rotatory pump was connected to the brass pipe via a ¼ in. stainless steel Swagelok® valve to reach a pre-vacuum pressure of $2 \cdot 10^{-2}$ mbar (fig. 3.18). The ¼ of inch valve was opened for five minutes and then closed again. After that the ½ inch brass valve which separates the chamber and the manipulator is slowly opened. In the meantime the pressure in the chamber is monitored. Finally the rod is pulled down and the tip of it is slid into the Teflon® block. The distance is adjusted so that the middle of the slot containing the sample matches with the nozzle body of the valve.

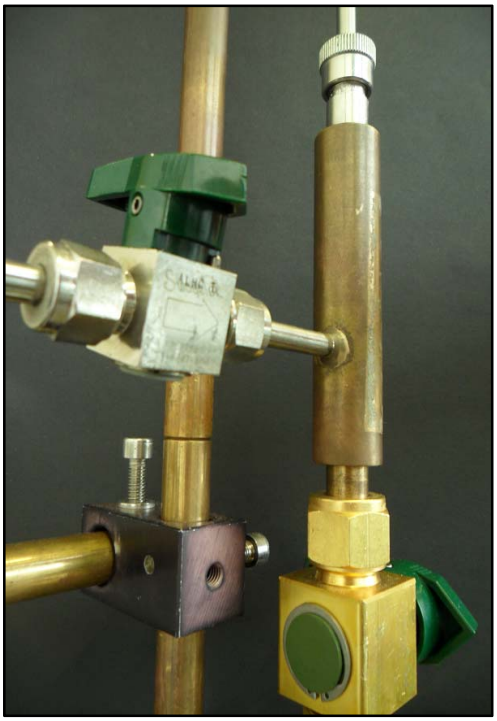

Figure 13.7. Manipulator. The sampling rod is sealed with an Ultra-Torr fitting.

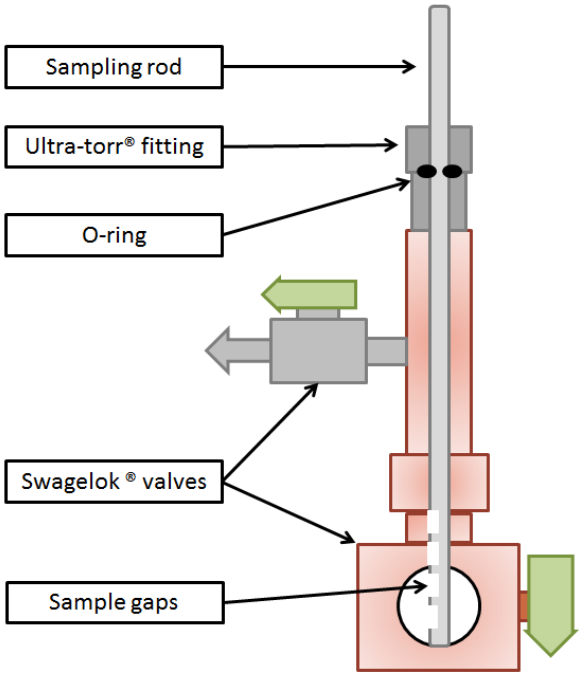


Figure 13.8. Sketch of the manipulator with the sampling rod.

### 13.3.3. **Sampling rod**

The sampling rod consisted in a stainless steel rod at the end of which a tip can be screwed. The rounded tip (¼ in.) is reduced to half of its diameter. The flat surface faces the nozzle body while the rounded part fits in the rounded groove.

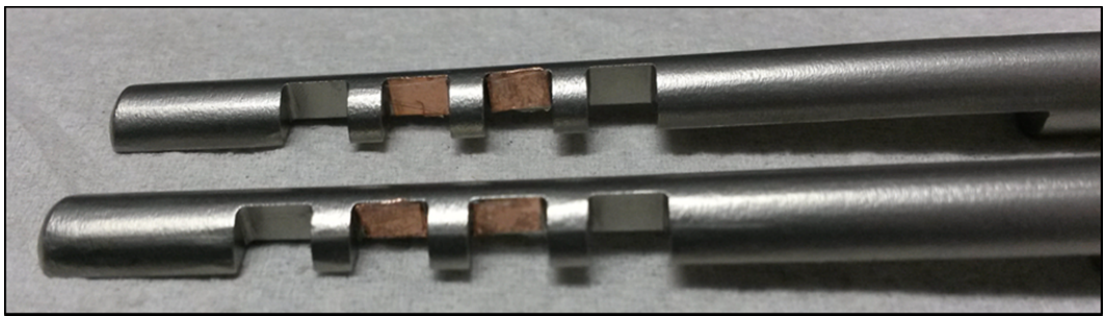

Figure 13.9. Tip of the sampling rod with four slots.

## 13.4. Desorption laser

To carry out the desorption a Soliton (THALES LASER, Typ = DIVA II 266, 20 Hz) Nd:YAG diode pumped laser was employed. The pulse duration of the laser is 10 ns, meantime the beam diameter ($1/e^2$) and divergence are 2mm and < 0.5 mrad respectively. The second harmonic with 532 nm (TEM 00) was used. The residual 1064 nm and the second harmonic waves were separated with the use of three dichroic mirrors HR@532 nm at 45˚ and HT@1064 nm at 45˚. Two of those dichroic mirrors were set in a periscope used to lead the laser light through the window up to the sampling slot. The pulse energy of the laser can be varied according to two parameters. The first one is the delay between the Pockels cell and the Q-Swith (gain of cavity), and the second one with the current applied to the diodes pumping the Nd:YAG rod. Figure 3.10 shows the energy per pulse (μJ) of desorption laser in front and behind the periscope. Blue points are the result of measuring both 1064 and 532 nm whereas the red ones refer only to the 532 nm. The variation of the energy per pulse along the diode current (mA) is linear ($R^2$ = 0.9953).

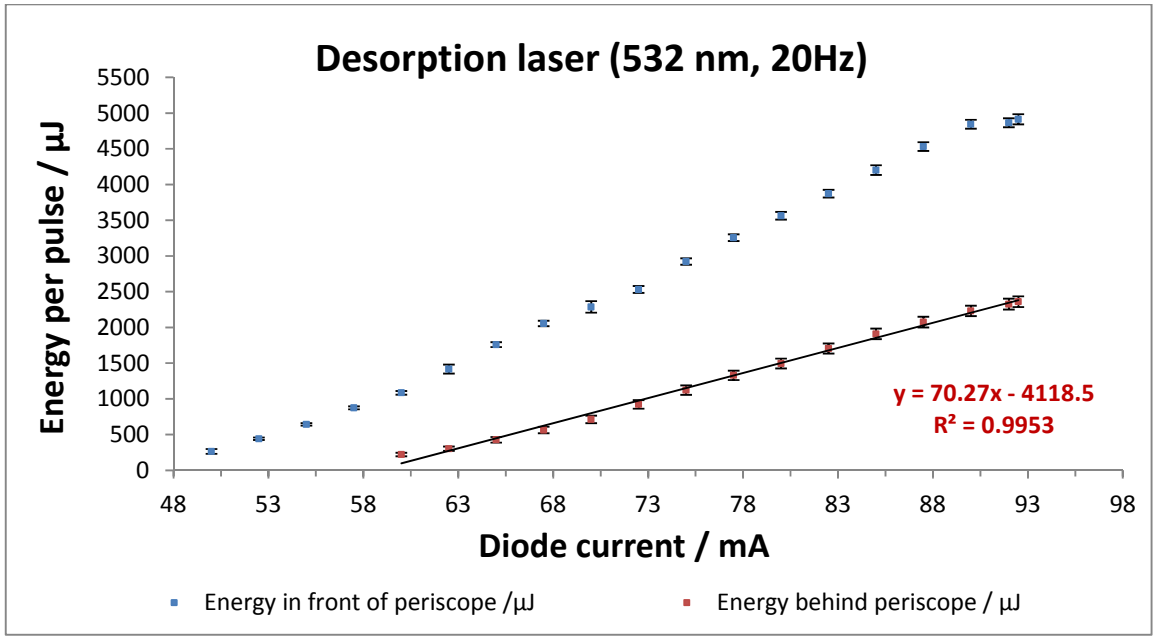


Figure 13.10. Picture showing the pulse energy of the laser versus the current applied to the diodes.

Table 13.2 shows the corresponding energy calculated for every current. In the case of peak intensity and fluence a laser spot area of 4 $mm^2$ was taken into account (1mm x 4 mm).

| mA | E/μJ | Peak power /W | Peak intensity /W·cm$^{-2}$ | Fluence / μJ·mm$^2$ | Fluence/ mJ·cm$^2$ |
|---|---|---|---|---|---|
| 60 | 97.7 | 9.77E+03 | 2.44E+05 | 24.4 | 2.44 |
| **65** | 449.1 | 4.49E+04 | **1.12E+06** | 112.3 | **11.23** |
| 70 | 800.4 | 8.00E+04 | 2.00E+06 | 200.1 | 20.01 |
| 75 | 1151.8 | 1.15E+05 | 2.88E+06 | 287.9 | 28.79 |
| 80 | 1503.1 | 1.50E+05 | 3.76E+06 | 375.8 | 37.58 |
| 85 | 1854.5 | 1.85E+05 | 4.64E+06 | 463.6 | 46.36 |
| 90 | 2205.8 | 2.21E+05 | 5.51E+06 | 551.5 | 55.15 |

Table 13.2. Relation between diode current and laser energy in different units. The current applied to the diodes is related to the E (μJ) through the calibration curve shown in figure 13.10.

## 13.5. Ionization laser

### 13.5.1. Soliton (THALES LASER, Typ = DIVA II 266, 20 Hz)

To ionize the desorbed molecules another Soliton (THALES LASER, Typ = DIVA II 266, 20 Hz) Nd:YAG diode pumped laser was utilized. The pulse duration, the divergence and the size of the beam (1/e$^2$) were 10 ns, < 0.5 mrad and 2 mm respectively.

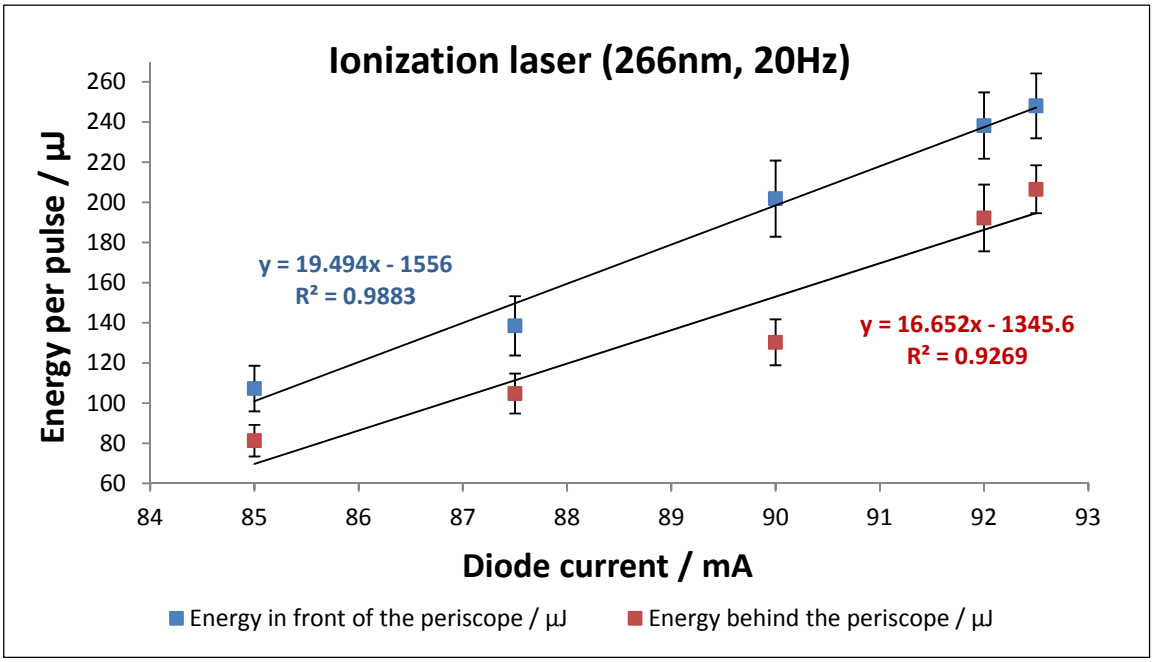


Figure 13.11. Energy per pulse of Soliton laser at 266 nm measured right after the laser and in front of the chamber window.

In figure 13.10 the energy delivered by the laser at 266 nm (TEM 00) is shown. Energy fluctuations are much higher than in the case of the desorption laser. This effect is due to the introduction of an extra non-linear process to generate the $4^{th}$ harmonic. Despite the small energy (250-550 μJ) ionization was feasible due to the good absorbance of the studied substances at 266 nm.

### 13.5.2. **Scan mate dye laser**

To perform wavelength scans of desorbed molecules a dye laser was set-up. A Scan Mate 2C (Lambda Physik, 20Hz) with a pumping Nd:YAG laser (Quantel) was tuned with a solution of dye Coumarine 47. The emission range has its maximum at 460 nm, with constant energy over 454-464 nm. Then it was doubled with a BBO crystal (Type I) to obtain a final range of 227-232 nm. The main purpose was to study the electronic structure of desorbed molecules such as decacyclene ($C_{36}H_{18}$) and others. It is crucial in spectroscopy (qualitative studies) to be able to tune wavelengths to a range where the molecule of interest absorbs. By using UV laser radiation, MPI and REMPI processes occur easily in polyatomic molecules especially those with aromatic rings or double bonds [10, 11].

## 13.6. Optical fiber

Laser desorption via optical fiber has been rarely used in TOF-MS with together with spectroscopy applications. It is well known the set-up of F. Piuzzi et al. [6] which was exceptionally applied to the study of the isolated guanine (tautomerism, spectroscopy and excited state dynamics) [7]. Laser desorption with an optical fiber presents some advantages with respect to the conventional mirror-lens array.

- Alignment results much easier.
- Energy losses are negligible in the short length.
- High adaptability to the geometry of existing chambers or apparatus.
- Desorption can be carried out without the necessity of having viewports in front of the sampling rod.

All the before mentioned factors together with the geometrical compactness of the final set-up where some reasons for which the utilization of this method was tried. Many factors must be taken into account to select the correct optical fiber. Material, diameter, numerical aperture, bend radius and damage threshold among others.

Optical fibers are based on a linear optical effect called total internal reflection. If one takes Snell´s law (eq. 13.7.a and b) (written in his current way by Ibn Sahl in the year of 984, Bagdad) a critical angle ($\theta_c$) can be defined (fig. 13.12 [6]). For this and higher ones 100 % of light is reflected and the transmission losses are zero.

$$\sin\theta_i = \sin\theta_t \frac{n_2}{n_1} \tag{13.7.a}$$

$$\theta_t = 90^\circ \rightarrow \sin\theta_t = 1 \tag{13.7.b}$$

$$\theta_c = \theta_i = \sin^{-1}\frac{n_2}{n_1} \tag{13.7.c}$$

Total internal reflection occurs between materials of different composition only if the refraction index of the outer material, called cladding, is lower than the inner one, called core.

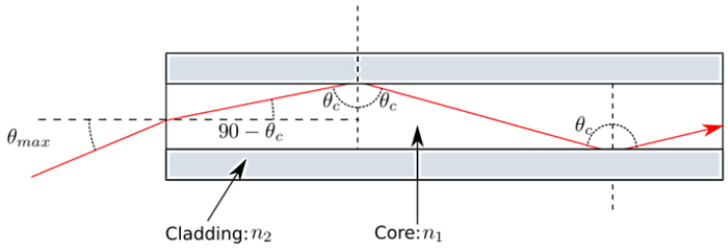


Figure 13.12. Typical scheme of an optical fiber showing the two different angles that must be considered to produce a total internal reflection [6].

The maximum angle is the one included in the definition of numerical aperture (NA) (eq. 13.8).

$$NA = n\ \sin\theta_{max} = \sqrt{n_{core}^2 - n_{clad}^2} \tag{13.8}$$

In 1820 A.J. Fresnel derived the equations which account for the portion of reflected light both for $\pi$ and $\sigma$ polarization. If one applies the Fresnel equations to different cladding-core material (different diffraction indexes) one can find always an angle which accomplishes the condition of critical angle. It is worth to mention that one can build different sorts of optical fibers depending on the variation of the diffraction index over the core-cladding interface (variation along diameter, fig. 13.13 [8]). The resulting shape of the out coupled light (beam profile) is characteristic for the different types of fibers (fig 13.13). During this work a step index fiber was selected. The reason for this is that the laser light must be focused always onto the sample which is the aim of desorption.

Thus the highly broaden beam profile of a step index fiber is anyway collimated with the cylindrical lens located in the Teflon® block (fig. 3.15).

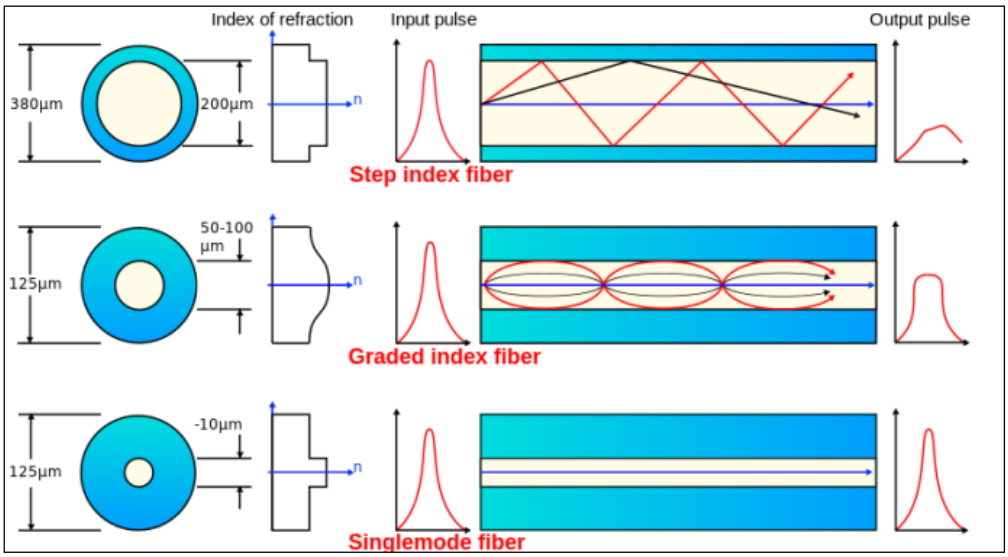


Figure 13.13. Different sorts of optical fibers depending on how refraction index varies between the cladding and the core [6].

In the following 2D and 3D pictures of the TEM 00 for 532 nm desorption laser are shown. Pictures were taken with a CCD camera. Figure 13.14 and 13.15 show a 2D image of the beam before the coupling and after the coupling respectively. Due to the step variation of refraction index within the optical fiber the beam profile broadens greatly when leaving the fiber.

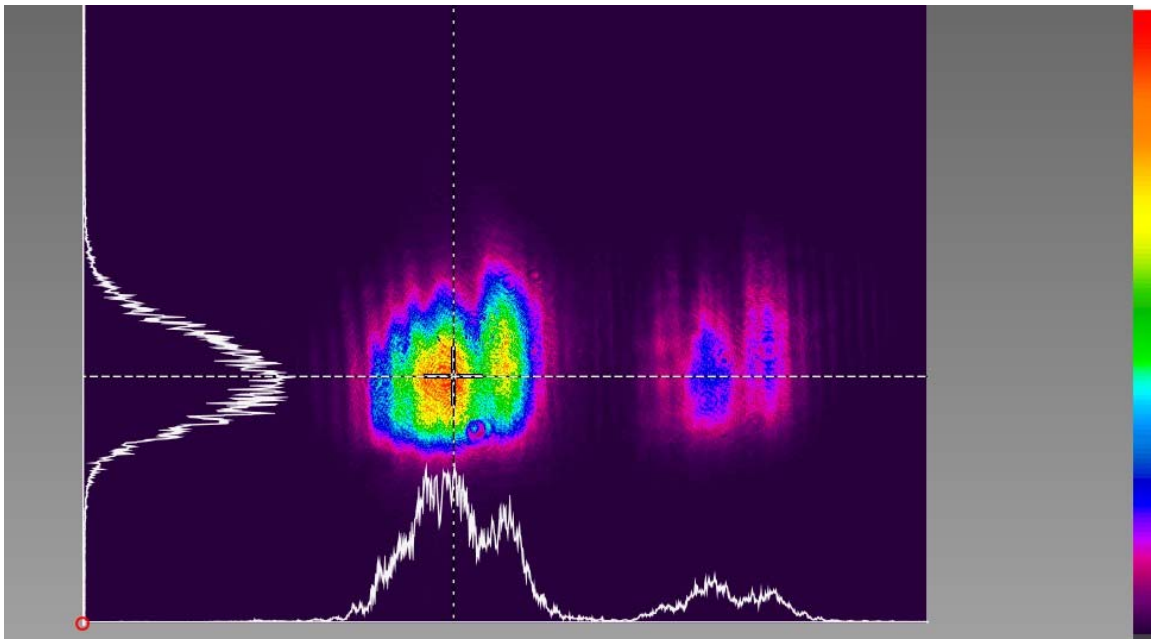

Figure 13.14. 2D picture of beam profile in front of the fiber (Resolution 965 x 533 Pixels).

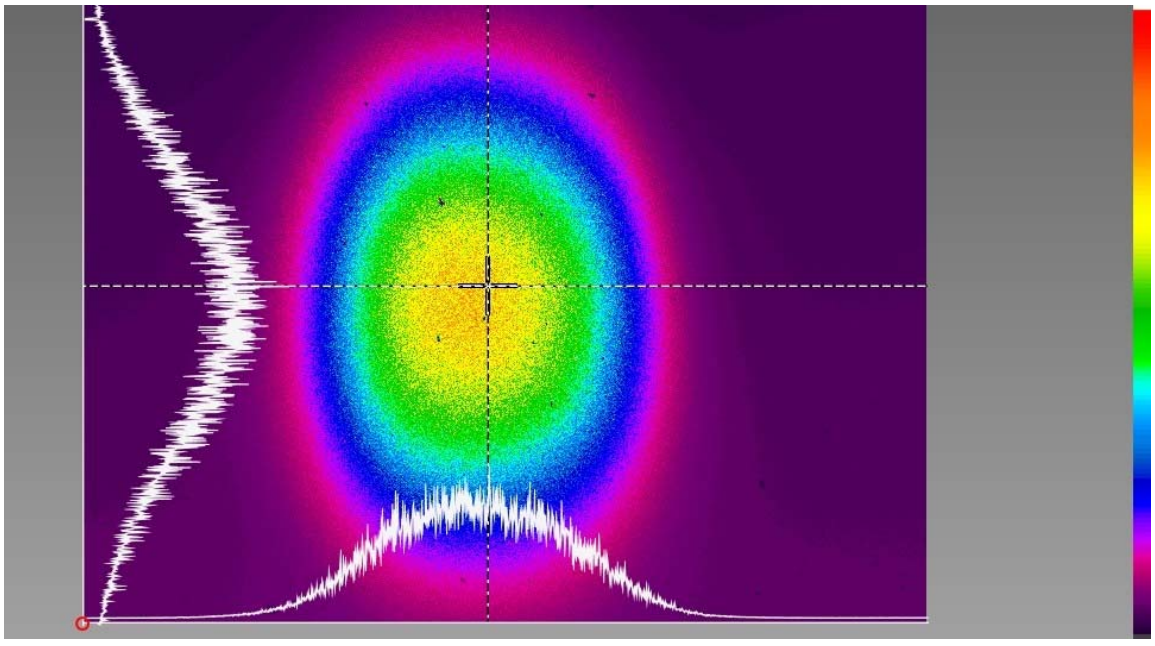

Figure 13.15. 2D picture of beam profile behind the fiber (Resolution 965 x 533 Pixels).

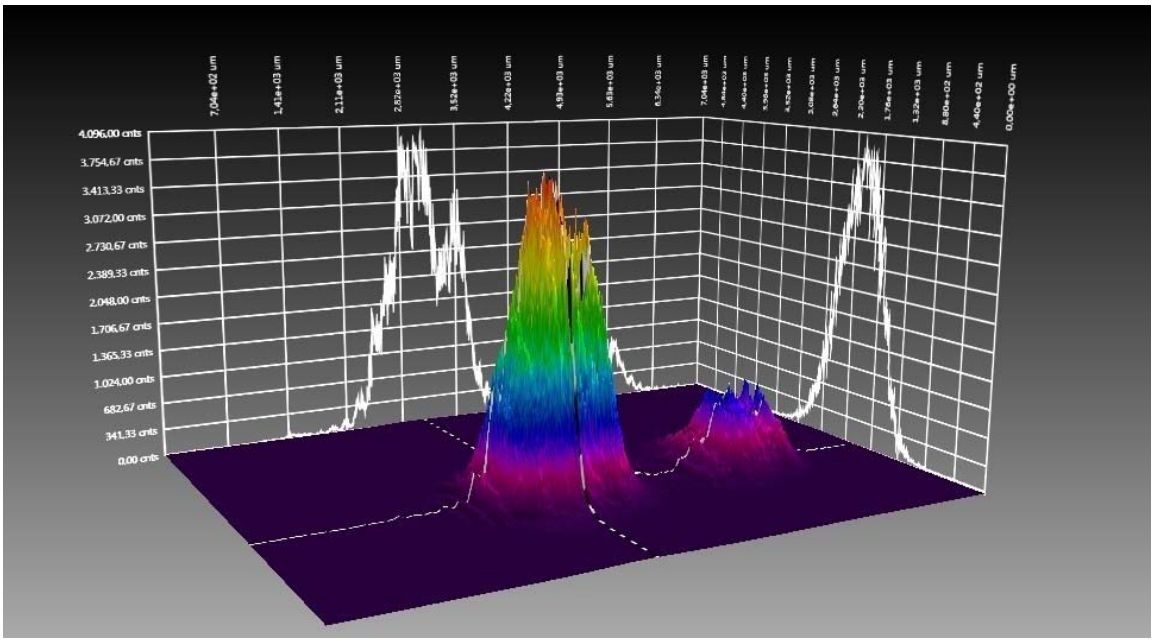


Figure 13.16.3D picture of beam profile in front of the fiber (Large x Width =7 x 5.28 mm).

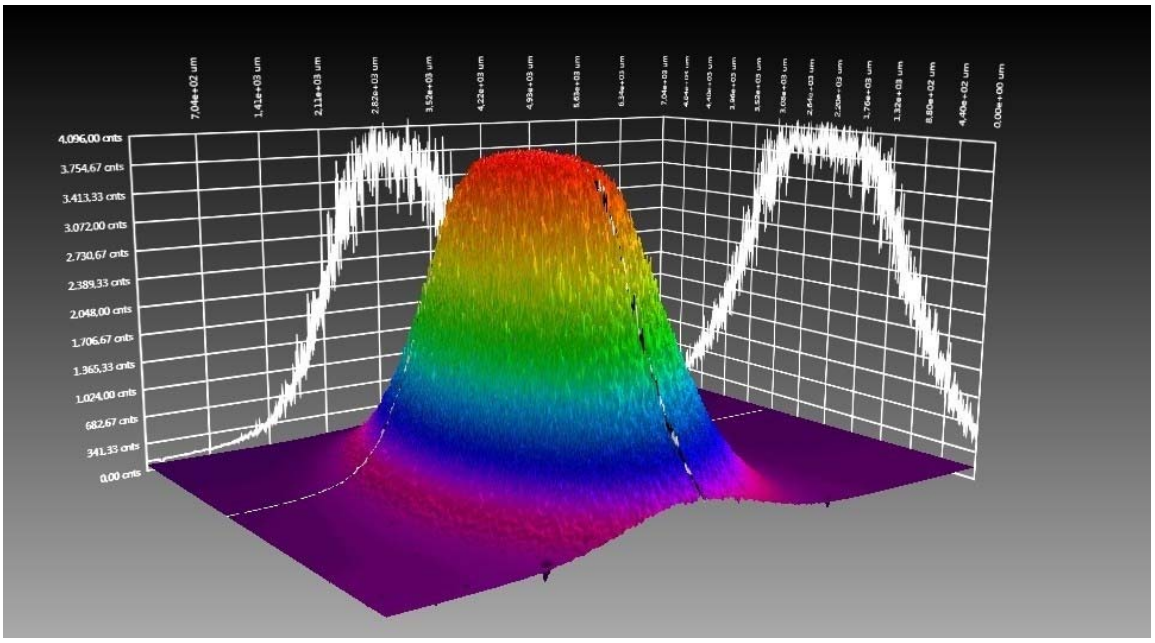


Figure 13.17.3D picture of beam profile in front of the fiber (Large x Width =7 x 5.28 mm).

The optical fiber employed in our apparatus had a core diameter of 600 μm, a cladding of 630 μm and a buffer of 1040 μm. This buffer is a protecting sheath which coated the buffer. The content of OH groups was high which means losses of ca. 20 dB/Km for 532 nm. The value of the numerical aperture was 0.48.

Figures 13.18 and 13.19 show the optical fiber fixed to the Teflon block, and the huge scattering losses at the maximum bending once the whole ion source is set into the chamber.

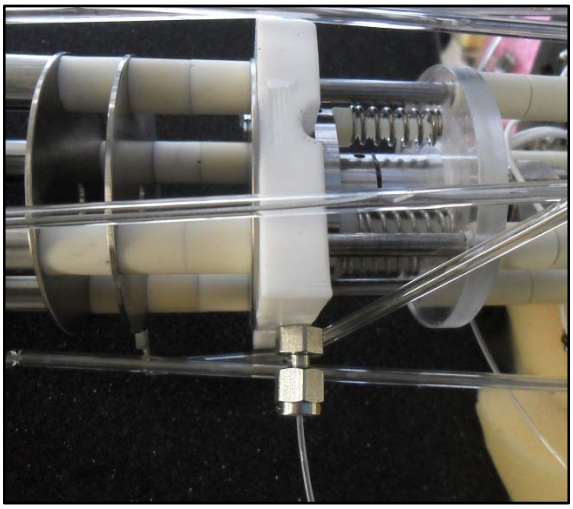

Figure 13.18. Detail of the optical fiber attached to the Teflon® block.

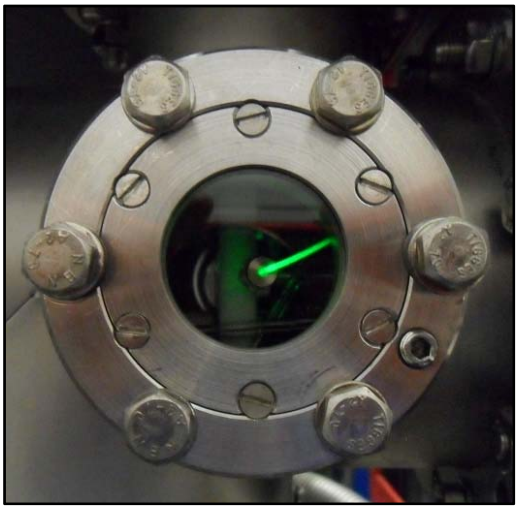

Figure 13.19. Scattering losses in the bent of optical fiber at 532 nm.

## 13.7. Pulsed high voltage switch

Desorption of molecules from a stainless steel rod or a copper substrate produces positive and negative charges. Because repeller plate is only 1 cm away from the rod and the valve nozzle body, breakthroughs can occur between them. This is possible because the repeller has voltage between 2000 and 3500 volts while the nozzle and the rod are grounded. To solve this problem the repeller was pulsed. A pulsed high voltage switch built by the electrical workshop [9] of chemistry faculty and connected to a commercial power supply (Fug). Then a delay generator was used to set the corresponding delay between desorption laser (Pockels cell) and the pulsed voltage given to the repeller. The duration of the pulse was set at 100 μs. Pulsation of repeller allows that ions from the plume flight into the ionization region and be detected afterwards. Delays are recorded in table 13.3 for all the different events.

## 13.8. Valve controller

The controller of the valve was also built by the electrical workshop of the chemistry faculty [9]. It enables the pulsing of the valve in broad time range 50 μs to 100 ms. It can be internally or externally triggered (as it was done). Besides, it has a safe mechanism to stop the pulsing in case that the pressure in the chamber increases over a certain value.

## 13.9. Synchronization

Two pulse generators (DG535, Standford Research Systems) were utilized to synchronize the experiment. Table 13.3 reports delays established for every channel and the device controlled from it.

| **Channel of Pulse generator 1** | **Device** | **Delay / μs** | **Channel of Pulse generator 2** | **Device** | **Delay / μs** |
|---|---|---|---|---|---|
| **Trigger:** Internal. 15-20 Hz | | | **Trigger:** External by pulse gen. 1 | | |
| **T0** | Valve | | **T0** | | |
| **A** | D. Desorption laser | T0 + 330μs | **A** | | T0 + 500μs |
| **B** | PC. Desorption laser | A + 110μs | **B** | | A + 100μs |
| | | | **A⎍B** | Pulser of repeller | |
| **C** | Parker® Valve | T0 + 0μs | **C** | D. Ionization laser | T0 + 420μs |
| **D** | | | **D** | PC. Ionization laser & scope trigger | C + 100μs |
| D: Diodes, PC: Pockels cell | | | | | |

Table 13.3. Optimized delays set in pulse generators for every device.

The pulse generator number one was internally triggered while the second one was triggered by the first one at Ext. channel. Repetition rate was adjusted in a range of 15 to 20 Hz. Time between diodes and Pockels cell was at minimum: 110 μs. Power of the laser can be controlled by varying this delay, however it is preferable to change the diode current (table 13.2). Symbol ⎍ means time difference between channel A and B (400 μs). In this channel the switcher of repeller plate was

connected. Trigger of scope is set in channel D (Pockels cell of ionization laser) of the second pulse generator.

## 13.10. Apparatus

The experimental set-up of small dimension (LxWxH = 109x58x123 cm) is shown in figures 13.20 and 13.21. In the front panel (fig. 13.20) power supplies (Fug), turbo pump controllers, pressure reader, valve controller and pulse generator were installed. Laser with its power supply and a scope (Lecroy 332A) on the top were set in an upper aluminum plate.

In figure 13.21 the pre vacuum pump (Pfeiffer, MOD-DUO 008B, 8 $m^3$/h), turbopumps (Pfeiffer, MOD-TMU 260, 2000 l/s) and the linear time of flight can be clearly seen. The Thales laser (Type = DIVA II, 266 nm) employed for ionization has been removed. A dye laser (Scan Mate 2C, Lambda Physik) was aligned and tuned in the range of 454-464 nm (Coumarine 47) to perform one color two photon ionization experiments. The laser was set in front of the apparatus and the UV radiation (227-232 nm, doubled of the Coumarine 47) was led in the space existing between the red frame. To lead the laser down and through the chamber an adjustable periscope was set. It has two dichroic mirrors (HT@440 nm and HR@230 nm). Furthermore, a lens (concave, F=25 mm), which allow the focusing into the ion source, was set in front of the viewport.

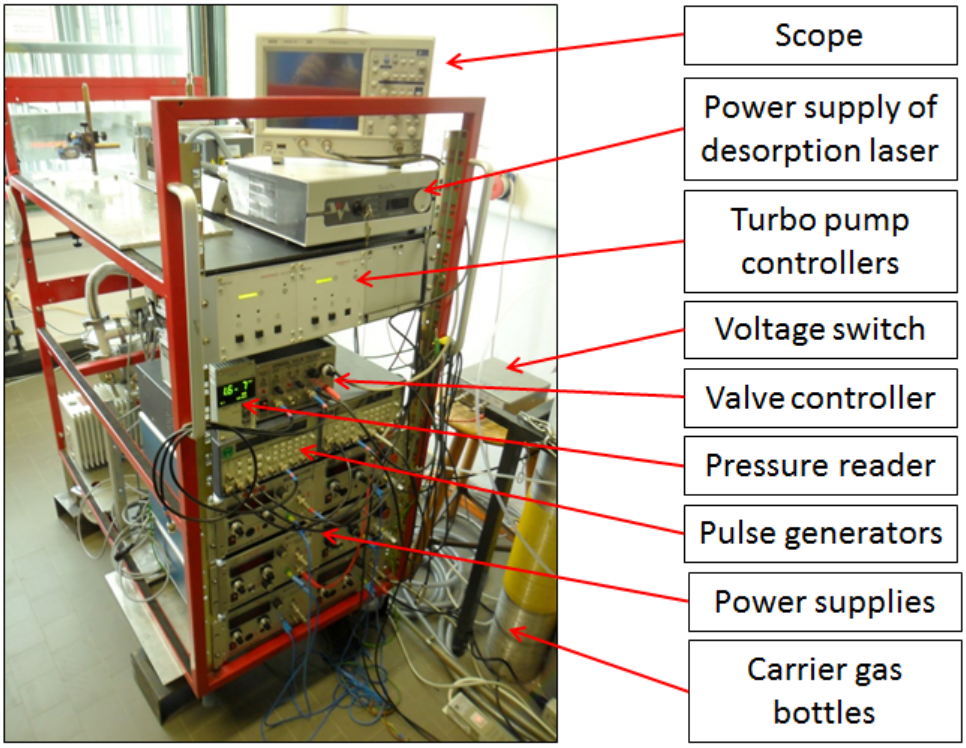


Figure 13.21. Front view of compact LD-TOF-MS.

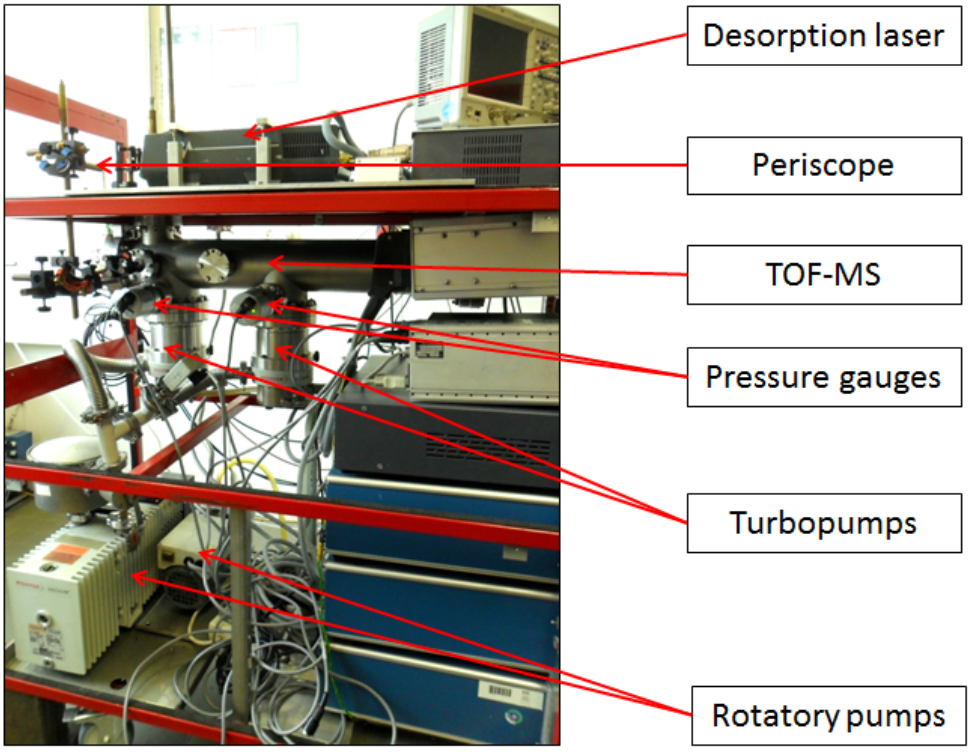


Figure 13.22. Side view of compact LD-TOF-MS.

## 13.11. Literature


1. M.C. Wiley, I.H. McLaren, *Rev. Scientific Instrum.* 26, 1150 (1955)
2. B.A. Mamyrin, V. Karataev, D. Shmikk, V. Zagulin, *Sov. Phys.* JEPT, 37, 1973, 45
3. M. Taherkhani, M. Riese, M.B. Yezzar, K. Müller-Dethlefs, *Review of Scientif. Instru.* 81, 063101, (2010)
4. J.E. Rink, U. Boesl, *Eur. J. Mass Spectrom*. 9, 23-32 (2003).
5. Hiroyuki Saigusa, *Journal of Photochemistry and Photobiology C: Photochemistry Reviews* 7 (2006) 197–210.
6. F. Piuzzi, I. Dimicoli, M. Mons, B. Tardivel, Q. Zhao, *Chemical Physics Letters* 320 (2000), 282–288
7. M. Mons, I. Dimicoli, F. Piuzzi, Chapter 13, M. K. Shukla, J. Leszczynski (eds.), *Radiation Induced Molecular Phenomena in Nucleic Acids*, 343–367.
8. Picture from Hecht.
9. Zentralbereich Elektronik, Department Chemie, Technische Universität München.
10. U. Boesl, H. J. Neusser, E. W. Schlag, *J. Chem. Phys.* 72, 4327 (1980)
11. U. Boesl, H.J. Neusser, E.W. Schlag , *Chemical Physics,* Volume 55, Issue 2, 15 February 1981, Pages 193–204
12. Grundlegende Untershuchung der Laserionisation und Laserdesorption für di Spurenanalytik organischen Stoffe in FestKörpern, J. E. Rink (2000)

# 14. Results

With the aim to test the LD-TOF-MS apparatus, pyrene and decacyclene were desorbed. Mass spectra for all were recorded. Besides, investigations of decacyclene clusters and fragmentation patterns were carry out for decacyclene.

## 14.1. Pyrene

Pyrene (fig. 14.1, 202.25 amu) is a PAH produce in big amounts during combustion processes. Although not harmful as other PAH, pyrene is toxic to kidneys and liver. Furthermore, pyrene and in general all PAH are being aim of many studies since they have been reported in meteorites [7] and they are the basis of the so called PAH world hypothesis [6].

An optical fiber with 532 nm was used to perform desorption. It must be mention that only for this molecule this method was used. The geometry of the chamber and the few space in the chamber made that the optical fiber was bent in excess. In close future slightly set-up modification will be done with the aim to incorporate a fiber with smaller diameter and a fewer bending radius.

Pyrene (yellowish solid) was deposited in the slots of a sample tip. An amount of compound was milled and solved in toluene. The resulting solution was dropped on slots till a noticeable layer of molecules was visible.

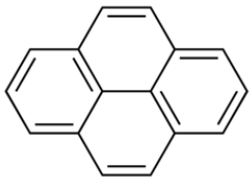

Figure 14.1 Pyrene ($C_{16}H_{10}$).

Desorption of molecules can start to occur at laser fluences of about 11 mJ/cm$^2$ [2] whereas ionization does not occur below a value of laser irradiance equal to $10^6$ W/cm$^2$ [2]. Both threshold values are attained when current of desorption laser power supply is increased till nearly 65 mA (tab. 13.2). Pyrene was observed in mass spectrum when flash lamps current was increased till this value which in terms of final desorbing energy means, $1.12^6$ W/cm$^2$ & 11.23 mJ/cm$^2$. Thus a considerable amount of desorbed pyrene can be already ionized before it reaches the laser ionization region. This results in an increment of fragments that can be observed in mass spectrum (fig. 14.2). Figure 14.2 shows a pyrene mass spectrum recorded with set-up as well as the one

published in NIST chemistry webbook [5]. For this last an electron impact ionization (EII) method was employed. As a background signal toluene (92.14 amu) and its fragments below 40 amu are observed. The spectrum obtained presents much more intense fragmentation pattern than the NIST one. Besides, the mass resolution did not enable the differentiation of the neighboring masses. This affected to bunch of fragments which showed up nearly every 12 amu. (44, 57, 69, 79, 92, 104, 116, 127, 140, 150, 162, 172, 182, 193 and 202 amu).

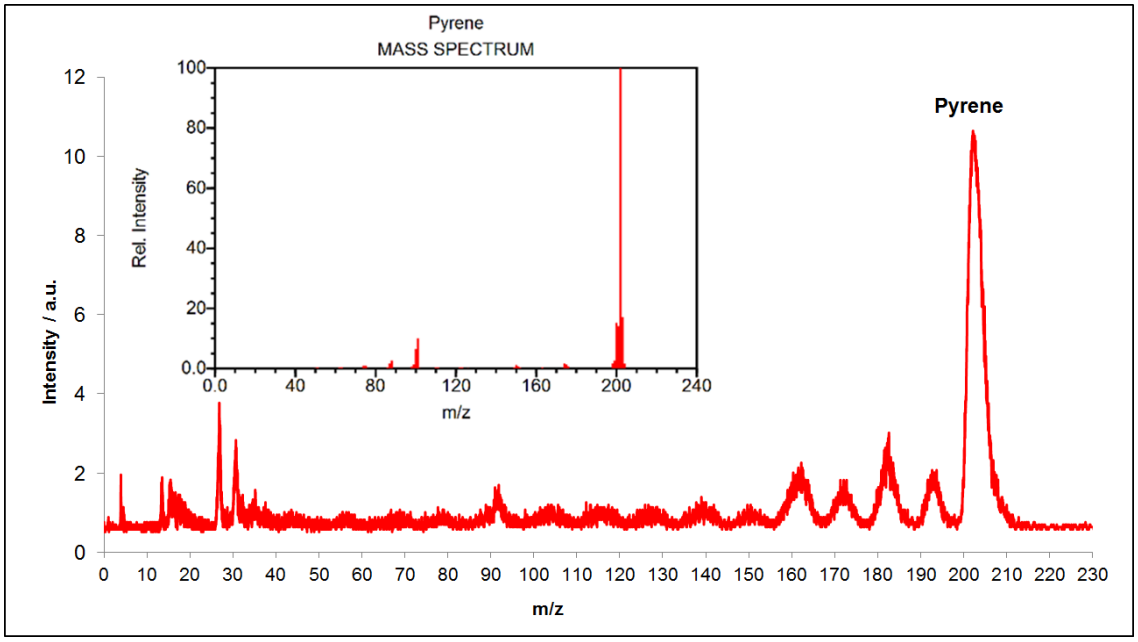


Figure 14.2. Mass spectrum of Pyrene desorbed by using a laser coupled into an optical fiber. The inside shows the mass spectrum from NIST chem. book. [5]

The broadening of all peaks can be explained by kinetic energy effects. When desorption takes place, a plasma plume is created and the kinetic energy distribution of molecules is broad. Then molecules flight through the channel pushed by the expansion of carrier gas when valve is opened. In the ionization region ionization laser is shot and molecules become ions after MPI. Molecules are first repelled and then accelerated into the field free region. The initial kinetic energy distribution of molecules and fragments is stretched within the supersonic beam, and this has allowed the formation of cluster till high numbers such in the case of guanine-water clusters observed by H. Saigusa et al. [10, 11]. However, in set-up herein presented neither a skimmer nor a good differential vacuum are used. What is more the different kinetic energy that particles with the same m/z ratio would need the use of a Re-TOF to achieve a mass resolution enough for such a

purpose [9]. Another possibility to improve mass resolution for laser desorption in line time of flights is the so called delayed pulsed extractions. This technique is based on stablishing a delay between creation of ions and extraction step. The desorbed molecules enter in the ionization region where repeller and accelerator plate have same voltages e.g. 2 KV. Then molecules are ionized and continue travelling in a way that those with same m/z but bigger initial kinetic energy move further toward the accelerator plate. After a time which can be in the range of hundred or a few thousands of nanoseconds a voltage higher to 2 kV (optimized) is applied e.g. 2.6 kV. At this time ions which had less energy and travelled less receive more kinetic energy. These ions reach the faster ones giving rise to narrow peaks and in consequence to a better mass resolution.

## 14.2. Decacyclene ($C_{36}H_{18}$)

Decacyclene (Diacenaphtho [1,2-j:1',2'-l] fluoranthene, fig. 14.3 [1]) is another PAH with molecular weight equal to 450.52 amu. This molecule could be a combustion product and thereby exist in the exhaust of an engine. This molecule shows a very different fragmentation pattern depending on desorption and ionization fluences as well as on the surface composition where it is deposited [8]. During combustion within an engine and after its formation, decacyclene and similar molecules could break into fragments. Those could be capable to react with each other, and steady clusters of several decacyclene molecules could give rise to bigger molecules. The ionization potential is 7.27 eV (170.54 nm) [4]. Two photons of 266 nm were used to ionize the molecule (MPI).

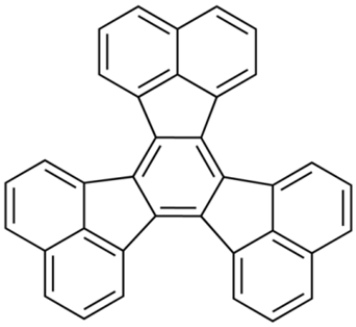

Figure 14.3. Decacyclene ($C_{36}H_{18}$)

Figure 14.4 shows a mass spectrum where the peak of the decacyclene is visible. Residual peaks of toluene and pyrene are observed. Figure 14.5 shows the same decacyclene spectrum after switching off the desorption laser. Fragments coming from decacyclene are present in mass channels of 40, 129, 132, 154 and 169 amu.

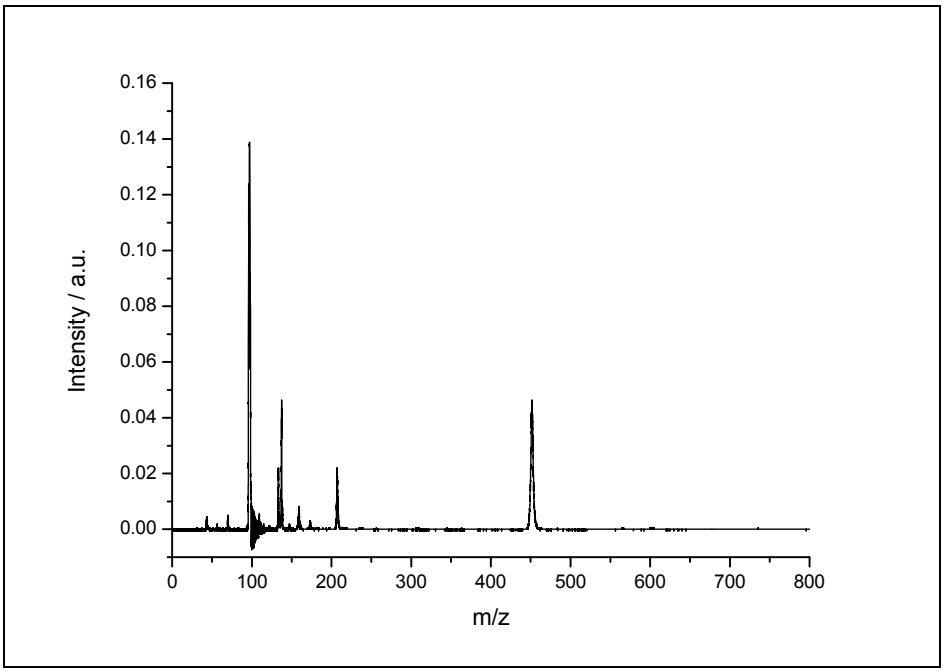


Figure 14.4.Decacyclene desorbed with residual pyrene (202.25 amu) and toluene (92.14 amu). The low intense peaks (129 and 132 amu) between pyrene and toluene are fragments from the decacyclene.

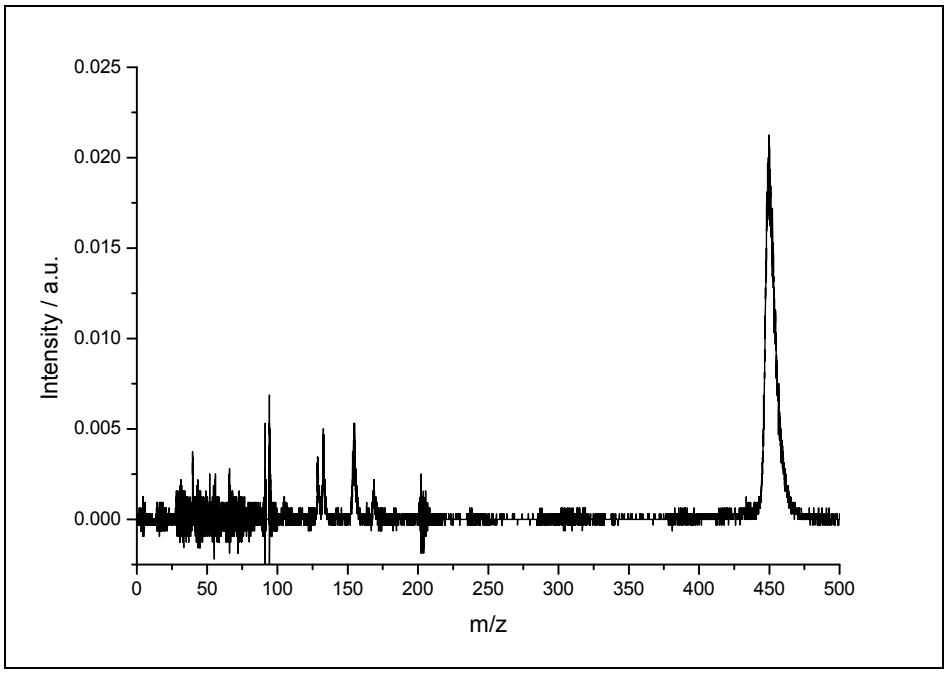


Figure 14.5.Corrected decacyclene mass spectrum and its fragmentation pattern.

When the energy of the desorption laser is increased the number of molecules of decacyclene and its fragments increase. The probability to create clusters between decacyclene and the fragments rises. Moreover, the intensity of the fragments observed in fig 14.7 increased. Fragments of masses 150 (one third), 300 (two thirds) and 600 (decacyclene + one third), were expected. Instead, the peaks have a slightly different mass; 154, 302 and 604 amu. This is evidence that hydrogenation reactions occur with a high probability at the plume. One third of decacyclene (150 amu) after desorption has a double bond in which every carbon has an electron. Those two radical sites are neutralized by hydrogens and the double bond hydrogenated afterwards. The result is a molecule with a molecular weight of 154 amu. This corresponds to a well-known molecule called acenaphthene ($C_{12}H_{10}$) [3].

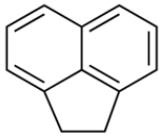

Figure 14.6. Ancenaphthene ($C_{12}H_{10}$).

The peak at 302 amu has mass equal to two thirds of decacyclene plus two. In this particular case the decacyclene breaks and two radical sites are again formed. Those are hydrogentated giving rise to the molecule drawn in figure 14.7. The hydrogenation does not continue in the two double bonds because they contribute to delocalize the electronic density over the two aromatic rings.

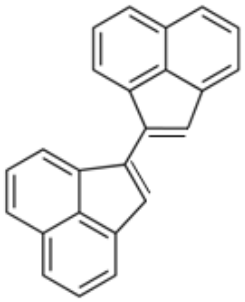

Figure 14.7. Fragment of 302 amu.

The peak at 604 amu can be easily explained if we take into account the ancenaphthene molecule. Thus a cluster of one with one of this molecules and one decacyclene is steady enough to survive in the post plume conditions (fig. 14.8). It is very difficult to decipher the final structure of the

steadiest conformer for the 604 amu cluster. Experiments involving complicated techniques such as IDIR spectroscopy and the comparison of IR spectra with quantum calculations must be performed. However, it is quite clear that $\pi-\pi$ (stack) interactions are in these cases the most probable ones.

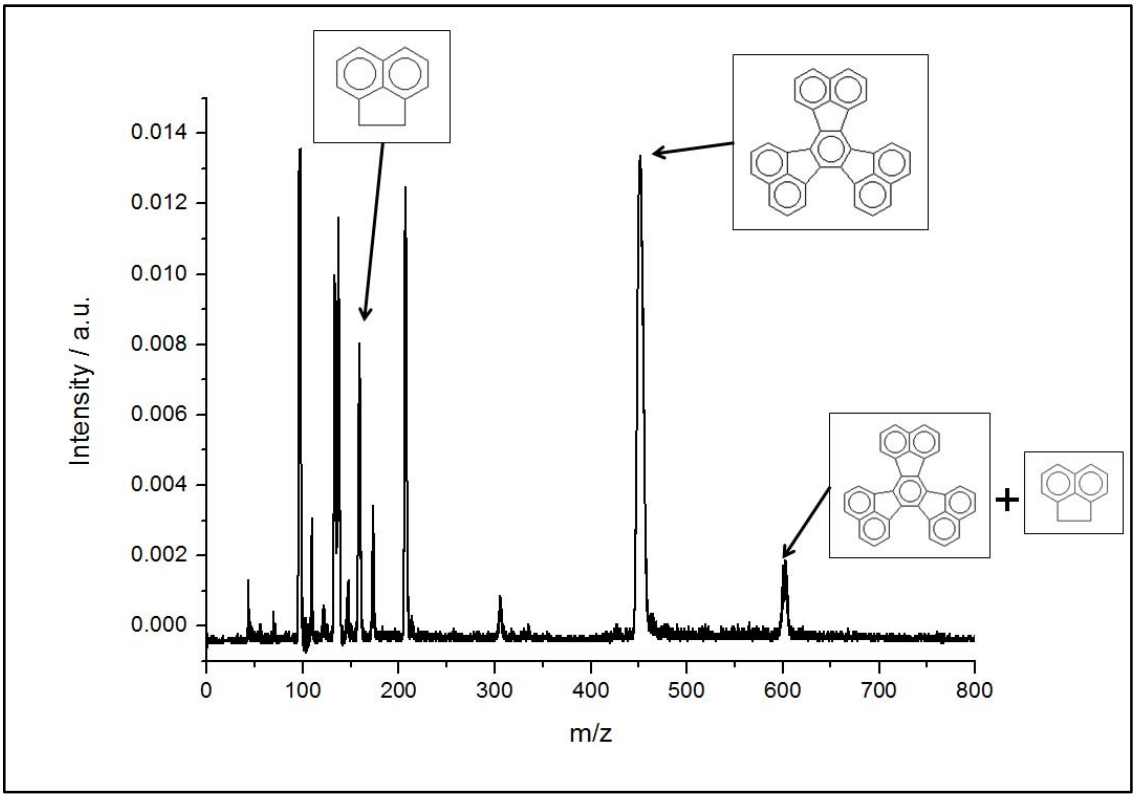


Figure 14.8. First observation of the peak corresponding to decacyclene plus one third of decacyclene (604 amu). At mass 302 amu another steady molecule is observed.

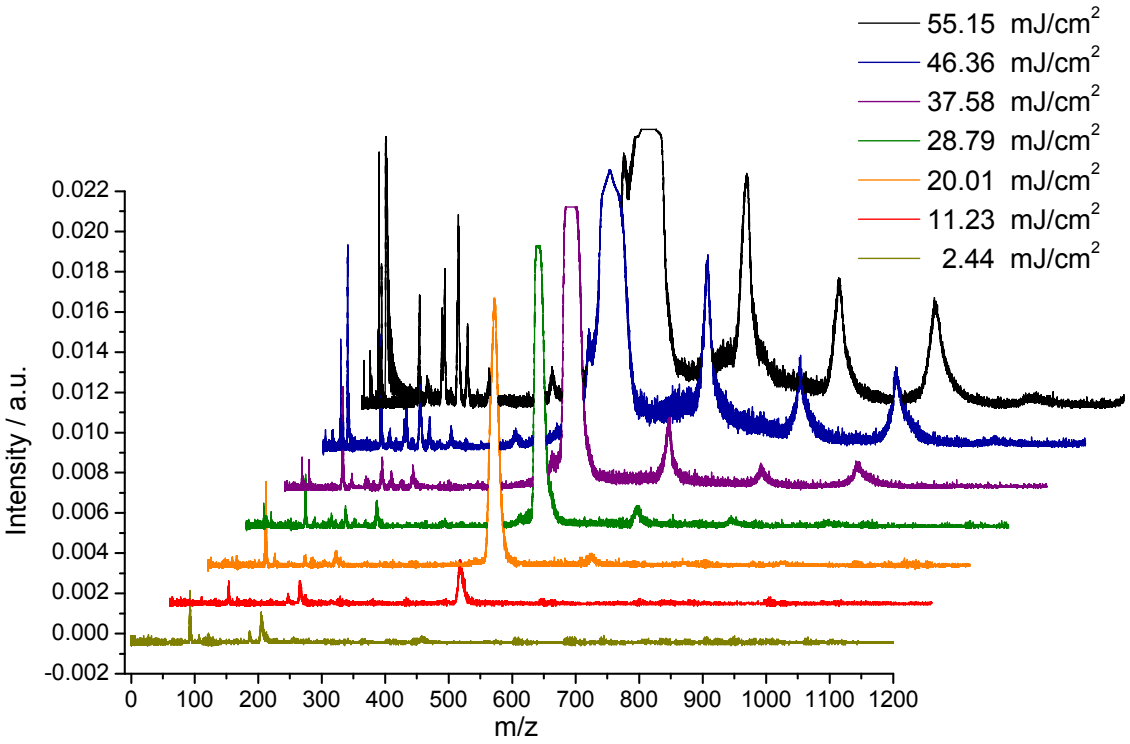


Figure 14.9.Decacyclene, clusters (604, 750, 902 and 1050 amu) and fragments formed at different fluences (mJ/cm$^2$).

Figure 14.9 shows the mass spectra of desorbed decacyclene for different fluences. Fluences between 20.1 and 55.15 mJ/cm$^2$ produce enough fragments in order to observe the 604 amu peak. With progressive laser energy increment, peaks at higher masses are visible. Thus, at fluences equal to 37.58 mJ/cm$^2$, 46.36 mJ/cm$^2$, 55.15 mJ/cm$^2$, clusters with masses corresponding to 750, 900 and 1050 amu respectively.

The masses at 750 amu, 900 amu and 1050 amu (fig. 14.9) correspond to clusters or products of reaction. Due to the bad mass resolution (width of the mass peaks) one could not conclude what is every peak. The peaks center at 750 should be a cluster of decacyclene plus the fragment with mass equal to 302 amu. However, this should then correspond to 752 amu. The peak at 900 amu clearly corresponds to two decacyclene molecules probably having stack interactions.

Figure 14.10. Detail of the sampling tip after desorption.

Figure 14.10 shows a tip of the sampling rod with decacyclene (brownish powder) after desorption. The place where the laser was focused can be clearly observed. Besides in one of the gap a black spot is visible. This could indicate formation of soot or charcoal due to high temperatures and dehydrogenated processes occurring within the plasma plume.

Several attempts to record wavelength spectra of decacyclene and their clusters were performed. Decacyclene shows an interesting electronic structure in ground state near 430 nm [3]. Several tries were made with the aim to identify and better see this part of the spectra. However, due to the bad mass resolution and abundance of fragmentation no concluding spectrum was obtained.

## 14.3. Literature


1. http://webbook.nist.gov/cgi/cbook.cgi?ID=C83329&Units=SI.
2. J. H. Gross, Mass Spectrometry, 2nd Edition, pag. 510 (2011).
3. R. Ruiterkamp, T. Halasinski, F. Salama, B. H. Foing, L. J. Allamandola, W. Schmidt, and P. Ehrenfreund, A&A 390, 1153–1170 (2002).
4. E. J. Gallegos, *J. Phys. Chem.,*1968, 72 (10), pp 3452–3456.
5. http://webbook.nist.gov/cgi/cbook.cgi?Name=pyrene&Units=SI
6. S. N. Platts, NASA's Astrobiology website, 2004.
7. R. Zenobi, J. M. Philippoz, P.R. Buseck, and R. N. Zare, *Science* 246, 1026-1029 (1989).
8. H. Böll, P. Püffel, C. Weickhardt, U. Boesl, *American Institute of Physics* (1995).
9. J.E. Rink, U. Boesl, *Eur. J. Mass Spectrom*. 9, 23-32 (2003).

10. H. Saigusa, A. Tomioka, T. Katayama, E. Iwase, *Chemical Physics Letters* 418 (2006) 119–125.
11. H. Saigusa, *Journal of Photochemistry and Photobiology C: Photochemistry Reviews* 7 (2006) 197–210.

# 15. Summary of part B

The second part of this work (B) was performed during the last period of the PhD and the main goal was the building up of a laser desorption source coupled to a linear time of flight mass spectrometer (LD-TOF). With this technique several thermolabile molecules can be investigated in the gas phase.

Formation and composition of substances such as soot particles can be studied. With the aim to study soot and other carbonaceous substances, also those containing sulfur, a LD-TOF was developed and constructed. The laser desorption source consists in a block of Teflon® where a cylindrical lens was set. This block was fixed to the nozzle body of a pulsed valve. Both were included and set in front of a short ion source. This was then located collinearly to the time of flight. Desorption by optical fiber was tried with the aim to develop and construct a compact and easy to handle instrument. However, the bent radius of the fiber, due to the small width of the TOF tube, made that scattering losses were too high. At this critical point fiber was several times damaged and in consequence discarded. Then conventional laser desorption using mirrors was carried on. To avoid ionization by the desorption laser or by the large electric fields at the edge of the repeller plate, a pulsed high voltage switch was installed. Desorption of a polyaromatic hydrocarbon (PAH) called decacyclene was performed and their clusters were observed for different fluencies of laser photons. Peaks were observed at masses much higher, even more than twice, than the mass of decacyclene. The compounds with those masses are in opinion of the author clusters in which $\pi$-$\pi$ (stack) interactions are the steadiest. These structures and their bounds are of great interest as it was recently reported on an international workshop [citation].

Finally with the aim to elucidate the electronic structure a dye laser was set up and tuned in the UV region. Several wavelength scans were made in different regions. However, due to the complex nature of this PAH and the instability of its desorbed signal, no conclusive wavelength spectra were acquired.

# 16. Conclusions and future perspectives

The work herein explained constitutes a theoretical and experimental description of an instrumental based PhD work. Both parts are related to development, improvement, setting up and testing of apparatus conceived for analytical purposes. During the performance of the PhD work most of the time was employed in mounting and fixing devices, solving instrumentation problems and improving measuring methods. Besides, lot of time was used in improving or designing new experiments and applications for both techniques: Laser induced fluorescence and laser desorption time of flight mass spectrometry. The author is totally sure that both systems were thought, designed and checked in an optimum way. Proof of principle has been performed for both systems and many good results are going to be obtained in next years. However, the lack of time made impossible the realization of some not indispensable but convenient improvements for the oil consumption set-up and an interesting experiment for the laser desorption one. All these are mention in the following.

Firstly, prototype-III is in opinion of the author able to measure even lower concentration of sulfur dioxide. This could be done by incorporating an amplifier connected to the PMT output. Thus the author believes that a detection limit as low as 5 ppb would be reached. Secondly, the use of a 100 Hz laser would make feasible a scope average of 128 times. It will reduce much further the electrical random noise without losing data acquisition speed (1 point per 1.28 seconds). Thirdly, a deconvolution routine could be implemented within the controlling program both to measure the amplitude of $SO_2$, which varies for each concentration, and to identify other fluorescent compounds in gas stream. Deconvolution is a powerful mathematical tool which might deliver all the contributions whose sum give rise to the signal displayed at the scope. The lifetime and amplitude for every fluorescent substance as well as scattering amplitude would be measured in a fast way. The amplitude corresponding to the $SO_2$ decay would be free of scattering influences which will result in better repeatability. Furthermore, with this procedure no subtraction method ($\alpha$) would be necessary.

Finally, the author wants to let constancy about an experiment conceived for the laser induced set-up. The main idea is to apply circular dichroism (g value) to substances which have L- & D-enantiomers (e.g. Dopa or Thalidomide) or exhibit chirality (e.g. organometallic clusters). In this way, enantiomer excess of certain selectively catalyzed reactions might be quantified.

# 17. Appendix

## 17.1. Table of devices included prototype-II & III

| | Device | Model |
|---|---|---|
| **1** | Membrane pump. knf | N 860.3 FT.40.18 |
| **2** | Photomultiplier | 9783B |
| **3** | Housing (ambient temperature) | SWH |
| **4** | Power meter; OPHIR. | PE25-C |
| **5** | Interference for Power meter: OPHIR-PE 25-C | JUNO |
| **6** | Spectrometer<br>(Calibrated in the bandwidth of 420-505 nm) | HR 4000 (2400mm-1 Grating and 5 um Slit); (Gratings H7 and H12) |
| **7** | Optical fiber | Qp400-2-UV-BX; 440 um Premium fiber; UV/VIS; 2m; BX Jacket (KB) |
| **8** | Flow meter | PR 4000B-F2-V2 |
| **9** | Flow regulator (500 st. Cm3/min) | 1479A01352CR1BM |
| **10** | Flow regulator (5000 st. Cm3/min) | 1479A01353CR1BM |
| **11** | Cable from flow meter to flow controller (x2) | CBE259-5-3M/CB259-5-10feet |
| **12** | LeCroy or<br>PicoScope | Wavejet 334A<br>6402A |
| **13** | Longpass filter | cut on: 235 nm Blocking <225 nm;<br>>OD4 /Diameter 38 mm |
| **14** | Collimating lens (x2) | UVFS bi/cx lens; dia:100+0,0/-0,2 mm; F=100+/-2% @355 nm;SQ 40-20 s/d; SF: 1/8 lambda; 0,3 x 45 deg; coated AR/AR @250-420 nm; R<1,5% per surface, AOI=0 deg |
| **15** | USB2.0 10-Port Hub | ON/OFF switch |
| **16** | Power supply (X2) | HCP 140-12000 and MCP 35-2000 |
| **17** | Dichroic mirror | S1: HRs @210-235 nm + HTp @355+400 nm ,<br>S2: ARp @355+400 nm, AOI=45 deg. |
| **18** | Pellin-Broca | UV FusedSilica;190-425 nm;11.47º;20 mm;<br>56-57º (Brewster angle) (Reference: ADBU-20) |
| **19** | Mechanical parts for Optics | Holders, posts, post holders, bases, rails, forks |
| **20** | Dual Gauge (pressure meter) | TPG 251, Dual Gauge |
| **21** | Rotatory pump | DUO 5 or Varian SD-451 |
| **22** | Compact Pinarni Gauge | TPR |
| **23** | Verbinder (x4) and VCR Dichtscheibe (x4) | SS-4-VCR-2 AND SS-4-WVCR-6-400 |
| **24** | Heating Cable and thermocouple | Additional Protective Braid HSS - 450 °C (4 m) |
| **25** | UV/VIS windows | UVFS window d40x3mm (Ref. 210-1403M) |
| **26** | Nozzle | 0.250 mm width & 1 mm length |
| **27** | Flexible PTFE Black hose | Typ H3006-010-04-250C or H13 (diameter ¼ inch or equivalent in mm) |
| **28** | Accordion pipe and vacuum KF connectors | Pfeiffer |
| **29** | Convoluted PTFE hose for membrane pump | ¼ inch or equivalent in mm |
| **30** | Temperature controller for black hose | HT20 or HT MC1 |
| **31** | Temperature controller | 300C (1 for nozzle ) Homemade (TUM, electrical workshop) |
| **32** | Glow discharge cell | Specifications in PhD |

| | Company | Feasible place to order | Web |
|---|---|---|---|
| **1** | knf | www.knf.de | http://www.knf.de |
| **2** | Electron tubes limited | ET enterprises | http://www.et-enterprises.com |
| **3** | Electron tubes limited | ET enterprises | http://www.et-enterprises.com |
| **4** | OPHIR | AcalBfi Germany | www.acaltechnology.com |
| **5** | OPHIR | AcalBfi Germany | www.acaltechnology.com |
| **6** | Ocean Optics | OceanOptics Germany | www.oceanoptics.com |
| **7** | Ocean Optics | OceanOptics Germany | www.oceanoptics.com |
| **8** | MKS Instruments | MKS Instruments, Deutschland | http://www.mksinst.com/ |
| **9** | MKS Instruments | MKS Instruments, Deutschland | http://www.mksinst.com/ |
| **10** | MKS Instruments | MKS Instruments, Deutschland | http://www.mksinst.com/ |
| **11** | MKS Instruments | MKS Instruments, Deutschland | http://www.mksinst.com/ |
| **12** | LeCroy or Pico | Lecroy Datatec | http://teledynelecroy.com/ www.datatec.de |
| **13** | Laser Components | Laser Components | www.lasercomponents.com |
| **14** | Eksmaoptics | Eksmoptics | www.eksmaoptics.com |
| **15** | LogiLink | Conrad | www.conrad.de |
| **16** | Fug | FuGElektronik | www.fug-elektronik.de |
| **17** | Eksmaoptics | Topag, eksmaoptics | www.eksmaoptics.com |
| **18** | Thorlabs | Thorlabs | www.thorlabs.com |
| **19** | Thorlabs | Thorlabs | www.thorlabs.com |
| **20** | Balzers | Pfeiffer | www.pfeiffer.de |
| **21** | Pfeiffer Vacuum | Pfeiffer | www.pfeiffer.de |
| **22** | Pfeiffer Vacuum | Pfeiffer | www.pfeiffer.de |
| **23** | Swagelok® | Swagelok® | www.Swagelok®.de |
| **24** | Horst | Horst | www.horst.de |
| **25** | Eskmaoptics | Eskmaoptics | www.eksmaoptics.com |
| **26** | BruckerDaltonics | Bruker Daltonics | www.bdal.de |
| **27** | Horst | Horst | www.horst.de |
| **28** | Pfeiffer Vacuum | Pfeiffer | www.pfeiffer.de |
| **29** | Swagelok® | Swagelok® | www.Swagelok®.de |
| **30** | Horst | Horst | www.horst.de |
| **31** | TUM | TUM | http://www.zentral.ch.tum.de/en/electronics-workshop/ |
| **32** | TUM | TUM | http://www.zentral.ch.tum.de/en/scientific-glassblowers-workshop/ |

## 17.2. Troubleshooting of prototype-II & III

### 17.2.1. Pressure

1. **Background pressure with roughing pump is not $3 \cdot 10^{-2}$ mbar.**
   1.1. Check whether the rotatory pump is working properly. It does not make any noise.
   1.2. It could be due to leakages.
   1.3. Swagelok®® nuts which connect the GDC and the pipe are loose. They are two and they can be easily adjusted by hand. If one wrench is used for this purpose, please do not tight hardly, glass can break.
   1.4. Lids closing the nozzle are not fully sealed. They must be tightened with the help of wrenches.
2. **It is not possible to reach the 3 mbar in the cell.** This could be due to a leakage.
   2.1. Check that the membrane pump works properly. It does not make any strange noise.
   2.2. Problem could come from a general leakage. Revise 1.3. and further.
3. **Pressure meter displays an oscillating value of pressure.**
   3.1. The system could have a leakage. Revise 1.1. and further.
   3.2. The pressure gauges (Compact Piranni Gauche, TCR) can be dirty, damage or excessively affected by vibrations (due to membrane proximity). Clean or change the Pirannis for new ones.
4. **Pressure drops suddenly during a measurement.**
   4.1. This can happened when different regimes are set in the engine during measurements. In this case wait 1 or 2 minutes and see if it gets constant at 3 mbar.
   4.2. This means that a nozzle could be blocked by soot or other particles. Blow the nozzles with pressurized air.
5. **Pressure increases suddenly during a measurement.**
   5.1. This could be due to water adsorption onto the cell walls. If this is the case but the increment is not higher than 8%, measurements could still running (see section 9 and table 1).

5.2. This can happened when different regimes are set in the engine during measurements. In this case wait 1 or 2 minutes and see if it gets constant at 3 mbar.

5.3. This could be due to a leakage. In this case on should revise the whole system following the steps of first and second point.

### 17.2.2. Scattering light

1. **Scattering signal is very high.** This could avoid both correct calibration and engine/test rig measurements.
   1.1. Set a narrower nozzle.
   1.2. Decrease the energy of the laser.
   1.3. Proof that any portion of 440 nm (VIS radiation) goes into the cell.
   1.4. GDC outlet is located close to the cell inlet. Build an elbow with Swagelok®® stainless steel parts to separate the GDC from the cell entrance.
   1.5. Long pass filter can be damaged or broken.

### 17.2.3. Glow discharge cell

1. **Glow discharge cell presents a flickering behavior.** This could be due to wrong values both in the current and the voltage.
   1.1. Follow process describe in section 3.
   1.2. GDC is petering out.
2. **Glow discharge cell does not work.**
   2.1. BNC cable is disconnected. **Attention!** Danger of shortcut or discharge. **Health danger!**
   2.2. GDC run out.

### 17.2.4. Laser

1. **Energy of the laser is not enough.** This could be due to the following.
   1.1. Lower voltage than 440 V applied to the Pocket Cell (PCs). Increase this value up to 440 V.
   1.2. Calibration is lost. Redo a new calibration adjusting only galvo2 but checking that wavelengths are the correct. That is to say galvo1 values still valid.
   1.3. Optical path of the either OPO or SHG is misaligned. Get on to Laser company.

1.4. SHG or THG of the solid state laser (Nd:YAG) are misaligned. Get on to Laser company.

2. **Wavelengths are not the correct ones.**
   2.1. Spectrometer can be saturated because too much light enters in the fiber optics.
   2.2. Redo the calibration of the both galvo1 and galvo2.
   2.3. Spectrometer could be damaged or broken.
   2.4. Optical fiber could be damaged or broken.
3. **No radiation comes out at all.**
   3.1. Check if the shutter is on. If not make it on.
   3.2. See manual of the laser or get on to Laser company.

### 17.2.5. Calibration

1. **Energy of the laser is not enough.** This could be due to the following.
   1.1. Lower voltage than 440 V applied to the Pocket Cell (PC). Increase this value up to 440 V.
   1.2. Calibration is lost. Redo a new calibration adjusting only galvo2 but checking that wavelengths are the correct. That is to say galvo1 values still valid.
   1.3. Optical path of the either OPO or SHG is misaligned. Get on to Laser company.
   1.4. SHG or THG of the solid state laser (Nd:YAG) are misaligned. Get on to Laser company.
2. **Wavelengths are not the correct ones.**
   2.1. Spectrometer can be saturated because too much light enters in the fiber optics.
   2.2. Redo the calibration of the both galvo1 and galvo2.
3. **No radiation comes out at all.**
   3.1. Check if the shutter is on. In that case make it on.
   3.2. See manual of the laser or get on to Laser company.

## 17.3. Simulations (Wolfram Mathematica software)

### 17.3.1. **Simulation of responses**

```
ClearAll["Global'*"]
(*Stray light "elastic"*)
A5=2000;\[Mu]2=-1*10^-7;\[Sigma]1=(9*10^-9)/2.3528;y5=0;A7=0;\[Tau]5=(9*10^-9)/2.3528;x7=0;y7=0;
(*GAUSSIAN-Laser pulse*)
A1=10;\[Mu]1=-1*10^-7;\[Sigma]1=(9*10^-9)/2.3528;y5=0;
(*Value of exponential of SO2 Max.*)
A2=3;\[Tau]2=36*10^-9;x1=0;y2=0;
(*Value of exponential of NO Min.*)
A3=40;\[Tau]3=2000*10^-9;x2=0;y3=0;A4=0;\[Tau]4=\[Infinity];
(*Value of exponential of NO2*)
A6=0;\[Tau]4=200*10^-9;x3=0;y6=0;
(*Value of integration limits*limit 2 equal to limit 3 or limit 3 = limit2 + 0.1*10^-7*)
lim1=0.9*10^-7;lim2=2.6*10^-7; lim3=0.1*10^-7+lim2;lim4=0.1*10^-7+lim2+(lim2-lim1);
(*Equations*)
g[x_]:=y5+A1 (E^(( -(x-\[Mu]1)^2/(2 \[Sigma]1^2)))) /(\[Sigma]1 Sqrt[2 \[Pi]]);
U[x_]:=A5 (E^(( -(x-\[Mu]2)^2/(2 \[Sigma]1^2)))) /(\[Sigma]1 Sqrt[2 \[Pi]]);
V[x_]:= E^( -(x-x1)/\[Tau]5);
h[x_]:=y2+A2 E^( -(x-x1)/\[Tau]2);
j[x_]:=y3+A3 E^( -(x-x2)/\[Tau]3);
f[x_]:=y6+A6 E^( -(x-x3)/\[Tau]4);
z[x_]:=y2+A2 E^( -(x-x1)/\[Tau]2)+A3 E^( -(x-x1)/\[Tau]3)+A4 E^( -(x-x1)/\[Tau]4)+A6 E^( -(x-x3)/\[Tau]5);

(*Convolution for Stray Light*)
k[x_]:=\!\(
\*SubsuperscriptBox[\(\[Integral]\), \(1*
\*SuperscriptBox[\(10\), \(-10\)]\), \(4.0*
\*SuperscriptBox[\(10\), \(-5\)]\)]\(U[x - y] V[x] \[DifferentialD]x\)\)
```

```
ConvK=Simplify[k[x]]

(*Convolution for SO2*)
ConvA[x_]:=\!\(
\*SubsuperscriptBox[\(\[Integral]\), \(1*
\*SuperscriptBox[\(10\), \(-10\)]\), \(4.0*
\*SuperscriptBox[\(10\), \(-5\)]\)]\(g[x - y] h[x] \[DifferentialD]x\)\)
ConvAS=Simplify[ConvA[x]]

(*Convolution for NO*)
ConvB[x_]:=\!\(
\*SubsuperscriptBox[\(\[Integral]\), \(1*
\*SuperscriptBox[\(10\), \(-10\)]\), \(4.0*
\*SuperscriptBox[\(10\), \(-5\)]\)]\(g[x - y] j[x] \[DifferentialD]x\)\)
ConvBS=Simplify[ConvB[x]]

(*Convolution for NO2*)
ConvD[x_]:=\!\(
\*SubsuperscriptBox[\(\[Integral]\), \(1*
\*SuperscriptBox[\(10\), \(-10\)]\), \(4.0*
\*SuperscriptBox[\(10\), \(-5\)]\)]\(g[x - y] f[x] \[DifferentialD]x\)\)
ConvDS=Simplify[ConvD[x]]

(*Convolution for tri-exponential*)
ConvBi[x_]:=\!\(
\*SubsuperscriptBox[\(\[Integral]\), \(1*
\*SuperscriptBox[\(10\), \(-10\)]\), \(4.0*
\*SuperscriptBox[\(10\), \(-5\)]\)]\(g[x - y] z[x] \[DifferentialD]x\)\)
ConvBiS=Simplify[ConvBi[x]]


(*Sum of convolutions for NO and SO2 plus stray light*)
```

**53.** S[x_]:=ConvA[x]+ConvB[x]+k[x]

**54.** (*Suma of convolutions for SO2 Max. plus stray light*)

**55.** T[x_]:=ConvA[x]+k[x]

**56.** (*Suma of convolutions for SO2 Min. plus stray light*)

**57.** M[x_]:=ConvB[x]+k[x]

**58.** (*Plotting*)

**59.** G=Plot[{S[x],ConvA[x],ConvB[x],k[x]},{y,5*10^-8,5.0*10^-7},GridLines->{{{lim1,Directive[Red,Thick]},{lim2,Directive[Red,Thick]},{lim3,Directive[Blue,Thick]},{lim4,Directive[Blue,Thick]}},{0}},PlotStyle->Thick,PlotRange-> Full,FrameLabel->{"Time / s","Intensity / mV","",""},Frame->True,RotateLabel->True,PlotLabel->Style["Signal simulation for SO2 and NO at 220.2 nm",Black,30],LabelStyle->Directive[Black,20]]

**60.** Gl=LogLinearPlot[{S[x],ConvA[x],ConvB[x],k[x]}, {y,5*10^-8,2.0*10^-5},GridLines->{{{lim1,Directive[Red,Thick]},{lim2,Directive[Red,Thick]},{lim3,Directive[Blue,Thick]},{lim4,Directive[Blue,Thick]}},{0}},PlotStyle->Thick,PlotRange-> Full,FrameLabel->{"Time / s","Intensity / mV","",""},Frame->True,RotateLabel->True,PlotLabel->Style["Signal simulation for SO2 and NO at 220.2 nm",Black,30],LabelStyle->Directive[Black,20]]

**61.** (*Alfa calculation with NO signal*)

**62.** IntAConB=NIntegrate[ConvB[x],{y,lim1,lim2}];

**63.** IntBConB=NIntegrate[ConvB[x], {y,lim3,lim4}];

**64.** alfa=\[Alpha]/.NSolve [{IntAConB-IntBConB*\[Alpha]==0},{\[Alpha]}, Reals, WorkingPrecision-> 10];

**65.** (*Window1-Window2*)

**66.** IntSignal=NIntegrate[S[x],{y,lim1,lim2}]-alfa*NIntegrate[S[x],{y,lim3,lim4}];

**67.** IntAStray =NIntegrate[ConvA[x]+k[y],{y,lim1,lim2}];

**68.** IntStray=NIntegrate[k[y],{y,lim1,lim2}];

**69.** IntaStray =NIntegrate[ConvA[x],{y,lim1,lim2}];

**70.** {"alfa factor",alfa,"NO first gate integral", IntAConB,"NO second gate integral", IntBConB,"Integral SO2 corrected",IntSignal,"Integral SO2 plus stray light", IntAStray}

```
71. (*Export data*)
72. Export["C:\\Users\\Edu\\Desktop\\TUM\\Maths\\Factor\\thesis\\Signal
    simulationSO2andNOB.tiff",G, "Graphics",ImageResolution->5000,ImageSize->{900,600}];
73. Export["C:\\Users\\Edu\\Desktop\\TUM\\Maths\\Factor\\thesis\\Signal
    simulationSO2andNO_logB.tiff",Gl, "Graphics",ImageResolution->5000,ImageSize-
    >{900,600}];
```

### 17.3.2. **Simulation of signal strength**

```
1. rutageneral="C:\\Users\\Edu\\Desktop\\TUM\\Maths\\Signal_strength\\prediction_100m
   V stray light_650uJ\\";
2. ruta1="1000ppb_min220.2.txt";
3. ruta2="straylight_100mV.txt";
4. ruta3="1000ppb_min220.2_straylight_100mV.gif";
5. nml1=StringJoin[rutageneral,ruta1];
6. nml2=StringJoin[rutageneral,ruta2];
7. nml3=StringJoin[rutageneral,ruta3];

8. (*PARAMETERS AND VALUES*)
9. Volt=670 (*Volt PMT*);
10. G=10^(8.088397*Log10[Volt]-17.403)(* Gain of PMT*);
11. conc=1000(*Concentration of SO2 / times 1ppbv*)
12. A2=0.1 (* Stray light coeficient in V*);
13. p=500;(*Energy uJ*)
14. q=1/(36*10^-9)/(1/(36*10^-9)+6.2*10^6)(*Fluorescence yield [1,2]*);
15. \[Sigma]=30*10^-18 (*Cross section for 220.2 cm^2 [3]*);
16. a=Pi*0.3^2(*Pin-hole radius cm^2*);
17. l1=2.4(*Probe distance cm*);
18. a2=1(*20*Pi*1.3^2 Area of FC / cm^2*);
19. l2=1(*12*High of FC / cm*);
20. f=1(*Population of SO2 in 000 level*);
21. btz=1.2(*CSSLB correction*);
22. P=(btz*900*10^-6)/((6.386*10^-34*3*10^8)/(220.2*10^-9))(*Photons*);
```

```
k=1(*Signal/processing electronic for PMT*);
S=1(*Optical saturation parameter*);
dia=100(*Diameter of lense / mm*);
foc=125 (*Focal length of lense / mm*);
R=100000(*Impedance of scope-input channel / Ohm*);
Q=1.6*10^-19(*Electron charge / C*);
t=4*10^-9(*Anode pulse FWHM / s*);
Tita=Solve[\[Theta]==ArcSin[dia/(2*foc)],{\[Theta]}] (*Angle of NA=nimerical apperture*);
Tita1=\[Theta]/.Tita[[1]];
Efficiency=\[Gamma]*\[Rho]*\[Beta]*\[Phi] ;
\[Rho]=(2*\[Pi]*(1-Cos[Tita1]))/(4*\[Pi])(*Solid angle / sr*);
\[Gamma]=1-4*0.015(*Optical efficientcy*);
\[Beta]=0.75(**);
\[Phi]=0.25(*PMT efficiency at 320 nm*);


(*SIGNAL STRENGTH DEFINITION*)
k*conc*f*S*\[Gamma]*\[Rho]*\[Beta]*\[Phi]*q*(a*l1)/(a2*l2) (1-Exp[-((P*\[Sigma])/a)])
A3=(k*Q*G*SO2*f*S*\[Gamma]*\[Rho]*\[Beta]*\[Phi]*q*R)/t*(a*l1)/(a2*l2) (1-Exp[-((P*\[Sigma])/a)]);
Klass=NSolve[x==(k*Q*G*conc*f*S*\[Gamma]*\[Rho]*\[Beta]*\[Phi]*q*R)/t*(a*l1)/(a2*l2) (1-Exp[-((P*\[Sigma])/a)]),{x}];(** V **)
l1=x/.Klass[[1]]


(*PLOTS OF SIGNAL STRENGTH LINEARITY AND ENERGY*)
Plot1=Plot3D[(k*Q*G*conc*f*S*\[Gamma]*\[Rho]*\[Beta]*\[Phi]*q*R)/t*(a*l1)/(a2*l2) (1-Exp[-((P*\[Sigma])/a)]),{P,(100*10^-6)/((6.36*10^-34*3*10^8)/(220.6*10^-9)),(1500*10^-6)/((6.36*10^-34*3*10^8)/(220.6*10^-9))},{conc,1,2000},PlotStyle->Thick,PlotLabel->Style[" Linear response of PMT vs SO2 concentrations and Nº Photons ",Black,35],LabelStyle->Directive[Black,30],AxesLabel->{" Pin-hole radius / cm "," Concentration / ppbv "," Voltage / V ","","","","","","","","",""}]
```

```
Export["C:\\Users\\Edu\\Desktop\\TUM\\Maths\\LinearvsEnergy.gif",Plot1,
"Graphics",ImageResolution->2000,ImageSize->{1200,1200}];

Plot2=Plot3D[(1-Exp[-((P*\[Sigma])/a)]),{a,0.1,1},{P,(100*10^-6)/((6.36*10^-
34*3*10^8)/(220.6*10^-9)),(1500*10^-6)/((6.36*10^-34*3*10^8)/(220.6*10^-
9))},PlotStyle->Thick,PlotLabel->Style[" Optical pumping vs. photon density and pin-hole
radius ",Black,35],LabelStyle->Directive[Black,30],AxesLabel->{" Pin-hole radius / cm "," 
Nº Photons ","","","","","","","","","","","","}]

Export["C:\\Users\\Edu\\Desktop\\TUM\\Maths\\EnergyvsPhoton.gif",Plot2,
"Graphics",ImageResolution->2000,ImageSize->{1200,1200}];


(*DATA FOR LINEARITY CHECKING AND FITTING*)
PP[CSO2_]:=(k*Q*G*CSO2*f*S*\[Gamma]*\[Rho]*\[Beta]*\[Phi]*q*R)/t*(a*l1)/(a2*l2)
(1-Exp[-((P*\[Sigma])/a)])
datCSO2x=Block[{$MaxPrecision=5},Flatten[Table[{PP[CSO2]+A2},{CSO2,N[1,5],N[1000,5],
N[10,5]}]]];
datCSO2y=Block[{$MaxPrecision=5},Flatten[Table[{CSO2},{CSO2,N[1,5],N[1000,5],N[10,5]}
]]];
dataCSO2S=Transpose[{datCSO2y,datCSO2x}];
{"concentration / ppbv, signal strength / V",dataCSO2S}
Export["C:\\Users\\Edu\\Desktop\\TUM\\Maths\\Signal_strength\\dataVoltageCSO2.txt"
,dataCSO2S,"Table"];
Ajuste1=LinearModelFit[dataCSO2S,{1,x},x]
R1=Ajuste1["RSquared"];{"R2",R1}
ListLinePlot[Ajuste1["FitResiduals"],InterpolationOrder->9,Frame->True]
Ajuste1["ParameterTable"]


(*RATIOA AND RATIOB CALCULATION*)
g[x_]:=A1 (E^(( -(x-\[Mu]1)^2/(2 \[Sigma]1^2)))) /(\[Sigma]1 Sqrt[2 \[Pi]]);
```

```
h[x_]:=E^( -(x)/\[Tau]2);
m[x_]:=A2 (E^(( -(x-\[Mu]1)^2/(2 \[Sigma]1^2)))) /(\[Sigma]1 Sqrt[2 \[Pi]]);
n[x_]:=E^( -(x)/\[Tau]3);
A1=I1;\[Mu]1=-1*10^-7;\[Sigma]1=(9*10^-9)/2.3528;\[Tau]2=36*10^-9;\[Tau]3=(9*10^-9)/2.3528;
lim1=0.9*10^-7;lim2=2.9*10^-7;
ConvA[x_]:=\!\(
\*SubsuperscriptBox[\(\[Integral]\), \(1*
\*SuperscriptBox[\(10\), \(-10\)]\), \(4.0*
\*SuperscriptBox[\(10\), \(-5\)]\)]\(g[x - y] h[x] \[DifferentialD]x\)\)
ConvB[x_]:=\!\(
\*SubsuperscriptBox[\(\[Integral]\), \(1*
\*SuperscriptBox[\(10\), \(-10\)]\), \(4.0*
\*SuperscriptBox[\(10\), \(-5\)]\)]\(m[x - y] n[x] \[DifferentialD]x\)\)
T[x_]:=ConvA[x]+ConvB[x]
findMA =FindMaximum[ConvA[x],{y,-\[Mu]1}];
findMB =FindMaximum[ConvB[x],{y,-\[Mu]1}];
MaxA=First[findMA];
MaxB=First[findMB];
RatioA=A1/MaxA;
RatioB=A2/MaxB;


(*SIGNAL STRENGTH SIMULATION*)
g[x_]:=RatioA*A1*(E^(( -(x-\[Mu]1)^2/(2 \[Sigma]1^2)))) /(\[Sigma]1 Sqrt[2 \[Pi]]);
h[x_]:=E^( -(x)/\[Tau]2);
m[x_]:=RatioB*A2*(E^(( -(x-\[Mu]1)^2/(2 \[Sigma]1^2)))) /(\[Sigma]1 Sqrt[2 \[Pi]]);
n[x_]:=E^( -(x)/\[Tau]3);

ConvSO2[x_]:=\!\(
\*SubsuperscriptBox[\(\[Integral]\), \(1*
\*SuperscriptBox[\(10\), \(-10\)]\), \(4.0*
```

**88.** *SuperscriptBox[\(10\), \(-5\)]\)]\(g[x - y] h[x] \[DifferentialD]x\)\)

**89.** ConvStray[x_]:=\!\(

**90.** *SubsuperscriptBox[\(\[Integral]\), \(1*

**91.** *SuperscriptBox[\(10\), \(-10\)]\), \(4.0*

**92.** *SuperscriptBox[\(10\), \(-5\)]\)]\(m[x - y] n[x] \[DifferentialD]x\)\)

**93.** L[x_]:=ConvSO2[x]+ConvStray[x]

**94.** ConvAS=Simplify[ConvA[x]]

**95.** {"Covolution of SO2 signal plus stray light",ConvAS}

**96.** G=Plot[{ConvSO2[x],ConvStray[x],L[x]}, {y,5*10^-8,5.0*10^-7},GridLines->{{{lim1,Directive[Red,Thick]},{lim2,Directive[Red,Thick]},{lim3,Directive[Blue,Thick]},{lim4,Directive[Blue,Thick]}},{0}},PlotStyle->Thick,PlotRange-> Full,FrameLabel->{"Time / s","Intensity / V","",""},Frame->True,RotateLabel->True,PlotLabel->Style["Signal Strenght Simulation for SO2 at 220.2 nm",Black,12],LabelStyle->Directive[Black,12]]

**97.** Export[nml3,G,"Graphics",ImageResolution->2000,ImageSize->{1000,1000}];

**98.** dat1x=Block[{$MaxPrecision=10},Flatten[Table[{L[x]},{y,N[5*10^-8,10],N[5.0*10^-7,10],N[1.123*10^-9,10]}]]];

**99.** dat1y=Block[{$MaxPrecision=10},Flatten[Table[{y},{y,N[5*10^-8,10],N[5.0*10^-7,10],N[1.123*10^-9,10]}]]];

**100.** data1S=Transpose[{dat1y,dat1x}];

**101.** Export[nml1,data1S, "Table"];

**102.** dat2x=Block[{$MaxPrecision=10},Flatten[Table[{ConvStray[x]},{y,N[5*10^-8,10],N[5.0*10^-7,10],N[1.123*10^-9,10]}]]];

**103.** dat2y=Block[{$MaxPrecision=10},Flatten[Table[{y},{y,N[5*10^-8,10],N[5.0*10^-7,10],N[1.123*10^-9,10]}]]];

**104.** data2S=Transpose[{dat2y,dat2x}];

**105.** Export[nml2,data2S, "Table"];

**106.** IntConvAB=NIntegrate[ConvA[x],{y,lim1,lim2}];

**107.** (*DATA FOR LINEARITY CHECKING OF INTEGRATED SIGNAL STRENGTH AND FITTING*)

```
g[x_]:=RatioA*A3*(E^(( -(x-\[Mu]1)^2/(2 \[Sigma]1^2)))) /(\[Sigma]1 Sqrt[2 \[Pi]]);
h[x_]:=E^( -(x)/\[Tau]2);
m[x_]:=RatioB*A2*(E^(( -(x-\[Mu]1)^2/(2 \[Sigma]1^2)))) /(\[Sigma]1 Sqrt[2 \[Pi]]);
n[x_]:=E^( -(x)/\[Tau]3);

ConvSO2[x_]:=\!\(
\*SubsuperscriptBox[\(\[Integral]\), \(1*
\*SuperscriptBox[\(10\), \(-10\)]\), \(4.0*
\*SuperscriptBox[\(10\), \(-5\)]\)]\(g[x - y] h[x] \[DifferentialD]x\)\)
ConvStray[x_]:=\!\(
\*SubsuperscriptBox[\(\[Integral]\), \(1*
\*SuperscriptBox[\(10\), \(-10\)]\), \(4.0*
\*SuperscriptBox[\(10\), \(-5\)]\)]\(m[x - y] n[x] \[DifferentialD]x\)\)
T [x_]:=ConvSO2[x]+ConvStray[x]

\[Mu]1=-1*10^-7;\[Sigma]1=(9*10^-9)/2.3528;\[Tau]2=36*10^-9;\[Tau]3=(9*10^-
9)/2.3528;
TS=Simplify[T[x]];
Integrate[T[x],{y,lim1,lim2}];
IntTSO2[SO2_]:=Integrate[T[x],{y,lim1,lim2}];
Intercept=Integrate[ConvStray[x],{y,lim1,lim2}];
{"Stray light or intercept b",Intercept}
datSO2x=Block[{$MaxPrecision=5},Flatten[Table[{IntTSO2[SO2]},{SO2,N[0,5],N[1000,5],
N[10,5]}]]];
datSO2y=Block[{$MaxPrecision=5},Flatten[Table[{SO2},{SO2,N[0,5],N[1000,5],N[10,5]}]]]
;
{"concentration / ppbv, integral / V*s",dataSO2S=Transpose[{datSO2y,datSO2x}]}
Export["C:\\Users\\Edu\\Desktop\\TUM\\Maths\\Signal_strength\\MindataIntegralSO2.
txt",dataSO2S,"Table"];
Ajuste2=LinearModelFit[dataSO2S,{1,x},x]
R2=Ajuste2["RSquared"];{"R2",R2}
ListLinePlot[Ajuste2["FitResiduals"],InterpolationOrder->9,Frame->True]
```

```
Ajuste2["ParameterTable"]
GraphicsGrid[{{ListLinePlot[Ajuste1["FitResiduals"],PlotLabel->Style["Residuals Voltage signal",Black,12],InterpolationOrder->9,Frame->True],ListLinePlot[Ajuste2["FitResiduals"],PlotLabel->Style["Residuals Integral signal",Black,12],InterpolationOrder->9,Frame->True]}}]


(*CALCULATION FOR LIMIT OF DETECTION CRITERIA*)
g[x_]:=RatioA*A1*(E^(( -(x-\[Mu]1)^2/(2 \[Sigma]1^2)))) /(\[Sigma]1 Sqrt[2 \[Pi]]);
h[x_]:=E^( -(x)/\[Tau]2);
w[x_]:=RatioA*A4*(E^(( -(x-\[Mu]1)^2/(2 \[Sigma]1^2)))) /(\[Sigma]1 Sqrt[2 \[Pi]]);
j[x_]:=E^( -(x)/\[Tau]2);
m[x_]:=RatioB*A5*(E^(( -(x-\[Mu]1)^2/(2 \[Sigma]1^2)))) /(\[Sigma]1 Sqrt[2 \[Pi]]);
n[x_]:=E^( -(x)/\[Tau]3);

Conv1SO2[x_]:=\!\(
\*SubsuperscriptBox[\(\[Integral]\), \(1*
\*SuperscriptBox[\(10\), \(-10\)]\), \(4.0*
\*SuperscriptBox[\(10\), \(-5\)]\)]\(g[x - y] h[x] \[DifferentialD]x\)\)
Conv10SO2[x_]:=\!\(
\*SubsuperscriptBox[\(\[Integral]\), \(1*
\*SuperscriptBox[\(10\), \(-10\)]\), \(4.0*
\*SuperscriptBox[\(10\), \(-5\)]\)]\(w[x - y] j[x] \[DifferentialD]x\)\)
ConvStray[x_]:=\!\(
\*SubsuperscriptBox[\(\[Integral]\), \(1*
\*SuperscriptBox[\(10\), \(-10\)]\), \(4.0*
\*SuperscriptBox[\(10\), \(-5\)]\)]\(m[x - y] n[x] \[DifferentialD]x\)\)

T1 [x_]:=Conv1SO2[x]+ConvStray[x]
T10 [x_]:=Conv10SO2[x]+ConvStray[x]
P1[A4_,A5_]:=Integrate[T1[x],{y,lim1,lim2}];
P10[A4_,A5_]:=Integrate[T10[x],{y,lim1,lim2}];
```

**159.** Sry[A5_]:=Integrate[ConvStray[x],{y,lim1,lim2}]

**160.** rat=NSolve[{P10[A4,A5]==10*P1 [A4,A5],P1 [A4,A5]==10*Sry[A5]},{A4,A5}]

**161.** ratA=A4/.rat[[1]]

**162.** ratB=A5/.rat[[1]]

**163.** RAT=ratA/ratB

## 17.4. Literature


1. T. Ebata, O. Nakazawa. M. Ito, *Chem. Phys. Lett.* 143, 31 (1988).
2. Man-Him Hui and S. A. Rice, *Chem. Phys. Lett.* 17, 474 (1972).
3. Y. Matsumi, H. Shigemori, K. Takahashi , *Atmospheric Environment* 39, 3177–3185, (2005).